Heterolytic Activation of Hydrogen Promoted by Ruthenium Nanoparticles immobilized on Basic Supports and Hydrogenation of Aromatic Compounds

by

MINFENG FANG

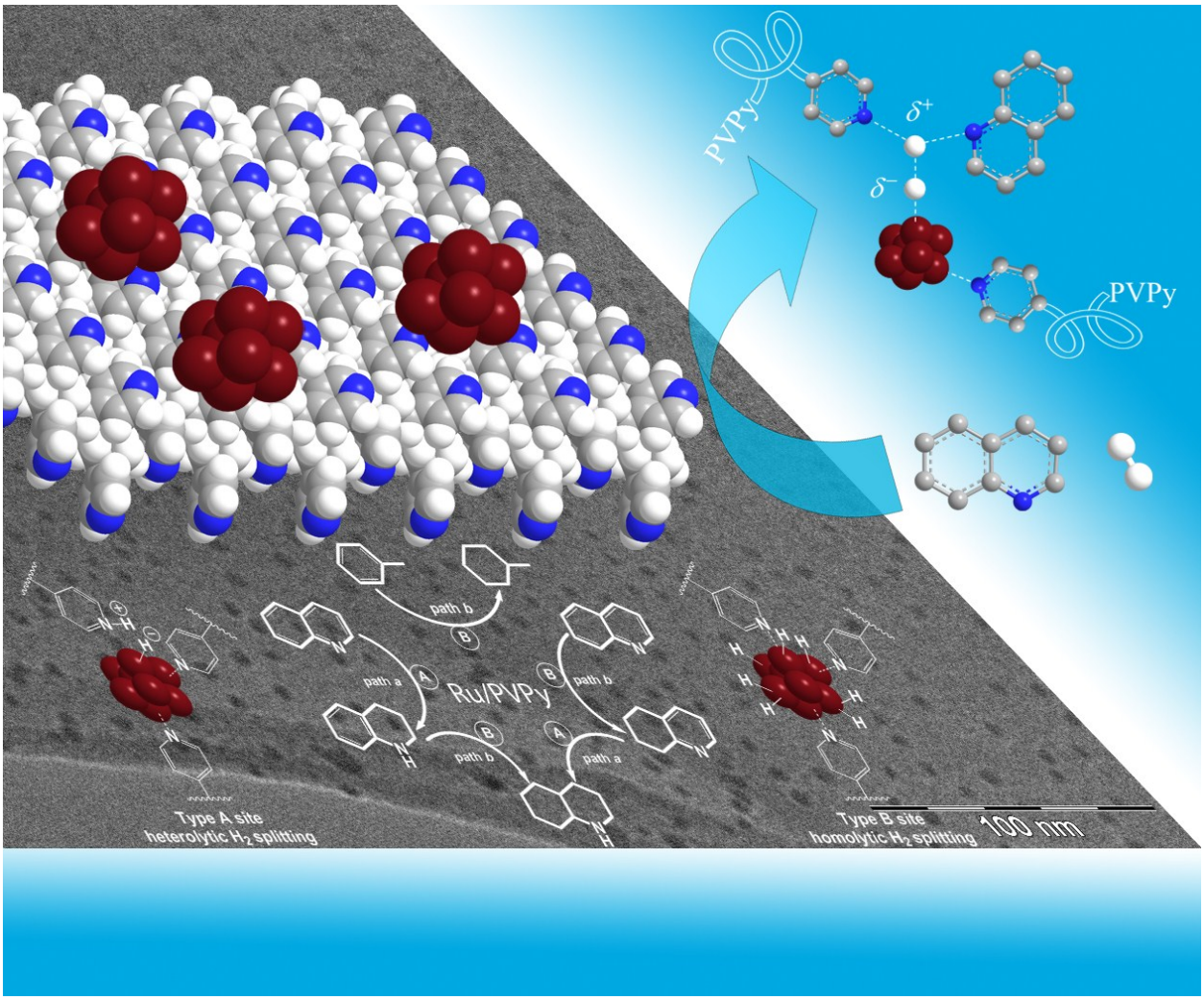

A dissertation submitted to the Graduate Faculty in Chemistry in partial fulfillment of the requirements for the degree of Doctor of Philosophy, The City University of New York

2013

This manuscript has been read and accepted for

the Graduate Faculty in Chemistry in satisfaction of

the dissertation requirements for the degree of Doctor of Philosophy.

Prof. Roberto A. Sánchez-Delgado

Date **Chair of Examining Committee**

Prof. Maria Tamargo

Date **Executive Officer**

Prof. Roberto A. Sánchez-Delgado

Prof. Charles M. Drain

Prof. Maria Contel

Prof. Lynn C. Francesconi

Prof. Andrei Jitianu

Supervisory Committee

THE CITY UNIVERSITY OF NEW YORK

Abstract

Heterolytic Activation of Hydrogen Promoted by Ruthenium Nanoparticles immobilized on Basic Supports and Hydrogenation of Aromatic Compounds

by

MINFENG FANG

Advisor: Roberto A. Sánchez-Delgado

Despite the aggressive development and deployment of new renewable and nuclear technologies, petroleum-derived transportation fuels—gasoline, diesel and jet fuels—will continue to dominate the markets for decades. Environmental legislation imposes severe limits on the tolerable proportion of aromatics, sulfur and nitrogen contents in transportation fuels, which is difficult to achieve with current refining technologies. Catalytic hydrogenation plays an important role in the production of cleaner fuels, both as a direct means to reduce the aromatics and as a key step in the hydrodenitrogenation (HDN) and hydrodesulfurization (HDS) processes. However, conventional catalysts require drastic conditions and/or are easily poisoned by S or N aromatics. Therefore, there is still a need for new efficient catalysts for hydrogenation reactions relevant to the production of cleaner fossil fuels.

Our catalyst design involves metallic nanoparticles intimately associated with a basic support, with the aim of creating a nanostructure capable of promoting the heterolytic activation of hydrogen and ionic hydrogenation mechanisms, as a strategy to avoid catalyst poisoning and enhance catalytic activity.

We have designed and prepared a new nanostructured catalytic material composed of RuNPs immobilized on the basic polymer P4VPy. We have demonstrated that the Ru/P4VPy catalyst can promote heterolytic hydrogen activation and a unique surface ionic hydrogenation mechanism for the efficient hydrogenation of N-aromatics. This is the first time these ionic hydrogenation pathways have been demonstrated on solid surfaces. For the RuNPs surfaces without basic sites in close proximity, the conventional homolytic H_2 splitting is otherwise involved.

Using the mechanistic concepts from Ru/P4VPy, we have designed and prepared the Ru/MgO catalyst, with the aim to improve the catalytic efficiency for the hydrogenation of heteroatom aromatics operating by the ionic hydrogenation mechanism. The Ru/MgO catalyst significantly improves the catalytic efficiency for hydrogenation of a variety of N-/S-heteroaromatics and mono-/polycyclic aromatic hydrocarbons representative of components of petroleum-derived fuels. The catalyst is superior to the few other known supported noble metal catalysts for these reactions. Mechanistic studies also point to the ionic hydrogenation mechanism on the Ru/MgO surfaces. In addition, the Ru/MgO catalyst is highly recyclable and long-lived.

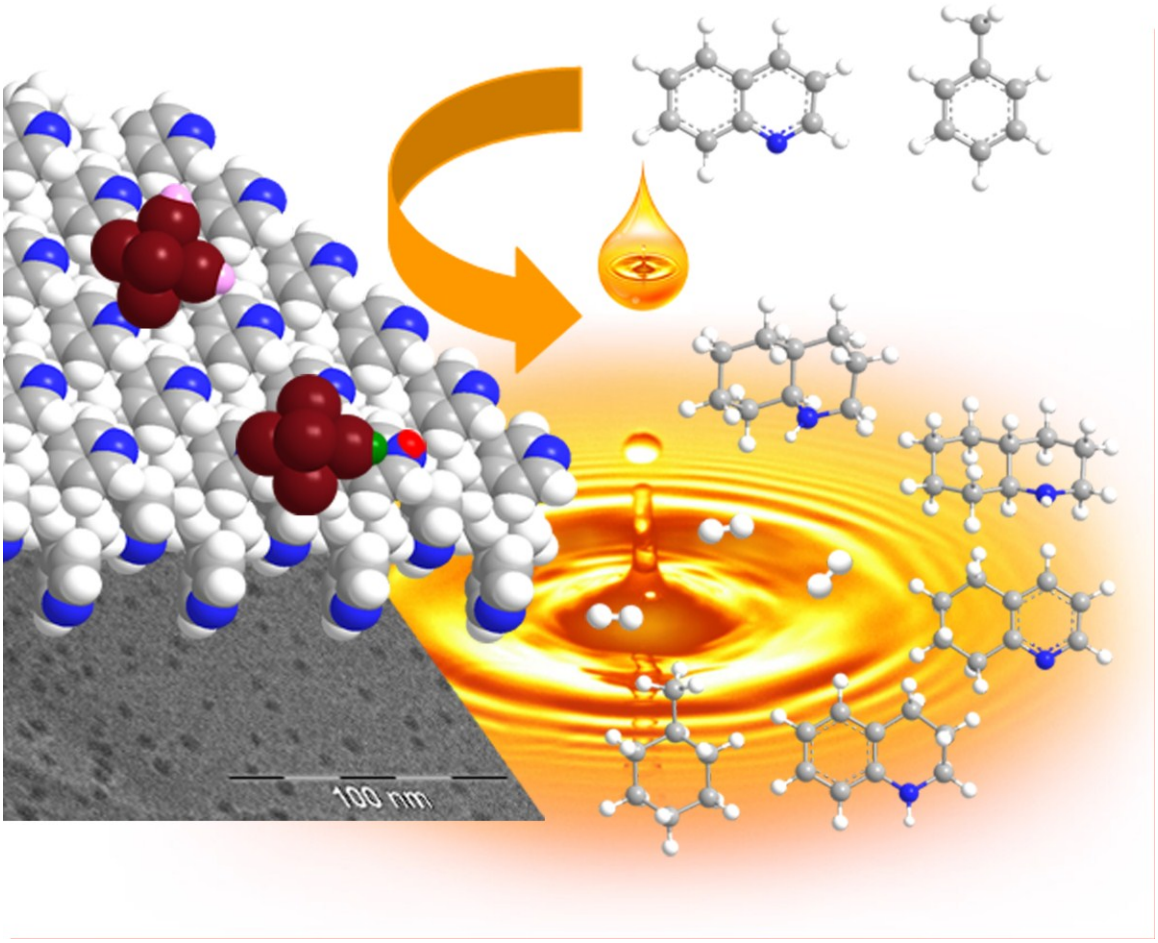

(The two distinct sites on the Ru/P4VPy surfaces for a unique heterolytic hydrogen activation and a conventional homolytic hydrogen splitting, both acting in parallel for hydrogenation of quinoline and toluene.)

(Cover image: the model of the dual-site structure of the Ru/P4VPy catalyst and the corresponding hydrogenation pathways, wherein heterolytic splitting of H_2 is assisted by the support.)

Dedicated to My Family

Acknowledgments

I am heartily thankful to many people who have contributed in numerous ways to the successful outcome of this dissertation work. Foremost, I owe special thanks to my advisor Prof. Roberto A. Sánchez-Delgado for his guidance, encouragement and constant support throughout the whole course of my Ph.D. studies. I am also grateful to my other committee members Prof. Charles M. Drain, Prof. Maria Contel, Prof. Lynn Francesconi and Prof. Andrei Jitianu for their critical questions, insightful suggestions and illuminating comments during committee meetings, which motivated me to evaluate my research from different perspectives. I would also like to thank all my teachers and colleagues who helped, supported and encouraged me all the way to the completion of my Ph.D. studies.

I would like to extend my great appreciation to my family and all my friends for their support and encouragement towards the competition of my educational endeavor.

Finally I acknowledge the Chemistry Department at the Graduate Center and the Department of Chemistry of the Brooklyn College, the City University of New York for their support throughout the duration of my graduate studies.

Table of Contents

List of Symbols and Abbreviations

BET	Brunauer–Emmett–Teller
BT	benzothiophene
Btu	British thermal unit
CARB	the California Air Resources Board
CCD	charge-coupled device
CNFs	carbon nanofibers
C-THQ	5,6,7,8-tetrahydroquinoline
D	metal dispersion
DBT	dibenzothiophene
DDS	direct desulfurization
DHBT	dihydrobenzothiophene
DHQ	decahydroquinoline
4,6-DMDBT	4,6-dimethyldibenzothiophene
EDX	energy-dispersive X-ray spectroscopy
FDU-15	Fudan University No.15
HAP	hydroxyapatite
HDA	hydrodearomatization
HDN	hydrodenitrogenation
HDS	hydrodesulfurization
HYD	hydrogenation
ICDD	the International Center for Diffraction Data
ILs	ionic liquids

JCPDS	the Joint Committee on Powder Diffraction Standards
MAH	monocyclic aromatic hydrocarbon
MCM-41	Mobile composition of matter No. 41
MeCy	methylcyclohexane
MgO^*	a MgO powder prepared in the lab
MgO_{500}	the commerical MgO powder calcined at 500 °C for 2h
MMT	montmorillonite
mol%	mole percent
NPs	nanoparticles
N-THQ	1,2,3,4-tetrahydroquinoline
P4VPy	poly(4-vinylpyridine)
PAH	polycyclic aromatic hydrocarbon
PDF	Powder Diffraction File
PDMP	polydimethylphosphazene
POM	polyoxomolybdate
PVP	poly(N-vinyl-2-pyrrolidone)
PXRD	powder X-ray diffraction
Q	quinoline
$Ru(acac)_3$	$Ru(acetylacetonate)_3$
Ru(COD)(COT)	Ru(1,5-cyclooctadiene)(1,3,5-cyclooctatriene)
SBA-15	Santa Barbara amorphous No. 15
SEM	scanning electron microscopy
T	thiophene

TEM	transmission electron microscopy
THF	tetrahydrofuran
TOF	turnover frequency
TOF_{corr}	TOF corrected for the number of surface Ru atoms
Tol	toluene
TPD	temperature-programmed desorption
TTO	total turnover
UHV	ultra-high vacuum
ULSD	ultra low sulfur diesel
UV–Vis	ultraviolet–visible spectroscopy
v%	volume percent
wt%	weight percent
XPS	X-ray photoelectron spectroscopy

List of Figures

List of Schemes

List of Tables

Chapter 1
Background and Significance

1.1 Fossil fuels: the predominant energy sources

"Fossil fuels – coal, oil and natural gas – currently provide more than 85% of all the energy consumed in the United States, nearly two-thirds of our electricity, and virtually all of our transportation fuels. Moreover, it is likely that the nation's reliance on fossil fuels to power an expanding economy will actually increase over at least the next two decades even with aggressive development and deployment of new renewable and nuclear technologies."

——Department of Energy, U.S.A[1]

Despite the aggressive development of renewable energy sources, fossil fuels—coal, oil and natural gas—are still the predominant sources of energy in the United States. According to the U.S. Department of Energy, fossil fuels currently provide over 80% of all energy consumed in the nation (Figure 1-1).[2] While the renewable energy production

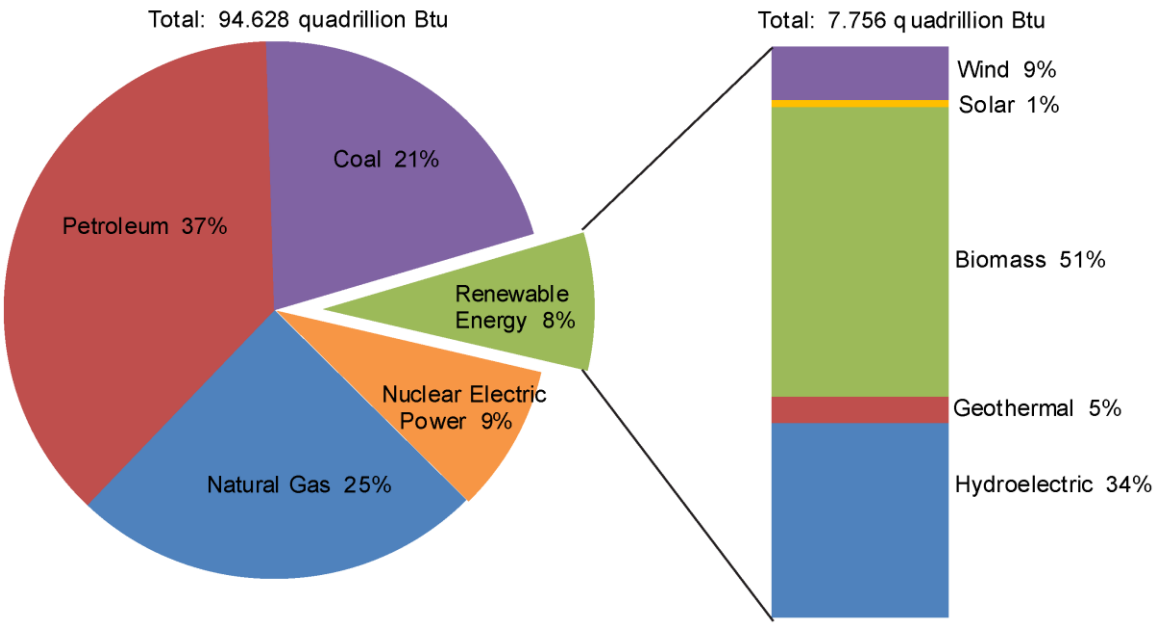

Figure 1-1. U.S. energy consumption in 2009.[2]

is expected to grow rapidly in the future, its increased implementation will be limited by a number of economic, technical and social barriers. Therefore, as the consumption of all fuels increases significantly, fossil fuels will contribute a major part of the total share of energy production towards 2035, with a 78% share of total energy in 2035 (Figure 1-2).[3]

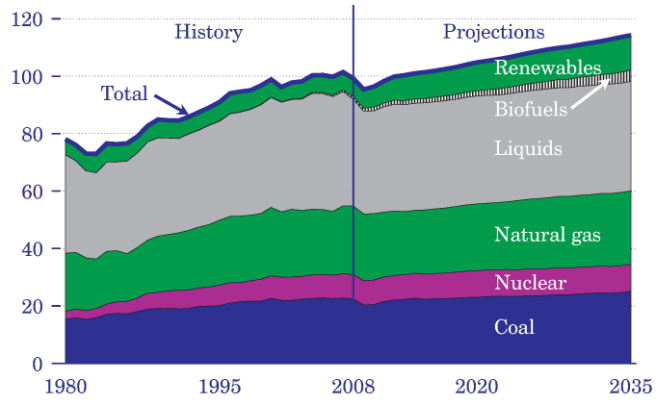

Figure 1-2. US energy use by fuels, 1980–2035 (quadrillion Btu).[3]

The predominance of fossil fuels over other energy sources will continue in the foreseeable future not only in the U.S. but also worldwide. According to the International Energy Agency,[4] global primary energy demand will increase by about 1.5% to 2.5% per year from now to 2035 and fossil fuels will remain the dominant sources, with about 80% share of the energy demand in 2035 (Figure 1-3).

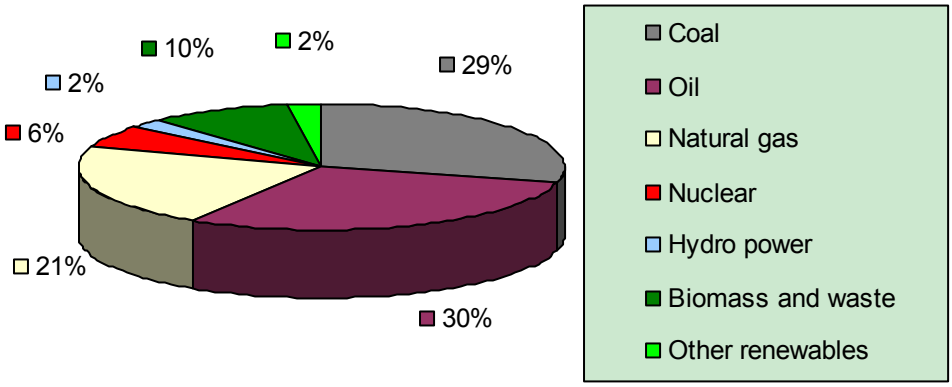

Figure 1-3. Primary global energy demand in 2035.

Fossil fuels are commonly used in the day-to-day generation of electricity and propulsion of vehicles in transportation. In particular, petroleum remains the dominant energy source for transportation, by road, sea and air, though there is increasing competition from alternative fuels, notably biofuels and electricity for cars and trains. The conventional liquid transportation fuels derived from petroleum—gasoline, diesel and jet fuels—will continue to dominate transportation markets for decades.

1.2 Composition of petroleum and environmental impact

Crude oil is a complex mixture of hydrocarbons, heteroatom-containing organic compounds and other chemicals. The composition varies depending where and how the petroleum was formed. Although there is a considerable variation between the ratios of different species, the elemental composition of petroleum is well-defined,[5] as shown in Table 1-1.

Table 1-1. Elemental composition of petroleum[5]

Element	wt%
C	83.0–87.0
H	10.0–14.0
N	0.1–2.0
S	0.05–6.0
O	0.05–1.5
Metal (Fe, Ni, V)	< 0.1

In terms of types of molecules, petroleum consists predominantly of hydrocarbons, mainly as paraffins (alkanes), naphthenes (cycloalkenes), aromatics (arenes) and asphaltenes (large hydrocarbons), of which arenes take a percentage of about 3–30% by weight; it also contains large concentrations of heteroatom-containing compounds, which

span a large range of boiling points in the straight-run distillate fraction. Table 1-2 shows some typical aromatic hydrocarbons and heteroatom compounds found in petroleum fractions. Nitrogen content is usually around 0.1 wt% but may be as high as 2 wt% in crudes, and is generally concentrated in heavier fractions, mainly in the form of basic compounds (pyridine nucleus) and relatively non-basic compounds (pyrrole nucleus). Sulfur is the most abundant heteroatom impurity in petroleum crudes, taking up as high as 6 wt% in some crudes. Apart from thiols, sulfides and disulfides, it exists in the forms of thiophenes, benzothiophenes and dibenzothiophenes.

Table 1-2. Some typical aromatic hydrocarbons and heteroatom compounds in petroleum

Heteroatom compounds	Typical structures
Aromatic hydrocarbons monocyclic	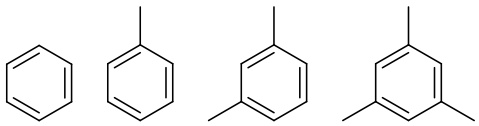
bicyclic	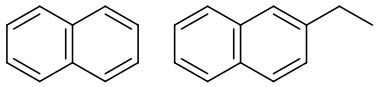
tricyclic	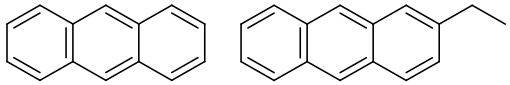
N-heteroaromatics pyrrole nucleus	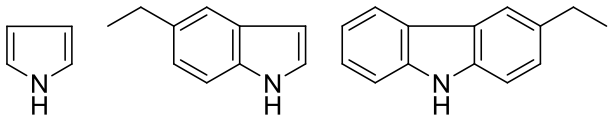
pyridine nucleus	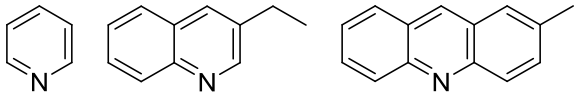
S-heteroaromatics	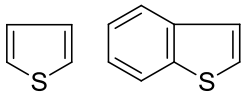
	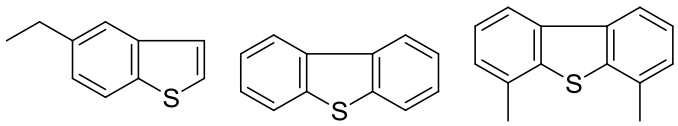
O-heteroaromatics	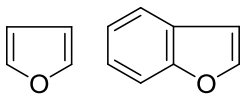

The combustion of fuels derived from petroleum, due to the remainder of aromatic hydrcocarbons, nitrogen and sulfur content, releases harmful emissions such as carcinogenic constituents, NO_x and SO_x, leading to severe direct air pollution, increased level of ozone in troposphere and formation of acid rain. These inevitably render adverse impacts on the environment, threatening all human beings as well as other living organisms.

The problem of current petroleum-derived fuels in the market is that they still contain too much aromatic compounds, nitrogen and sulfur contents from the refinery, especially in developing countries. The complete removal of all those is still a big technology challenge today in fuel refining.

1.3 Legislation and regulation: fuels must be cleaner

To mitigate the environmental impact from combustion of fuels, legislation and regulation have become more and more stringent on the allowable amount of aromatic hydrocarbons as well as nitrogen and sulfur content, leading to increasingly tightened fuel specifications. For example, U.S. federal fuel specifications require the on-road diesel fuel sulfur levels must be reduced to 15 ppm, known as Ultra Low Sulfur Diesel (ULSD);[6] the European Union has an even more severe limit on sulfur content, requiring a level below 10 ppm from January, 2011.[7] The current most stringent fuel specifications perhaps come from the California Air Resources Board (CARB), which limits nitrogen and sulfur not exceeding 10 and 15 ppm, respectively, and aromatic hydrocarbons less than 10%, in which benzene must have a maximum percentage of 0.7% and polycyclic hydrocarbons can not exceed 1.4%.[8-9]

The severe fuel specifications impose significant technical challenges in fuel refining. Especially, considering the current level of oil consumption and the fact that its global reserve is limited, it can be expected that with the passage of time liquid fuels will necessarily come from technically less satisfactory unconventional sources, such as heavy, extra-heavy oil and bitumen deposits, with increasing levels of large polycyclic aromatics, nitrogen and sulfur, all of which need to be removed or transformed to make cleaner fuels.[10] This means the current fuel refining technologies must be improved to more effectively remove aromatic hydrocarbons and heteroatom compounds in order to meet the stringent specifications and environmental objectives.

1.4 Catalytic hydrogenation in fuel manufacture

In fuel refineries, crude petroleum and various refinery streams are subject to a series of hydrotreatment to saturate a variety of unsaturated hydrocarbons and remove heteroatoms such as sulfur, nitrogen, oxygen and metals. Such processes are routinely practiced in the refining industry. Figure 1-4 illustrates the applications of these hydrotreating processes in a hypothetical refinery, in which the desalted crude oil is initially separated into different fractions by distillation and the so-called straight-run fractions are further upgraded in hydrotreaters, where catalytic hydrogenation takes place.

Catalytic hydrogenation plays a pivotal role in the manufacture of cleaner fuels. The proportion of aromatic hydrocarbons is lowered by hydrodearomatization (HDA) process through direct H_2 addition (Scheme 1-1), wherein the hydrogenation reaction initially results in partially de-saturated products, which are subsequently reduced to fully saturated products; the initial reactants, both partially and fully saturated products all co-exist in equilibria. Removal of nitrogen and sulfur aromatics is routinely achieved

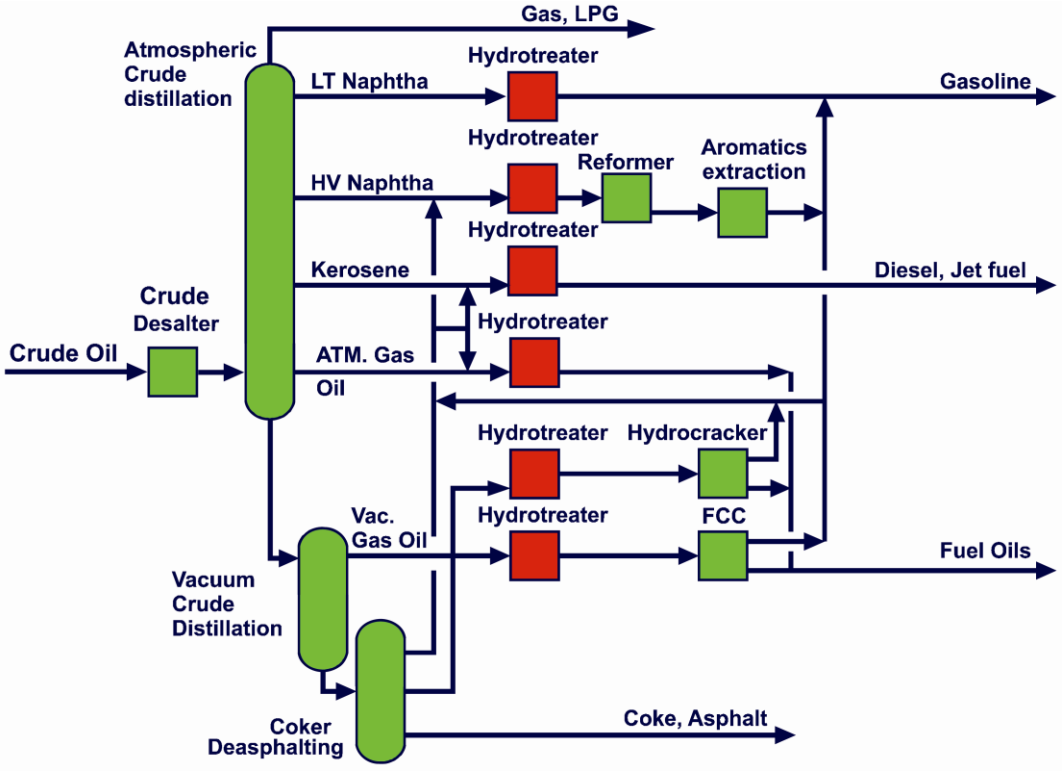

Figure 1-4. The schematic of a simple refinery illustrating hydrotreatment applications.

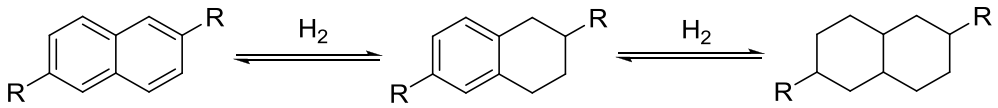

Scheme 1-1. Hydrodearomatization (HDA) process for aromatic hydrocarbons.

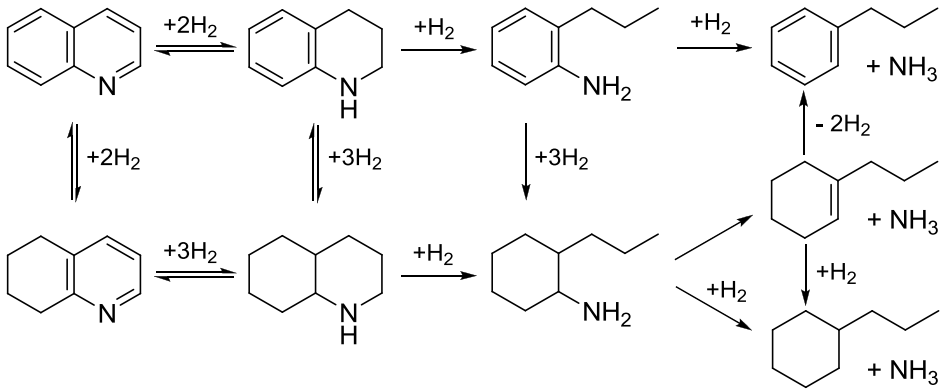

Scheme 1-2. Hydrodenitrogenation (HDN) process for quinoline.

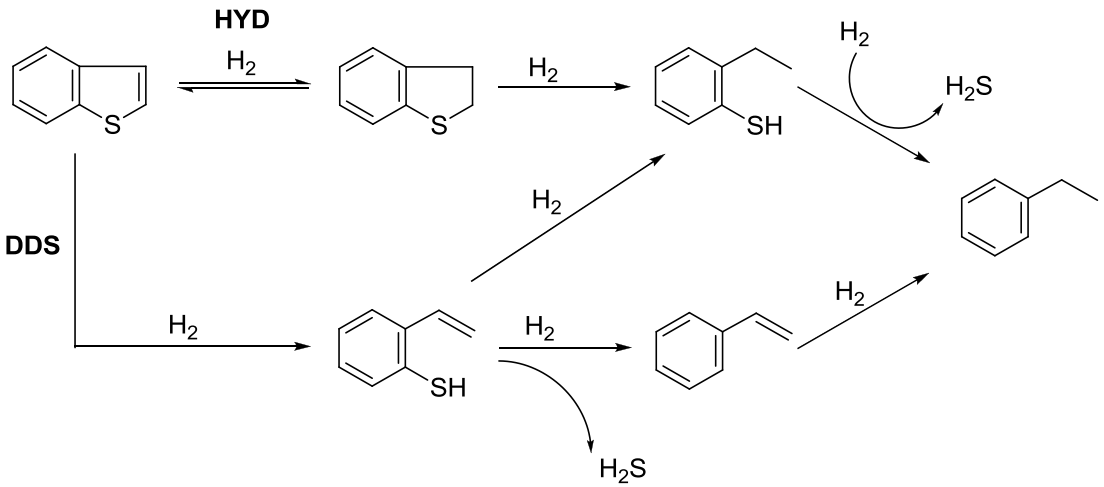

Scheme 1-3. Hydrodesulfurization (HDS) process for benzothiophene.

through hydrodenitrogenation (HDN) and hydrodesulfurization (HDS) processes, as exemplified for quinoline in Scheme 1-2 and for benzothiophene in Scheme 1-3, respectively. The HDN scheme is essentially a combination of three major types of reactions at catalytic sites: hydrogenation of N-heterocyclic ring, hydrogenation of carbocyclic ring and cleavage of C-N bonds. There are various proposals for the detailed HDN steps, but it is generally accepted that prehydrogenation of at least the N-heterocyclic ring is mandatory for C-N bonds cleavage.[11] For HDS process, there are two alternative pathways suggested in literature: hydrogenation pathway (HYD) and direct desulfurization pathway (DDS). The former involves prehydrogenation of S-heterocyclic ring prior to C-S bond scission, while in the latter the initial step is the direct cleavage of C-S bond. Whether or not the DDS pathway involves prehydrogenation in the initial step to form prehydrogenated S-intermediates is still under debate, and there are always contradictory proposals by different authors.[12] On balance, it appears likely that for large S-containing compounds, which constitute the majority of S-heteroaromatics in petroleum, prehydrogenation paths are competitive and even necessary. Overall, catalytic hydrogenation is a key step in fuel upgrading, and the efforts to make cleaner fuels

should be directed towards the promotion of more efficient hydrogenation reactions in refining.

1.5 Hydrogenation catalysts in fuel upgrading

Heterogeneous catalysis is dominant in industrial practice not only because of the stability of solid catalysts under industrial conditions but also because of the easy separation and recycling of solid catalysts. Most catalysts used for fuel upgrading are conventional sulfided metal catalysts such as Co-Mo, Ni-Mo and Ni-W catalysts with combination of active elements. Nevertheless, these catalysts require drastic reaction conditions (300–400 °C, 50–100 atm) for HDN and HDS reactions. On the other hand, hydrogenation of aromatic hydrocarbons is exothermic and reversible (Scheme 1-1): complete conversion is not possible owing to the equilibrium limitations; at the same high temperatures required for HDN and HDS reactions, the conversion of aromatic hydrocarbons is actually unfavorable. Thus only a moderate proportion of aromatic hydrocarbons can be saturated under typical hydrotreating conditions due to the thermodynamic equilibrium limitations.[12]

Supported noble metal catalysts (*e.g.* Pt, Pd) can function at lower temperatures far from equilibrium conditions but often they are easily poisoned by small amounts of N- and S-containing compounds present in refinery feeds. The heteroatoms can bind strongly to the metallic sites through σ-bonding and do not leave easily, leading to the loss of activity of metallic sites. Therefore, supported noble metal catalysts are generally used for sulfur- and nitrogen-free feedstocks.[13]

Homogeneous catalysts are rarely exploited in industry due to the impractical and expensive separation and recycling, although they can work under very mild conditions,

have high selectivity and render easier tuning of catalytic properties. Moreover, the catalytic activities of metal complexes towards aromatic hydrocarbons in solution are very limited.

Therefore, there is a continuing need for new efficient catalysts capable of promoting hydrogenation of aromatics under moderate reaction conditions (temperature under 150 °C, pressure below 50 atm) while being resistant to poisoning by nitrogen and sulfur containing species in the feeds.

1.6 Transition metal nanoparticles as catalysts

Although hydrogenation by metals is a well developed field,[14-15] the use of nanoparticles (NPs) in catalysis has been attracting increasing interest owing to the advantageous activity and selectivity features associated with the small particle size.[16] Metal nanoparticles dispersed in liquid phases exhibit interesting catalytic properties but they are unstable and difficult to recover. It is important to stabilize them against aggregation and to control their spatial arrangement. Stabilization of metal suspensions can be achieved by use of ligands, surfactants or ionic liquids (ILs) but immobilizing nanoparticles on solid supports can be more advantageous. There have been a large number of publications in the literature on supported metal nanoparticles, and I will provide a brief overview in Chapter 2 on the preparation and characterization of nanoparticles, and different supports used, with emphasis on ruthenium nanoparticles. Generally, these supports include carbon, alumina, silica, zeolite, montmorillonite (MMT), hydroxyapatite (HAP) and polymers. The role of these supports, in most instances, is to avoid NPs aggregation and to facilitate catalysts recovery for recycling, but seldom to intervene directly in the key steps of the reaction.

1.7 Hydrogenation mechanisms on solid surfaces

Concerning hydrogenation mechanisms, the most widely accepted pathway on solid catalysts involves the homolytic splitting of hydrogen molecules into hydrogen atoms on the metal surface, followed by transfer to the chemisorbed substrate and subsequent desorption of hydrogenated products from the surface (Scheme 1-4).[14-15] The intimate details of how these steps take place depend on the specific composition and structure of the catalysts. Catalyst poisoning usually occurs when the chemisorbed species are S- or N-containing compounds, which bond to metals strongly and subsequently block the sites for further hydrogen activation, leading to catalyst deactivation or reaction ceases when enough S-/ N-species are present blocking all available catalytic sites.

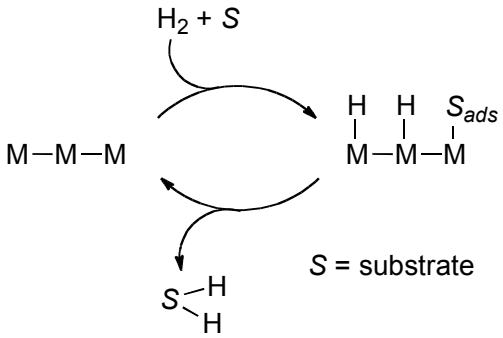

Scheme 1-4. Homolytic splitting of hydrogen and hydrogen transfer on metallic surface.

An interesting alternative hydrogenation pathway on solid surface is the base-assisted heterolytic splitting of H_2 into H^+ and H^- (Scheme 1-5), which are attached to the base and metal, respectively, and subsequently transferred to the polar bonds of substrates being hydrogenated in a concerted way. Such "outer sphere interaction" is advantageous since it does not require the binding of substrates to the metal prior to hydrogen transfer, thus possible sulfur or nitrogen poisoning of active metal centers can be avoided, leading to enhanced catalytic activities. A base is necessary as the proton receptor for this mechanism, which can be an external base or a basic functionality on the support.

Scheme 1-6 hypothetically illustrates the ionic pathway on solid catalyst surface comprising metal NPs and basic sites from support, for hydrogenation of the C-N bond of pyridine. Heterolytic H_2 activation and ionic mechanisms are common in solution, notable examples being hydrogenation of C=O and C=N bonds by Noyori's catalysts.[17] However, they are extremely rare on solid surfaces.

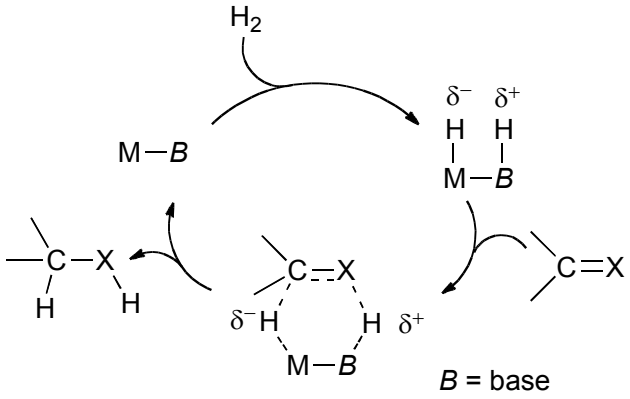

Scheme 1-5. Heterolytic splitting of hydrogen and ionic hydrogenation mechanism.

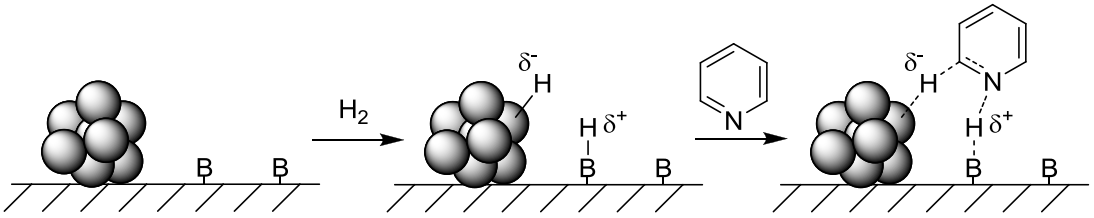

Scheme 1-6. Heterolytic H_2 activation and transfer to pyridine's C-N bond envisaged on solid catalyst surface comprising metal NPs and basic functionalities from support.

Heterolytic hydrogen activation has been envisaged as a possible reaction pathway on metal sulfide catalysts, with surface sulfur sites acting as proton acceptors.[18] However, evidence for such mechanism remains extremely scarce for supported metal catalysts; and there are, to our knowledge, no mechanistic studies on supported metal NPs promoting ionic hydrogenation pathways. A supported metal catalyst, with rich basic sites integrated in the support, bears potential surface structure that can provoke ionic hydrogenation mechanism through the metal-base bifunctional effect. Such bifunctional

action has also been observed in hydrogenase enzymes, where heterolytic hydrogen activation takes place at a metal site, with a sulfur atom from a neighboring cysteic moiety acting as the base.[19]

1.8 Hypothesis and aims of this work

In view of the above, it is possible that the heterolytic hydrogen activation and the ionic hydrogenation mechanism can also be promoted by metallic nanoparticles immobilized on supports with basic functionalities. The goal of this dissertation work is to demonstrate that this type of mechanism can be induced by RuNPs immobilized on functional basic support. We hypothesize that *a well-defined nanostructure consisting of metallic particles with adjacent basic sites on the catalyst surface will promote heterolytic splitting of H_2 and efficient ionic hydrogenation, thereby avoiding catalyst poisoning and enhancing catalytic activity*.

The specific aims of this work are: (1) To synthesize and characterize ruthenium nanoparticles immobilized on different supports bearing basic functionalities; (2) To study their catalytic properties in the hydrogenation of aromatic compounds and to understand the origin of the catalytic behavior as a function of catalyst composition, structure, features of supports and operational parameters; (3) To gain an understanding of structure-activity correlations and to gain mechanistic understanding of the hydrogenation reactions.

1.9 Catalyst design and overview of this work

The design of our supported RuNPs catalyst is aimed at promoting heterolytic hydrogen splitting and ionic hydrogenation pathways on catalyst surfaces by creating metal-base bifunctional units on solid surfaces composed of small RuNPs in close proximity to basic functionalities provided by the support. If ionic hydrogenation mechanism can operate on solid surfaces, poisoning effects can be avoided with enhanced catalytic activity, since neither the substrates nor the products would enter into a strong direct interaction with the active metal sites. Figure 1-5 illustrates the nanostructure of catalyst based on our design, wherein small NPs are surrounded by basic sites from support.

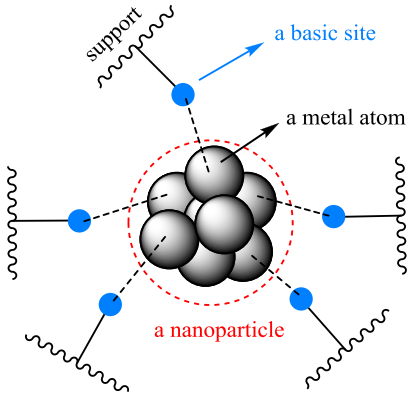

Figure 1-5. Our catalyst design: the nanostructure composed of RuNPs and basic sites from support for ionic hydrogenation mechanism.

The general work of this project can be divided into: (1) preparation of catalysts with modulation of synthesis parameters such as metal loading, temperature and different supports; (2) characterization of catalysts to well understand catalyst structures; (3) test the catalytic activity in hydrogenation of model toluene and quinoline substrates and investigate the scope of catalytic hydrogenation; (4) establish the structure-activity correlations, study the effect of different operating parameters on catalytic behavior and gain mechanistic insights into the principal hydrogenation mechanisms.

Chapter 2
Synthesis and Characterization of Supported Ruthenium Nanoparticles

The beginning of the 21st century has seen a drastically increased interest in catalysis by transition metal nanoparticles, as reflected by the exponential growth in the number of publications in this filed.[16] The preparation methods of metal NPs have been greatly diversified, and due to the tendency of aggregation, metal NPs are usually stabilized by a variety of stabilizing agents, including ligands, surfactants, ionic liquids, polymers, dendrimers and inorganic solid supports. From a practical point of view, immobilization or grafting of NPs on solid supports is more advantageous in terms of ease of handling, separation and catalyst recovery and there have been a great number of outstanding examples of application of supported metal NPs for catalyzing different reactions, such as hydrogenation, coupling reactions and oxidation reactions.[20]

In this chapter, I will provide a brief introduction to the common synthetic methods for supported metal NPs that are widely adopted in literature; I will also give a short introduction to different characterization techniques for solid catalysts that are applied in this project. Finally, I will review recent works from different groups on aromatics hydrogenation using supported metal NPs, specifically RuNPs, that are relevant to the work of this project.

2.1 Synthetic methods for transition metal nanoparticles

Catalyst preparation, to a large extent, determines the performance of a catalyst in terms of activity, selectivity and stability and thus can be considered as one of the most important operation steps both in laboratory and industrial scale. Deposition of metal NPs onto a support can not only achieve an optimal dispersion of active precious metal but also stabilize the active phase against any sintering processes under the reaction conditions employed. Among the many methods to prepare supported metal catalysts, impregnation, deposition precipitation, ion-exchange and sol-gel process are the most common ones.[21-22]

2.1.1 Impregnation and drying

The impregnation method is perhaps the most prevalent one used in the preparation of supported metal NPs. In this method, a support is brought into contact with a solution containing the precursor of active phase so that the solution can be drawn into the pores of support by capillary suction. The volume of the solution is usually equal to the pore volume of support so that after proper wetting of the support there is no excess of solution remaining outside the pore space—so called "incipient wetness impregnation". As the solution diffuses into the pores, the precursor can interact with the support and adsorb on the support surface so that a distribution of precursor on the support can be achieved. After impregnation, the solid is dried by means of heating or flowing gas to eliminate the solvent in the pores.

The dried impregnated system is usually subjected to calcination at elevated temperature under inert gas or reducing gas, or to reduction at ambient condition, to deposit the metal on the support surface, depending on the types of precursor.

Most supported ruthenium catalysts were synthesized using this method. It is generally suitable for inorganic supports since these supports can withstand high temperature without any significant structural change during the final thermal treatment. Common supported ruthenium catalysts include RuNPs supported on C,[23-26] alumina,[27-28] silica[26,29-30] and hydroxyapatite (HAP)[31] using $RuCl_3$ as ruthenium precursor. Organometallic precursors with zerovalent ruthenium e.g. Ru(COD)(COT) were also used for this method and its mild decomposition lead to RuNPs supported on silica,[32] alumina[33] and polydimethylphosphazene (PDMP).[34] Other precursors include $Ru_3(CO)_{12}$,[35] $Ru(acac)_3$[36-38] and $Ru(OH)Cl_3$.[38-39]

2.1.2 Deposition precipitation

Deposition precipitation is a generic method to place metals, metal oxides, metal sulfides or metal hydroxides onto the surface of support. This method involves a chemical reaction in the liquid phase, resulting in the formation of metals or metal compounds with low solubility in the solvent, followed by the precipitation of these metals or metal compounds exclusively onto the surface of a suspended support. The precipitation can be caused by pH increase of the system, reduction reactions or ligand removal brought about by condition change. In case of precipitating metals by reduction, the reaction can be triggered by addition of a reducing agent, or by change of conditions such as temperature when a reducing agent pre-exists in the reaction medium, to precipitate metal M from metal salt MX_n:

$$MX_n + m\text{Red} \rightarrow M(0) + m\text{Red}' + n\text{X}$$

The presence of the support facilitates the nucleation of M(0) and growth of a stable crystalline phase, which is finally stabilized on support.

This method is desirable for organic supports such as polymers since organic supports are unstable under high temperatures which are usually required in impregnation method for drying and calcination. The reduction can take place at room temperature, making it suitable to deposit metals on organic supports. For instance, RuNPs were precipitated by sodium borohydride reduction of $RuCl_3$ at room temperature and supported on poly(4-vinylpyridine) (P4VPy).[40]

The reducing agent is usually added during the preparation to bring about the immediate reduction, such as borohydride reduction. In some cases, the reducing agent is pre-mixed with the catalytic precursor and support and then the reaction conditions are adjusted to trigger the reduction. Common examples are polyol reduction using $RuCl_3$ as precursor and ethylene glycol as the reducing agent.[28,41-44]

Examples of precipitation of other forms of ruthenium onto support, such as ruthenium hydroxide, are also available. Claus and co-workers used NH_4OH to precipitate ruthenium hydroxide from $RuCl_3$ onto alumina and calcined the resulting material to obtain alumina supported RuNPs.[36]

2.1.3 Ion-exchange and reduction

Ion-exchange is another method to achieve the deposition of an active component precursor onto a support. The support usually contains ions in electrostatic interaction with the surface. In this method, the support is immersed into an excess volume of solution containing the ions of the active component that is to be introduced so that the solution can penetrate into pores of support and the ions of the active component in solution replace the ions on the support. In contrast to the impregnation method, the resulting solid is washed to eliminate the ions from the support and the counter ions of

precursor ions. After washing, the resulting solids are subjected to reduction so that the ions of the active component inside the pores become metallic, forming metal NPs stabilized by the support.

RuNPs prepared by this method has been supported on silica MCM-41,[29] HAP[45] and zeolites.[35,46-47] The reduction was brought about by either hydrogen flow at elevated temperature or borohydride at room temperature.

2.1.4 Sol-gel process

Sol-gel process is a route to prepare porous materials by condensation of colloidal particles in the solution ("sol") to produce an integrated network ("gel") of either discrete particles or network polymers. It consists of a sequence of operations starting from activation of sol-gel precursors and polycondensation of these activated precursors into nanoclusters to form a colloidal solution. Sol-gel precursors are usually solvated metal ions in aqueous solution or metal alkoxides in alcohol-water solution. These precursors are activated by hydrolysis and undergo condensation chemistry to connect the metal centers with oxo (M-O-M) or hydroxo (M-OH-M) bridges, therefore generating metal-oxo or metal-hydroxo polymers in solution. After gelation, aging, washing and desolvation steps, a porous solid material can be obtained. Catalytic chemical functionality can be introduced during the process so that catalytic materials are entrapped in porous matrices leading to solid catalytic materials; catalytic phases or functionalized moieties can also be deposited, grated or anchored on sol-gel-derived supports after the sol-gel process.

Examples of ruthenium catalysts prepared through sol-gel process include MgO-supported ruthenium catalysts for ammonia synthesis.[48-49] The synthesis used magnesium

ethoxide as the sol-gel precursor and water-ethanol mixture as the solvent. $Ru_3(CO)_{12}$ was introduced as catalytic precursor during the process; after devolvation and heating, a black catalyst powder with metallic ruthenium entrapped in MgO matrices was obtained.

2.2 Characterization techniques for solid catalysts

Catalyst characterization plays an important role in catalysis. It provides us with information on the physico-chemical properties of catalyst and also enables us to gain understanding of the catalytic act at microscopic level. Different characterization techniques, including microscopic and spectroscopic methods, have been applied to study solid catalysts.[21] Herein the characterization techniques utilized in this project will be briefly described.

2.2.1 Transmission electron microscopy (TEM)

Transmission electron microscopy as a microscopic method has been extensively used in the field of nanoscience since it allows the direct visualization of small features such as the size and shape of nanoparticles that cannot be observed under light microscopes. The basic principles of transmission electron microscopes are the same to that of light microscopes but electron rays are used instead of light; this significantly increases the resolution since electron has much smaller wavelength than light so that observation of features limited by the wavelength of light becomes possible.

In a transmission electron microscope, the electron source at the top of the microscope generates electrons that are focused by electromagnetic lenses to form an electron beam that travels through vacuum in the column of microscope (Figure 2-1). After the electron beam travels through a thin sample placed in the column, the unscattered electrons hit a fluorescent screen on the bottom of column, giving rise to a

shadow image of the specimen with different parts displayed with varied darkness depending on the density of the specimen. The formed image then can be studied directly on the fluorescent screen or photographed with a CCD camera which is controlled by a computer.

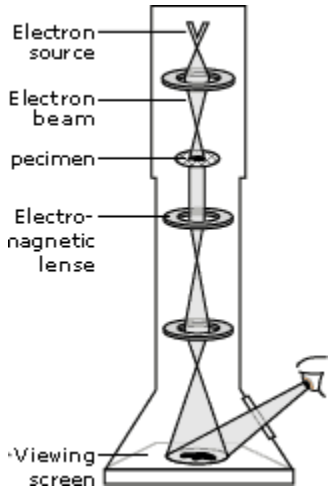

Figure 2-1. Formation of image in the transmission electron microscope.[50]

Sample preparation is a critical step in TEM measurement because the image quality is highly dependent on how the solid is dispersed on the grid and the sample thickness. The sample has to be very thin (less than 100 nm) to be "electron transparent" so that electrons can pass through the specimen to form the image. The thinner the sample, the better the resolution and contrast. There are many ways to prepare TEM samples for solid catalysts. If the catalyst powder has very small grains (less than 100 nm in size), then the powder can be dispersed in a volatile solution and a drop of this suspension can be placed on a copper grid coated with carbon films so that after evaporation of solvent the sample powder of small size can be deposited on the grid. Use of holey film is recommended so that the features of the sample can be observed across the holes. If the catalyst grains are too thick for direct observation, they can be embedded in a resin and then cut into thin pieces to achieve "electron transparency".

2.2.2 Powder X-ray diffraction (PXRD)

Powder X-ray diffraction is the most frequently applied technique to identify the bulk phase and composition of a crystalline sample. A powder X-ray diffractometer consists of an X-ray source, a sample stage, a detector and a way to vary the angle θ (Figure 2-2). The generated monochromatic X-rays are energetic and can penetrate solids; when the rays are interacting with a crystalline sample, constructive interference can be produced if the condition satisfies Bragg's Law (Figure 2-2):

$$n\lambda = 2d \sin\theta$$

(λ: the wavelength of X-rays; d: the lattice spacing; θ = the incoming angle of X-rays.)

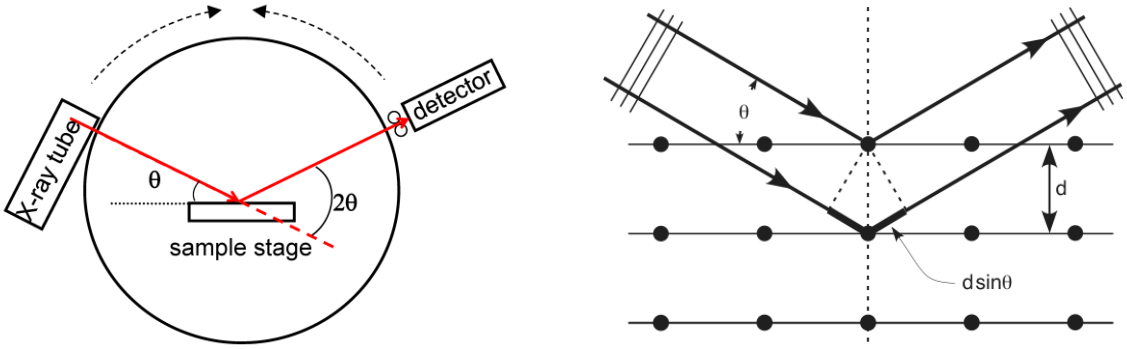

Figure 2-2. The construction of a powder X-ray diffractometer and Bragg's law.[51]

The diffracted X-rays can be detected, processed and counted. Because of the random orientation of the powder sample, all possible diffraction directions of the lattice can be obtained when the sample is scanned through a range of 2θ angle. Since each different crystal has a distinctive diffraction pattern comprising line positions together with the relative intensities, the "fingerprint" diffraction pattern allows the identification of the sample. Usually, this is achieved by comparison with standard reference patterns. The International Center for Diffraction Data (ICDD) has the database of Powder Diffraction Files (PDF) for different materials.

2.2.3 Energy-dispersive X-ray spectroscopy (EDX)

Energy-dispersive X-ray spectroscopy is used to identify the elemental composition of a sample. Interaction of an electron beam with the sample produces X-rays that are characteristic of different elements so that an energy spectrum can be obtained. EDX allows to find the chemical composition of material down to a very small area on the sample and to create element composition maps over a broad area. The EDX measurement can be carried out either in a transmission electron microscope or in a scanning electron microscope with an EDX detector. A typical EDX spectrum is a plot of x-ray counts *vs.* energy with different peaks corresponding to different elements in the sample. The weight percentage of each element can also be deduced from the peak intensities.

2.2.4 X-ray photoelectron spectroscopy (XPS)

Different from PXRD which gives information about the bulk phases of the sample, X-ray photoelectron spectroscopy is applied to analyze the surface of sample such as the surface element composition and chemical state. The generated X-ray photons are not energetic enough to penetrate the sample; they can only reach a few nanometers below the surface. The photoelectrons from the sample surface can be produced upon the interaction of X-ray with the sample (Figure 2-3) and can be detected; their kinetic energies are measured, which are characteristic of different elements. Based on the binding energy of a specific element from an XPS spectrum and the reference value of the zerovalent element, the oxidation state of the element on the surface can be determined, since the element with a different oxidation state causes a shift of binding energies. XPS requires the sample to be in an ultra-high vacuum (UHV) so that kinetic

energies can be accurately measured. A typical XPS spectrum is portrayed as a plot of the number of photoelectrons detected *vs.* the binding energies of the photoelectrons. The composition of elements can be roughly calculated from the peak areas corresponding to different elements. Usually the peaks of different chemical states or different elements are overlapped so peak deconvolution with the aid of software is required.

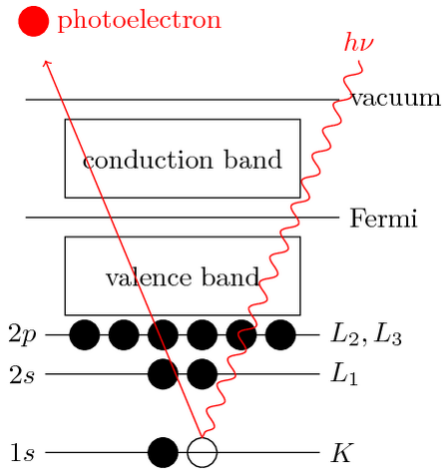

Figure 2-3. The generation of photoelectrons upon irradiation of sample by X-ray photons in XPS.[52]

2.2.5 Physisorption analysis

The surface area of solids can be determined by physisorption technique using nitrogen as the adsorptive gas, which is the most suitable for the determination of the surface area of non-porous, macroporous or mesoporous solids. At a low temperature of 77 K, N_2 are close-packed in the liquid state to form a monolayer on the surface of solids. Thus by knowing the cross-sectional area of a nitrogen molecule and the number of nitrogen molecules in the monolayer, the surface area of the solid can be derived:

$$a = \mathrm{L} n_m \sigma_{\mathrm{N}}$$

(a: specific surface area; L: the Avogadro constant; n_m: the number of nitrogen molecules in the monolayer; σ_{N}: the cross-sectional area of the nitrogen molecule.)

The Brunauer–Emmett–Teller (BET) method as a simple model of physisorption is widely applied for evaluating the surface area of solid materials. The single-point BET measurement was adopted in this project to measure the specific surface area of magnesia support.

2.2.6 Chemisorption analysis

Chemisorption analysis has long been employed as a valuable technique for determination of metal dispersion of a supported metal catalyst. Dispersion is an important property of supported metal particles; it is defined as the fraction of metal atoms that are exposed on surface:

$$D = N_S/N_T$$

(D: metal dispersion; N_S: the number of metal atoms exposed; N_T: the total number of metal atoms.)

Determination of metal dispersion is important. It provides a more accurate evaluation of catalytic activity since only surface atoms are actually involved in catalysis. Also, achieving maximum utilization of supported metals is always one of the goals in catalyst preparation and metal dispersion measurement offers a way to improve the preparation parameters to achieve the maximum use of precious metals.

H_2 and CO are most frequently used probe gases. They can chemically adsorb on the supported metal phases but not on the support. The measurement of the quantity of H_2 or CO gas adsorbed selectively on the metal at monolayer coverage gives the metal surface area, provided the stoichiometry for the chemisorption is known. The metal dispersion and the effective particle size of supported metals can then be derived from the metal surface area.

Chemisorption measurements can be static or dynamic. Pulse chemisorption as a dynamic method was applied in this project to measure the metal dispersion and estimate the particle size of ruthenium catalyst. In the pulse chemisorption, H_2 or CO probe gas is injected as successive small doses of known volume into the flow of an inert gas until there is no more H_2 or CO gas uptake as monitored by detector; the total quantity of the irreversibly chemisorbed gas can then be calculated to deduce the metal surface area, from which metal dispersion and effective particle size can be derived. It is a convenient method for routine metal dispersion measurements.

2.2.7 Temperature-programmed desorption (TPD)

Temperature-programmed methods can provide useful information on solid surfaces and their interactions with adsorbed gas molecules. In particular, temperature-programmed desorption can be used to characterize the acidic/basic strength of solid surfaces by using corresponding basic/acid probe gases. To conduct the TPD experiment, a sample is first degassed and then treated with a probe gas so that the probe gas molecules interact with different acidic/basic sites on the solid surface to bond chemically; as the temperature is increased at a linear heating rate in following steps, the chemical bonds between the probe gas molecules and surface sites start to break and the adsorbed gas molecules start to desorb in consequence at different temperatures. The desorbed gas is mixed into a stream of inert gas which is monitored by the detector so that a TPD profile of signal *vs.* temperature can be obtained. The desorption peaks at different temperatures in a TPD profile correspond to acidic/basic sites of different strength; the higher temperature at which the gas desorbs, the stronger the acidity/basicity of the corresponding site. CO_2 is usually used for characterizing basic sites of solid supports.

2.3 Supported ruthenium nanoparticles for hydrogenation of aromatics

Ruthenium has long been used for hydrogenation reactions both in homogeneous phase or heterogeneous phase as supported solid catalyst, due to its excellent ability to activate hydrogen. Ruthenium nanoparticles have been supported on various solid materials for a variety of reactions not limited to hydrogenation. In this section I will focus on supported RuNPs for hydrogenation of aromatics and provide a brief review on recently relevant works (since 2001) reported by other groups.

2.3.1 RuNPs supported on C or C nanofibers

Zhao and co-workers[25] prepared a sandwiched Ru/C catalyst in which RuNPs are incorporated into pore walls of porous carbon with the aid of zeolite Y or SBA-15 silica as synthesis templates. The particle sizes range from 1–2 nm and 7–8 nm, comparable to that of the channel sizes of zeolite Y and SBA-15 silica templates, respectively. The catalytic activity was tested in hydrogenation of benzene at different conditions; and a TOF of 1,000 h^{-1} was reported at 40 °C and 20 atm while higher TOFs were achieved at 110 °C /40 atm and 110 °C /80 atm, as about 5,000 h^{-1} and 10,000 h^{-1}, respectively. The same group also used a thermal reduction method to prepare RuNPs supported on various carbon supports, including C coated on SBA-15, activated carbon and carbon black.[26] The catalysts showed high activity and stability in hydrogenation of benzene and toluene at 110 °C and 40 atm, with TOFs as high as 20,000 h^{-1} for benzene and 10,000 h^{-1} for toluene.

In addition, Takasaki *et al.* immobilized RuNPs on carbon nanofibers (CNFs) for the hydrogenation of functionalized benzene derivatives including toluene, anisole and

aniline.[53] The RuNPs were of about 3 nm in average size and hydrogenation of toluene can reach a TOF of about 10,000 h^{-1} at 100 °C and 30 atm, with fully hydrogenated products observed.

2.3.2 RuNPs supported on alumina

There are not too many recent examples of alumina-supported RuNPs devoted to aromatics hydrogenation. Pertici and co-workers[33] have deposited trioctylamine-stabilized RuNPs on γ-alumina using the mild decomposition of Ru(COD)(COT) precursor. The particles are about 3 nm in average size and the catalyst was used for hydrogenation of the aromatic ring of methyl benzoate and its derivatives to the corresponding cyclohexane derivatives, providing an efficient synthesis of pharmaceutical products from largely available starting material.

2.3.3 RuNPs supported on silica

There have been many examples of RuNPs supported on silica for hydrogenation of aromatics. Bianchini and co-workers[54] prepared a silica-supported ruthenium catalyst using $Ru_3(CO)_{12}$ as the precursor. The particles have a uniform dispersion with an average size of about 1nm. The catalyst was tested in hydrogenation of a variety of aromatics, including arenes and N-/S-containing aromatics at 100 °C and 30 atm. Toluene can be fully hydrogenated to methylcyclohexane with a TOF of 360 h^{-1}; anthracene, on the other hand, can be hydrogenated with a TOF of about 15 h^{-1}, with the major product being 1,2,3,4-tetrahydroanthracene; N-heteroaromatics including indole, quinoline and acridine can also be hydrogenated to a mixture of partially and fully saturated products, with TOF values in the order of 100 h^{-1}. However, the catalyst

showed no catalytic activity towards S-heteroaromatics including benzothiophene and dibenzothiophene, being completely poisoned by these compounds.

Silica-supported RuNPs prepared by other groups are sometimes stabilized with the assistance of other stabilizing agents. Huang *et al.* applied ionic liquids to immobilize RuNPs onto SBA-15 silica for hydrogenation of benzene with a TOF value of about 200 h^{-1} at 35 °C /10 atm and 4,000 at 110 °C/ 60 atm.[55] Proust and co-workers[56] prepared silica-supported RuNPs with additional polyoxomolybdate (POM) stabilization. The resulting RuNPs are very small, with an average diameter in the 8–15 Å range, due to the stabilizing effect of POM and high specific surface area of silica. The benzene hydrogenation activity was found to increase with increased reduction temperature during sample preparation; no TOF values were reported.

Use of surface modified silica to stabilize RuNPs was also reported. Zhou *et al.* grafted poly(N-vinyl-2-pyrrolidone) (PVP) onto silica surface through a two-step method and supported RuNPs on this PVP-modified silica.[30] The RuNPs were found to be 2-5 nm in size and displayed very high activity in the hydrogenation of benzene, toluene and *p*-xylene, with TOF values of as high as 70,000 h^{-1} at 110 °C /80 atm for benzene, 30,000 h^{-1} and 7,000 h^{-1} for toluene and *p*-xylene at 110 °C /40atm, respectively.

2.3.4 RuNPs supported on zeolite

Ozkar's group synthesized ruthenium nanoclusters stabilized by the framework of zeolite-Y by ion-exchange of Ru^{3+} with Na^{+} ions within zeolite-Y followed by borohydride reduction of Ru^{3+} at room temperature.[46-47] The stabilized Ru nanoclusters remain both on the external surface (30%) and inside the cavities of zeolite-Y (70%). The catalyst was found to catalyze the hydrogenation of benzene, toluene, *p*-xylene and

mesitylene with TOF values of 1,800, 600, 290 and 150 h^{-1} at mild conditions (25 and 3 atm), respectively.

2.3.5 RuNPs supported on montmorillonite

Miao *et al.* deposited RuNPs onto montmorillonite (MMT) clay together with ionic liquids as a novel synthesis.[57] The RuNPs are uniformly distributed on the MMT surfaces with sizes of less than 3 nm. The catalyst was tested for hydrogenation of benzene and a TOF value of 4,000 h^{-1} was reported at 110 °C and 80 atm.

2.3.6 RuNPs supported on hydroxyapatite

Hydroxyapatite (HAP), with the formula $Ca_{10}(PO_4)_6(OH)_2$, has also been used as catalyst support. Li and co-workers[31] prepared RuNPs of 2–3 nm supported on HAP for hydrogenation of quinoline and some of its methylated derivatives. The quinolines can be hydrogenated at 150 °C and 50 atm with TOF values in the range of 50–150 h^{-1}. Ozkar and co-workers[45] also prepared Ru/HAP catalyst using the ion-exchange method and used it for the hydrogenation of benzene, toluene, *p*-/*m*-/*o*-xylene and mesitylene, with TOF values ranging from 100 h^{-1} to about 240 h^{-1} under mild condition (25 °C and 3 atm).

2.3.7 RuNPs supported on organic polymers

RuNPs have also been supported on polymers for heterogeneous hydrogenation of aromatics. Pertici and co-workers[34] deposited RuNPs on polydimethylphosphazene (PDMP) by decomposition of Ru(COD)(COT) under mild conditions. The aromatic ring of methyl benzoate can be hydrogenated over Ru/PDMP catalyst at room temperature and 50 atm. Song *et al.* prepared RuNPs entrapped into the FDU-15 mesopolymers with average particle size of about 2 nm.[58] Toluene can be hydrogenated exclusively to methyl-cyclohexane over this catalyst with a TOF value of 400 h^{-1} at 60 °C and 40 atm.

Chapter 3
Ru/P4VPy Promotes a Unique Surface Ionic Hydrogenation Mechanism

3.1 Introduction

Our catalyst design requires supported transition metal nanoparticles (ruthenium is chosen in this dissertation work) as hydride carriers together with basic functionalities on the supports for participation in heterolytic hydrogen activation. Functional polymers are good candidates for supports since the polymer chains can be well functionalized to provide the necessary basic sites. In addition, they are efficient supports to stabilize metal nanoparticles,[59-60] since they provide the steric bulk of their framework and several sites for simultaneous interactions with the metal and the substrates. Poly(4-vinylpyridine) (P4VPy) is attractive because of the strong affinity of the pyridyl group for the metal for effective stabilization of metallic nanoparticles and its ability to interact with polar species through hydrogen bonding.[61] Figure 3-1 shows the structure of P4VPy, wherein the number of pyridinic nitrogen atoms is about 2.80 mmol/g and the proportion of accessible nitrogen is close to 1 mmol/g.[61-62] The basic nitrogen atoms of the pyridyl groups can serve as the proton reservoir in heterolytic hydrogen activation.

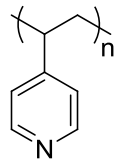

poly(4-vinylpyridine)

Figure 3-1. The structure of poly(4-vinylpyridine) (P4VPy).

P4VPy is commercially available as resins in various degrees of cross-linking with divinylbenzene. It is insoluble in common solvents and thermally stable. It is also resistant to degradation by acids, bases, oxidizing and reducing agents. Most importantly, it provides a means to immobilize RuNPs in close proximity to quaternizable nitrogens (Figure 3-2). The deposition of RuNPs on P4VPy (Ru/P4VPy) creates the nanostructure required for the heterolytic activation of hydrogen, with the hydride attached to Ru atoms and the proton accepted by a nearby nitrogen atom (Figure 3-3).

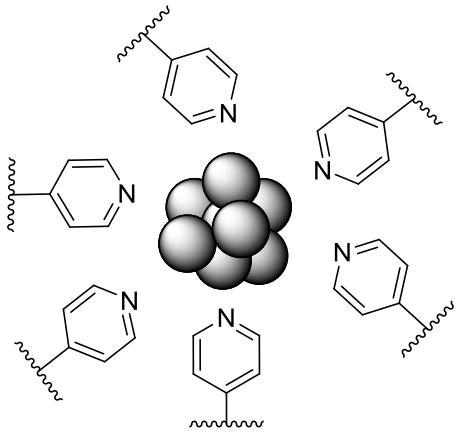

Figure 3-2. Schematic representation of the nanostructure created by immobilization of RuNPs on P4VPy.

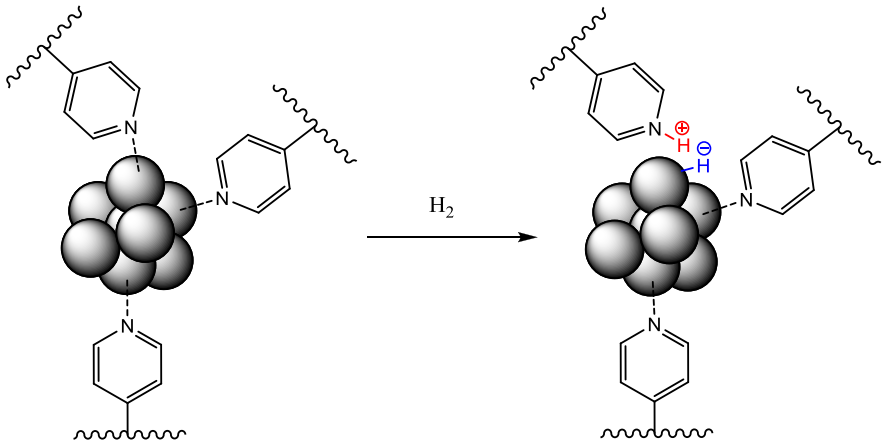

Figure 3-3. Heterolytic splitting of hydrogen by Ru-N bifunctional action on Ru/P4VPy.

RuNPs on P4VPy have been reported for magnetic applications but no catalytic reactions were described;[63] Pd colloids on polystyrene-poly(4-vinylpyridine) block copolymers were used to hydrogenate C=C and C≡C bonds;[64-65] acetophenone hydrogenation by Pd/P4VPy was also reported[66] but no mechanistic proposal was presented in either case. Thus the use of Ru/P4VPy as hydrogenation catalysts operating by ionic mechanisms is a very promising and largely unexplored field.

3.2 Experimental section

3.2.1 Materials

Ruthenium trichloride hydrate (Pressure Chemicals, Inc.) and sodium borohydride (Sigma-Aldrich) were used as received. Solvents (analytical grade, Sigma-Aldrich) were purified using a PureSolv purification unit from Innovative Technology, Inc. Substrates and other reagents (Sigma-Aldrich) were purified by distillation or recrystallization prior to use when necessary. Poly(4-vinypyridine) (2% cross-linked with divinylbenzene) was purchased from Sigma-Aldrich and dried under vacuum at 50 °C overnight before use.

3.2.2 Synthesis of Ru/P4VPy catalyst

The Ru/P4VPy catalyst was synthesized by $NaBH_4$ reduction of $RuCl_3 \cdot 3H_2O$ in the presence of poly(4-vinypyridine) in methanol under nitrogen at room temperature (Scheme 3-1).

$$RuCl_3 \cdot 3H_2O + NaBH_4 \xrightarrow[MeOH,\ r.t.]{P4VPy\ (2\%\ cross\text{-}linked)} Ru(0)/P4VPy$$

Scheme 3-1. The synthesis of the Ru/P4VPy catalyst.

The reaction is performed in a three-neck round bottom flask fitted with two pressure-equalizing dropping funnels and a vacuum adapter (Figure 3-4). Using Schlenk

techniques, the apparatus was evacuated and purged with nitrogen three times. Poly(4-vinypyridine) (1.0 g) was suspended in methanol (20 mL) inside the flask under nitrogen; $RuCl_3 \cdot 3H_2O$ (0.26 g, which contains 1.0 mmol of Ru) in methanol (10 mL) and $NaBH_4$ (0.38 g, 10 mmol) in methanol (20 mL) were placed in the two dropping funnels, respectively. While the polymer suspension was being stirred at room temperature, 10 mL of the $NaBH_4$ solution was quickly added to the flask, after which both $RuCl_3$ and $NaBH_4$ solutions were simultaneously added into the mixture at the same rate of about one drop per second. After addition was completed, the mixture was further stirred for 2 h at room temperature. At the end, the solution was colorless and the solid was dark brown. The solid was filtered off, washed three times with deionized water (10 mL) and three times with methanol (10 mL) and dried under vacuum at room temperature, affording a fine brown powder containing 10 wt% Ru.

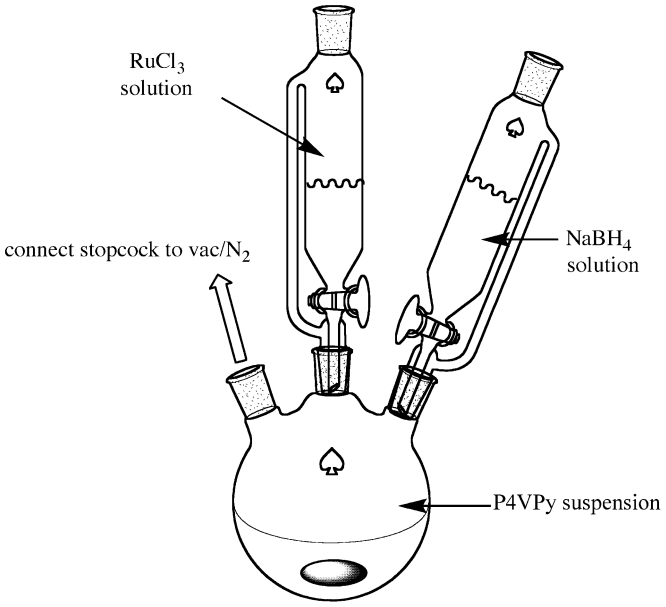

Figure 3-4. The experimental apparatus for the synthesis of the Ru/P4VPy catalyst.

3.2.3 Characterization of Ru/P4VPy catalyst

3.2.3.1 TEM studies

Transmission electron microscopy (TEM) micrographs were obtained on a Zeiss EM 902 microscope operating at an accelerating voltage of 80 kV with a line resolution of 0.34 nm and a point resolution of 0.5 nm. Images were captured digitally using a Mega View III CCD camera with a resolution of 1.3 Megapixels. The metal particle size (Feret diameter) distribution was estimated from the measurement of about 300 particles, found in an arbitrarily chosen area in an enlarged micrograph.

Since the cross-linked P4VPy is an insoluble resin, the catalyst powder is not fine enough to allow the direct preparation of sample on carbon-coated copper grids. Thus TEM samples were prepared as follows (Figure 3-5): about 50 mg of catalyst was ground

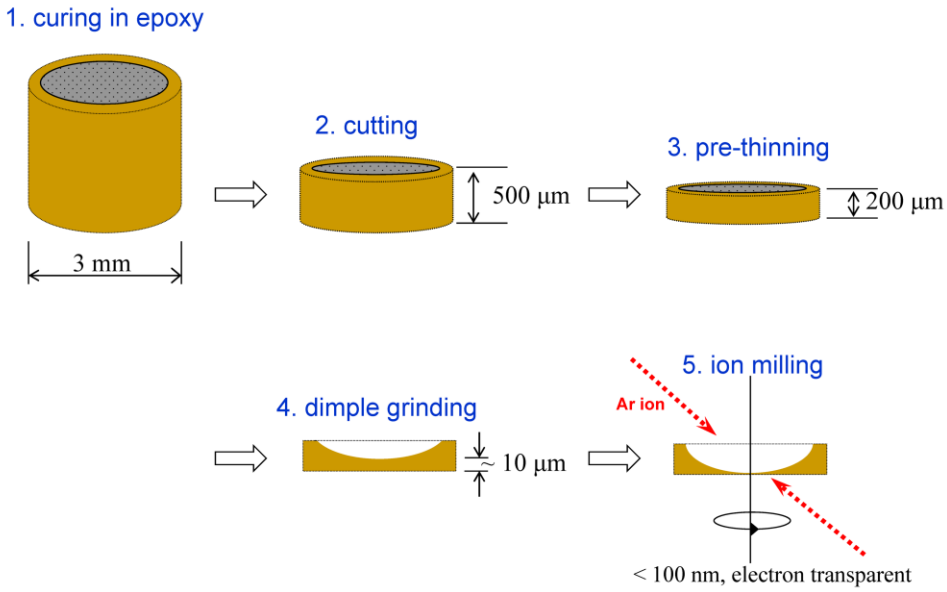

Figure 3-5. Ru/P4VPy sample preparation for TEM measurement.

in a mortar and subsequently mixed with M bond 610 two-part epoxy (E.A. Fischione Instruments, Inc., part A : part B = 10 : 1). The mixture was transferred into a 3 mm brass tube and then cured at 150 °C for 40 minutes. A disk of about 500 µm thickness was cut

off from the filled brass tube using an IsoMet® low speed diamond wafering saw (Buehler) and then mechanically pre-thinned to about 200 μm thick on an EcoMet® variable speed grinder-polisher (Buehler). The disk was further polished by dimple grinding on a Model 200 dimpling grinder (E.A. Fischione Instruments, Inc.) to about 10 μm in the central area. The final sample was prepared by dual gun Ar^+ ion milling in a Fischione Model 1010 low angle ion milling & polishing system to reach a perforation in the central area of the dimple ground disk.

3.2.3.2 PXRD measurements

Powder X-ray diffraction (PXRD) patterns were recorded on a Philips X'PERT MPD diffractometer using monochromatic Cu Kα radiation at 45 kV and 40 mA and 2θ scanning from 10° to 75°. Samples were ground in a mortar before being placed in a sample holder and analyzed immediately in the air at room temperature.

3.2.3.3 XPS measurements

XPS spectra were recorded with an Omicron XPS spectrometer equipped with a multichannel hemispherical analyzer and a dual Al/Mg X-ray source using the Al Kα excitation (1486.6 eV). The binding energy scale was previously calibrated and the base pressure in the analysis chamber was around 2.0×10^{-9} torr. The powdered samples were mounted on studs using a double-sided adhesive tape with a short time of air exposure. The pressure in the analysis chamber was maintained below 5.0×10^{-8} torr during the measurements. The asymmetrical XPS peaks were deconvoluted by the curve fitting approach by use of XPSPEAK 4.1, applying Shirley background subtraction and Lorentzian-Gaussian functions (20% L, 80% G).

3.2.4 Catalytic tests

Catalytic hydrogenation were carried out using a 5513 Parr reactor (100 mL) fitted with an internal stirrer and a dip tube, a thermocouple, a sampling valve and a high-pressure burette, coupled to a 4836 controller. In a typical hydrogenation run, the reactor was loaded with the desired amount of catalyst and 20 mL of THF and then sealed. H_2 was introduced into the reactor through the high-pressure burette and released through the releasing valve. This process was repeated three times in order to deoxygenate the system, after which the reactor was re-pressurized to 6 atm and heated to 120 °C to reach 10 atm. After the catalyst was incubated at 120 °C and 10 atm for 1 h, 10 mL of substrate solution in THF was placed into the high-pressure burette, which was subsequently charged with 10 atm of H_2. The reactor was depressurized to about 2–3 atm and the substrate solution in the burette was then quickly injected into the reactor, when was taken as the zero time of the reaction. The pressure was kept at 10 atm by feeding H_2 through an open connection to the hydrogen tank. Samples of the reaction mixture were periodically withdrawn from the reactor and analyzed immediately by use of a Varian 3900 gas chromatograph fitted with a SP-2330 capillary column and a Saturn 2100T mass detector. The identity of each product was verified through comparison of its mass spectrum with the instrument's library and the molar percentage of each product was calculated based on peak areas and relative response factors previously determined by using standard solutions containing known amounts of each component. Each experiment was repeated at least twice in order to verify reproducibility; the variations in the calculated turnover frequency (TOF) values for repeat experiments were typically within 5%. Blank tests were also carried out using the polymer support alone and toluene as the substrate under

analogous reaction conditions and no hydrogenation products were observed, ruling out other factors that may induce hydrogenation.

3.2.5 Substrate competition experiments

The procedure for substrate competition experiments was analogous to the one described in section 3.2.4, except that the two substrates (toluene and quinoline) in equimolar amounts were placed in the high-pressure burette.

3.2.6 Selective thiophene poisoning tests

The procedure for selective poisoning experiments was analogous to the one described in section 3.2.4, except that the substrate (toluene or quinoline) was mixed with thiophene (~ 1 mol%) before being placed in the high-pressure burette.

3.2.7 Recycling experiments

Recycling experiments were carried out using the same batch reactor as in section 3.2.4. At the end of a hydrogenation run, the reactor was allowed to cool to room temperature, vented, opened and the mixture was completely transferred into a Schlenk flask under a nitrogen atmosphere. The supernatant liquid was carefully withdrawn by use of a syringe, 10 mL of deoxygenated solvent was added and the mixture was then stirred for five minutes. This procedure was repeated three times. At the end, the residual solvent was removed and the catalyst was dried under vacuum for 2 h. A second hydrogenation run was then performed with this catalyst; further recycling steps were carried out by repeating this procedure.

3.3 Results and discussion

3.3.1 Catalyst design and preparation

Our working hypothesis is that the combination of small metal particles with basic functionalities provided by the support will lead to a nanostructure capable of promoting the heterolytic splitting of hydrogen and ionic hydrogenation mechanisms. The catalyst design is aimed at creating such nanostructures by using RuNPs and functional supports. We have successfully synthesized and immobilized RuNPs on P4VPy by using a simple one-pot borohydride reduction method at room temperature, and a nominal metal loading of 10 wt% was adopted for the Ru/P4VPy catalyst. During the preparation, the formation of the NPs and their attachment to the polymer was followed by the discoloration of the solution and the darkening of the solid. The completeness of the reaction was verified by the lack of any UV–Vis bands of the final solution, other than those ascribed to the solvent. Thus the real metal loading of the catalyst should be very close to the theoretical value. The catalyst was routinely stored under nitrogen but quickly weighed in the air.

3.3.2 Catalyst characterization

3.3.2.1 TEM measurements

To see the morphology and dispersion of RuNPs immobilized on P4VPy, we carried out TEM measurements. Sample preparation is an important step in TEM measurements. The sample has to be in the form of 3-mm disc and obtaining samples of uniform thickness from 10 to 200 nm is critical. There are different ways to make TEM samples of particulate materials such as powdered catalysts. For catalysts of small grain size (< 100 nm in diameter), the common way is to make a suspension of the catalyst in a volatile

solvent and deposit some drops on the top of carbon-coated cupper grids. Once it becomes dry, the remainders are very small grains, parts of which can reach "electron transparency" to be suitable for TEM measurements. However, the Ru/P4VPy catalyst has large grain size, thus the TEM sample for Ru/P4VPy had to be prepared in a different way: the catalyst powder was embedded into epoxy; after being cured, the hardened epoxy with the catalyst embedded was cut into thin disks, which were further subjected to a series of thinning process to reach the ideal thickness suitable for TEM observation (see section 3.2.3.1).

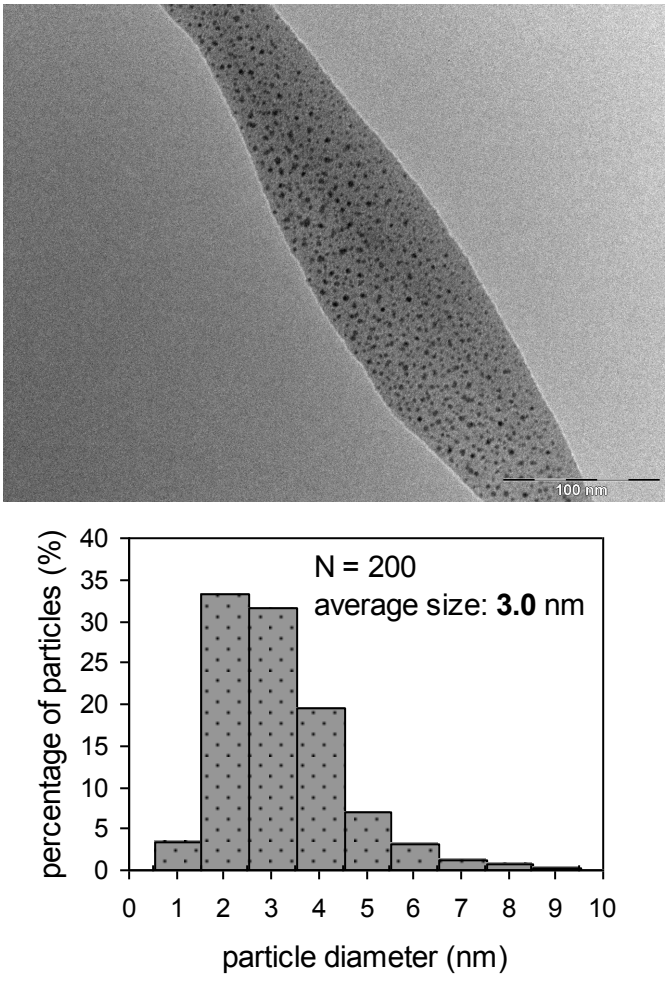

Figure 3-6. The transmission electron micrograph of a fresh sample of Ru/P4VPy with the corresponding RuNPs size distribution histogram.

Figure 3-6 shows a typical TEM image of a freshly prepared Ru/P4VPy catalyst, which reveals a very narrow particle size distribution with an average particle size of 3.0 nm. This means the borohydride reduction method is a reliable means to synthesis well-dispersed RuNPs supported on P4VPy. After being subjected to a hydrogenation run (hydrogenation of toluene at 120 °C and 10 atm), the average Ru particle size exhibits a moderate increase to 5.0 nm, compared to 3.0 nm for fresh catalyst, indicating a reasonable stability under typical reaction conditions.

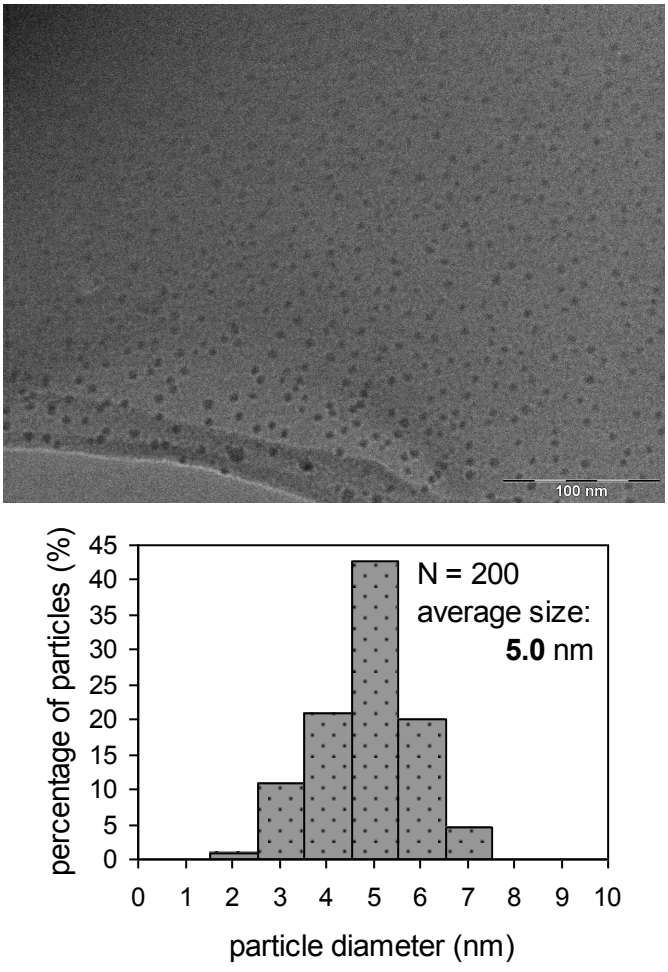

Figure 3-7. The transmission electron micrograph of a used sample of Ru/P4VPy (Tol hydrogenation, 120 °C and 10 atm) with the corresponding RuNPs size distribution histogram.

3.3.2.2 PXRD studies

PXRD measurements were taken to identify the crystalline structure of RuNPs dispersed on P4VPy. Figure 3-8 depicts the diffraction patterns of the polymer support, a fresh sample of Ru/P4VPy catalyst and a used sample of catalyst recovered from hydrogenation of quinoline at 150 °C and 50 atm. Diffuse peaks were observed in all cases. The polymer displays a wide peak at $2\theta = 20°$ due to the amorphous structure. The

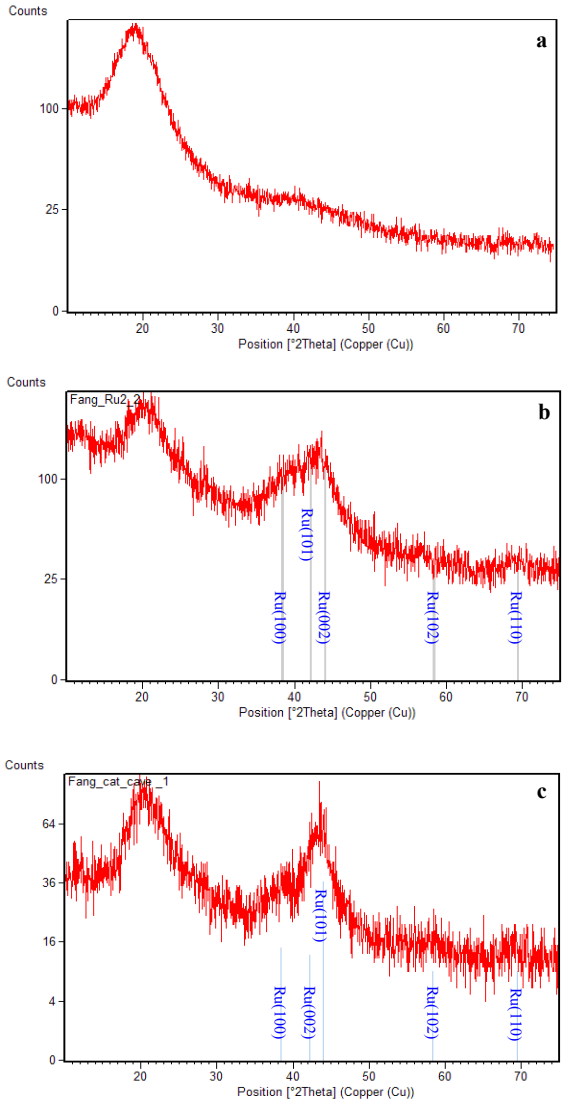

Figure 3-8. Powder XRD diffraction patterns of a). P4VPy support; b). A fresh sample of Ru/P4VPy; c). A used sample of Ru/P4VPy (Q hydrogenation, 150°C and 50 atm).

RuNPs have diffuse peaks in the range of 30°–50° rather than sharp peaks usually observed for metals, due to the homogeneous distribution of very small metal particles, which is consistent with the TEM results. The diffraction peaks centered at 2θ = 44° (Figure 3-8b) is consistent with the *d* value (2.06 Å) due to the (101) plane of Ru metal,[67] allowing us to characterize the particles as metallic Ru. No RuO_2 diffraction peaks were observed in the whole range of the diffractogram. After a quinoline hydrogenation run at 120 °C under 10 atm, the XRD pattern of the recovered catalyst is essentially identical to that of the fresh catalyst (Figure 3-8c), confirming that the oxidation state and the structure of the RuNPs remains unchanged after a hydrogenation reaction.

3.3.2.3 XPS analysis

In order to further establish the oxidation state of the RuNPs, XPS experiments were performed on a fresh catalyst and a used catalyst recovered from hydrogenation of quinoline at 150 °C and 50 atm of H_2. In the survey scans of both samples, Ru 3p, 3d and 4p peaks, O 1s, N 1s and C 1s peaks were observed, located at around 490–460, 280–290 and 43–46, 530, 400 and 288 eV, respectively (Figure 3-9). No B or Cl peaks were observed around 188 eV (B 1s), 200–202 eV (Cl 2p) and 270 eV (Cl 2s),[68] suggesting that the catalyst surface is clean and free of any Cl or B contaminants from preparation steps.

The narrow scan spectra within the Ru 3d region show highly overlapped Ru 3d peaks and C 1s peaks (Figure 3-10). At least six component peaks are necessary to fit correctly the experimental peaks for both fresh and used catalyst samples: Ru (0) $3d_{5/2}$ and $3d_{3/2}$, Ru(IV) $3d_{5/2}$ and $3d_{3/2}$, and C 1s peaks. The C 1s experimental peak at around 284.5 eV is too complicated to deconvolve: it has contributions from at least three

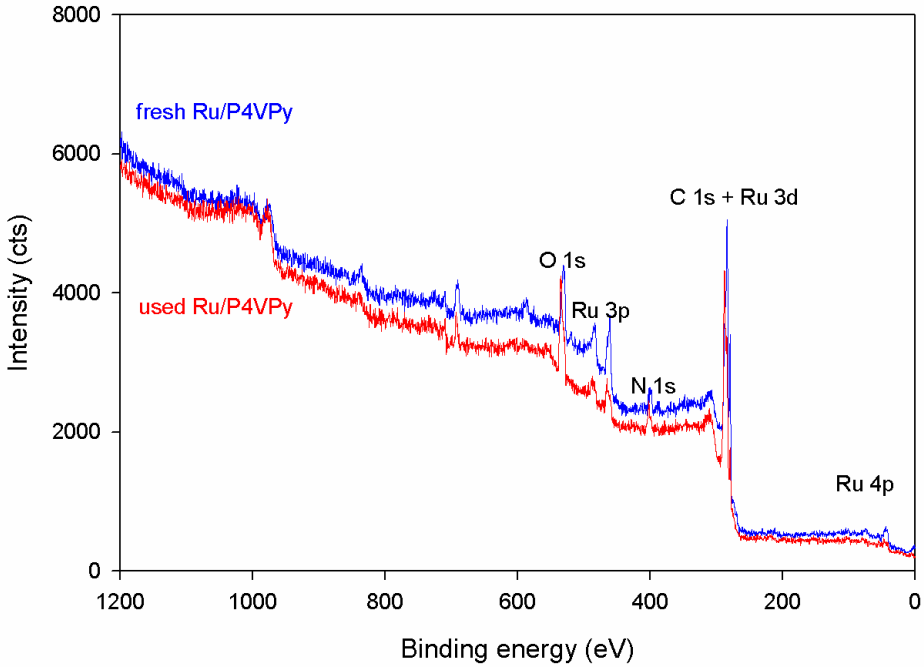

Figure 3-9. XPS survey scans of fresh and used 10 wt% Ru/P4VPy catalyst.

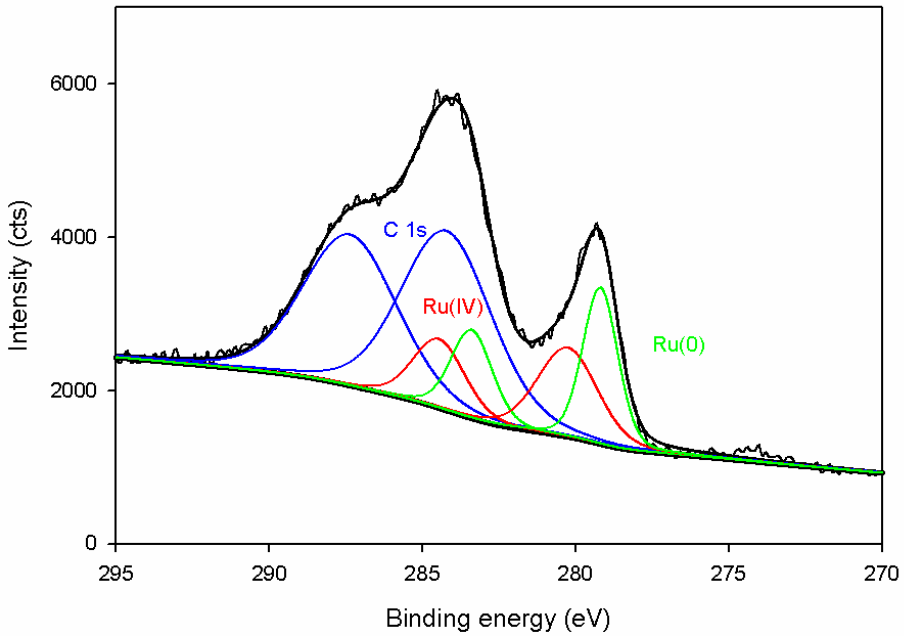

Figure 3-10. XPS narrow scan in C 1s and Ru 3d region for a fresh sample of Ru/P4VPy.

different types of carbons (C–C, C=C and C=N) of the poly(4-vinylpyridine) support, with binding energies of 285.0, 285.5 and 286 eV,[69] respectively, plus carbonaceous contaminants such as CH_x species accumulated on the catalyst surface. Since the carbon peaks are not of particular relevance to our discussion, only a single contributing peak was applied for simplicity. A further C 1s experimental peak at around 287 eV can be attributed to C–O bonds,[68] most likely due to residual methanol from the synthesis adsorbed on the catalyst surface. After a quinoline hydrogenation run, the relative intensity of both C 1s peaks was increased, with the C 1s peak at 287.4 eV being the largest peak in the used catalyst (Figure 3-11); these signals can be attributed to adsorbed organic material containing C–O and C–N bonds, including THF, quinoline and/or its hydrogenation products.

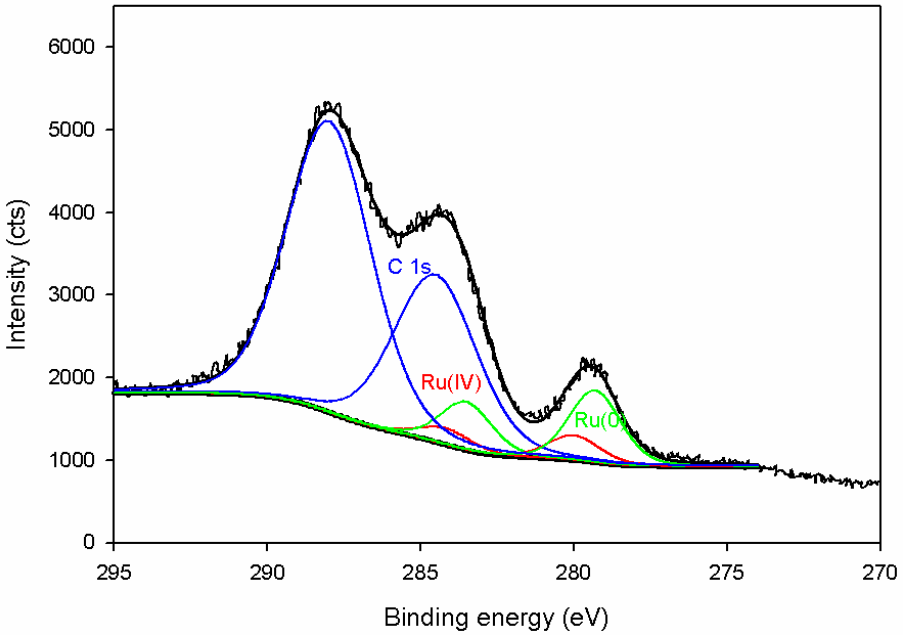

Figure 3-11. XPS narrow scan in C 1s and Ru 3d region for a used sample of Ru/P4VPy (Q hydrogenation, 150 °C and 50 atm).

Of more interest for our purposes, the peaks at 279.2 eV and 279.3 eV (Figure 3-10 and Figure 3-11) are assigned to Ru $3d_{5/2}$ spin-orbit components in the zerovalent state, whose binding energies are generally given as 280.1 eV for pure Ru metal.[68] The Ru $3d_{3/2}$ binding energies for both samples were observed at about 283.4 eV, which are also lower than that of bulk Ru metal (284.2 eV). The negative shift of the Ru 3d core level binding energies (about 0.8 eV) with respect to that of the standard metallic Ru is possibly derived from the strong interaction of the Ru particles with the N atoms of the PVPy, resulting in an electron density transfer from the basic support to the metallic particles. Similar effects have been observed for Ru metal particles supported on magnesia.[39] Finally, the separation of the Ru 3d peaks is 4.2 eV, consistent with the Ru 3d spin-orbit splitting value. The surface percentage of Ru(0) is roughly 40% for both fresh and used catalyst, based on the calculation of $A_{Ru(0)}/(A_{Ru(0)}+A_{Ru(IV)})$. The presence of a Ru(IV) component in both fresh and used catalyst is believed to result from air exposure during sample preparation since both fresh and used catalysts have the same surface ratio of Ru(IV). We believe that the RuNPs involved in the hydrogenation reactions are predominantly in the zerovalent state.

In the narrow scan spectra within the Ru 3p region, the experimental curve for the fresh catalyst is well-fitted by a main signal with maxima at 483.3 and 460.9 eV (Figure 3-12), which corresponds to the binding energy of Ru $3p_{1/2}$ and Ru $3p_{3/2}$ of Ru(0), respectively. An additional signal at higher energies (486.7 and 464.1 eV) is attributed to a Ru(IV) component. The binding energy of Ru $3p_{3/2}$ (460.9 eV) is also lower than that of standard Ru metal (461.5 eV), consistent with the negative shift of Ru 3d core level spectrum and due to the ability of basic polymer support to donate electrons to the

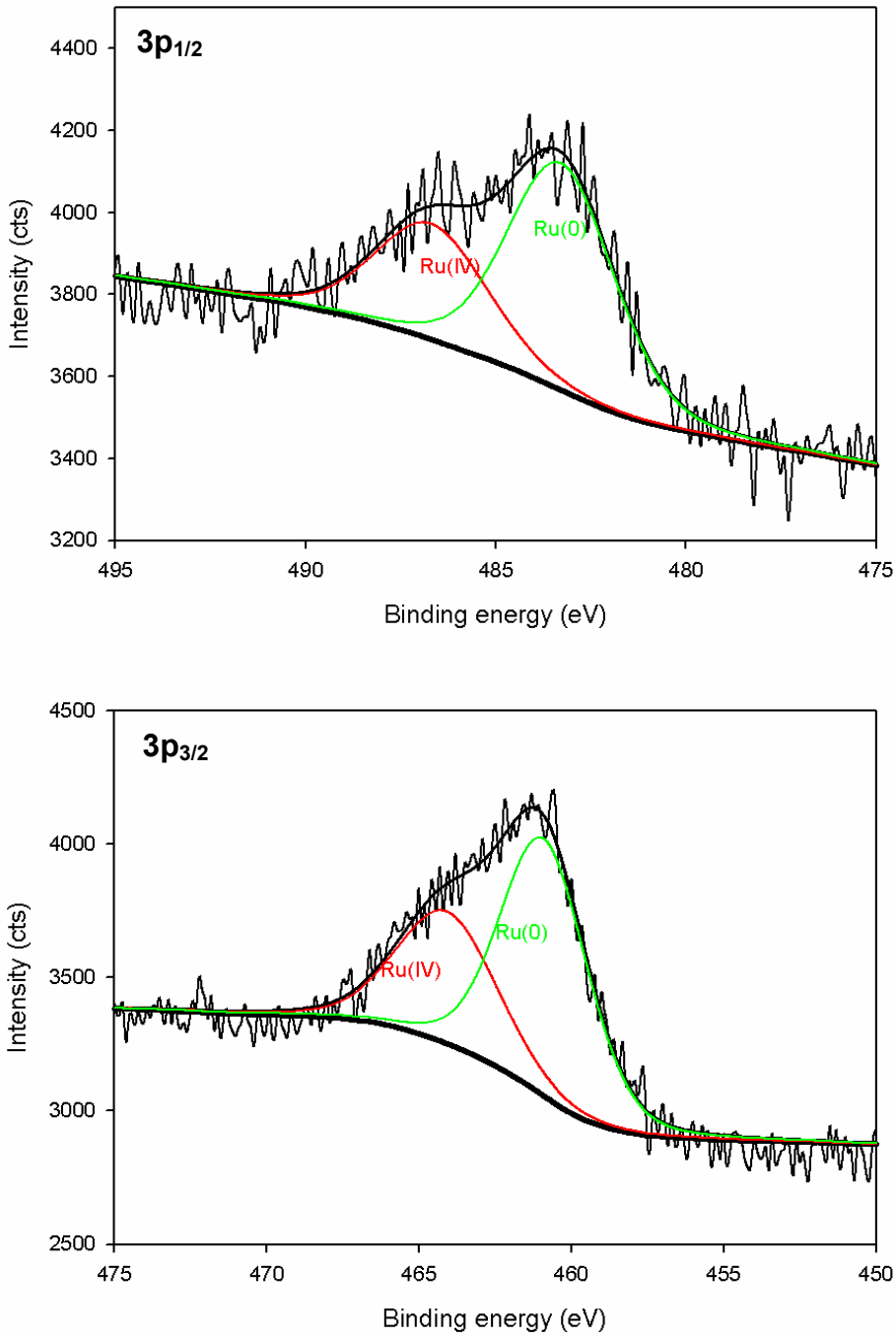

Figure 3-12. XPS narrow scan in Ru 3p region for a fresh sample of Ru/P4VPy.

surface Ru metal atoms. For the used catalyst at least two contributing peaks in both the Ru $3p_{1/2}$ and $3p_{3/2}$ regions are necessary to fit the experimental bands (Figure 3-13). The peaks at 483.3 eV in the $3p_{1/2}$ region and 461.1 eV in the $3p_{3/2}$ region correspond to Ru(0),

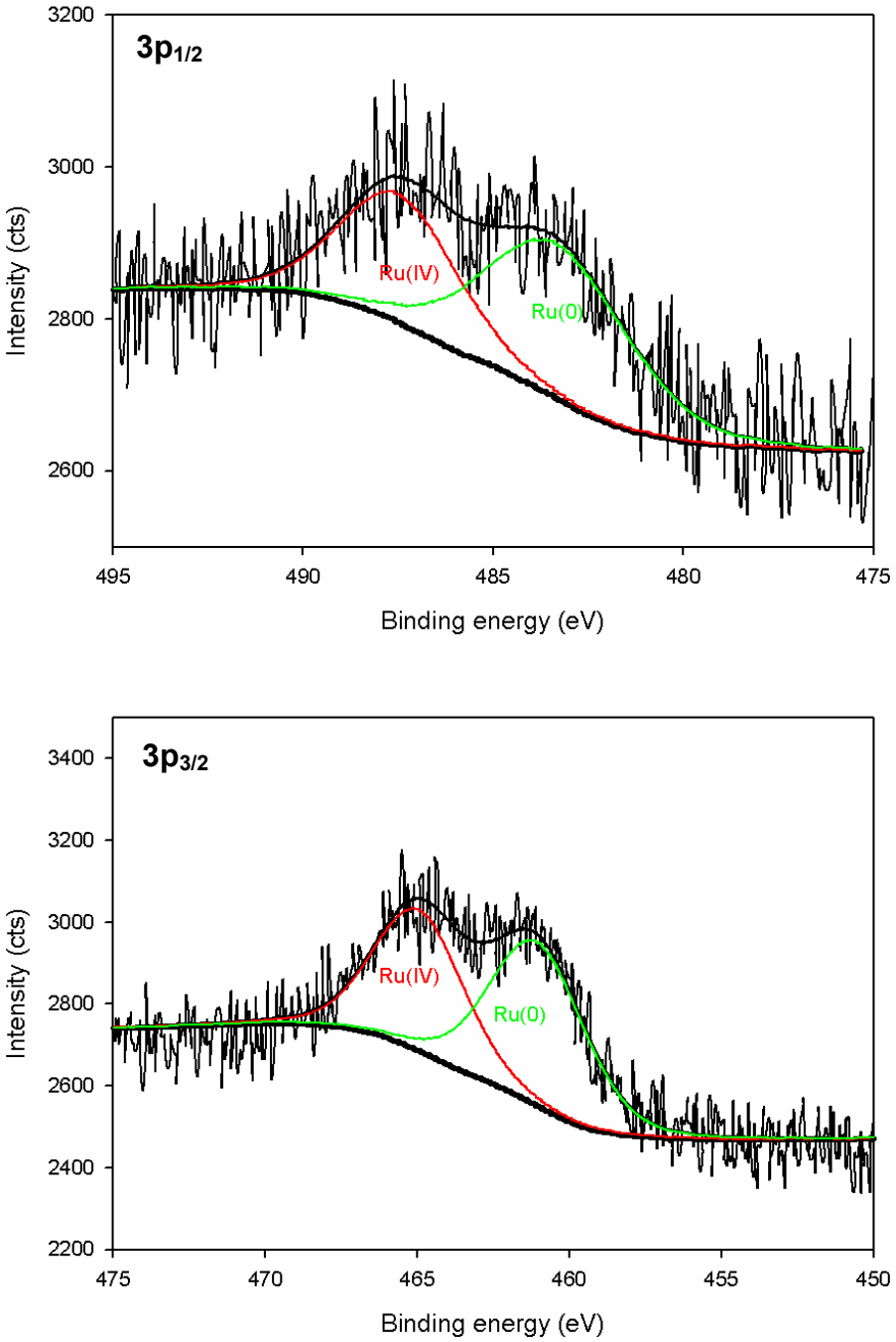

Figure 3-13. XPS narrow scan in Ru 3p region for a used sample of Ru/P4VPy (Q hydrogenation, 150 °C and 50 atm).

in agreement with the data for fresh catalyst. However, the peaks at 487.5 eV and 464.9 eV both have a positive shift by 0.8 eV compared to the peaks assigned to RuO_2 in fresh

catalyst, and the relative intensities also increase significantly. These peaks can be assigned more likely to Ru atoms bonding to O or N atoms of residual organic material from hydrogenation reactions, in agreement with the increase in peak intensities observed in the C 1s region for the used catalyst (Figure 3-11).

3.3.3 The unique ionic hydrogenation mechanism on Ru/P4VPy surfaces

Supported metal catalysts most commonly operate by homolytic hydrogen activation and transfer of atomic hydrogen to chemisorbed substrate molecules (Scheme 1-4). Catalyst poisoning frequently occurs in the presence of *e.g.* N-heterocycles due to strong adsorption of the substrate and/or of their hydrogenation products on the active metal sites. Our catalyst design involves metallic nanoparticles intimately associated with a basic support, with the aim of creating a nanostructure capable of promoting the heterolytic activation of hydrogen and ionic hydrogenation mechanisms (Scheme 1-6), as a strategy to avoid catalyst poisoning. In this context, the support not only stabilizes the RuNPs, but also may become directly involved in the catalytic reactions.

We investigated the catalyst behavior in the hydrogenation of aromatics compounds using toluene as the model arene and quinoline as the model N-heteroaromatic compound. In order to gain insights into the principal mechanisms operating in the hydrogenation reactions, particularly to demonstrate that our designed Ru/P4VPy catalyst is capable of promoting heterolytic H_2 activation and ionic hydrogenation mechanism for N-heteroaromatics, we investigated the effect of solvent polarity and the effect of addition of external acid or base in the hydrogenation of our model substrates; we also carried out substrate competition experiments and selective thiophene poisoning tests.

3.3.3.1 Hydrogenation of toluene and quinoline over Ru/P4VPy

The liquid-phase hydrogenation of toluene and quinoline was carried out in a batch reactor and the reaction course was monitored by GC or GC-MS analysis of samples periodically taken from the reactor. The data from the analysis were converted into hydrogenation rates reported as TOF values, *i.e.* moles of aromatic substrate converted per mol of Ru per h to evaluate the catalytic activities of the Ru/P4VPy catalyst.

Toluene is found to be exclusively hydrogenated to methylcyclohexane over the Ru/P4VPy catalyst at 120 °C and 10 atm H_2. A very small amount of methylcyclohexene was also detected from the reaction as minor products (Scheme 3-2). The hydrogenation profile is linear up to 80% conversion, providing a TOF value of 80 h^{-1} (Figure 3-14).

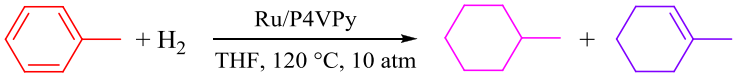

Scheme 3-2. Hydrogenation of toluene to methylcyclcohexane (MeCy) and methylcyclohexene.

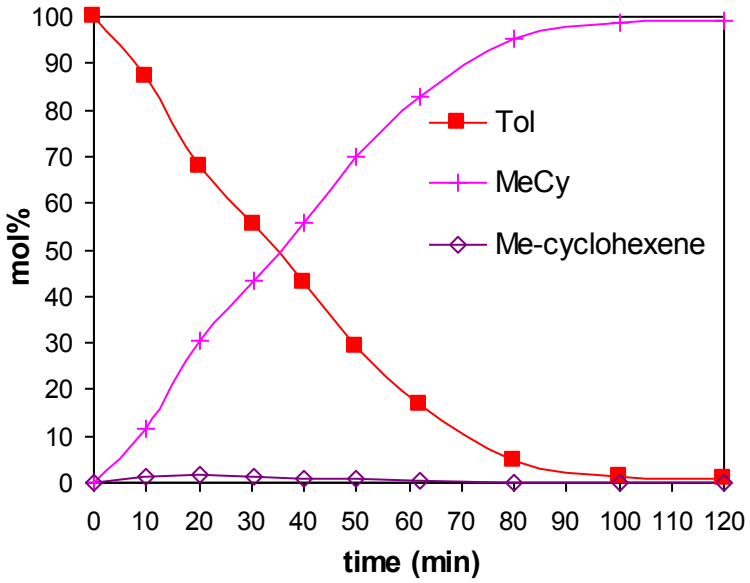

Figure 3-14. The profile of toluene hydrogenation over Ru/P4VPy (n_{Tol} : n_{Ru} = 100 : 1; 120 ºC, 10 atm; in THF).

Quinoline as the common N-heteroaromatic compound usually acts as a catalyst poison. However, the Ru/P4VPy catalyst can hydrogenate quinoline under moderate reaction conditions, being resistant to its poisoning effect (Scheme 3-3). At 150 °C and 50 atm, an initial TOF of 170 h^{-1} can be achieved. The hydrogenation profile (Figure 3-15) indicates that both the heterocyclic and the carbocyclic rings can be hydrogenated: the heterocyclic ring is preferentially reduced to have 1,2,3,4-tetrahydroquinoline (N-THQ) as the major product; the carbocyclic ring is also hydrogenated to yield 5,6,7,8-tetrahydroquinoline (C-THQ) but at a slower rate. Both tetrahydroquinolines can be further hydrogenated, ending up with decahydroquinoline (DHQ) as the final product.

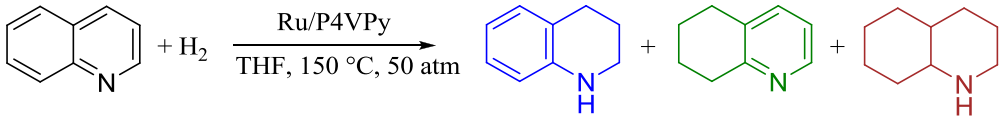

Scheme 3-3. Hydrogenation of quinoline to 1,2,3,4-tetrahydroquinoline (N-THQ), 5,6,7,8-tetrahydroquinoline (C-THQ) and decahydroquinoline (DHQ).

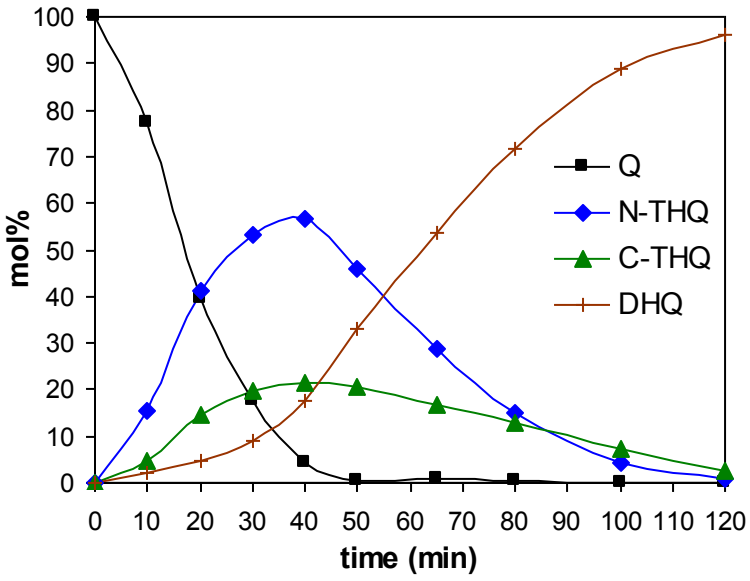

Figure 3-15. The profile of quinoline hydrogenation over Ru/P4VPy (n_Q : n_{Ru} = 100 : 1; 120 ºC, 50 atm; in THF).

3.3.3.2 Solvent effects

A variety of solvents with different polarities were used for hydrogenation of quinoline or toluene under analogous reactions conditions. The results of those experiments are depicted in Figure 3-16 and Figure 3-17 for quinoline and toluene, respectively. Figure 3-16 shows that the use of polar solvents results in an enhancement of the catalytic activity in hydrogenation of quinoline, with methanol producing the highest rate. The correlation between higher solvent polarity and higher catalytic activity for quinoline is in agreement with an ionic mechanism.

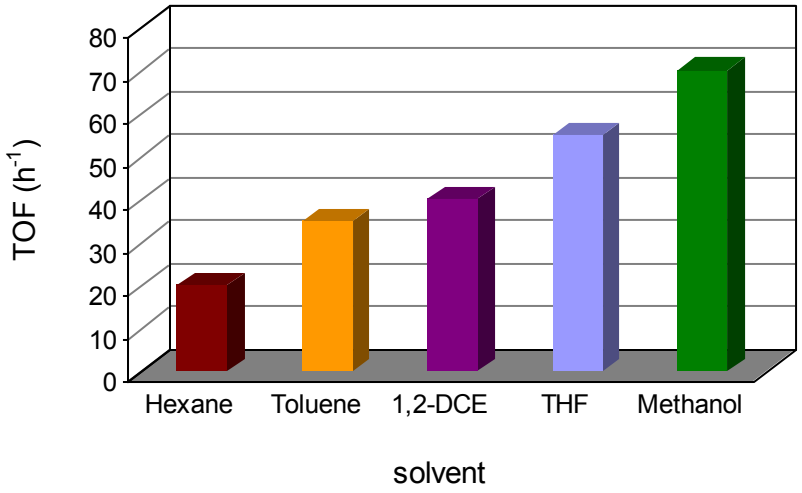

Figure 3-16. Effect of solvent on the hydrogenation of quinoline over Ru/P4VPy (120 ºC, 30 atm; $n_Q : n_{Ru} = 84 : 1$).

For toluene, on the other hand, there is no correlation between TOF values and solvent polarities (Figure 3-17). Hydrogenation in THF gives the highest TOF value, while hydrogenation in polar methanol and non-polar hexane has comparable rates. This suggests a possible classical homolytic pathway for hydrogenation of toluene over Ru/P4VPy.

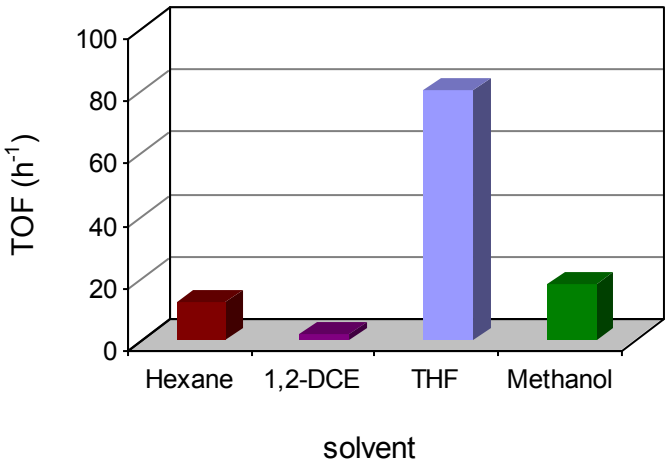

Figure 3-17. Effect of solvent on the hydrogenation of toluene over Ru/P4VPy (120 ºC, 10 atm; $n_{Tol} : n_{Ru} = 100 : 1$).

3.3.3.3 Effect of adding external acid or base

Upon addition of small amount of the strong base triethylamine (pK_a *ca.* 11), an enhancement of quinoline hydrogenation rates (TOF from 50 h^{-1} to 140 h^{-1}) was observed (Figure 3-18). This could be related to heterolytic H_2 splitting since Et_3N is a stronger base than P4VPy (pK_a 10.8 vs. 7.4) and therefore heterolytic hydrogen activation is favored by forming a metal hydride and a triethylammonium ion. Enhancement of catalytic activity by addition of base is very common in homogeneous catalysis, *e.g.* for $RuCl_2(PPh_3)_3$, which readily reacts with H_2 in the presence of the amine to yield the active hydride $RuHCl(PPh_3)_3 + Et_3N{\cdot}HCl$.[70] For our Ru/P4VPy catalyst, the heterolytic splitting mechanism envisaged in the case of quinoline could be initiated by either the basic pyridine groups of the support, or by the basic substrates themselves. In either case, protonation of the N atom of the substrate would be assisted by hydrogen bonding to the N atom of a pyridine group in the support (Figure 3-19).

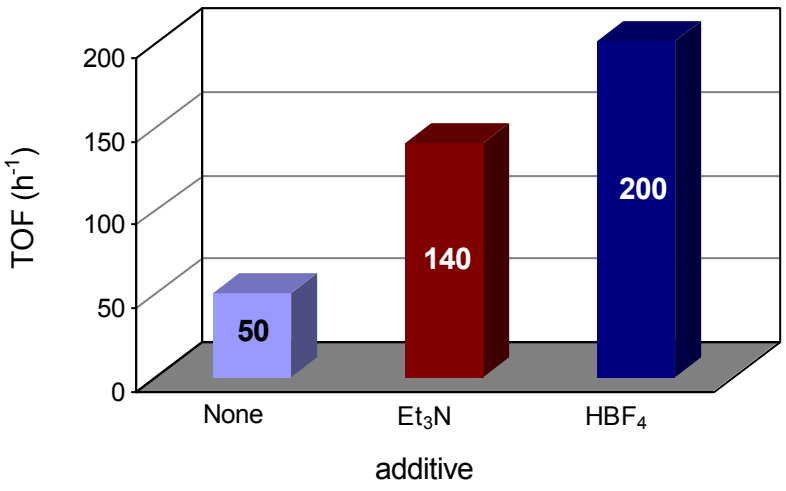

Figure 3-18. Effect of adding external acid or base on the hydrogenation of quinoline over Ru/P4VPy (120 ºC, 30 atm; $n_Q : n_{Ru} = 84 : 1$, in toluene).

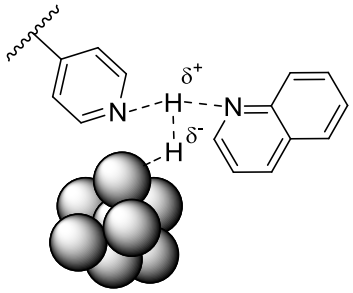

Figure 3-19. Heterolytic splitting of H_2 assisted by the support on Ru/P4VPy.

Addition of HBF_4 also produced a significant increase in TOF from 50 h^{-1} to 200 h^{-1} for hydrogenation of quinoline under the same conditions (Figure 3-18). This is most likely due to protonation of the pyridine groups of the support or of the substrate, leading to the same type of hydrogen bonded intermediate on the surface as formed in heterolytic splitting of hydrogen (Figure 3-19).

However, in the case of toluene hydrogenation, addition of Et_3N did not have a noticeable effect on the TOF, while addition of HBF_4 had a deleterious effect. This is in accord with a homolytic pathway, since a proportion of the adsorbed H atoms on the

metal active sites would react with H^+ to release hydrogen gas and would therefore not be available for transfer to the substrate.

Therefore, the results of hydrogenation of quinoline and toluene with the addition of acid or base strongly point to the heterolytic hydrogen splitting and an ionic hydrogenation pathway for quinoline on the Ru/P4VPy surfaces, while a homolytic pathway for toluene.

3.3.3.4 Substrate competition and selective poisoning experiments

In order to provide further evidence for the ionic hydrogenation mechanism for quinoline on the Ru/P4VPy surfaces, substrate competition and selective poisoning experiments were carried out. Substrate competition experiments were performed using equimolar amounts of toluene and quinoline, while keeping the molar ratio of each substrate to Ru at 100 : 1. The reaction profile is depicted in Figure 3-20. At the early stages of hydrogenation (30 min), only quinoline was reduced with a TOF of 160 h^{-1}, predominantly at the heterocyclic ring to yield N-THQ but also at the carbocyclic ring to produce C-THQ as a minor product (25 %); at longer reaction times (> 45 min), both N-THQ and C-THQ were further reduced to DHQ, the former at a more pronounced rate. Toluene, on the other hand, was only hydrogenated to an important degree after all the quinoline and most of the THQs had been consumed; this observation indicates that the presence of quinoline, and to a lesser extent N-THQ inhibited the hydrogenation of toluene.

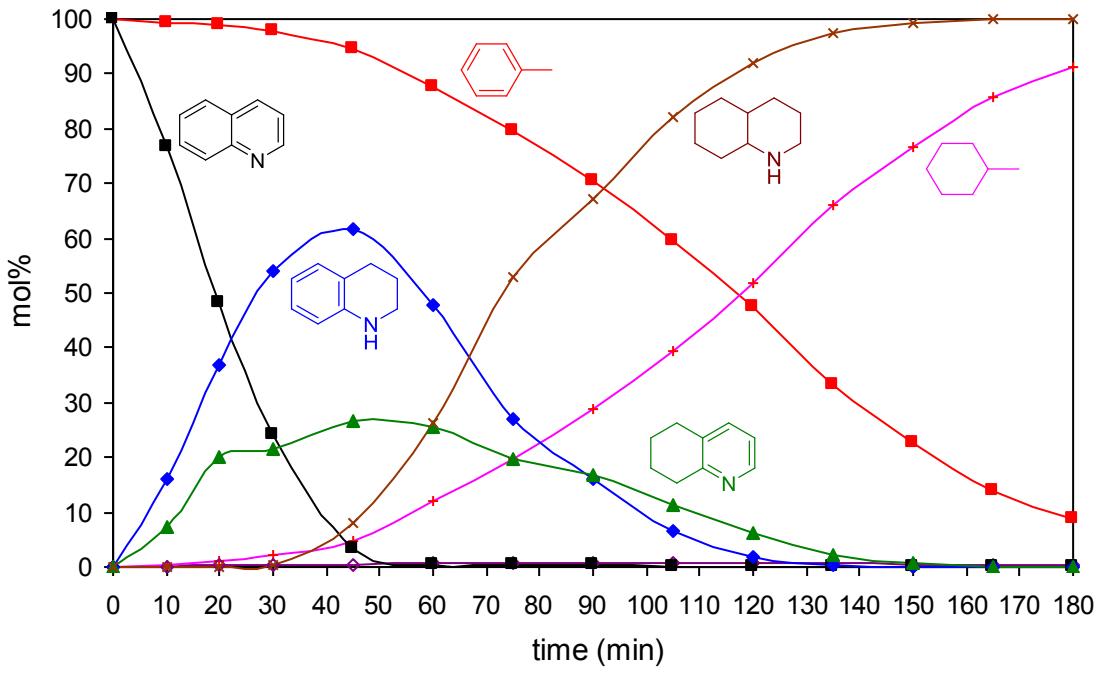

Figure 3-20. Hydrogenation profile of equimolar quinoline and toluene (150 ºC, 50 atm; $n_Q : n_{Tol} : n_{Ru} = 100 : 100 : 1$; in THF).

This suggests the possibility of two different hydrogenation mechanisms acting in parallel on two distinct sites on the Ru/P4VPy catalyst, as illustrated in Figure 3-21. The first involves heterolytic H_2 splitting and ionic hydrogenation of polar N-heteroaromatics (path *a*) taking place at Type A sites (Ru-N bifunctional units), while the second one (path *b*) operates for non-polar aromatics and most likely involves conventional homolytic H_2 splitting on Type B sites (only Ru surfaces). Quinoline would thus be hydrogenated simultaneously at the heterocyclic ring at Type A sites through pathway *a* to produce N-THQ and at the carbocyclic ring at Type B sites through pathway *b* to give C-THQ; these parallel reactions on quinoline would block the access of toluene to the B type sites. Once quinoline and most THQs are consumed, toluene can effectively compete for the Type B sites and be hydrogenated through path *b* to methylcyclohexane.

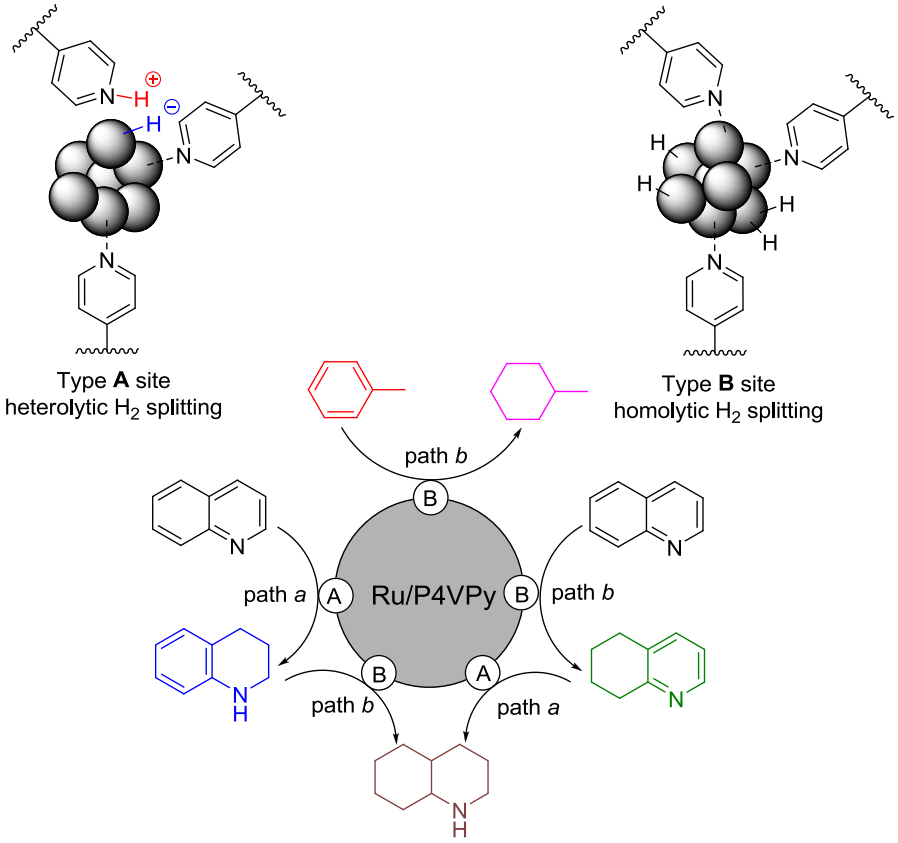

Figure 3-21. The dual-site substrate-dependent mechanism involving a unique ionic hydrogenation pathway.

Further evidence for the proposed dual site mechanism on Ru/P4VPy was obtained from selective poisoning caused by addition of small amounts of thiophene. In a poisoning test, 10 μL of thiophene was mixed into 1 mL of quinoline (n_Q : n_T : n_{Ru} = 100 : 1.5 : 1) prior to the hydrogenation run. The reaction profile is depicted in Figure 3-22. At 150 ºC and 50 atm, quinoline was exclusively hydrogenated to N-THQ, with an initial TOF value of 160 h^{-1}, essentially the same as for the substrate competition experiment. There was no evidence for the formation of even traces of C-THQ or DHQ; this implies that thiophene selectively blocks Type B sites (and consequently pathway *b*) for the hydrogenation of the carbocyclic ring of quinoline but has no effect on the hydrogenation of the heterocyclic ring.

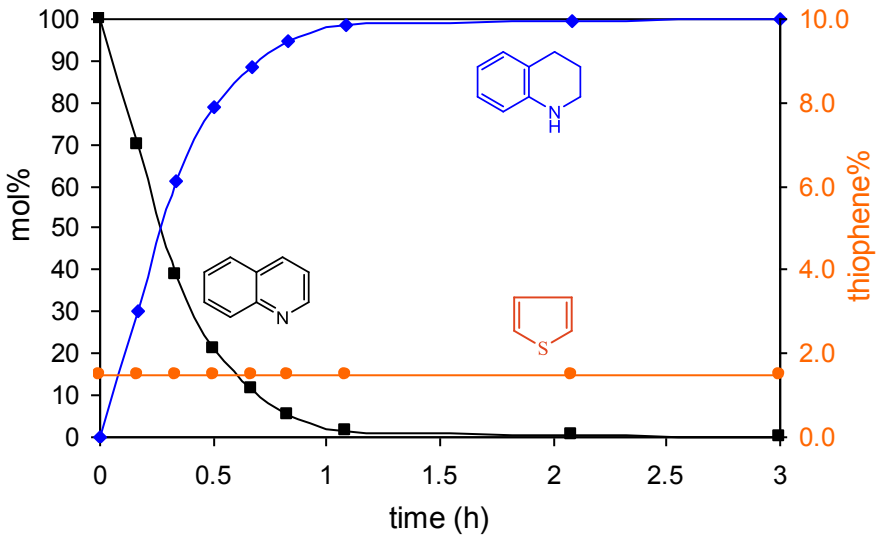

Figure 3-22. Hydrogenation profile of quinoline with 1 v% thiophene (150 ºC, 50 atm; $n_Q : n_T : n_{Ru} = 100 : 1.5 : 1$; in THF).

On the other hand, when toluene was used as the substrate, the presence of small amounts of thiophene fully inhibited the hydrogenation reaction (Figure 3-23). Thiophene was not hydrogenated in either case. An explanation consistent with all the details extracted from the combined results is that carbocyclic rings (of quinoline or toluene) are hydrogenated at type B sites in Ru/P4VPy, through a homolytic hydrogen splitting pathway *b*, but thiophene binds strongly to such sites, effectively poisoning their catalytic activity. N-heterocyclic rings, in contrast, are hydrogenated at type A sites through an ionic mechanism *a*, involving the heterolytic splitting of H_2 assisted by the basic support; thiophene probably has little or no affinity for this type of site and thus the only effect of thiophene on the hydrogenation of quinoline is to suppress the hydrogenation of the carbocyclic ring at type B sites and drive the selectivity for N-THQ to 100%.

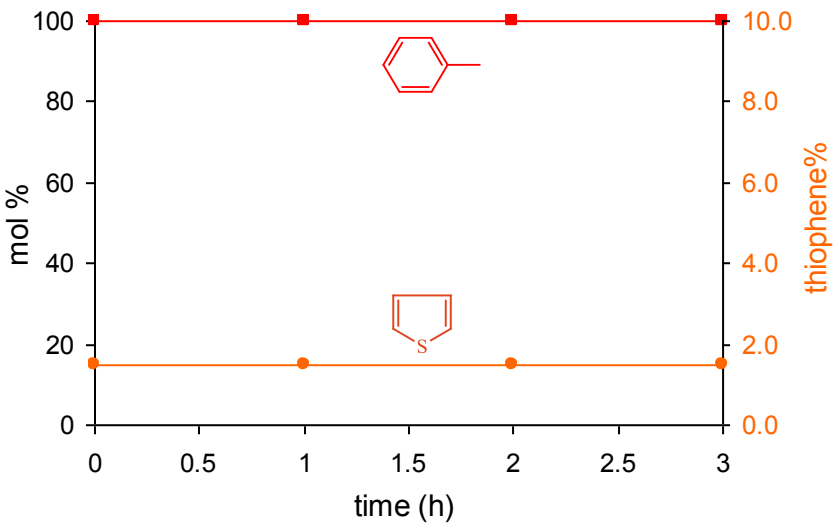

Figure 3-23. Hydrogenation profile of toluene with 1 v% thiophene (120 ºC, 10 atm; n_{Tol} : n_T : n_{Ru} = 100 : 1.5 : 1; in THF).

Therefore, a unique ionic hydrogenation mechanism was demonstrated on the Ru/P4VPy surfaces, supporting our hypothesis; this unique ionic mechanism is promoted by the nanostructure consisting of RuNPs intimately associated with a basic support and operates through the Ru-N bifunctional effects. This is **the first time** these ionic hydrogenation pathways have been demonstrated on surfaces.[71] For the RuNPs surfaces without basic sites in close proximity, the conventional homolytic H_2 splitting is otherwise involved.

3.3.4 The scope of hydrogenation over Ru/P4VPy

In order to verify that the unique ionic hydrogenation mechanism promoted by the Ru/P4VPy nanostructure also works for other heteroatom aromatics, we investigated the scope of the Ru/P4VPy catalyst for the hydrogenation of a variety of other N-/S-heteroaromatics, as well as of simple mono-/polycyclic aromatic hydrocarbons (MAHs and PAHs), that are representative of components of petroleum-derived fuels, as shown in Figure 3-24. To check the stability of the Ru/P4VPy catalyst under typical reaction conditions, the influence of hydrogenation pressure and temperature on the catalytic activity of Ru/P4VPy was also investigated using model substrates toluene and quinoline.

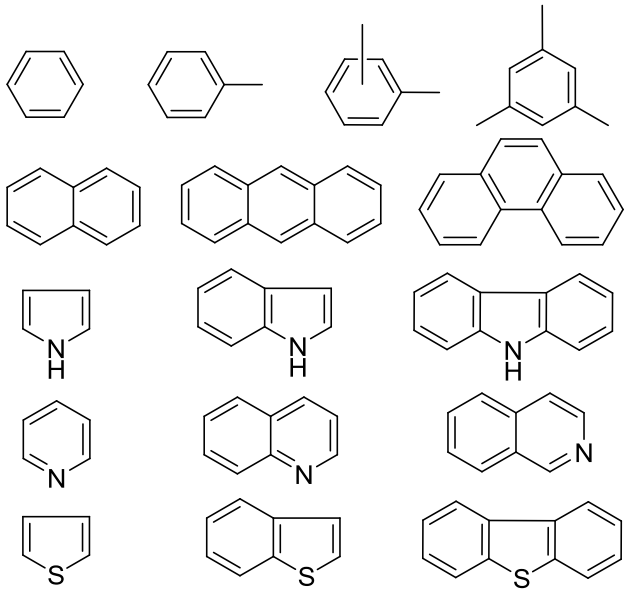

Figure 3-24. Representative substrates investigated for hydrogenation over Ru/P4VPy.

3.3.4.1 Effect of pressure and temperature

For toluene hydrogenation, within the pressure range of 10–50 atm, TOF values increased steadily with increased pressure (Figure 3-25a). This indicates that sintering or other deactivation processes do not take place to an important extent on the Ru/P4VPy catalyst at H_2 pressures up to 50 atm. The hydrogenation rates for toluene also increase with increasing temperature in the range 25–150 °C (Figure 3-25b), indicating the catalyst is stable within this temperature range. Under the combined maximum temperature and pressure within our experimental range (150 °C and 50 atm), toluene could be hydrogenated with a TOF of about 2,000 h^{-1}.

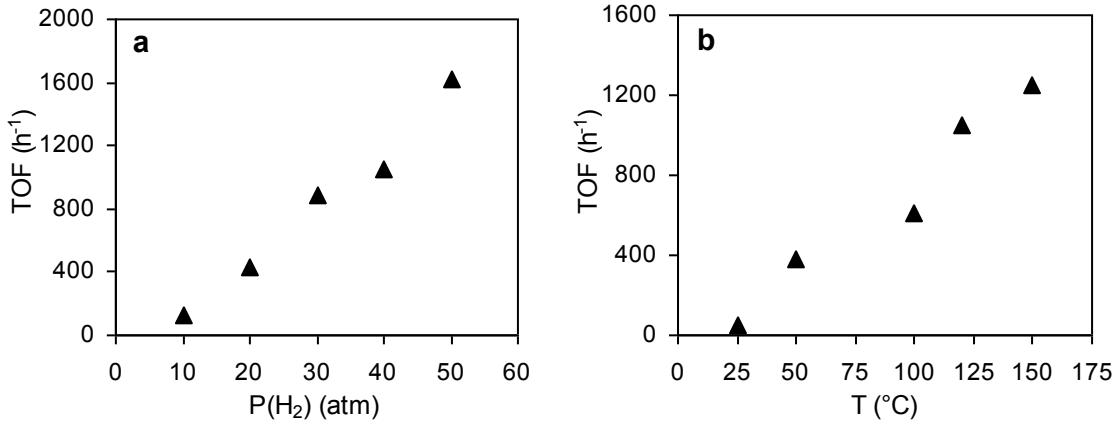

Figure 3-25. Influence of a) pressure (120 °C, $n_{Tol} : n_{Ru} = 1000 : 1$) and b) temperature (40 atm, $n_{Tol} : n_{Ru} = 1000 : 1$) on toluene hydrogenation rates.

In contrast to the case of toluene, the effect of H_2 pressure on the catalytic activity of Ru/P4VPy for quinoline hydrogenation displays a "volcano" shape relationship (Figure 3-26). The activity increases with increased pressure in the range of 20–40 atm but decreases when pressure is further increased to 50 atm, leaving the maximum around 40 atm at 120 °C. This suggests some deactivation processes take place at pressure over

40 atm, possibly due to some aggregation of RuNPs, as a moderate increase of RuNPs size was observed after a hydrogenation run (section 3.3.2.1).

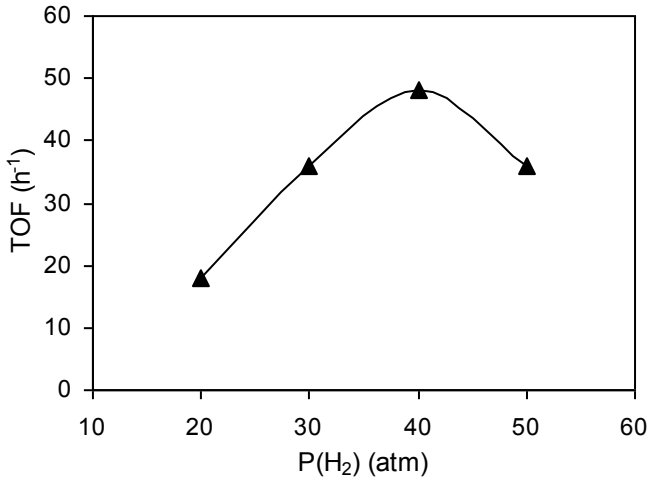

Figure 3-26. Effect of pressure on quinoline hydrogenation rates (120 ºC, $n_Q : n_{Ru} = 84 : 1$).

3.3.4.2 Hydrogenation of arenes

The catalytic activities of Ru/P4VPy on hydrogenation of different monocyclic aromatic hydrocarbons (MAHs) including toluene are summarized in Table 3-1. Ru/P4VPy is effective for the hydrogenation of these aromatics at low temperature and pressures. The hydrogenation rate decreases with increasing steric congestion on the arene ring; a comparison of entries 1–6 shows a steady decrease in the TOF values from 120 h^{-1} for benzene to 3 h^{-1} for mesitylene. On the other hand, the hydrogenation rate is rather insensitive to electronic effects, as revealed by comparison of entries 2, 8 and 9, where the presence of the electron-withdrawing substituent $–CF_3$ and the electron-donating $–OCH_3$ on the ring produces only a moderate deactivating effect. This is consistent with Dupont's work[72] on RuNPs immobilized in ionic liquids, where relative reaction rates were found to be dominated by steric factors. Benzene and toluene are exclusively

Table 3-1. Hydrogenation of monocyclic aromatic hydrocarbons (MAHs) over Ru/P4VPy

entry	substrate[a]	TOF (h^{-1})	products distribution at 1 h			
			main		minor	
1		120		100%	–	–
2	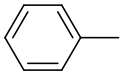	70	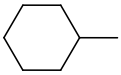	99%	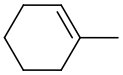	1%
3	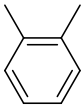	25	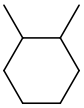	80%	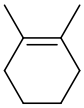	20%
4	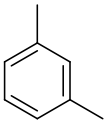	20	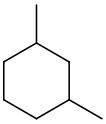	80%	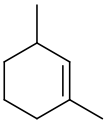	20%
5	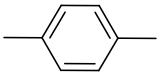	15	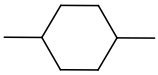	70%	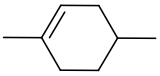	30%
6	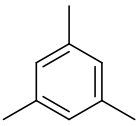	3	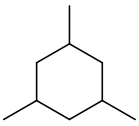	60%	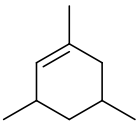	40%
7[b]		40		90%		10%
8	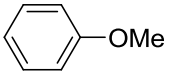	40	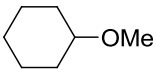	80%	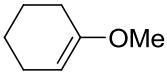	20%
9	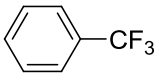	60	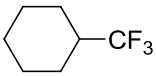	98%	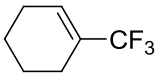	2%

[a] In THF; n_{sub}: n_{Ru} = 100 : 1; 120 °C and 10 atm; [b] 150 °C and 50 atm.

hydrogenated to the corresponding cyclohexanes (entries 1 and 2), but the more resistant substrates yield mixtures of cycloalkenes and cycloalkanes, with the latter being the major products; the cyclohexenes formed are those with the more highly substituted double bond (entries 3–9). As expected, an increase in temperature and pressure increased the hydrogenation rates for MAHs, raising the TOF value, in the case of mesitylene, from 3 h^{-1} at 120 ºC and 10 atm to 40 h^{-1} at 150 ºC and 40 atm (entries 6 and 7). The proportion of fully hydrogenated product also increased at higher temperatures and pressures or at longer reaction times.

A number of other supported Ru catalysts are also known to hydrogenate MAHs, mostly benzene and toluene; *e.g.* toluene can be hydrogenated with TOF values ranging from *ca.* 100–600 h^{-1} at moderate conditions[45,47,54,58] and 10,000–30,000 h^{-1} at elevated temperature and pressure.[26,30]

Bicyclic and tricyclic aromatic hydrocarbons, which are generally difficult to reduce, were also hydrogenated efficiently over Ru/P4VPy (Table 3-2). Naphthalene was hydrogenated mainly to 1,2,3,4-tetrahydronaphthalene, with minor amounts of deca-hydronaphthalene and traces of octahydronaphthalene, with a TOF of 60 h^{-1}; anthracene was hydrogenated to 1,2,3,4-tetrahydroanthracene as the major product, along with several other minor hydrogenation products, with a TOF of 45 h^{-1}. Polycyclic aromatic hydrocarbons (PAHs), as expected, are more resistant to hydrogenation than MAHs, thus requiring higher temperature and pressure to get comparable rates with those of MAHs. The outer rings of the tricyclic arene are hydrogenated more easily than the inner benzene ring, as shown in the products distribution for the hydrogenation of anthracene.

Only two examples of supported Ru catalysts are known for hydrogenation of PAHs. Hydrogenation of naphthalene and anthracene has been observed over Ru particles supported on polydimethylphosphazenes (PDMP)[34] and on silica,[54] respectively. We are not aware of any other reports on hydrogenation of PAHs by RuNPs.

Table 3-2. Hydrogenation of polycyclic aromatic hydrocarbons (MAHs) over Ru/P4VPy

substrate[a]	TOF (h^{-1})	products distribution at 1 h
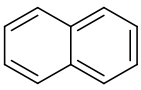	60	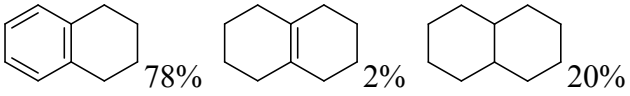 78% 2% 20%
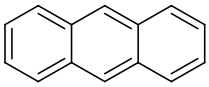	45[b]	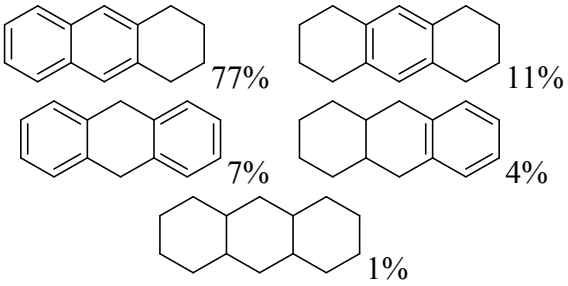 77% 11% 7% 4% 1%

[a] In THF; $n_{sub} : n_{Ru} = 100 : 1$; 150 ºC and 50 atm; [b] $n_{sub} : n_{Ru} = 50 : 1$.

3.3.4.3 Hydrogenation of N-heteroaromatics

N-heteroaromatics are of great concern not only because they contribute NO_x emissions but also because they commonly act as catalyst poisons, by strong adsorption on the active sites of catalysts. However, it has been shown that the Ru/P4VPy catalyst can efficiently hydrogenate quinoline under moderate reaction conditions, being resistant to its poisoning effect owing to the unique ionic hydrogenation mechanism promoted by the nanostructure of the Ru/P4VPy catalyst.

Functioning through this ionic hydrogenation mechanism, Ru/P4VPy is also efficient for the hydrogenation of a variety of other N-heteroaromatic compounds representative of fuel components under moderate conditions (150 ºC and 30/50 atm), as summarized in Table 3-3. Pyridine and quinoline were easily reduced at 120 °C under 10 atm (entries 5 and 7), while hydrogenation of pyrrole and other five-membered N-heterocycles required higher temperatures and pressures (150 ºC and 50 atm, entries 1–4). Interestingly, quinoline is more easily hydrogenated than isoquinoline under the same conditions but less selectively (entries 8 and 10); specific reduction of the heterocyclic

Table 3-3. Hydrogenation of N-heteroaromatics over Ru/P4VPy[a]

entry	substrate	T (°C)	P_{H2} (atm)	TOF (h^{-1})	Products distribution at 1 h
1	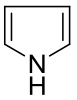	120	30	5	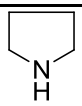 100%
2	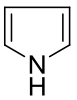	150	50	70	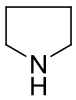 100%
3	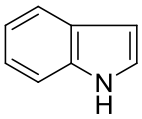	150	50	45	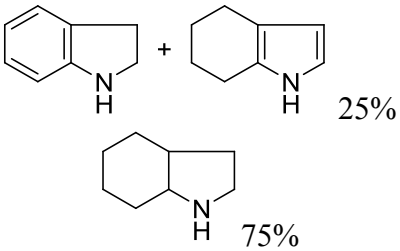 25% 75%
4	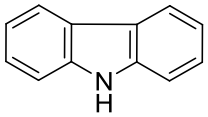	150	50	20	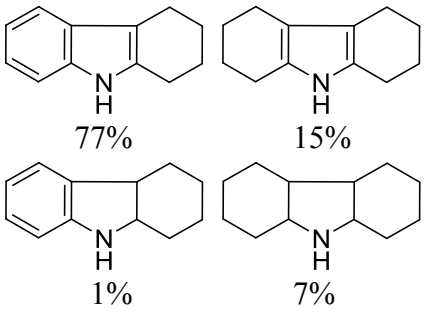 77% 15% 1% 7%
5	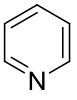	120	10	10	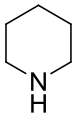 100%
6	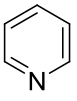	150	50	100	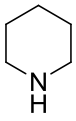 100%
7	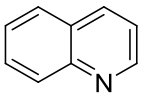	120	10	20	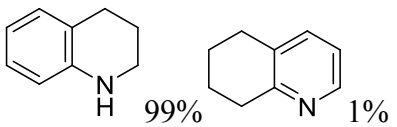 99% 1%
8	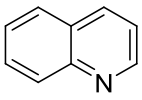	150	50	170	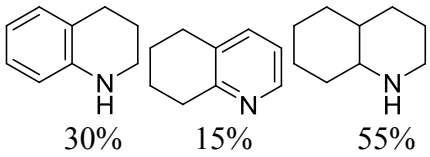 30% 15% 55%
9	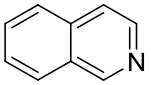	150	30	15	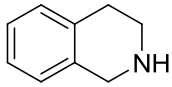 100%
10	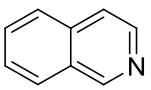	150	50	30	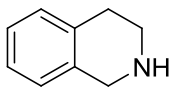 100%

[a] In THF; $n_{sub} : n_{Ru} = 100 : 1$.

ring was observed even when both the temperature and the pressure were increased (entries 9 and 10), in contrast to the case of quinoline (entries 7 and 8). There are, to our knowledge, no other reports on such versatility in the hydrogenation of N-heteroaromatic compounds catalyzed by supported RuNPs.

Other supported Ru catalysts have been reported to be poisoned by N-heteroaromatics. For instance, a commercial Ru/Al_2O_3 was reported to be inactive towards hydrogenation of quinoline.[73] Only a few other supported Ru catalysts are known to hydrogenate N-aromatics: Spitaleri *et al*. reported the reduction of pyridine and quinoline by RuNPs on polydimethylsphazenes (PDMP) in homogeneous phase, with a TOF of about 200 h^{-1} at 25 ºC and 50 atm H_2;[34] Bianchini and coworkers used silica-supported Ru particles to hydrogenate quinoline, indole and at 100 ºC and 30 atm H_2 with TOF values ranging from 50–200 h^{-1};[54] Li and coworkers used a hydroxyapatite-supported Ru catalyst for hydrogenation of quinoline and some of its methylated derivatives at 150 ºC and 40 atm with TOF values from 50 to 150 h^{-1}.[31] Although there were no mechanistic studies carried out for these catalysts, we now believe heterolytic hydrogen activation and the ionic hydrogenation mechanism were also involved in these hydrogenation reactions.

3.3.4.4 Hydrogenation of S-heteroaromatics

S-heteroaromatics are more resistant to hydrogenation over Ru/P4VPy than their nitrogen counterparts under similar reaction conditions (Table 3-4). There was no hydrogenation of thiophene and benzothiophene (BT) at 120°C and 10 atm (entries 1 and 3). However, when the temperature and pressure were increased (150 °C and 50 atm), hydrogenation products were observed, although the rate was slow: about 1% thiophene and 1% BT

were hydrogenated to tetrahydrothiophene and dihydrobenzothiophene (DHBT), respectively, with a TOF value of 0.5 h^{-1} in both cases (entries 2 and 4); the conversion of BT was increased to 2% after 24 h. Dibenzothiophene (DBT), on the other hand, can not be hydrogenated at all at 150 °C and 50 atm (entry 5) and possibly requires even higher temperature and pressure to have detectable conversions.

Table 3-4. Hydrogenation of selected S-heteroaromatics over Ru/P4VPy[a]

entry	substrate	T (°C)	P_{H2} (atm)	products	conversion	TOF
1		120	10	NR	–	–
2		150	50		1% (2h)	0.5 h^{-1}
3	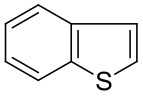	120	10	NR	–	–
4	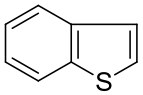	150	50	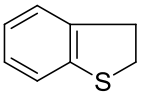	1% (2h) 2% (1d)	0.5 h^{-1} 2 d^{-1}
5	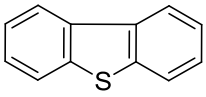	150	50	NR	–	–

[a] In THF; $n_{sub} : n_{Ru} = 100 : 1$.

There are no other supported RuNPs reported to have activity towards hydrogenation of S-heteroaromatics. RuNPs supported on silica were used for hydrogenation of S-aromatics but did not catalyze BT or DBT hydrogenation to any extent.[54] Indeed, S-heteroaromatics are generally hard to hydrogenate over supported noble metal catalysts due to their poisoning effect, especially larger molecules such as DBTs. Our Ru/P4VPy showed certain hydrogenation activities for thiophene and BT at low temperature and pressure compared to industrial level, albeit at low reactions rates.

3.3.5 Catalyst recyclability

To evaluate the recyclability of the Ru/P4VPy catalyst, a catalyst sample was used in three consecutive hydrogenation runs of either neat toluene or quinoline in THF. After each run, the catalyst was carefully recovered under a nitrogen atmosphere and re-used in subsequent cycles. Table 3-5 summarizes the TOF values during different cycles. For both toluene and quinoline, catalyst activities displayed small variation. Consistently, the average Ru particle size was only moderately increased after the first toluene hydrogenation run and no important further changes in particle size distribution were observed by TEM after three consecutive hydrogenation runs. These suggest the Ru/P4VPy catalyst can be recovered and reused for at least three hydrogenation cycles without any appreciable loss of catalytic activity.

Table 3-5. Catalytic activities of Ru/P4VPy in recycling experiments

substrate	cycle	TOF (h^{-1})
	1	400
toluene[a]	2	550
	3	545
	1	20
quinoline[b]	2	25
	3	20

[a] 25 mL of toluene; 230 mg of catalyst; solventless; 120 °C, 20 atm.
[b] 1 mL of quinoline; 84 mg of catalyst; solvent: THF; 120 °C, 10 atm.

3.4 Conclusion

We have designed a new nanostructured catalytic material composed of RuNPs immobilized on the basic polymer P4VPy based on our hypothesis and synthesized the Ru/P4VPy catalyst by $NaBH_4$ reduction of $RuCl_3 \cdot 3H_2O$ in the presence of the polymer in methanol at room temperature. TEM measurements show the RuNPs are well-dispersed with an average diameter of 3.0 nm. Both powder XRD diffraction patterns and XPS measurements confirm that the RuNPs are predominantly in the zerovalent state.

The new Ru/P4VPy catalyst is capable of promoting unique surface heterolytic H_2 activation and ionic hydrogenation mechanisms for hydrogenation of N-heteroaromatics through the Ru-N bifunctional effects within the nanostructure consisting of RuNPs intimately associated with a basic support, as predicted by our hypothesis; this unique ionic hydrogenation mechanism is well demonstrated by the solvent effect studies, the acid and base effects studies, substrate competition experiments and selective thiophene poisoning tests in hydrogenation of model toluene and quinoline substrates. This is **the first time** these ionic hydrogenation pathways have been demonstrated on surfaces.[71] For the RuNPs surfaces without basic sites in close proximity, the conventional homolytic H_2 splitting is otherwise involved.

The unique ionic hydrogenation mechanism on the Ru/P4VPy surfaces can also work for other heteroatom aromatics. Ru/P4VPy has proven to be a versatile catalyst for the efficient hydrogenation of a variety of MAHs, PAHs and N-heteroaromatics at low temperature and pressure compared to industrial level, being resistant to the nitrogen poisons; it is also active towards hydrogenation of S-heteroaromatics, albeit at low rates. Additionally, the catalyst is stable and recyclable.

Chapter 4
Ru/MgO Improves the Catalyst Efficiency for the Hydrogenation of Aromatic Compounds

4.1 Introduction

After successfully demonstrating a unique ionic mechanism on the Ru/P4VPy surfaces, we aimed at developing a more efficient catalyst based on the same mechanistic concepts for hydrogenation of heteroatom aromatics. The results from the work on Ru/P4VPy support our hypothesis, *i.e.* immobilizing small RuNPs on the surface of basic supports can promote heterolytic hydrogen splitting and ionic hydrogenation on solid catalyst surfaces. We reasoned that if heterolytic hydrogen splitting can be promoted in the nanostructure composed of RuNPs and basic pyridine groups, the use of a more basic support together with RuNPs would create a similar nanostructure but would better favor the heterolytic hydrogen splitting since the more basic functionality in the nanostructure would lower the hydrogen activation energy by taking the H^+ more readily. Thus the combination of RuNPs with a more basic support would result in more efficient ionic hydrogenation of heteroatom aromatics.

Alkaline earth oxides, *e.g.* magnesium oxide (MgO), are superior to the polymer counterpart as a support, since P4VPy has only limited basicity (pK_a 7.4) while alkaline earth oxide bear abundant surface O atoms acting as basic sites of higher strength (pK_a 9–10). MgO has very rich base and surface features.[74-75] Figure 4-1 depicts different crystal planes on the MgO surface, with (100) planes being the most stable. The rich basic features of MgO arise from the surface inhomogeneity: different surface basic sites can be assigned to oxygen atoms with different coordinating numbers: oxygen atoms on (100)

planes are typically 5-fold coordinated, while 4-fold coordinated on edges between planes and 3-fold coordinated on kinks and corners.[76] Sites of lower coordination exhibit stronger basicity and are thus capable of interacting with acidic species more strongly. The different coordination modes of oxygen atoms render rich basic sites of weak, medium and high strength on the MgO surfaces.

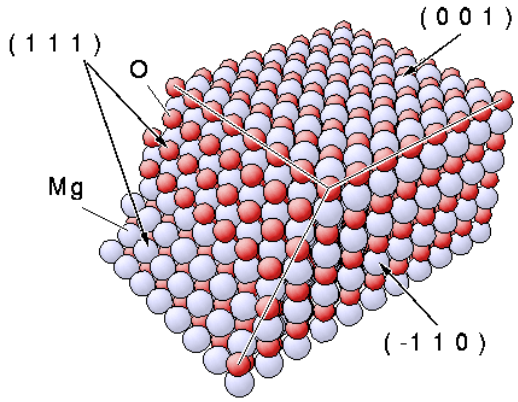

Figure 4-1. The surface structure of MgO.[77]

MgO has been applied as a basic solid catalyst for different organic syntheses.[78] Heterolytic dissociation of hydrogen into H^+ and H^- was also claimed to occur over Mg^{2+}–O^{2-} pairs on the MgO surfaces in the base-catalyzed hydrogenation and amination of 1,3-butadiene.[79] Scheme 4-1 shows the heterolytic dissociation of D_2 into D^- and D^+ on Mg^{2+}–O^{2-} pairs and 1,4-addition of D^- and D^+ to yield 2-butenes, wherein the transfer of D^- and D^+ is stepwise: D^- first attacks 1,3-butadiene to form the to have both *cis*-/*trans*-isomers, followed by addition of D^+ to terminal carbon to yield 2-butenes.

However, the claimed heterolytic dissociation of hydrogen seems to be only applied to hydrogenation and amination of conjugated dienes; there is no hydrogenation of other substrates such as aromatic compounds promoted by MgO itself. Since the O atoms can act as strong basic sites, their combination with good hydride carriers such as

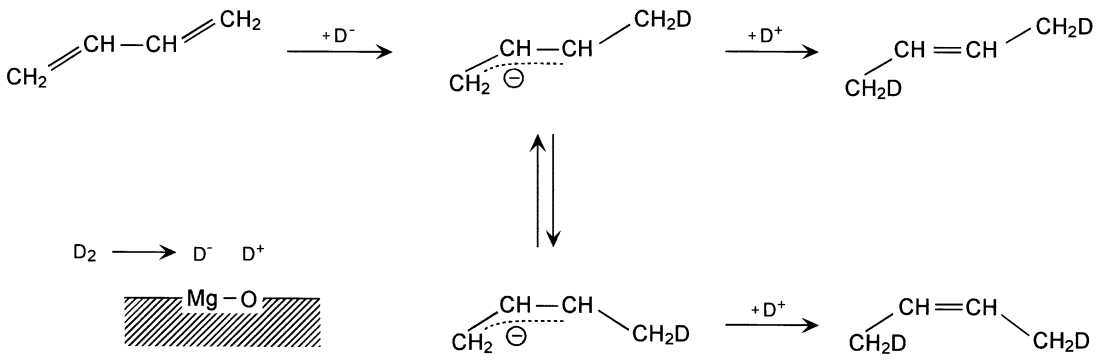

Scheme 4-1. Heterolytic dissociation of hydrogen on the MgO surfaces and hydrogenation of 1,3-butadiene to form 2-butenes.

Ru atoms could create the nanostructure capable of promoting more efficient ionic hydrogenation mechanism through the Ru-O bifunctional effects, as compared to the case of the Ru/P4VPy catalyst, thereby not only expanding the reaction scope to the hydrogenation of heteroatom aromatic compounds but also improving the efficiency for these reactions. Catalysts based on Ru and MgO support has been previously reported for NO reduction,[80-81] transfer hydrogenation of carbonyl compounds[82] and ammonia synthesis,[39,44,48-49] but never for hydrogenation of aromatic compounds. Thus immobilization of RuNPs on the MgO surfaces would lead to novel catalysts with improved efficiency for hydrogenation of heteroatom aromatics operating by ionic mechanism.

4.2 Experimental section

4.2.1 Materials

$RuCl_3 \cdot 3H_2O$ (Pressure Chemicals, Inc.), $NaBH_4$, $MgCl_2$ and NaOH (Sigma-Aldrich) were used as received. Solvents (analytical grade, Sigma-Aldrich) were purified using a PureSolv purification unit from Innovative Technology, Inc. Aromatic substrates (Sigma-Aldrich) were purified by distillation or recrystallization prior to use when necessary.

Naphthalene (≥ 99%, Sigma-Aldrich) was treated with $AlCl_3$ to remove trace amounts of thianaphthene before use. MgO (≥ 99%, ~325 mesh, Sigma-Aldrich) was calcined in the air at 500 °C (MgO_{500}) for 2 h and then stored in a desiccator for subsequent use.

4.2.2 Synthesis of Ru/MgO catalysts

The Ru/MgO catalyst was also synthesized by $NaBH_4$ reduction of $RuCl_3 \cdot 3H_2O$ in the presence of MgO_{500} in methanol under nitrogen at room temperature (Scheme 4-2).

$$RuCl_3 \cdot 3H_2O \xrightarrow[MgO_{500},\ MeOH,\ r.t.]{NaBH_4} Ru/MgO$$

Scheme 4-2. The synthesis of the Ru/MgO catalyst.

The synthesis apparatus and procedure were the same as that for Ru/P4VPy except MgO was used instead of the polymer P4VPy (section 3.2.2). Under a nitrogen flow, MgO (1.0 g) was suspended in methanol (20 mL) inside the flask; the desired amount of $RuCl_3 \cdot 3H_2O$ (*e.g.* 0.13 g, containing 0.5 mmol of Ru, for 5 wt% Ru/MgO) in methanol (10 mL) and $NaBH_4$ (0.38 g, 10 mmol) in methanol (20 mL) were placed in the two dropping funnels, respectively. While the MgO suspension was being stirred at room temperature, 10 mL of the $NaBH_4$ solution was added to the flask, after which both $RuCl_3$ and $NaBH_4$ solutions were simultaneously added into the mixture at the same rate of about one drop per second. After addition was complete, the dropping funnels were removed and the mixture was stirred under N_2 atmosphere at room temperature overnight. At the end, the solution was colorless and the solid was grey or dark. The solid was filtered off, washed with methanol (10 mL) six or more times until no Cl^- could be detected in the filtrate by use of a $AgNO_3$ aqueous solution. The catalyst was dried under vacuum at room temperature, affording a fine grey to dark grey powder, depending on the metal loading.

4.2.3 Characterization of Ru/MgO catalysts

4.2.3.1 TEM studies

Transmission electron micrographs were obtained on a JEOL JEM-2010 microscope operating at an accelerating voltage of 200 kV with a point-to-point resolution of 0.19 nm and magnification up to 1,500,000×. Images were captured digitally using an AMT Advantage CCD camera system (HRB Bottom Mount DVC Camera, 1 Megapixel) controlled by the AMT Image Capture Engine Software (Version 600.163) at varied high magnifications. The linear measurements on images had been calibrated previously at different high magnifications using known lattice spacing of crocidolite crystals standard (d = 0.906 nm) and graphited carbon crystals standard (d = 0.34 nm). Since the Ru/MgO catalyst exist as very fine powder in some portion, TEM samples were simply prepared by placing a drop of a catalyst suspension in THF on a copper grid coated by holey carbon film and allowing the evaporation of the solvent in the air, different from the sample preparation procedure for the Ru/P4VPy catalyst. The particle size (Feret diameter) distribution histogram was constructed from the measurement of about 300 particles found in representative images. The normal size distribution curve was also obtained based on the mean value and the standard deviation of the particle size.

4.2.3.2 Powder XRD measurements

Powder X-ray diffraction patterns for the Ru/MgO catalyst were also recorded on the Philips X'PERT MPD diffractometer using monochromatic Cu Kα radiation (λ = 1.5406 Å) at 45 kV and 40 mA. Sample powder was placed in the holder with a flat surface and analyzed in the air at room temperature. Spectra data were collected at a scanning rate of 0.10 °/s in a step size of 0.050° for 2θ over the range from 10° to 75° using the X'Pert

Data Collector software (V. 2.2f). Phase identification was achieved by comparing the diffraction patterns of the sample under study with that of ICDD (JCPDS) standards within the X'Pert HighScore software (V. 2.2c).

4.2.3.3 EDX analysis

The elemental composition of the catalyst was assessed by energy-dispersive X-ray spectroscopy using a Zeiss Supra 55VP field emission scanning electron microscope equipped with an EDX detector. The samples were dispersed onto carbon tape and sputter coated with carbon before analysis. The spectra were acquired using the EDAX Genesis software, with an operating voltage at 15 kV and a working distance of 8.5 nm.

4.2.3.4 XPS analysis

X-ray photoelectron spectroscopy analysis was also performed with the Omicron XPS spectrometer equipped with an EA125 multichannel hemispherical energy analyzer and a dual Al/Mg X-ray source using the monochromatic Al Kα radiation (1486.6 eV). The binding energy scale was previously calibrated and the base pressure in the ultra-high-vacuum analysis chamber was around 2.0×10^{-9} torr. The powdered samples were mounted on studs in the air using a double-sided adhesive tape. Spectra recording was controlled by the EIS software (V. 2.2.4), using a scan step of -0.5 eV for survey scans and -0.1 eV for narrow scans. The binding energy scale was corrected for charging effect according to the position of Mg 2s photoelectron line (88.1 eV).[38-39] The asymmetrical XPS peaks were deconvoluted by the curve fitting approach by use of XPSPEAK 4.1, applying Shirley background subtraction and Lorentzian-Gaussian functions (20% L, 80% G).

4.2.3.5 N_2 Physisorption

The single-point BET surface area of support was measured in a dual station Micromeritics Chemisorb 2750 analyzer attached with a ChemiSoft TPx System. About 200 mg of sample was placed in a U-shaped borosilicate sample tube and degassed at 200 °C in a stream of 30% N_2/He gas at 15 mL/min for 2 h. After cooling down to room temperature, the sample tube was immersed into liquid nitrogen in a Dewar to get a N_2 adsorption peak, after which the Dewar was removed to get a N_2 desorption peak. This was repeated three times; all adsorption and desorption peaks were recorded by the TPx system, and the latter were used to calculate BET surface area by use of the TPx software.

4.2.3.6 H_2 and CO pulse chemisorption

The catalyst active surface area was measured using a pulse chemisorption technique at room temperature in the same Micromeritic Chemisorb 2750 analyzer. H_2 and CO were used as two probe gases. For H_2 pulse chemisorption, approximately 100 mg of catalyst was placed in a U-shaped quartz tube along with a thermocouple in a temperature-controlled furnace. The sample was first reduced at 200 °C in a stream of 9.9% H_2/Ar gas flow at approximately 25 mL/min for 30 min and then purged with pure Ar gas for 30 min at 200 °C. After the sample was cooled down to ambient temperature in a stream of Ar gas at approximately 25 mL/min, doses of 9.9% H_2/Ar gas were injected into the carrier gas stream through an injector loop of known volume at about six-minute intervals until no more H_2 uptake was noted as indicated by no further change of the resultant H_2 peak area. The active surface area, metal dispersion and metal crystalline size were all automatically generated by the ChemiSoft TPx software, with an assumption of a stoichiometry of $H/Ru_s = 1$.[28] After one measurement, the sample was once again purged

with pure Ar gas for 30 min at 200 °C and cooled for subsequent measurements following the same procedure. The measurement was repeated three times for the same sample and average values of the parameters of interest were reported. The CO chemisorption experiments were conducted with the same procedure above except He and 9.9% CO/He were used as the carrier and loop gas, respectively. The measurement was only conducted once and fresh samples were used to repeat the measurement. The stoichiometry of $CO/Ru_s = 1$ was used to calculate the metal dispersion.

4.2.3.7 CO_2-TPD measurements

CO_2 temperature-programmed desorption (CO_2-TPD) measurements were conducted in the same Micromeritic Chemisorb 2750 analyzer to reveal the surface basicity of MgO. About 100 mg of samples in the quartz tube was pretreated in a flow of He (25 mL/min) at 500 °C for 1 h in the furnace and then cooled down to room temperature. A blank test was then first conducted by heating up the sample at 10 °C/min to 500 °C to get the blank desorption curve, after which the sample was cooled down again to room temperature and treated with 10% CO_2/He (25 mL/min) for 30 min. After being purged by a He stream for 30 min, the sample was heated up to 500 °C at a rate of 10 °C/min to get the CO_2 desorption profile.

4.2.4 Catalytic tests

Hydrogenation experiments were carried out using the same 5513 Parr reactor (100 mL) as for the Ru/P4VPy catalyst. Reactions were performed in a glass liner setting inside the vessel of the reactor. The detailed reaction procedure is the same as for the Ru/P4VPy catalyst (section 3.2.4). Samples were analyzed by use of the Varian 3900 gas chromatograph fitted with a polar Supelco SP-2330 capillary column and the Saturn

2100T mass detector, or in a Shimadzu 2010 fitted with a Restek Rtx-5 or Supelco SE-30 capillary column and an FID detector, when necessary. Anthracene and sulfur compounds were added into the reactor together with the catalyst at the beginning of the experiment, without catalyst incubation. Each experiment was repeated at least twice in order to verify reproducibility; the variations in the calculated TOF values for repeat experiments were typically within 10%.

4.2.5 Recycling experiments and catalyst life time determination

Recycling experiments were carried out using the same batch reactor as above. About 100 mg of 10 wt% catalyst and 50 mL of neat toluene were placed in a glass liner inside the vessel of the reactor. The system was deoxygenated by flushing with H_2 three times. The reactor was first kept under 1 atm H_2 and then heated to 120 °C; after the temperature became stable, the reactor was pressurized to 10 atm, and this was taken as the zero time for the reaction. The pressure was kept constantly during the whole reaction course by uninterruptedly feeding gas from a high pressure reservoir. Samples were periodically withdrawn and the composition was analyzed by use of GC or GC-MS. The hydrogenation course was followed at least until the half-life of toluene, after which the reaction was left to reach 100% conversion. After the reactor was cooled down and catalyst settled down to the bottom, the methylcyclohexane product was carefully withdrawn as much as possible, using a syringe fitted with a filter paper on the needle tip. Care was taken to minimize the loss of catalyst. The glass liner with the catalyst and some remaining methylcyclohexane was then placed into a big three-neck flask connected to a Schlenk line and the catalyst was dried under vacuum for the next run. This procedure was repeated for at least six times.

4.2.6 Substrate competition and selective thiophene poisoning tests

The procedures for substrate competition experiments and selective thiophnene poisoning tests are the same to those described in section 4.2.4, except that two substrates (toluene and quinoline) in equimolar amounts were used or a substrate (toluene or quinoline) mixed with ~1 mol% thiophene were used, respectively.

4.3 Results and discussion

4.3.1 The simple one-pot synthesis of Ru/MgO catalysts

The Ru/MgO catalyst was prepared in a one-pot procedure at room temperature by $NaBH_4$ reduction of $RuCl_3 \cdot 3H_2O$ in methanol in the presence of suspended MgO, which had been previously calcined at 500 °C in the air for 2 h. The reaction was kept under a nitrogen atmosphere to avoid possible oxidation of metallic Ru during the early stages of Ru(0) formation; RuNPs were formed upon nucleation of "naked" Ru atoms and were subsequently stabilized on the MgO surface through strong interaction with surfaces oxygen sites. The reduction of Ru(III) by $NaBH_4$ is fast and thorough, and the stabilization of RuNPs on the MgO surface is effective: the formation of RuNPs and their attachment to the support can be visualized by the quick discoloration of the solution and the darkening of the solid; the completeness of reaction can be verified by the lack of any UV–Vis bands of the final solution, other than those ascribed to solvent. The catalyst was collected by filtration and cleaned by successive washing with methanol until no Cl^- can be detected by *aq.* $AgNO_3$. The catalyst was routinely stored under nitrogen but weighed quickly in the air prior to use. Three catalysts with different nominal Ru content (1 wt%, 5 wt% and 10 wt%) were prepared with this one-pot approach, using the commercial MgO powder. For comparison purposes, an analogous catalyst with a nominal 5 wt% Ru

loading was also synthesized using a MgO powder (MgO^*) prepared in the lab by the addition of $MgCl_2$ (*aq.*) into NaOH (*aq.*) and the subsequent calcination of the collected and washed $Mg(OH)_2$ at 500 °C in the air for 2 h.

4.3.2 Structure, texture and composition of Ru/MgO catalysts

4.3.2.1 TEM measurements

The Ru/MgO catalysts appear as fine grey to dark powder, depending on the metal loading. The TEM images of the 1 wt%, 5 wt% and 10 wt% Ru/MgO catalysts reveal the presence of highly dispersed RuNPs of about 2 nm in diameter on the MgO support, regardless of the metal loading (Figure 4-2). The 1 wt% Ru/MgO has RuNPs with average particle size of 1.5 nm (Figure 4-2a); when the metal loading is increased five and ten times, the average particle size does not increase by the same magnitude, but only slightly, to 1.8 nm for 5 wt% Ru/MgO and 2.1 nm for 10 wt% Ru/MgO. Despite the different metal loading, all three catalysts have the majority of RuNPs falling within the narrow range of 1–3 nm in diameter, as depicted in the size distribution histograms. This renders the one-pot synthesis described above a reliable means of preparing small RuNPs of similar size with varying concentration of catalyst precursor. After a quinoline hydrogenation run at 150 °C and 50 atm, the average particle size and size distribution of 5 wt% Ru/MgO remain essentially unchanged (Figure 4-3), indicating the RuNPs are well stabilized on the MgO surface and can withstand the reaction conditions without any sintering process taking place. Compared to P4VPy, RuNPs can be better stabilized on the MgO surface since the use of MgO can produce smaller particles and the size remained essentially unchanged at 150 °C and 50 atm, which is not the case for Ru/P4VPy (section 3.3.2.1).

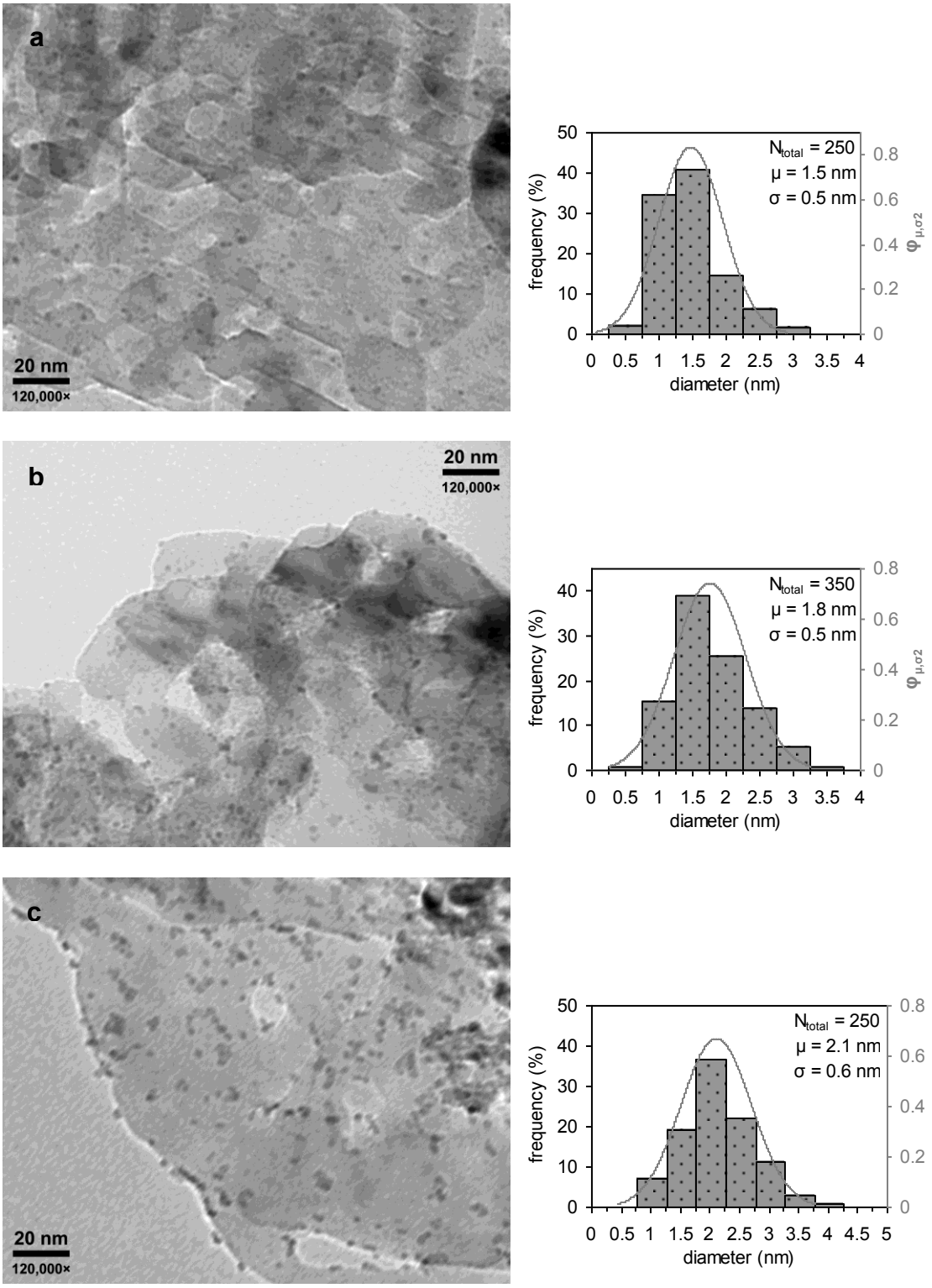

Figure 4-2. Representative TEM images of a) 1 wt%, b) 5 wt% and c) 10 wt% Ru/MgO and the corresponding RuNPs size distribution histograms with normal distribution curve.

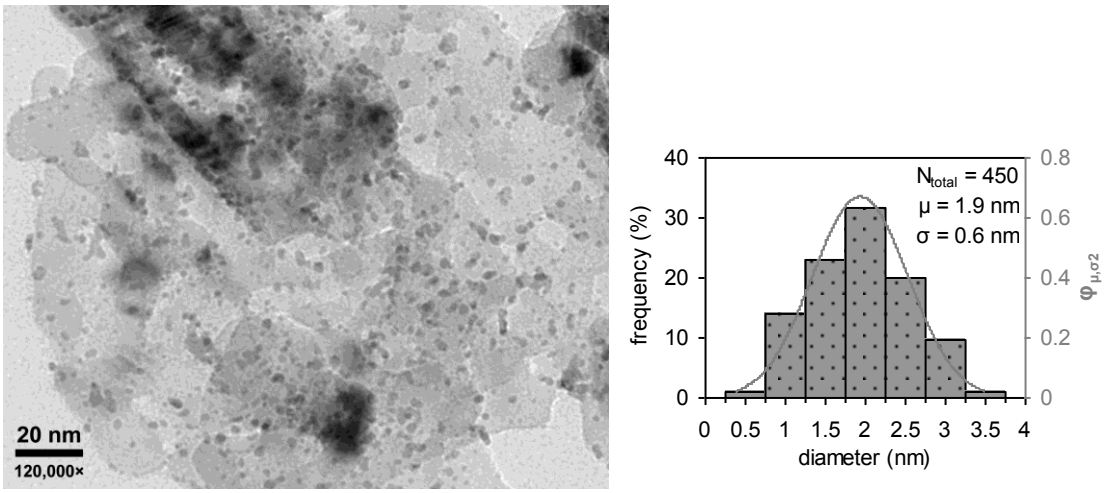

Figure 4-3. The TEM image of a used sample of the 5 wt% Ru/MgO catalyst recovered from hydrogenation of quinoline and the corresponding RuNPs size distribution histogram.

To identify the crystalline structure of RuNPs on the MgO surface, a TEM image at high magnification (500,000x) was taken for a 10 wt% catalyst sample (Figure 4-4). Lattice fringes were observed on a particle with the spacing of 2.3 Å (1.17 nm for 5 consecutive fringes), which corresponds to the $\{10\bar{1}\,0\}$ planes in hexagonal close-packed Ru with a = 0.272 nm and c = 0.433 nm,[37] indicating the Ru phase on the MgO surface is single crystalline elemental Ru. The area along the perimeter of the crystalline RuNPs

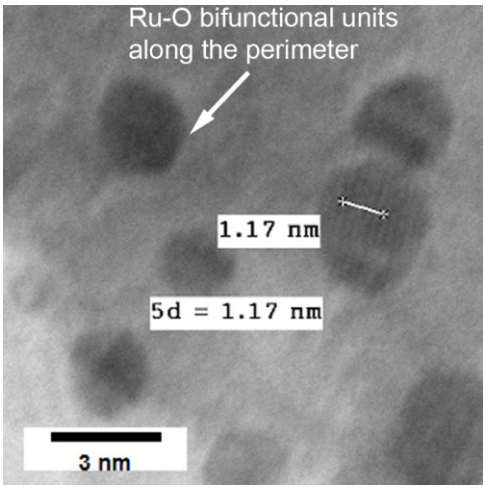

Figure 4-4. The transmission electron micrograph of a sample of 10 wt% Ru/MgO at magnification of 500,000×.

as seen from the image should be rich in Ru-O bifunctional units accessible to incoming hydrogen and substrate, and that is where we think heterolytic hydrogen activation and ionic hydrogenation are promoted.

4.3.2.2 PXRD measurements

The powder XRD pattern of the 10 wt% Ru/MgO catalyst was also obtained (Figure 4-5), which however was found to be indistinguishable from that of pure MgO support; no diffraction attributable to the Ru phase was observed, with all three peaks at 2θ = 37.0 °, 43.0 ° and 62.4 ° assigned to MgO phase.[83] This suggests that the ruthenium phase is nanocrystalline in the Ru/MgO catalyst, without ordered crystalline structure over significant distances; RuNPs are highly dispersed and very small to be detectable, which is in consistence with TEM results.

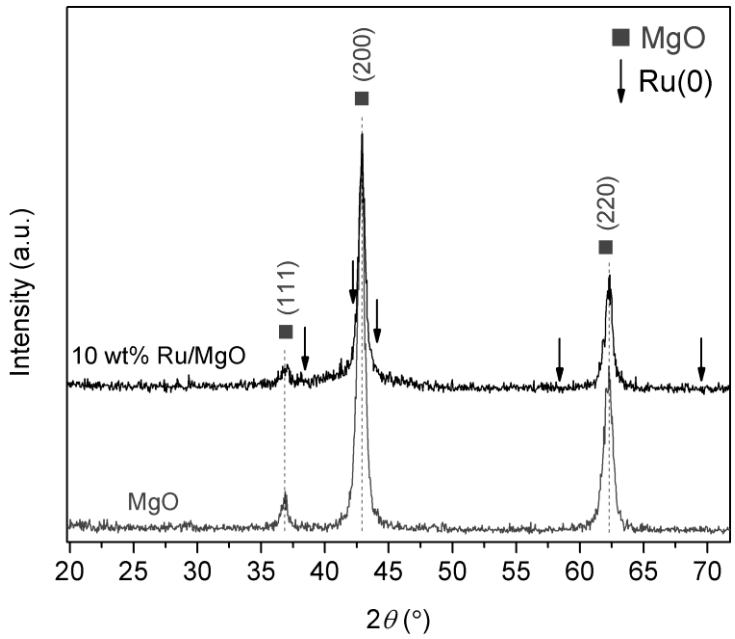

Figure 4-5. Powder X-ray diffraction patterns of the 10 wt% Ru/MgO and the MgO support.

4.3.2.3 EDX analysis

The elemental composition of the Ru/MgO catalysts was analyzed by energy-dispersive X-ray spectroscopy (EDX) in a scanning electron microscope. Since MgO is not electron conductive, all samples of catalysts were coated with carbon prior to the EDX analysis. Figures 4-6 and 4-7 show the EDX spectra and the corresponding elemental composition for all three carbon coated catalyst samples. Four detectable elements are present in each sample: Mg, O, Ru and C; C is from the coating as required by the analysis for the non-conductive material. The determined weight percentage of Ru content in the Ru/MgO catalysts is therefore 10.1%, 5.1% and 1.3%, for the nominal 10 wt%, 5 wt% and 1 wt% catalysts, respectively, confirming the complete deposition of Ru atoms onto MgO support in the synthesis. There is no Cl detected, confirming all the chloride from the starting Ru salts was removed from the catalyst after the washing steps.

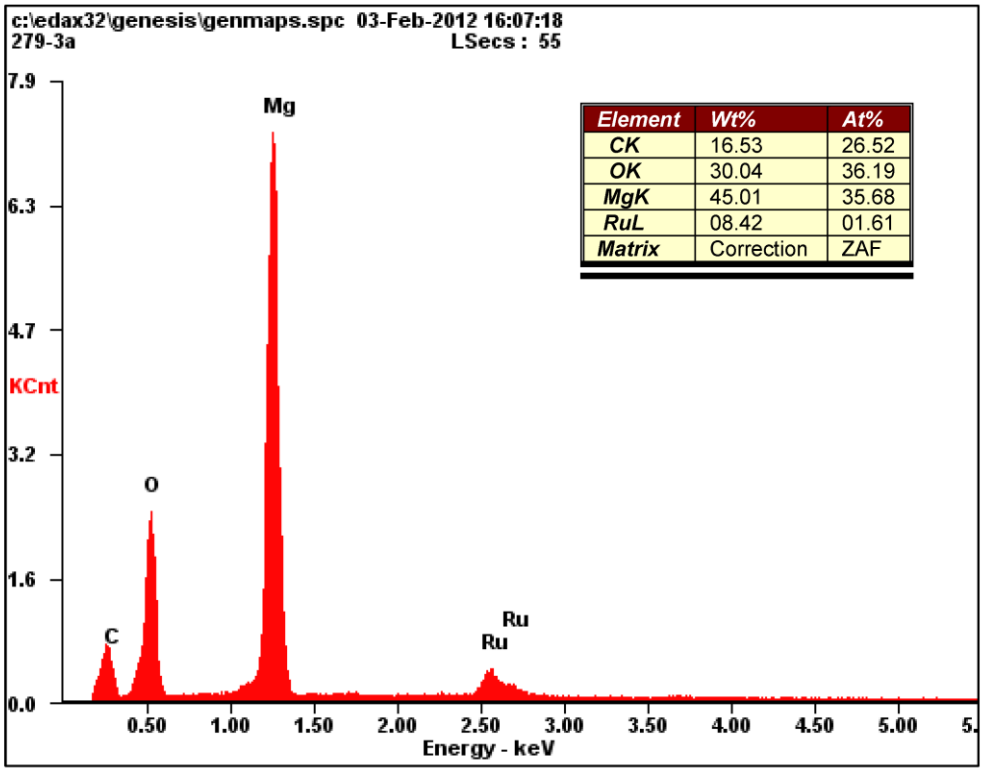

Figure 4-6. The EDX spectrum and the element composition of the 10 wt% Ru/MgO.

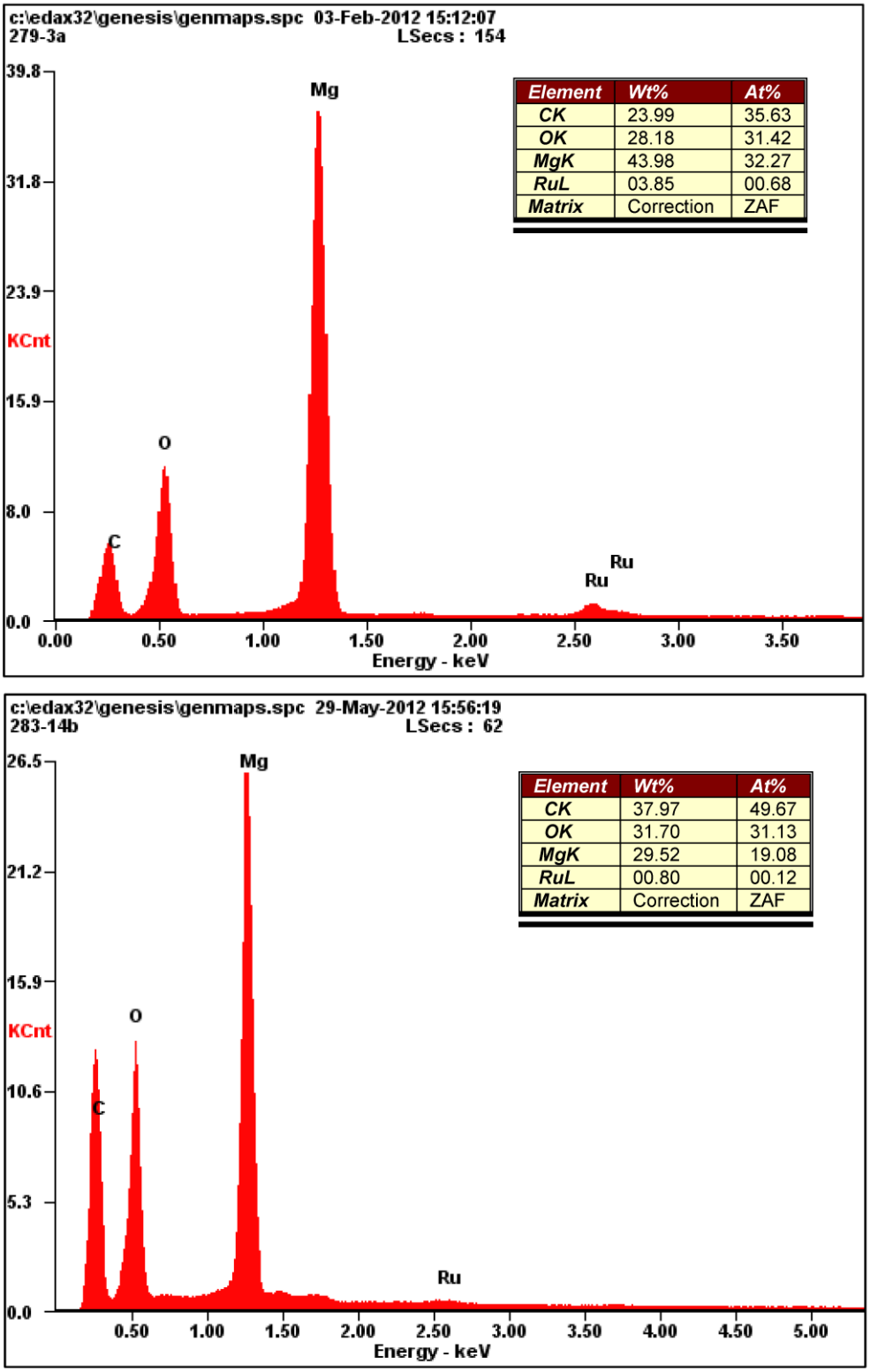

Figure 4-7. EDX spectra and the corresponding elements composition of the 5 wt% Ru/MgO (top) and the 1 wt% Ru/MgO (bottom).

4.3.2.4 XPS analysis

In order to further investigate the nature of RuNPs on the catalyst surfaces, XPS analysis was also performed. Figure 4-8 shows the full XPS spectra of fresh samples of different catalysts as well as the commercial MgO. While the presence of C 1s peak is inevitable as carbonaceous species generally accumulate in the spectrometer chamber, the spectra show no detectable Cl (200 eV) or B (190 eV) species on the catalyst surface, indicating that the catalyst surface is free of contaminants from the starting materials after washing during the preparation process. This is advantageous in terms of surface cleanliness, as other preparation methods using $RuCl_3$ precursor *e.g.* impregnation methods[27-29] and ion-exchange method[29] usually lead to catalyst surfaces contaminated with Cl^-.

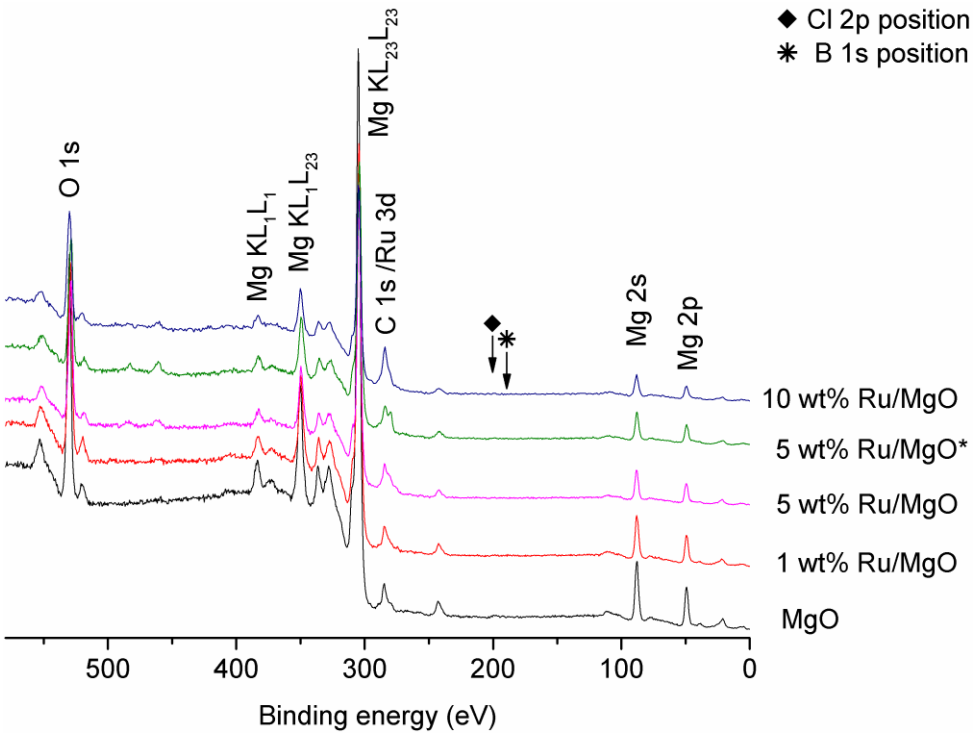

Figure 4-8. XPS survey scans of the Ru/MgO catalysts and the 5 wt% Ru/MgO* as well as the commercial MgO.

The narrow scan for the 5 wt% Ru/MgO catalyst in the Ru 3d and 3p regions (Figure 4-9a) clearly indicates the presence of metallic ruthenium on the MgO surface by the signals at 280.2, 460.8 and 483.2 eV, which correspond to Ru $3d_{5/2}$, $3p_{3/2}$ and $3p_{1/2}$ spin-orbit components in the zerovalent state, respectively;[68] there is no evidence for the presence of other Ru species. Similar results were observed for the 10 wt% Ru/MgO catalyst. The Ru $3d_{1/2}$ region is highly interfered by C 1s peak resulting from carbonaceous contaminants in the spectrometer, rendering deconvolution in the region around 285 eV invaluable. The 1 wt% catalyst displays very weak Ru XPS signal due to the very low metal loading, not allowing a reliable characterization by this method.

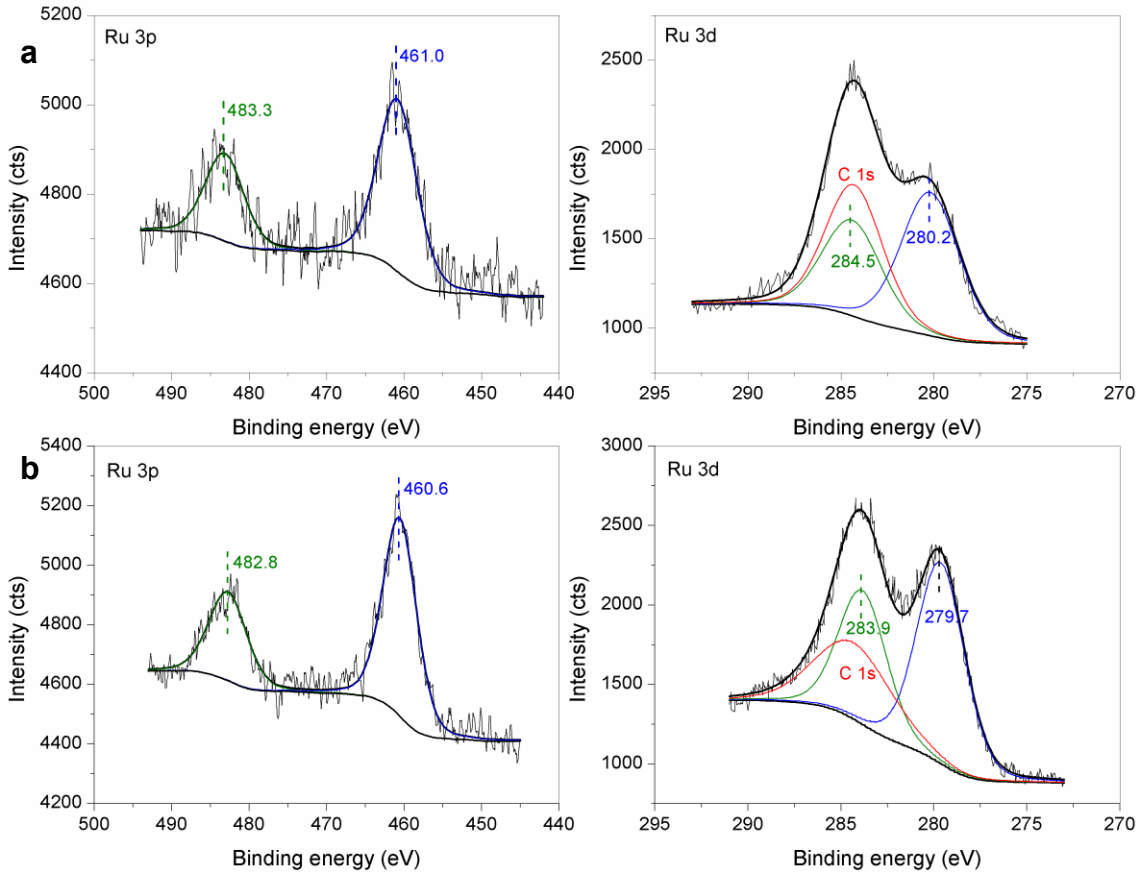

Figure 4-9. XPS spectra (Al Kα radiation) of a) the 5 wt% Ru/MgO and b) the 5 wt% Ru/MgO* catalysts in Ru 3d and 3p regions.

Interestingly, the 5 wt% Ru/MgO* displays a negative shift of Ru 3d and 3p core level binding energies (Figure 4-9b), as compared to the 5 wt% Ru/MgO, suggesting a stronger metal-support interaction in the Ru/MgO* catalyst. This will be discussed in section 4.3.4.2.

4.3.2.5 BET surface area and metal dispersion

The BET surface area of the magnesia support and the specific surface area of Ru metal in the catalysts were determined by gas sorption techniques. Table 4-1 contains the data from physisorption and chemisorption measurements. N_2 physisorption results show that the commercial MgO, after calcination at 500 °C for 2 h, has a specific surface area of 88 $m^2 \cdot g^{-1}$, while the lab-made MgO* has a much larger surface area of 150 $m^2 \cdot g^{-1}$.

Table 4-1. Physicochemical and textural properties of the catalysts and magnesia support

material	Ru loading[a]	BET surface area (m^2/g)[b]	D_{H2}[c]	D_{CO}[c]	$\bar{d}_{H2}$ (nm)[d]	d_{TEM} (nm)
MgO	–	88 ± 2	–	–	–	–
MgO*	–	150 ± 20	–	–	–	–
1 wt% Ru/MgO	1.3%	–	4 ± 1%	–	35	1.5 ± 0.5
5 wt% Ru/MgO	5.1%	–	28 ± 3%	23 ± 2%	4.7	1.8 ± 0.5
5 wt% Ru/MgO*	5.0%	–	22 ± 2%	–	6.0	1.8 ± 0.4
10 wt% Ru/MgO	10.1%	–	25 ± 1%	21 ± 1%	5.3	2.1 ± 0.6

[a] Determined by EDX.

[b] Single-point BET value.

[c] Metal dispersion, determined by H_2 or CO pulse chemisorption.

[d] Effective particle size calculated from H_2 chemisorption results by $d_{H_2} = \frac{F}{\rho_{Ru} \cdot S}$ (F: crystallite geometry factor, 6 for hemisphere; S: active Ru surface area per g of Ru).

The metallic surface area was determined by pulse chemisorption using H_2 as the probe molecules, since the stoichiometry of $H/Ru_s = 1$ is well established, and H_2 chemisorption can be used as a reliable tool for the determination of the metallic surface area hence the metal dispersion for ruthenium catalysts free of Cl^- contamination,[28] which is applicable to our catalyst. Although CO has also been frequently used for chemisorption, it tends to form multiple adsorption bonds with ruthenium and the number of bonds varies depending on surface morphology.[28] Therefore, the results from H_2 chemisorption were used to determine the metal dispersion of our Ru/MgO catalysts while that from CO chemisorption were used for reference purpose.

H_2 pulse chemisorption was carried out on the Micromeritics Chemisorb 2750 analyzer. A typical profile of H_2 pulse chemisorption is displayed in Figure 4-10. Doses of H_2 gas of known volume were injected into inert gas stream which swept through the pre-treated catalyst sample to the TCD detector, where the amount of leftover H_2 in the

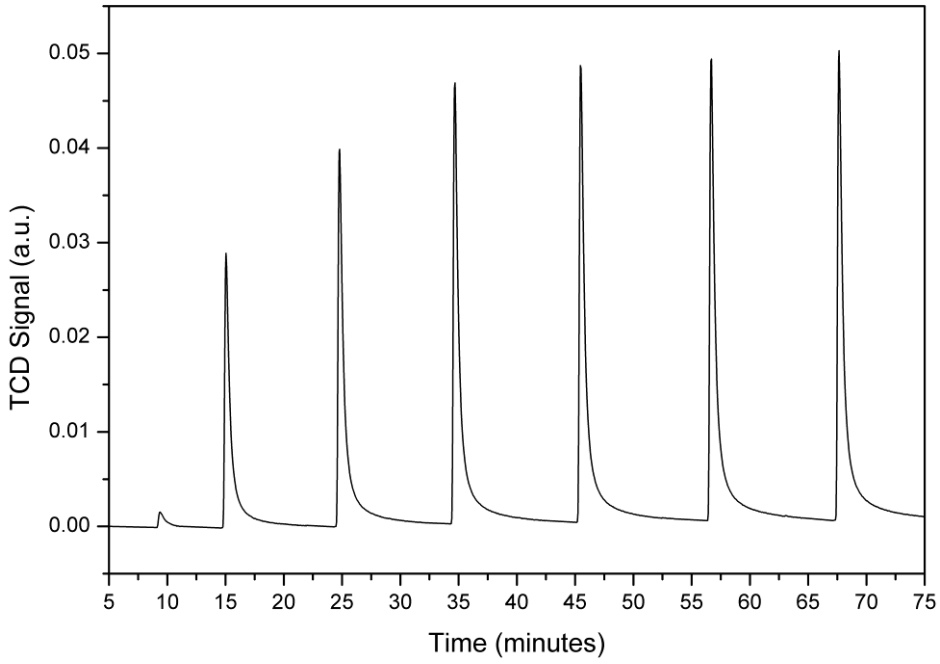

Figure 4-10. A typical H_2 pulse chemisorption profile for the Ru/MgO catalyst measured by the Chemisorb 2750 analyzer.

gas stream is monitored and H_2 peaks are displayed in response. The full coverage of exposed Ru surface by chemisorbed hydrogen atoms is indicated by the saturation of hydrogen peak, and the total amount of H_2 gas consumed can be used to calculate Ru surface area, from which Ru disperson and effective size of Ru crystallite can be derived.

As seen from H_2 chemisorption results in Table 4-1, the 5 wt% and 10 wt% Ru/MgO catalysts share similar high metal dispersion (28% *vs.* 25%) and therefore very similar average size of RuNPs (4.7 *vs*. 5.3 nm), as verified by the similar TEM results (1.8 *vs*. 2.1 nm). The 1 wt% catalyst, however, has very low Ru dispersion (4%), probably because at such a low metal loading the majority of RuNPs penetrate into pore structures of MgO, leaving a very limited amount of Ru exposed to surface. When a larger amount of Ru loading is used, the majority of RuNPs will remain on surface and therefore metal dispersion increases significantly, as in the case of the 5 wt% and 10 wt% Ru/MgO as well as the 5 wt% Ru/MgO*. The effective crystalline sizes derived from H_2 chemi-sorption data are larger than those determined by TEM, as seen in the last two columns of Table 4-1. These differences arise from the assumptions used in calculation of particle size from chemisorption results, that the particles are spherical and all metal surfaces are accessible, which however is not true in practice. The shape of particles is not perfectly spherical, and particularly importantly, not all RuNPs' surfaces are available as some particles reside in pore structures of magnesia. The 1 wt% Ru/MgO is an extreme example for this, resulting very large calculated particle size (35 nm).

The metal dispersion derived from CO chemisorption is consistently lower than that from H_2 chemisorption (see the D values for the 5 wt% and 10 wt% Ru/MgO), due to the tendency of CO to form multiple adsorption bonds, as stated before.

4.3.2.6 Surface basic features of MgO support

The surface basic features of MgO support were evaluated by temperature programmed desorption (TPD) techniques using CO_2 as the probe molecule. Since the MgO support was pretreated at 500 °C, the temperature in CO_2-TPD experiments was programmed in the range not exceeding 500 °C. Figure 4-11 depicts the TPD profiles of the two MgO and MgO* supports and the corresponding 5 wt% catalysts, from where approximately three CO_2 desorption peaks at different temperatures were observed for each sample, indicating the presence of three types of basic sites of different strength on the surface of magnesia. These basic sites are assigned to O^{2-} sites with different coordination numbers:[76,84] the peak around 110 °C can be assigned to the O^{2-} sites with high coordinating numbers, specifically the fivefold coordinated O^{2-} sites on the MgO(100) plane; the peak at about 180 °C should correspond to the fourfold coordinated O^{2-} sites and therefore medium strength of basicity on edges between planes; the peak at about 270 °C is for those O^{2-} sites with low coordinating numbers located at corners of the MgO crystal lattice, which display basicity of high strength and thus require high temperature to allow desorption of chemically bond CO_2 molecules.

Compared to MgO, MgO* displays a larger number of basic sites of each type, as seen by the larger area under desorption peaks. Deposition of RuNPs onto the support, in both cases, diminishes the quantity of basic sites, as a certain portion of them is occupied by RuNPs for stabilization through metal-oxygen interaction, resulting in smaller peak areas for the desorption peaks of catalyst compared to that of the support in the CO_2-TPD profile.

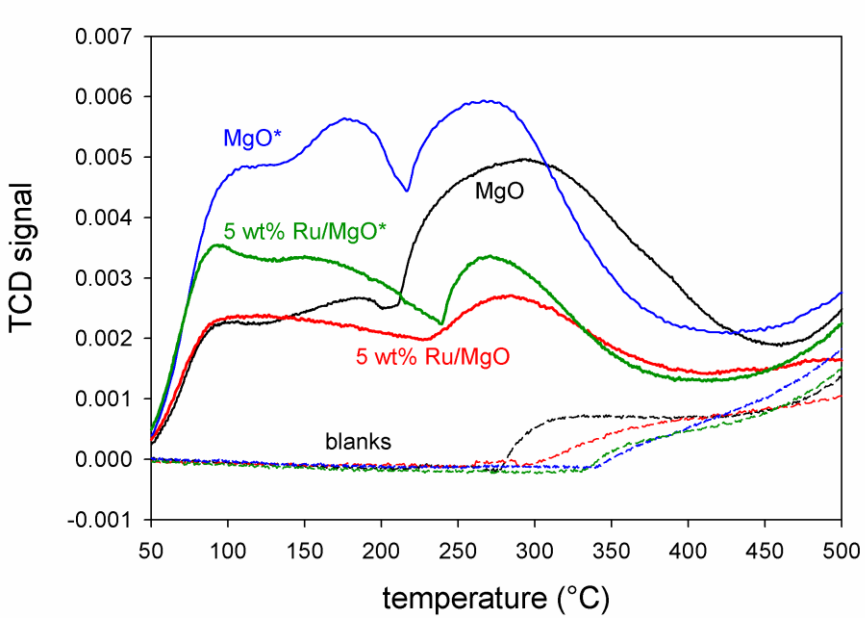

Figure 4-11. CO_2-TPD profiles of the two magnesia supports, the 5 wt% Ru/MgO and the 5 wt% Ru/MgO* catalysts.

4.3.3 The hydrogenation of aromatic compounds over Ru/MgO: high catalytic efficiency

4.3.3.1 General consideration

The catalytic activity of the Ru/MgO catalysts was tested in the bench-scale batch reactor for liquid-phase hydrogenation of a wide variety of aromatic substrates. The plots of substrate and products composition *vs.* time were converted into turnover number *vs.* time plots, whose slopes were used to determine TOF values.[85] The metal dispersion was also taken into consideration to more accurately evaluate the catalytic activity, as only the exposed Ru surface was involved in reaction. The metal dispersion values measured by H_2 chemisorption (D_{H2}, Table 4-1) were adopted since they are more accurate than those by CO chemisorption (D_{CO}) for ruthenium, as discussed before. Thus TOF values in this chapter are corrected for the metal dispersion D_{H2} (TOF_{corr}), which is expressed as the number of moles of substrate converted per mol of active surface Ru atoms per h.

Factors relating to the validity and reliability of the hydrogenation experiments were also taken into account. New batches of catalysts were always tested in toluene hydrogenation prior to use, and reproducible TOF_{corr} values (variation < 10%) were obtained, suggesting catalyst homogeneity from different batches. No mass transfer limitations in the reactions were observed, as different stirring speeds cause little variation on reaction rate. Blank tests under analogous reaction conditions revealed no toluene or quinoline hydrogenation activity for the magnesia support alone or with $NaBH_4$, excluding other agents that may induce hydrogenation. All hydrogenation runs were repeated at least twice in order to ensure reproducibility of TOF_{corr} values (variation below 10%) and average TOF and TOF_{corr} values are reported.

4.3.3.2 Effects of hydrogenation parameters

The effects of different reaction conditions (catalyst amount, substrate amount, Ru loading and pressure) on hydrogenation rates were studied using toluene and quinoline as model substrates. Figure 4-12 shows the hydrogenation profiles for toluene and quinoline over the Ru/MgO catalyst under typical reaction conditions. The different hydrogenation parameters were evaluated by changing each one of the variables at a time while keeping the other conditions constant. Two temperatures were adopted by convention in our lab, 120 °C for toluene hydrogenation and 150 °C for quinoline hydrogenation, and the total reaction volume was kept at 30 mL. Figure 4-13 depicts the influence of these parameters on the initial rate of hydrogenation. As more catalyst is used, the reaction rates increase correspondingly as expected (Figure 4-13a); while the toluene hydrogenation rate increases in response to the increased amount of toluene, quinoline seems to have an optimal amount and further increase of quinoline amount to 100 mmol (~11.4 mL) has an

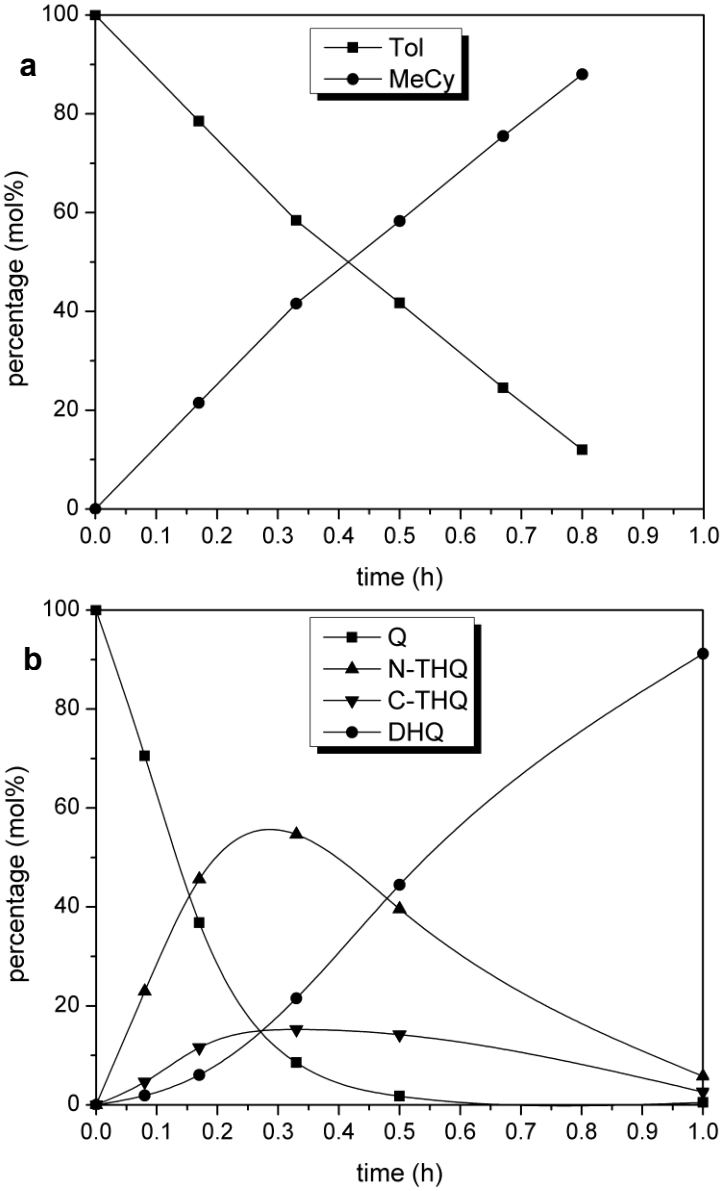

Figure 4-12. Hydrogenation profiles of a) Tol (1 mL; 5 wt% Ru/MgO: 100 mg; in THF; 120 °C, 10 atm.) and b) Q (1 mL; 5 wt% Ru/MgO: 100 mg; in THF; 150 °C, 50 atm.).

adverse impact on the hydrogenation rate (Figure 4-13b). Catalysts with higher Ru content also result in higher rates as expected, although the degree is less significant in the case of quinoline (Figure 4-13c).

Noteworthily, when pressure was increased from 10 to 50 atm, which is the limit in our lab, hydrogenation rates were observed to steadily increase for both toluene and

quinoline (Figure 4-13d), indicating that the Ru/MgO catalysts are stable against any possible sintering process at least up to 50 atm, in agreement with the TEM measurements of the used Ru/MgO catalyst disclosed in section 4.3.2.1.

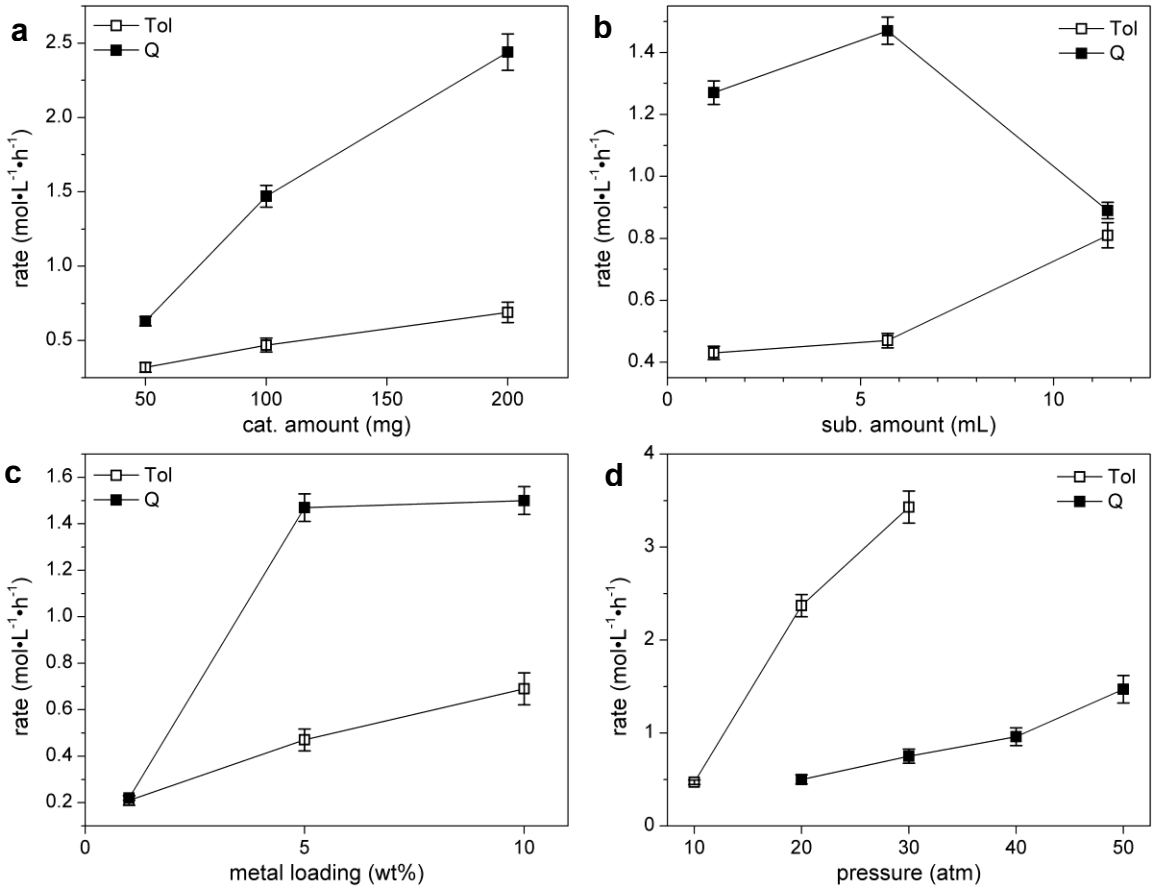

Figure 4-13. Effects of reaction conditions on the hydrogenation rates of Tol and Q in THF: a). Effect of catalyst amount (5 wt% Ru/MgO; substrates: 50 mmol; 120 °C, 10 atm for Tol and 150 °C, 50 atm for Q); b). Effect of substrate amount (5 wt% Ru/MgO: 100 mg; 120 °C, 10 atm for Tol and 150 °C, 50 atm for Q); c). Effect of metal loading (Ru/MgO: 100 mg; substrates: 50 mmol; 120 °C, 10 atm for Tol and 150 °C, 50 atm for Q); d). Effect of pressure (5 wt% Ru/MgO: 100 mg; substrates: 50 mmol; 120 °C for Tol and 150 °C for Q).

4.3.3.3 Scope and efficiency of hydrogenation over Ru/MgO

In order to investigate the scope of activity of the Ru/MgO catalyst, the hydrogenation of a series of mono-/polycyclic aromatic hydrocarbons and N-/S-heteroaromatics was carried out over the 5 wt% Ru/MgO in THF under low temperature and pressure (120 °C, 10 atm or 150 °C, 50 atm). Table 4-2 is a summary of hydrogenation results for monocyclic and polycyclic arenes over the 5 wt% Ru/MgO. As reflected by the TOF_{corr} values, the Ru/MgO catalyst is highly active for hydrogenation of arenes; there is a large enhancement of activity from Ru/P4VPy to Ru/MgO as shown by the comparison of the corresponding TOF values (Table 4-2 *vs.* Tables 3-1 and 3-2).

The hydrogenation activity for the monocyclic arenes decreases with increasing steric congestion on the rings, with the highest rate for benzene and the lowest for mesitylene, as seen from entries 1–4 in Table 4-2. Polycyclic arenes are generally difficult to reduce and require increased temperature and pressure compared to the monocyclic arenes for efficient hydrogenation; however, they can be hydrogenated over the Ru/MgO catalyst with high TOF_{corr} values of 6,600 h^{-1} and 4,000 h^{-1} at 150 °C and 50 atm, respectively, as seen in entries 5 and 6 in Table 4-2. All monocyclic arenes were hydrogenated over Ru/MgO to fully saturated hydrocarbons, while polycyclic arenes have mainly partially hydrogenated products along the course of hydrogenation at least until the substrates half-life time. What are notable for the Ru/MgO catalyst in hydrogenation of different arenes are the wide scope and the high activity, especially towards polycyclic arenes. Other supported Ru catalysts for the hydrogenation of PAHs reported so far are silica-supported RuNPs[54] for anthracene hydrogenation and polydimethylphosphazenes-supported RuNPs[34] for naphthalene hydrogenation, which

can only reach an TOF value of 14 at 100 °C /30 atm and 190 at 80°C /50 atm, respectively, one to two orders of magnitude lower than the TOF values achieved on the Ru/MgO catalyst.

Noteworthily, the Ru/MgO catalyst can also efficiently hydrogenate a variety of N-heteroaromatics, being resistant to these catalyst poisons, as summarized in Table 4-3. All mono-, bi- and tricyclic N-heteroaromatics can be hydrogenated with high TOF_{corr} values ranging from 1,000 h^{-1} for indole (entry 2, Table 4-3) to 6,000 h^{-1} for acridine (entry 6, Table 4-3); the pyridine-based series seem to be hydrogenated more easily than their pyrrole-based counterparts, as concluded from comparison of the corresponding TOF_{corr} values. Pyrrole and pyridine were exclusively reduced to pyrrolidine and piperidine (entries 1 and 4, Table 4-3), while other polycyclic substrates yielded mixed products; quinoline and indole afford predominantly the products resulting from hydrogenation of N-heterocyclic rings, with only a small portion arising from hydrogenation of carbocyclic rings (entries 2 and 5, Table 4-3).

The Ru/MgO catalyst displays much higher catalytic activity for the hydrogenation of N-heteroaromatics than the Ru/P4VPy catalyst, as concluded by the comparison of TOF values in Table 4-3 and Table 3-3. This indicates that a more efficient ionic hydrogenation mechanism can be promoted on the Ru/MgO surfaces by the nanostructure consisting of Ru-O bifunctional units. Thus the combination of RuNPs with a more basic support can result in more efficient ionic hydrogenation of heteroatom aromatics.

Apart from Ru/P4VPy catalyst, very few other supported Ru catalysts in literature are known for hydrogenation of N-aromatics and they display much poorer activity.

Ru/Al_2O_3 was found inactive towards hydrogenation of quinoline;[73] Ru/HAP catalysts can catalyze hydrogenation of quinoline and its methylated derivatives with TOFs in the range of 50 h^{-1} to 150 h^{-1} at 150 °C and 50 atm;[31] Ru/PDMP catalyst has TOFs of about 200 h^{-1} for homogeneous hydrogenation of quinoline and pyridine at 25 °C and 50 atm;[34] Ru/SiO_2 extended the hydrogenation scope to acridine and indole in addition to quinoline at 100 °C and 30 atm, with TOFs from about 50 h^{-1} to 200 h^{-1} and a mixture of products observed.[54] Therefore, the Ru/MgO catalyst is superior to all these reported Ru catalysts for hydrogenation of N-heteroaromatic compounds.

Hydrogenation of S-heteroaromatics perhaps is the biggest challenge for supported noble metal catalysts due to the strong poisoning effect of the sulfur compounds. Indeed, there are very scarce examples in literature regarding hydrogenation of S-heteroaromatics using noble metal NPs catalysts. RuNPs supported on silica did not catalyze benzothiophene (BT) or dibenzothiophene (DBT) hydrogenation to any extent at 100 °C and 30 atm;[54] Rh colloidal suspensions stabilized by surfactants show no activity towards hydrogenaiton of thiophene (T) and BT under ambient condition;[86] monometallic and multimetallic nanoparticles supported on alumina gave only 3% conversion of BT to dihydrobenzothiophene (DHBT) at 10 atm after 24 h, with a TOF of only 0.1 h^{-1}.[87]

Outstandingly, the Ru/MgO catalyst can hydrogenate a variety of S-heteroaromatics at moderate temperature and pressure (Table 4-4). Thiophene and benzothiophene can be hydrogenated to tetrahydrothiophene and DHBT at 150 °C and 50 atm with TOF_{corr} values of 0.5 h^{-1} and 5 h^{-1}, respectively, while larger S-containing molecules, dibenzothiophene and 4,6-dimethyldibenzothiophene (4,6-DMDBT) require increased temperature (200 °C) for observable conversion. Compared to thiophene, BT

can be hydrogenated more easily under the same conditions (entries 1 *vs.* 3 and 2 *vs.* 4, Table 4-4); a conversion of about 30% can be reached in 1 h at 200 °C and 50 atm, with a TOF_{corr} value of about 11 h^{-1}, compared to the TOF_{corr} value of 2 h^{-1} for thiophene under the same condition. Hydrogenation of 4,6-DMDBT is extremely challenging; however, the Ru/MgO catalyst showed activity under moderate temperature and pressure.

Although S-heteroaromatics are hydrogenated slower over the Ru/MgO catalyst compared with their nitrogen counterparts under similar reaction conditions, the hydrogenation activity of Ru/MgO for S-aromatics is a breakthrough, since the Ru/MgO catalyst is the first example of supported Ru catalyst known for these reactions and it can work more efficiently than the only other known example of supported transition metal catalyst.[87] The improved efficiency of Ru/MgO for hydrogenation of S-aromatics as compared to Ru/P4VPy (Table 4-4 *vs.* Table 3-4) further supports that the nanostructure consisting of Ru-O bifunctional units on the Ru/MgO surface is capable of promoting more efficient ionic mechanism.

For all sulfur substrates, as the reaction was continued, hydrogenation rates became slower (T and BT) or completely halted (DBT and 4,6-DMDBT), as seen from their TOF_{corr} values at 1 h and 24 h, suggesting some catalyst deactivation process took place under these reactions conditions after a considerably long time.

In addition to hydrogenation, direct desulfurization (DDS) products were also observed: mixed butenes for thiophene, ethyl benzene for BT and biphenyl series for the larger S-containing compounds. The detailed DDS steps are unknown yet but the results shed some lights into the ionic mechanism on the Ru/MgO surfaces (see section 4.3.4.3).

Table 4-2. Hydrogenation of MAHs and PAHs over Ru/MgO

entry	substrate	rate ($mol \cdot L^{-1} \cdot h^{-1}$)	$t_{1/2}$ (h)	TOF (h^{-1})	TOF_{corr}[a] (h^{-1})	products distribution at $t_{1/2}$			
1[b]		1.03	1.0	660	2,300		100%		
2	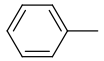	0.47	1.5	300	1,000	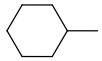	100%		
3		0.27	2.9	170	590		100%		
4	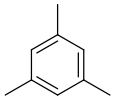	0.08	8.0	40	150	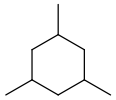	100%		
5[c]	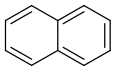	1.44	0.05	1,900	6,600	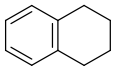	80%	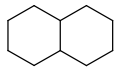	15%
6	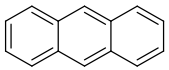	0.90	–[d]	1,100	4,000	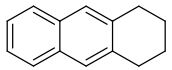	75%	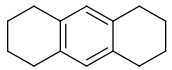	20%

[a] The corrected TOF values for the actual number of surface Ru atoms using D_{H2}.

[b] Entries 1–4: liquid substrates, ~50 mmol; catalyst, 100 mg of 5 wt% Ru/MgO; $n_{sub} : n_{Ru} = 4000 : 1$; 120 °C 10 atm; in THF.

[c] Entries 5–6: solid substrates, ~5 mmol; catalyst, 50 mg of 5 wt% Ru/MgO; $n_{sub} : n_{Ru} = 700 : 1$; 150 °C, 50 atm; in THF; other minor products (< 5%) are not listed.

[d] No catalyst incubation thus no measurement of the half-life.

Table 4-3. Hydrogenation of N-heteroaromatics over Ru/MgO[a]

entry	substrate	rate ($mol \cdot L^{-1} \cdot h^{-1}$)	$t_{1/2}$ (h)	TOF (h^{-1})	TOF_{corr}[b] (h^{-1})	products distribution at $t_{1/2}$			
1[c]		1.60	0.7	1,000	3,700		100%		
2[d]	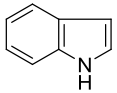	0.22	0.4	280	1,000	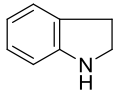	90%	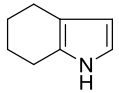	10%
3[e]	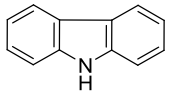	0.44	0.2	560	2,000	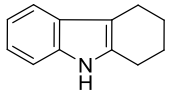	75%	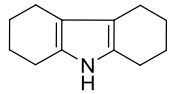	20%
4		1.96	0.4	1,200	4,400		100%		
5	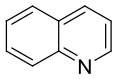	1.47	0.7	960	3,400	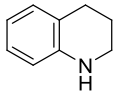	92%	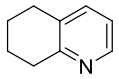	7%
6	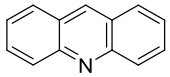	1.34	0.05	1,700	6,000	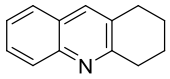	46%	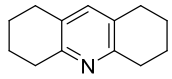	12%
						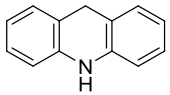	28%	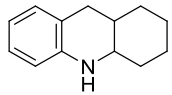	12%

[a] 5 wt% Ru/MgO; 150 °C, 50 atm; in THF. [b] The corrected TOF values for the actual number of surface Ru atoms using D_{H2}. [c] Entries 1 & 5: liquid substrates, ~50 mmol; catalyst, 100 mg; $n_{sub} : n_{Ru} = 4000 : 1$. [d] Entries 2–4, 6: solid substrates, ~5 mmol; catalyst, 50 mg; $n_{sub} : n_{Ru} = 700 : 1$. [e] Entries 3, 5 & 6: other minor products (< 5%) are not listed.

Table 4-4. HYD and DDS of S-heteroaromatics over Ru/MgO[a]

entry	substrate	conditions	HYD pathway					DDS pathway		
			products	1 h		24 h		products	con.%	
				con.%	TOF_{corr} (h^{-1})	con.%	TOF_{corr} (d^{-1})		1 h	24 h
1		150 °C, 50 atm		1	0.5	2	1	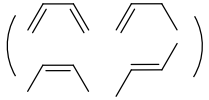	1	1
		200 °C, 50 atm		4	2	11	4		2	4
2	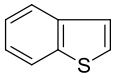	150 °C, 50 atm	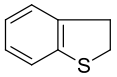	13	5	22	9	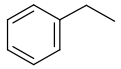	1	1
		200 °C, 50 atm		28	11	61	25		3	6
3	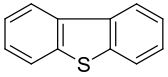	200 °C, 50 atm	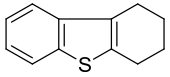	1	0.5	1	0.5	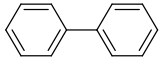	2	2
								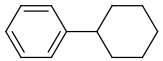	2	2
								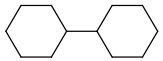	trace	trace
4	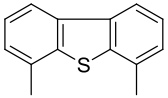	200 °C, 50 atm	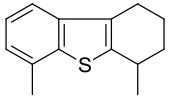	2	1	2	1	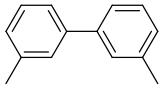	trace	trace
								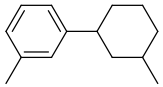	2	1
								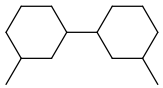	1	2

[a] 100 mg of 10 wt% Ru/MgO, $n_{sub} : n_{Ru} = 40 : 1$, in undecane.

4.3.3.4 Catalyst recyclability and lifetime

The recyclability and lifetime of the Ru/MgO catalyst was evaluated in the hydrogenation of neat toluene in successive cycles at 120 °C and 10 atm using the 10 wt% Ru/MgO (see section 4.2.5 for detailed procedure). In each cycle toluene was 100% converted, and the resulting pure methylcyclohexane, with good separation from the solid catalyst, could be simply withdrawn. The catalyst was then dried and used for next cycle. Figure 4-14 shows the catalyst activity in six consecutive cycles. Interestingly, instead of losing activity when being reused, which is usually the case for solid catalysts due to the loss or deactivation of active phase, the Ru/MgO catalyst displayed enhanced activities in following cycles, as seen from the increased TOF_{corr} values after the first recycling cycle. The catalyst seemed to reach a maximum TOF_{corr} of 4,000 h^{-1} in the fourth cycle and then maintained the activity more than twice as high as in the first cycle, with TOF_{corr} values above 2,000 h^{-1}. Repeated cycle 1–3 experiments consistently showed the same activity trends, excluding experimental errors as responsible factors for the observation.

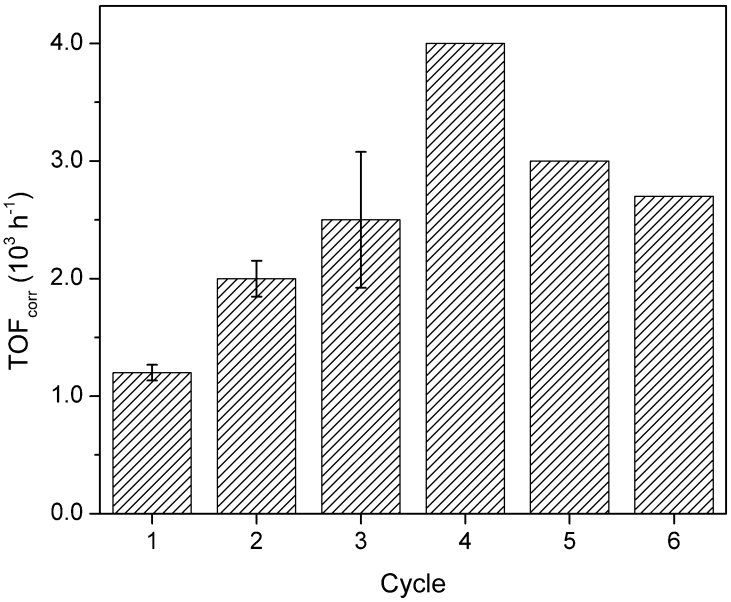

Figure 4-14. The activity of the 10 wt% Ru/MgO catalyst in each cycle during recycling.

Efforts to account for the catalyst activation have also been made. Shown in Figure 4-15 and Figure 4-16 are TEM and XPS studies for the fresh and used 10 wt% Ru/MgO catalyst in recycling experiments. TEM images show no apparent changes either in average particle size or in the size dispersity for catalyst used twice or six times compared to the fresh catalyst; XPS also shows no change in RuNPs oxidation state, as Ru phase is still in zerovallent state after being used six times. The large C 1s peak is due to the accumulation of carbonaceous species from reaction, which is normal for XPS spectra of used catalysts. While it is still not clear about the origin of catalyst activation, there is no doubt that the high catalyst activity can be maintained above 2,000 h^{-1} after the catalyst is once activated for at least five consecutive cycles. The total turnover (TTO) for hydrogenation of neat toluene over the 10 wt% Ru/MgO catalyst, based on the six cycles of recycling experiment, is calculated to be 120,000, which of course is not the limit of our Ru/MgO catalyst. Thus the Ru/MgO catalyst exhibits excellent recyclability for hydrogenation reactions with a very long catalyst lifetime, which is estimated to be far more than 120,000 in TTO.

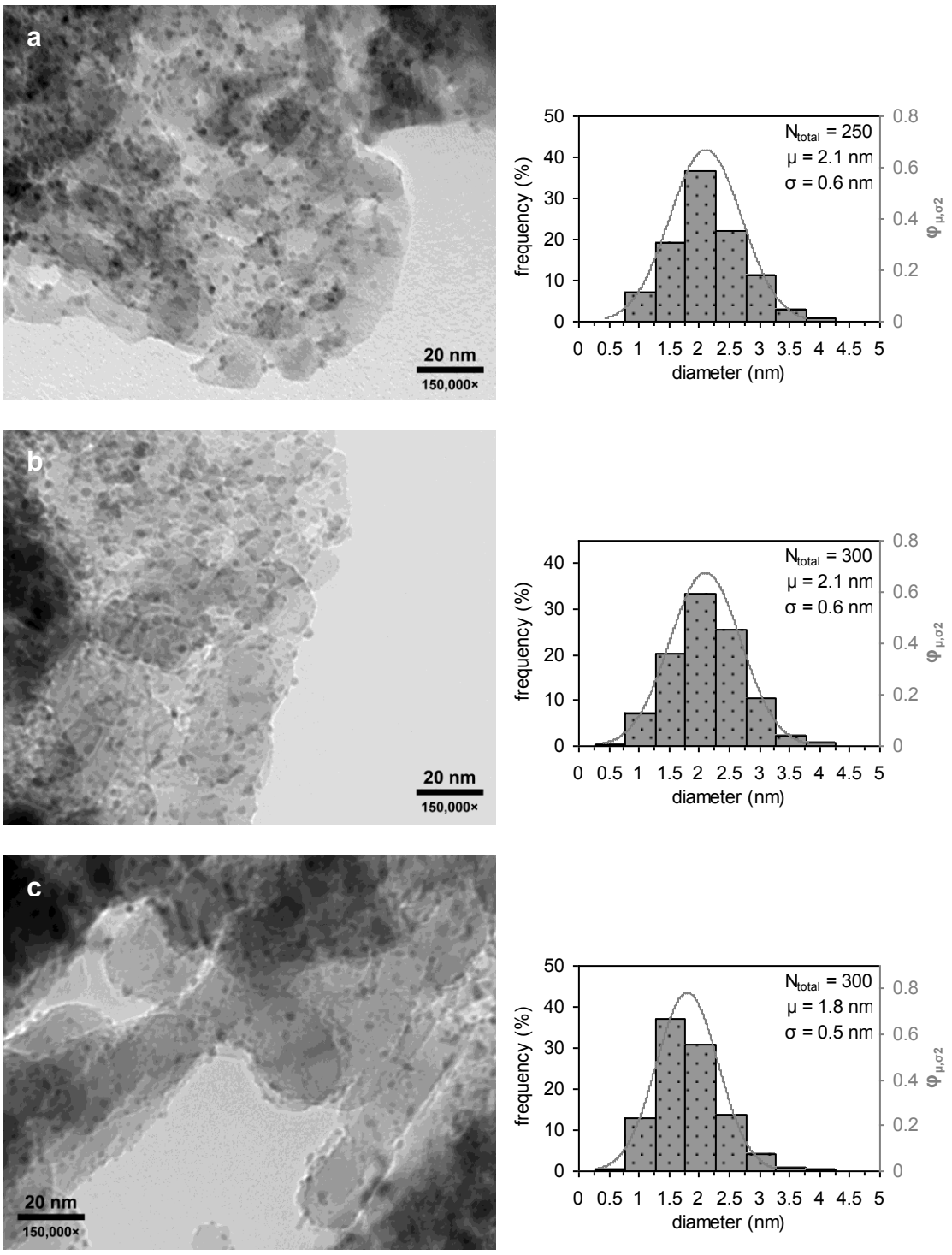

Figure 4-15. TEM studies for the 10 wt% Ru/MgO catalyst in different cycles in the recycling experiment: a). Fresh sample; b). After cycle 2; c). After cycle 6.

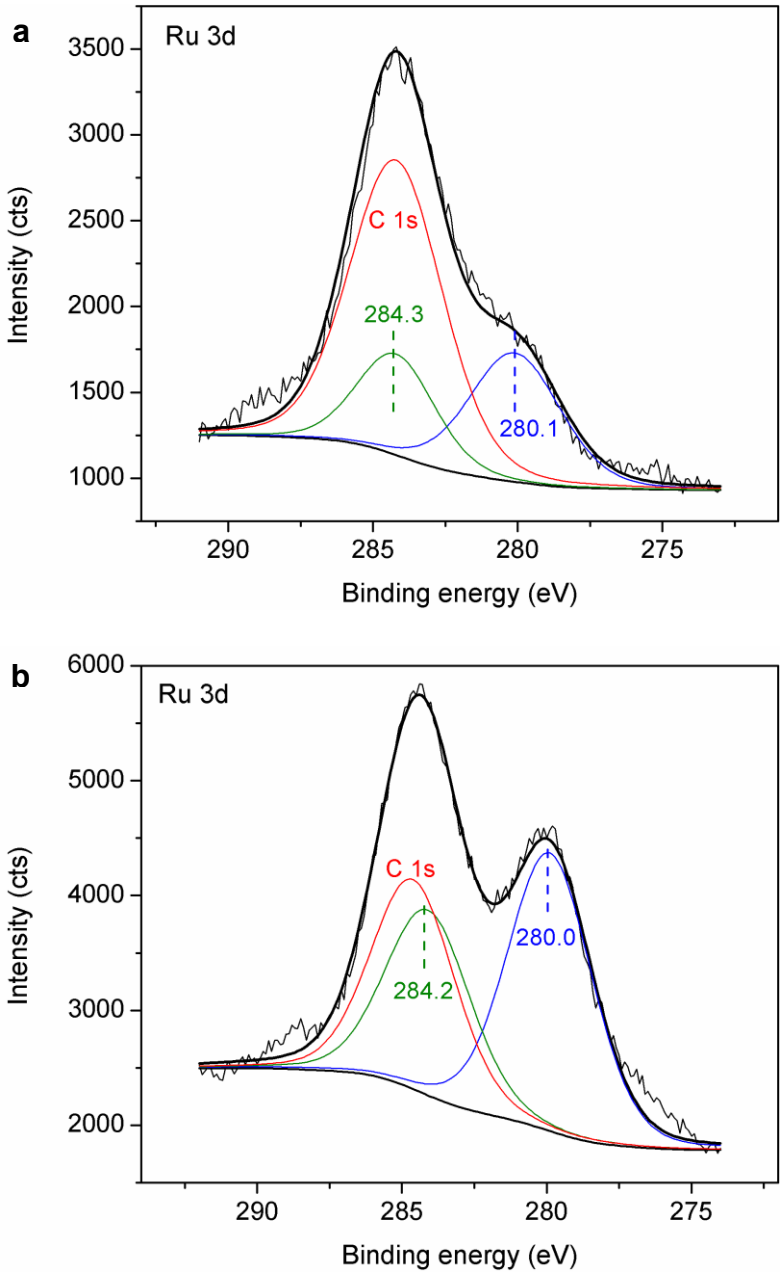

Figure 4-16. XPS analysis for the 10 wt% Ru/MgO catalyst in different cycles in the recycling experiment: a). Fresh sample; b). After cycle 6.

4.3.4 Ionic mechanism on the Ru/MgO surface

Our catalyst design involves RuNPs intimately associated with a basic support to create rich metal-base bifunctional units on solid surfaces, with the aim of promoting heterolytic activation of hydrogen and ionic hydrogenation mechanisms, as a strategy to avoid catalyst poisoning. We have demonstrated this ionic hydrogenation pathway, along with a conventional homolytic H_2 activation pathway—the dual mechanism associated with a dual-site structure for the Ru/P4VPy catalyst (section 3.3.3). We reasoned that by use of a more basic support the dual-site structure could be retained with a more efficient ionic hydrogenation mechanism. When MgO is used as support, the surface O atoms of magnesia could function as basic sites instead of N sites in P4VPy, to create more effective Ru-O bifunctionalities. As shown in Figure 4-17, the Ru atoms in close proximity to surface oxygen atoms from MgO support, particularly those along the perimeter of particles seen from TEM images (Figure 4-4), together with the nearby O atoms, generate the sites for heterolytic splitting of hydrogen (site A); while the RuNPs

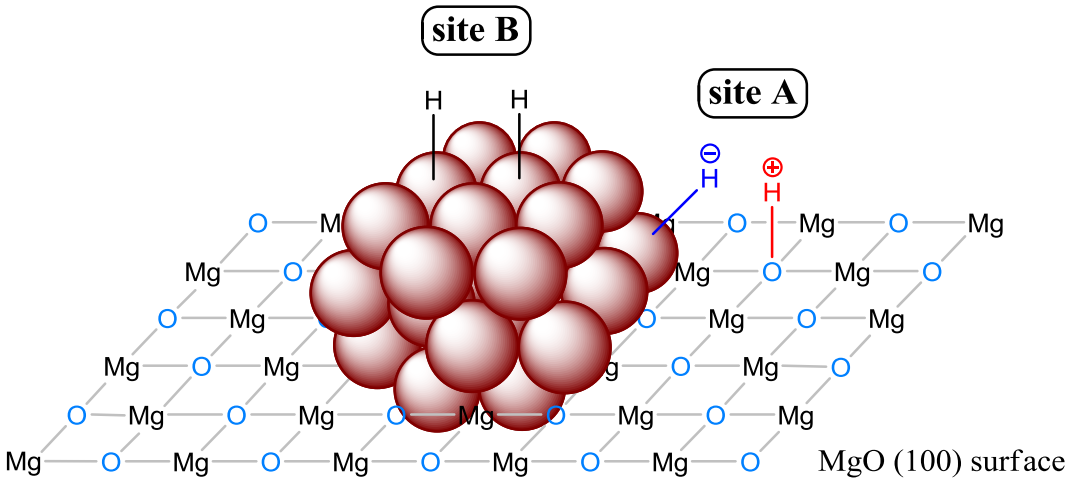

Figure 4-17. The dual-site structure of the Ru/MgO catalyst illustrated by a Ru nanoparticle supported on the MgO (100) surface.

surfaces which are not close enough to the surface O atoms behave as conventional sites for the common homolytic splitting of hydrogen (site B). Therefore, the ionic hydrogenation mechanism and a homolytic H_2 splitting pathway will act in parallel on these two distinct sites in hydrogenation reactions.

4.3.4.1 Substrate competition experiments and thiophene selective poisoning tests point to the ionic mechanism

To test the possibility of this dual-site mechanism on the Ru/MgO catalyst, substrate competition experiments and thiophene selective poisoning tests were also conducted at 150 °C and 50 atm. These reaction profiles were depicted in Figure 4-18. Similar to the case of Ru/P4VPy, quinoline was preferably hydrogenated over toluene at the early stage of reaction, predominantly at the heterocyclic ring to yield N-THQ but also at the carbocyclic ring to produce C-THQ as minor products, while hydrogenation of toluene was suppressed; toluene was only hydrogenated to an important degree after most of quinoline and N-THQ had been consumed (Figure 4-18a). The presence of toluene has no influence on the hydrogenation of quinoline, as the quinoline concentration change is identical to that observed in the hydrogenation of quinoline alone (Figure 4-18c). When thiophene is present, quinoline is exclusively hydrogenated at heterocyclic ring to N-THQ without any traces of other products (Figure 4-18b), in contrast to hydrogenation of quinoline alone (Figure 4-12b); the hydrogenation rate also decreases responsively (Figure 4-18c). The hydrogenation of toluene, on the other hand, is fully inhibited by the presence of thiophene.

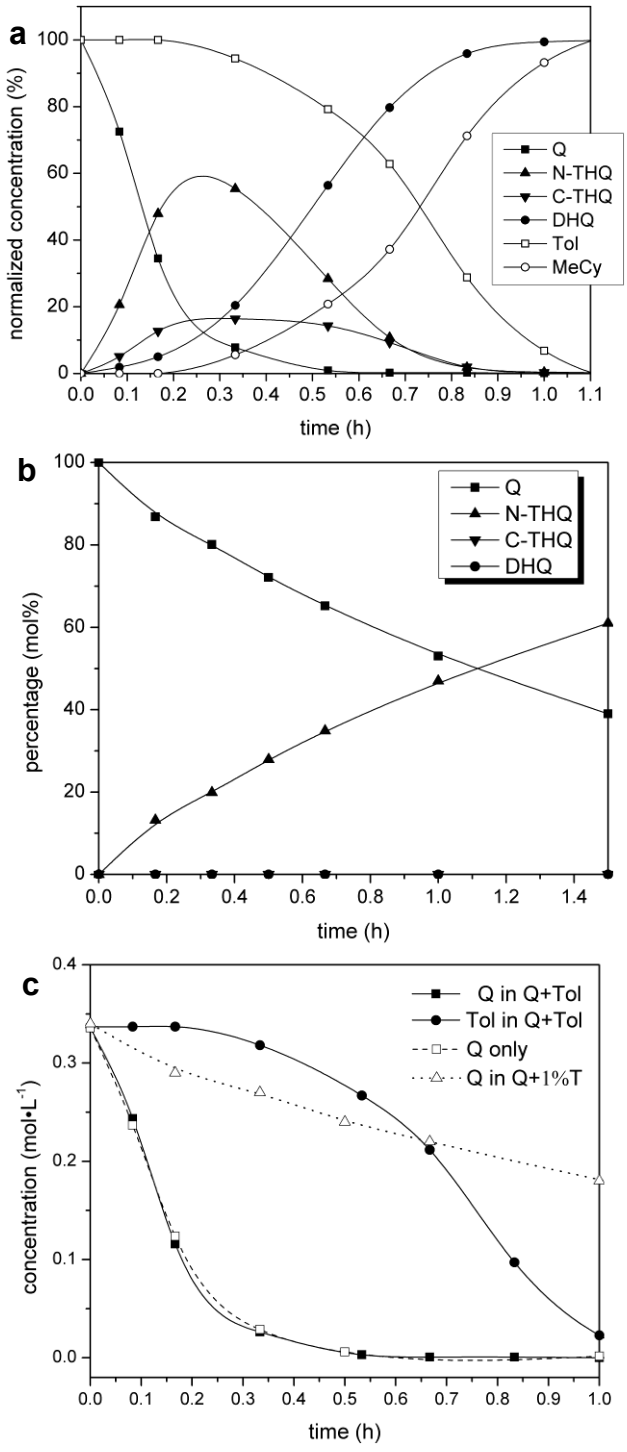

Figure 4-18. Hydrogenation profiles of a) Equimolar Q and Tol (n_Q: n_{Tol} : n_{Ru} = 800 : 800 : 1; in THF; 150 °C, 50 atm); b) Q and 1 mol% thiophene (n_Q: n_T : n_{Ru} = 800 : 5 : 1; in THF; 150 °C, 50 atm). c) Concentration *vs.* time plots for substrate competition experiments, selective poisoning tests and hydrogenation of Q alone (Figure 4-12b).

All of these observations are consistent with those in the case of Ru/P4VPy, pointing to the dual mechanism operating on the dual-site structure (Scheme 4-3): quinoline can be hydrogenated simultaneously at the heterocyclic ring through ionic mechanism (path *a*) on type A sites to produce N-THQ and at the carbocyclic ring through conventional homolytic H_2 activation (path *b*) on type B sites to form C-THQ; these parallel reactions would block the access of toluene to type B sites, where hydrogenation of toluene takes place (path *b*), suppressing its hydrogenation. Once most quinoline and N-THQ are consumed, toluene can effectively compete for type B sites to be hydrogenated. When thiophene is present, it selectively poisons type B sites through strong binding but has little or no affinity for type A sites, thus blocking type B sites for hydrogenation of toluene and the carbocyclic ring of quinoline while leaving type A sites for hydrogenation of heterocyclic ring of quinoline, yielding N-THQ as the exclusive product.

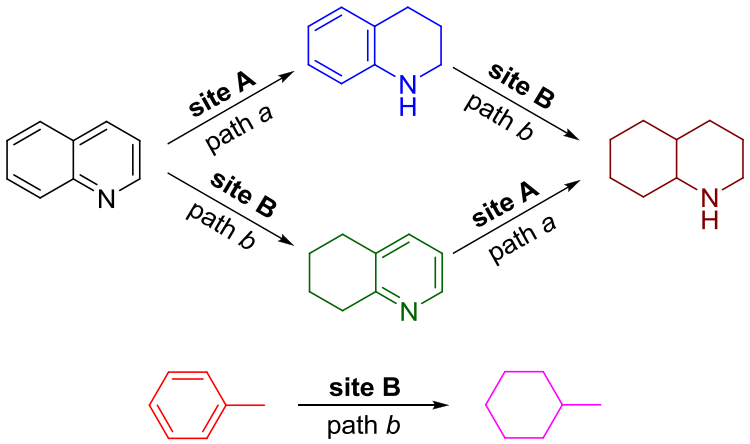

Scheme 4-3. The dual-site mechanism acting in parallel for hydrogenation of Q and Tol on the Ru/MgO catalyst.

4.3.4.2 Effect of magnesia support

To gain further insights into the hydrogenation mechanisms operating on the Ru/MgO catalyst, RuNPs were also supported on the MgO^* powder prepared in the lab (Ru/MgO^*) for the hydrogenation of model substrates toluene and quinoline. MgO^* has a larger surface area (150 $m^2 \cdot g^{-1}$), compared to that of the commercial MgO (Table 4-1) and a larger quantity of surface basic sites, as revealed by CO_2-TPD (Figure 4-11). The RuNPs deposited on MgO^* with a metal loading of 5 wt% has almost the same average particle size and size dispersity compared to that of the 5 wt% Ru/MgO catalyst, as shown by TEM measurements (Figure 4-19 *vs.* Figure 4-2b); the Ru content and dispersion of the 5 wt% Ru/MgO and Ru/MgO^* are also similar (Table 4-1). However, XPS analysis of both 5 wt% Ru/MgO and Ru/MgO^* catalysts showed that Ru/MgO^* has a negative shift of Ru 3d and 3p core level binding energies by 0.5 eV compared to Ru/MgO (Figure 4-9 and Table 4-5), implying a stronger metal-support interaction in the 5wt% Ru/MgO^*, owing to the richer surface basic features of MgO^* support.

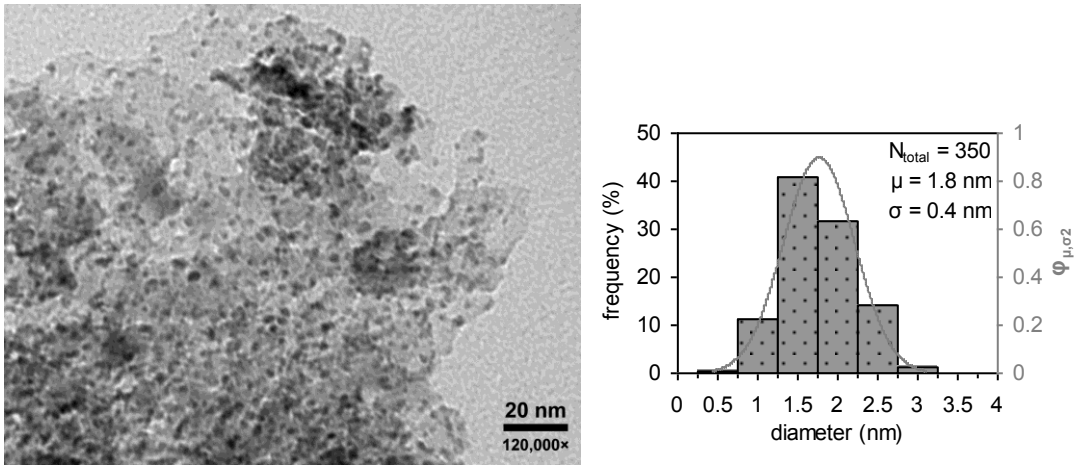

Figure 4-19. The representative TEM image of the 5 wt% Ru/MgO^* and the corresponding RuNPs size distribution histogram with normal distribution curve.

Table 4-5. The Ru 3d and 3p core level binding energies (eV) of the 5 wt% Ru/MgO and the 5 wt% Ru/MgO* catalysts measured by XPS

	$3p_{1/2}$	$3p_{3/2}$	$3d_{3/2}$	$3d_{5/2}$
5 wt% Ru/MgO	483.3	461.0	284.5	280.2
5 wt% Ru/MgO*	482.8	460.6	283.9	279.7
difference	-0.5	-0.4	-0.6	-0.5

The impact of MgO and MgO* supports on the hydrogenation rates of toluene and quinoline is different: toluene is hydrogenated on the two catalysts under analogous conditions at almost the same rates, while quinoline is hydrogenated much faster on Ru/MgO* than on Ru/MgO, as depicted in Table 4-6. This could be explained by the dual-site mechanism: toluene is hydrogenated at only type B sites, which have no direct contact with the support and thus would display similar activities for the two catalysts; while quinoline is also hydrogenated at type A sites, and the stronger Ru-O interaction in Ru/MgO* catalyst would promote more efficient heterolytic H_2 activation and ionic hydrogenation on type A sites, leading to more efficient hydrogenation of quinoline.

Table 4-6. Hydrogenation of toluene and quinoline over 5 wt% Ru/MgO and Ru/MgO*[a]

substrate	catalyst	rate ($mol \cdot L^{-1} \cdot h^{-1}$)	TOF_{corr}[b] (h^{-1})
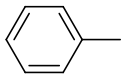	5 wt% Ru/MgO	0.47	1,100
	5 wt% Ru/MgO*	0.50	1,500
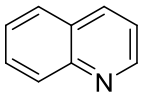	5 wt% Ru/MgO	1.5	3,400
	5 wt% Ru/MgO*	2.6	7,500

[a] Catalyst: 100 mg; substrate: 50 mmol; $n_{sub} : n_{Ru} = 4000 : 1$; solvent: THF; 120 °C /10 atm (Tol), 150 °C /50 atm (Q).

[b] The corrected TOF values for the actual number of surface Ru atoms using D_{H2}.

4.3.4.3 Implications from Vrinat's HDS mechanism

Herein it is worth mentioning Vrinat's mechanism proposed for hydrodesulfurization (HDS) of DBT and its derivatives,[88] wherein H_2 is heterolytically dissociated over Mo and S^{2-} sites on the catalytic surface for the partial hydrogenation of DBT to DHBT intermediates and the subsequent DDS route is achieved via the elimination step assisted by basic sites (Scheme 4-4). Considering the composition and the DDS activity of the Ru/MgO catalysts (Table 4-4), it is possible that the same DDS mechanism also operates on the Ru/MgO catalyst at the type A sites, where the elimination is completed by the presence of H^+ resulting from heterolytic H_2 splitting and a basic attack by O atoms from MgO support. Thus the DDS activity of the Ru/MgO catalysts further implies the existence of type A sites and the associated heterolytic H_2 activation on the Ru/MgO surfaces.

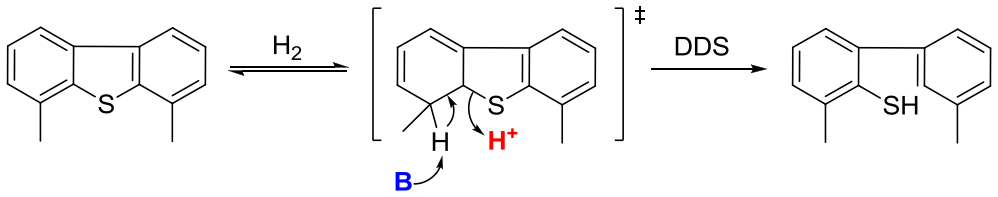

Scheme 4-4. The DDS step in Vrinat's mechanism for HDS of dibenzothiophenes.[88]

4.4 Conclusions

Using the mechanistic concepts from Ru/P4VPy, we have designed and prepared the Ru/MgO catalyst, with the aim to improve the catalytic efficiency for the hydrogenation of heteroatom aromatics. We deposited RuNPs onto magnesia supports through the $NaBH_4$ reduction method at room temperature. Three Ru/MgO catalysts were prepared with a nominal 1, 5 and 10 wt% Ru content supported on a commercial magnesia; an additional catalyst composed of 5 wt% Ru on a lab-made MgO^* powder was also prepared for comparison purposes. TEM measurements show all catalysts have well dispersed RuNPs with similar average particle size (~ 2 nm) and dispersity, regardless of Ru content and the magnesia support, and the catalyst can remain stable against any sintering process under hydrogenation conditions (150 °C, 50 atm). EDX and XPS analyses reveal no B or Cl contamination resulting from the preparation steps. The Ru 3d and 3p XPS spectra clearly indicate the presence of Ru in the zerovalent state for both Ru/MgO and Ru/MgO^* catalyst, while the latter displays a negative shift of Ru 3d and 3p binding energies. The BET surface area of support and the Ru dispersion of all catalysts as well as the surface basic features were also determined by N_2 physisorption, H_2 pulse chemisorption and CO_2-TPD, respectively.

The Ru/MgO catalyst significantly improves the catalytic efficiency: it is versatile and highly efficient for hydrogenation of a series of mono-/polycyclic aromatic hydrocarbons and N-heteroaromatics representative of components of petroleum-derived fuels under mild conditions, as expected from the design; it can also catalyze the hydrogenation of S-heteroaromtaics at moderate temperature and pressure, in which both hydrogenation and desulfurization products were observed. The catalyst is superior to the

few other known supported Ru catalysts for these reactions. These results support that the nanostructure consisting of Ru-O bifunctional units on the Ru/MgO surfaces is capable of promoting more efficient ionic mechanism.

The catalyst is also highly recyclable and has a long lifetime; catalyst activation was observed in the second recycling, with the high activity maintained for the following five consecutive cycles, with a TTO of at least 120,000.

The results of substrate competition experiments and selective thiophene poisoning test point to the dual-site mechanism involving the ionic hydrogenation mechanism on the Ru/MgO catalyst surfaces. The dual-site mechanism was further supported by the hydrogenation of toluene and quinoline on the 5 wt% Ru/MgO and Ru/MgO* catalysts, which give similar toluene hydrogenation rate but enhanced quinoline hydrogenation rate over Ru/MgO* catalyst due to the more effective type A sites and more efficient ionic mechanism in Ru/MgO*. Furthermore, the structure and desulfurization activity of the Ru/MgO catalyst also imply the presence of type A sites and the associated heterolytic splitting of hydrogen for the elimination step in DDS route as in Vrinat's mechanism.

Closing Remarks and Future Prospects

The goal of the dissertation work was to demonstrate that heterolytic splitting of hydrogen and the associated ionic hydrogenation mechanism, which have been well known in solution but extremely rare on solid surfaces, can be promoted by ruthenium nanoparticles immobilized on functional basic supports through metal-base bifuncitonal effect. This hydrogenation pathway is advantageous in that it can avoid catalyst poisoning brought about by the N-/S-containing aromatics since it does not require bonding of substrates to the active metal centers prior to hydrogen transfer during hydrogenation. Deposition of RuNPs onto basic supports would create nanostructures consisting of small ruthenium nanoparticles surrounded by basic functionalities that are rich in metal-base bifunctional units ideal to provoke this ionic hydrogenation pathway, while also retain the advantages of solid catalysts, thus leading to novel high performance and recyclable catalytic materials. As discussed in Chapters 3 and 4, the goal was accomplished by the successful development of the Ru/P4VPy and Ru/MgO catalysts, which display excellent tolerance to N-heteroaromatics poisons and high catalytic activity in hydrogenation of these N aromatics and other various aromatics; additionally, results from the mechanistic studies carried out for both Ru/P4VPy and Ru/MgO catalysts point to the existence of heterolytic hydrogenation activationand ionic hydrogenation pathway over these catalysts, together with a conventional homolytic hydrogen splitting pathway, constructing a dual mechanism that is operating on the dual-site structure of both catalysts.

To develop further more efficient catalytic material using the same mechanistic concepts from Ru/P4VPy and to gain further evidence to the heterolytic hydrogen splitting pathway on our catalysts, future endeavors in the laboratory are suggested towards the following three mains aspects:

Firstly, seeking more basic solid materials with large specific surface area as the support and improving preparation methodology to achieve smaller RuNPs on the support. Heterolytic hydrogen splitting would be more effective on more basic support, as evidenced by the catalytic activities of the Ru/P4VPy and Ru/MgO catalysts toward hydrogenation of N-heteroaromatics. The metal-base bifunctional effect on solid surfaces can be greatly enhanced with the increased basicity of the support. Also, to stabilize RuNPs well under reaction conditions, the support must have a large specific surface area. Particle size and metal dispersion are under consideration as well. Smaller nanoparticles and maximum dispersion are preferred so that the active metal phase can be utilized to a maximum extent and most importantly a higher proportion of Ru atoms on the surface would be intimately associated with basic functionalities thus creating more "type A sites" that are desired for hydrogenation of N-heteroaromatics through the ionic mechanim. Probably new synthetic methodologies are needed, both for the support itself and the supported catalyst.

Secondly, improving hydrogenation activities especially for hydrogenation of S-heteroaromatics. The Ru/MgO catalyst has displayed very efficient hydrogenation toward arenes and N-heteroaromatics, but the activity for hydrogenation of S-heteroaromatics is still not satisfactory. Optimization of catalyst preparation or hydrogenation reaction conditions is thus desired to achieve more efficient hydrogenation of S-aromatics using

the existing catalysts. Development of new efficient catalyst employing other supports as stated above would be another strategy. The development of the Ru/P4VPy and Ru/MgO catalysts has worked in the right direction and I believe advancing towards the right direction will continue.

Last but not least, conducting mechanistic studies with more modern analytic techniques. Admittedly, the mechanistic studies on solid surface are complicated and challenging. The mechanistic insights through the work of this project are based on the indirect evidence and are of great value towards the understanding of the hydrogen activation process and catalytic behavior of our catalysts. With the emergence of advanced *in situ* analyzing instruments, the direct evidence can be obtained by studying the catalyst under *in situ* conditions microscopically and spectroscopically and a better mechanistic understanding can be achieved, which in turn will benefit the development of more efficient catalyst.

A period of work ends; a long way of endeavors will continue.

Appendices

- Reports of BET surface area measurements for the magnesia supports.
- Reports of CO/H_2 pulse chemisorption measurements for the Ru/magnesia catalysts.
- Reports of the hydrogenation of aromatic substrates representative of components of petroleum-derived fuels over the Ru/magnesia catalysts.

Sample: BET MgO(c500)-2nd
File: E:\RESEARCH\CHEMIS~1\REPORT~1\DATA\FANG-010.SMP

Started: 8/25/2011 5:06:48PM
Completed: 8/25/2011 6:08:05PM

Sample Mass: 0.2071 g
Report Time: 1/7/2013 2:16:29PM

Comments: pretreated at 200 C in He for 30 min; no powder stuck on the upper part of the inside wall in the tube

BET Single Point Tabular Report

Experiment 1: BET surface area

Analysis Type: Physisorption Surface Area
Calibration: (CHM_0000) BET Calibration
Measured Flow Rate: 15.00 mL STP/min
Signal Offset: 0.02785
Signal Inverted: No

Peak Summary

Experiment Number	Active Concen-tration	Relative Pressure	Cumulative Volume (mL/g STP)	1 / [Q(Po/P-1)] (g/cm³ STP)
1	0.0000	0.0000	29.03124	0.000000

BET Analysis Summary

Ambient Pressure: 764 mmHg
Saturated Pressure: 779.00 mmHg
Cross-Sectional Area: 0.162 nm²
Monolayer Volume: 20.490 cm³/g
BET Surface Area: 89.1952 m²/g

Experiment 2: BET surface area

Analysis Type: Physisorption Surface Area
Calibration: (CHM_0000) BET Calibration
Measured Flow Rate: 15.00 mL STP/min
Signal Offset: 0.03096
Signal Inverted: No

Peak Summary

Experiment Number	Active Concen-tration	Relative Pressure	Cumulative Volume (mL/g STP)	1 / [Q(Po/P-1)] (g/cm³ STP)
2	0.0000	0.0000	28.96792	0.000000

BET Analysis Summary

Ambient Pressure: 764 mmHg
Saturated Pressure: 779.00 mmHg
Cross-Sectional Area: 0.162 nm²
Monolayer Volume: 20.445 cm³/g
BET Surface Area: 89.0006 m²/g

Experiment 3: BET surface area

Analysis Type: Physisorption Surface Area
Calibration: (CHM_0000) BET Calibration
Measured Flow Rate: 15.00 mL STP/min
Signal Offset: 0.03046
Signal Inverted: No

Sample: BET MgO(c500)-2nd
File: E:\RESEARCH\CHEMIS~1\REPORT~1\DATA\FANG-010.SMP

Started: 8/25/2011 5:06:48PM
Completed: 8/25/2011 6:08:05PM

Sample Mass: 0.2071 g
Report Time: 1/7/2013 2:16:29PM

Comments: pretreated at 200 C in He for 30 min; no powder stuck on the upper part of the inside wall in the tube

Peak Summary

Experiment Number	Active Concen-tration	Relative Pressure	Cumulative Volume (mL/g STP)	1 / [Q(Po/P-1)] (g/cm³ STP)
3	0.0000	0.0000	29.00113	0.000000

BET Analysis Summary

Ambient Pressure: 764 mmHg
Saturated Pressure: 779.00 mmHg
Cross-Sectional Area: 0.162 nm²
Monolayer Volume: 20.468 cm³/g
BET Surface Area: 89.1027 m²/g

Sample: BET MgO(c500)-2nd
File: E:\RESEARCH\CHEMIS~1\REPORT~1\DATA\FANG-010.SMP

Started: 8/25/2011 5:06:48PM
Completed: 8/25/2011 6:08:05PM

Sample Mass: 0.2071 g
Report Time: 1/7/2013 2:16:29PM

Comments: pretreated at 200 C in He for 30 min; no powder stuck on the upper part of the inside wall in the tube

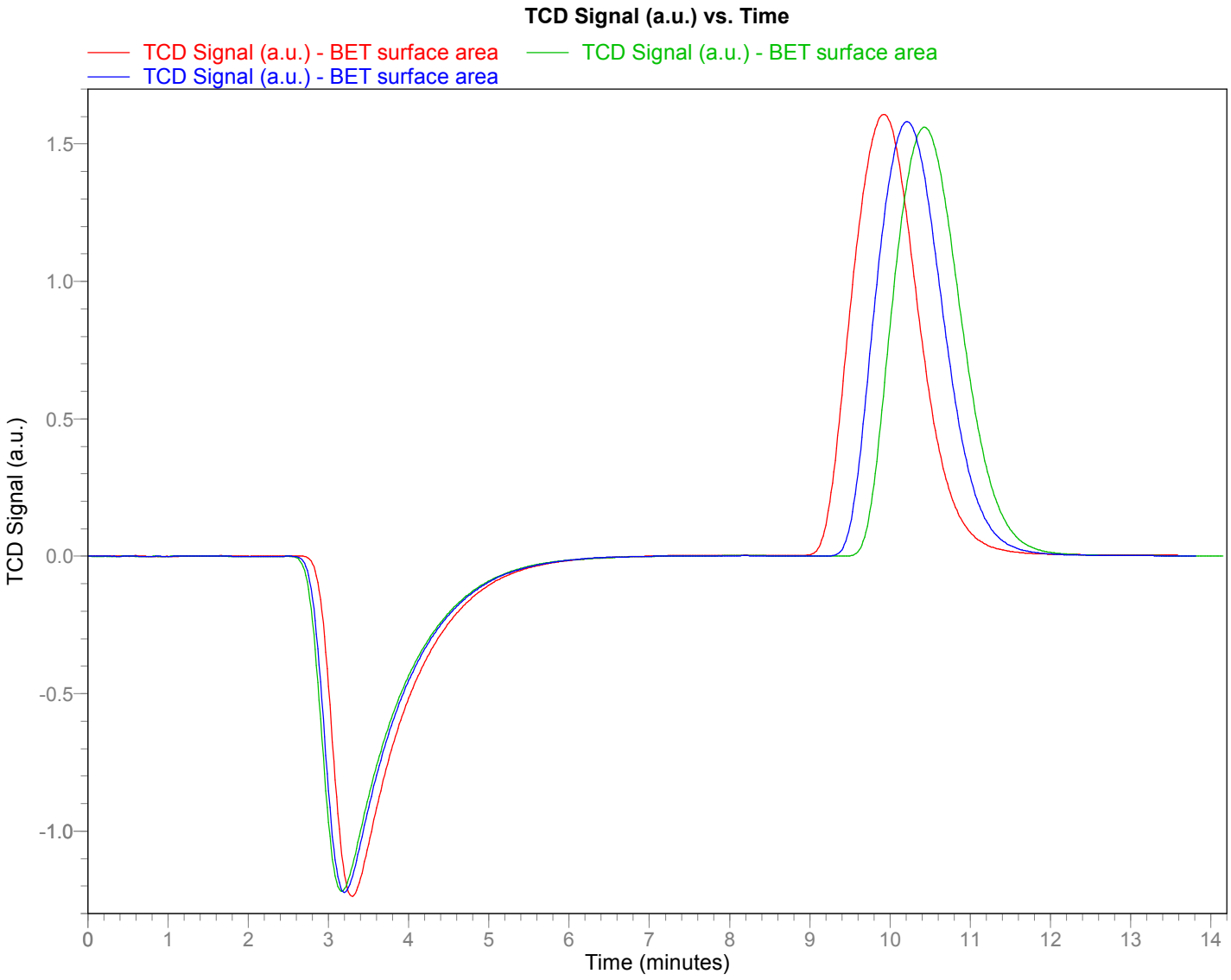

Sample: BET MgO(s500)-2nd
File: E:\RESEARCH\CHEMIS~1\REPORT~1\DATA\FANG-011.SMP

Started: 8/26/2011 3:00:49PM
Completed: 8/26/2011 4:08:23PM
Sample Mass: 0.0524 g
Report Time: 1/7/2013 2:16:29PM

Comments: pretreated at 200 C in He for 30 min; no powder stuck on the upper part of the inside wall in the tube

BET Single Point Tabular Report

Experiment 1: BET surface area

Analysis Type: Physisorption Surface Area
Calibration: (CHM_0000) BET Calibration
Measured Flow Rate: 15.00 mL STP/min
Signal Offset: 0.03027
Signal Inverted: No

Peak Summary

Experiment Number	Active Concen-tration	Relative Pressure	Cumulative Volume (mL/g STP)	1 / [Q(Po/P-1)] (g/cm³ STP)
1	0.0000	0.0000	47.06672	0.000000

BET Analysis Summary

Ambient Pressure: 764 mmHg
Saturated Pressure: 779.00 mmHg
Cross-Sectional Area: 0.162 nm²
Monolayer Volume: 33.219 cm³/g
BET Surface Area: 144.6071 m²/g

Experiment 2: BET surface area

Analysis Type: Physisorption Surface Area
Calibration: (CHM_0000) BET Calibration
Measured Flow Rate: 15.00 mL STP/min
Signal Offset: 0.03027
Signal Inverted: No

Peak Summary

Experiment Number	Active Concen-tration	Relative Pressure	Cumulative Volume (mL/g STP)	1 / [Q(Po/P-1)] (g/cm³ STP)
2	0.0000	0.0000	46.89876	0.000000

BET Analysis Summary

Ambient Pressure: 764 mmHg
Saturated Pressure: 779.00 mmHg
Cross-Sectional Area: 0.162 nm²
Monolayer Volume: 33.100 cm³/g
BET Surface Area: 144.0911 m²/g

Experiment 3: BET surface area

Analysis Type: Physisorption Surface Area
Calibration: (CHM_0000) BET Calibration
Measured Flow Rate: 15.00 mL STP/min
Signal Offset: 0.03019
Signal Inverted: No

Sample: BET MgO(s500)-2nd
File: E:\RESEARCH\CHEMIS~1\REPORT~1\DATA\FANG-011.SMP

Started: 8/26/2011 3:00:49PM
Completed: 8/26/2011 4:08:23PM

Sample Mass: 0.0524 g
Report Time: 1/7/2013 2:16:29PM

Comments: pretreated at 200 C in He for 30 min; no powder stuck on the upper part of the inside wall in the tube

Peak Summary

Experiment Number	Active Concen-tration	Relative Pressure	Cumulative Volume (mL/g STP)	1 / [Q(Po/P-1)] (g/cm³ STP)
3	0.0000	0.0000	46.70065	0.000000

BET Analysis Summary

Ambient Pressure: 764 mmHg
Saturated Pressure: 779.00 mmHg
Cross-Sectional Area: 0.162 nm²
Monolayer Volume: 32.960 cm³/g
BET Surface Area: 143.4824 m²/g

Sample: BET MgO(s500)-2nd
File: E:\RESEARCH\CHEMIS~1\REPORT~1\DATA\FANG-011.SMP

Started: 8/26/2011 3:00:49PM
Completed: 8/26/2011 4:08:23PM

Sample Mass: 0.0524 g
Report Time: 1/7/2013 2:16:29PM

Comments: pretreated at 200 C in He for 30 min; no powder stuck on the upper part of the inside wall in the tube

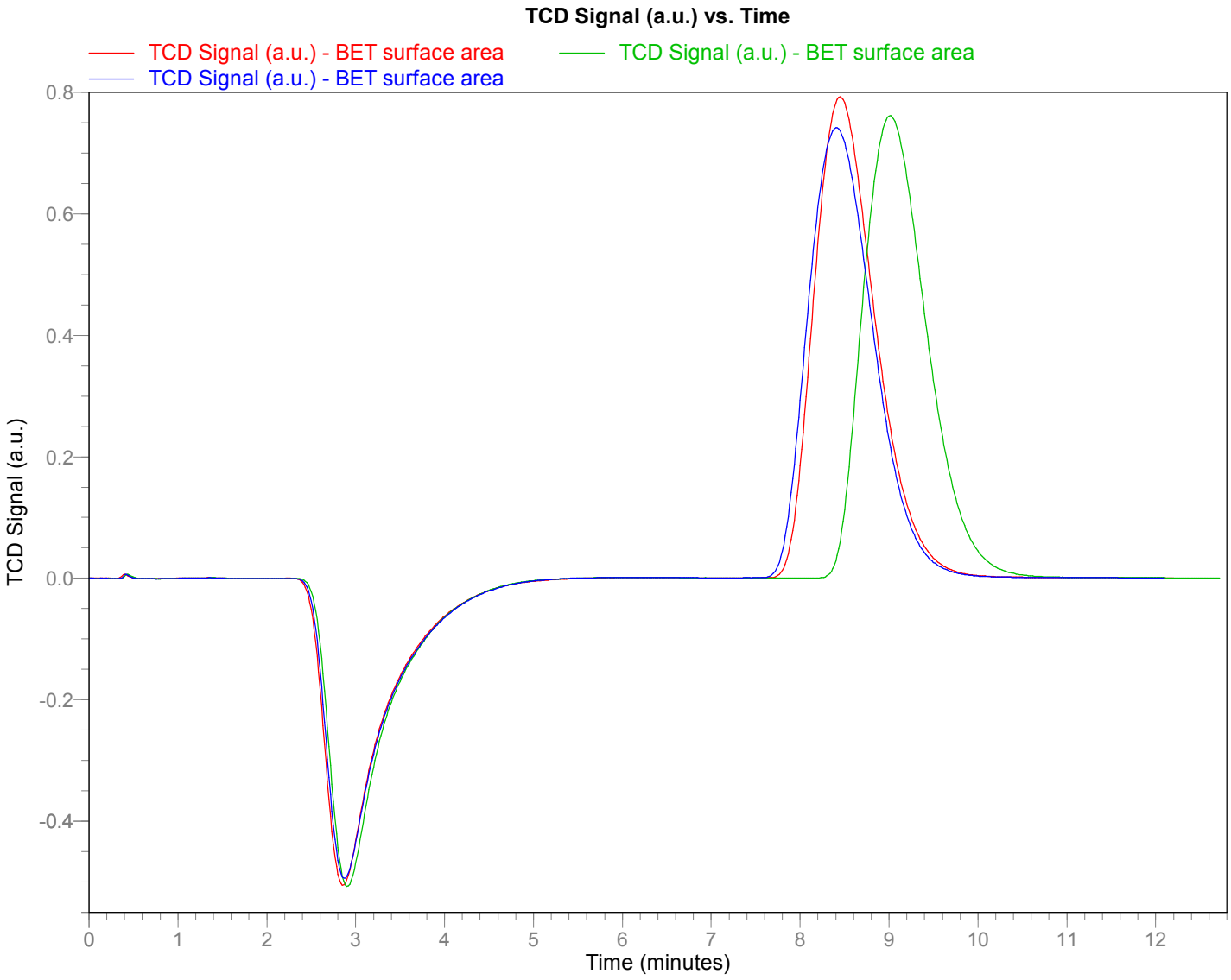

Sample: H2 pulse chemisorption 1 wt% Ru/MgO-b
File: E:\RESEARCH\CHEMIS~1\REPORT~1\DATA\FANG-022.SMP

Started: 9/21/2011 4:54:22PM
Completed: 9/21/2011 7:57:38PM

Sample Mass: 0.5040 g
Report Time: 1/7/2013 2:18:04PM

Comments: w/ use of thermocouple; increase amount to 500 mg

Pulse Chemisorption Report

Experiment 1: H2 pulse chemisorption

Analysis Type: Pulse Chemisorption
Calibration: None
Measured Flow Rate: 25.00 mL STP/min
Signal Offset: -0.03160
Signal Inverted: Yes

Peak Table

Peak Number	Temperature at Maximum (°C)	Volume Adsorbed (mL/g STP)	Cumulative Volume (mL/g STP)
1*	24.7	0.00179	0.05158
2	24.3	0.00085	0.05243
3	24.3	0.00000	0.05243
4	24.4	0.00000	0.05243

* 2 doses were completely adsorbed with a cumulative volume of 0.04979 mL/g.

Pulse Chemisorption Analysis Summary

Element	Percent of Sample Mass (%)	Atomic Weight	Stoichiometry Factor	Atomic Cross-Sectional Area (nm²)	Density (g/cm³)
Ru	1.0000	101.070	2.000	0.0613	12.400

Active Loop Volume at 24.5 °C: 0.01255 mL STP
Cumulative Volume: 0.05243 mL/g STP
Metal Dispersion: 4.7281%
Metallic Surface Area: 0.1727 m²/g sample
Metallic Surface Area: 17.2719 m²/g metal
Active Particle Diameter: 28.0149 nm

Sample: H2 pulse chemisorption 1 wt% Ru/MgO-b
File: E:\RESEARCH\CHEMIS~1\REPORT~1\DATA\FANG-022.SMP

Started: 9/21/2011 4:54:22PM
Completed: 9/21/2011 7:57:38PM

Sample Mass: 0.5040 g
Report Time: 1/7/2013 2:18:04PM

Comments: w/ use of thermocouple; increase amount to 500 mg

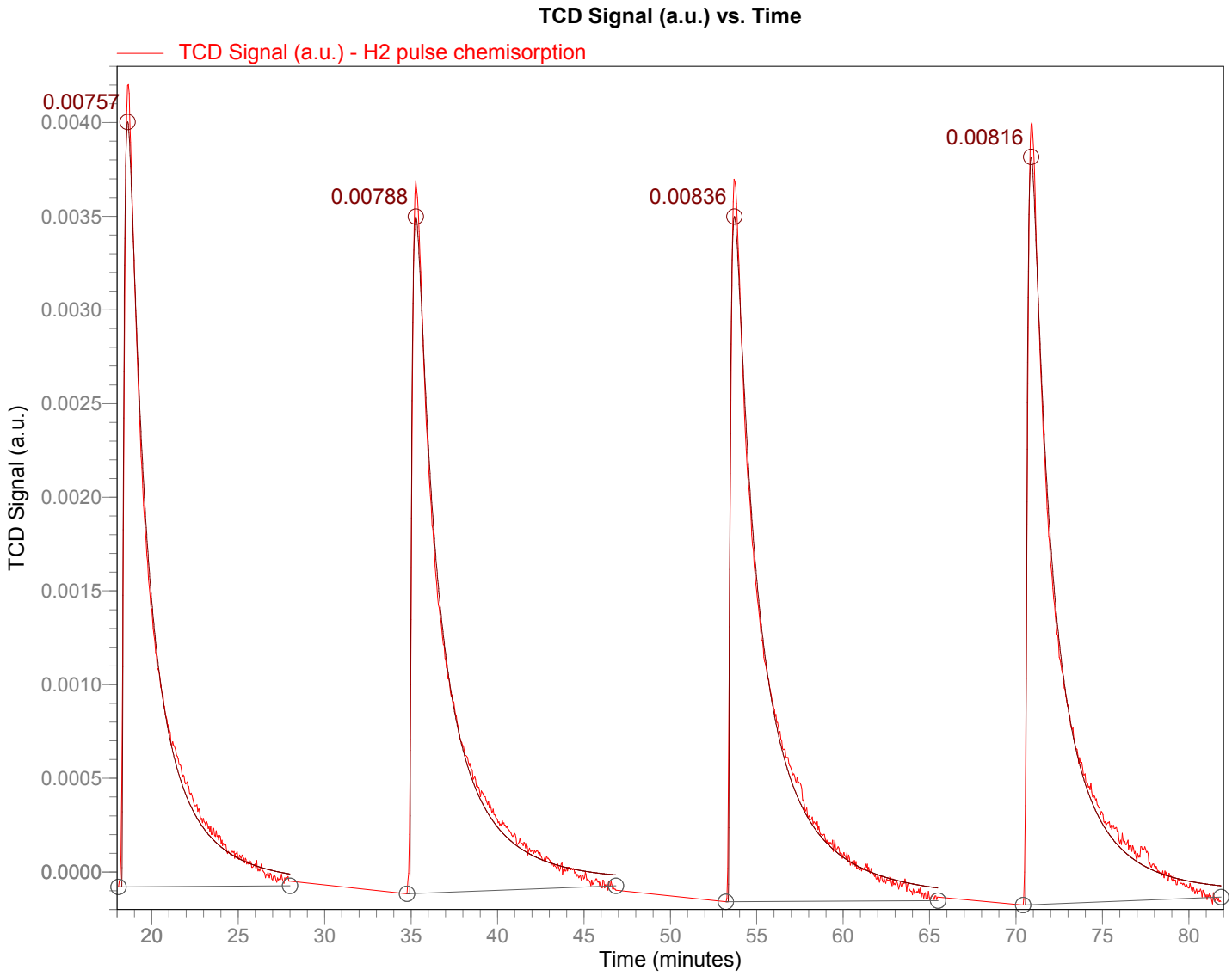

Sample: H2 pulse chemisorption 5 wt% Ru/MgO(5g)-c2
File: E:\RESEARCH\CHEMIS~1\REPORT~1\DATA\FANG-019.SMP

Started: 9/15/2011 12:37:10PM
Completed: 9/15/2011 4:45:22PM

Sample Mass: 0.1103 g
Report Time: 1/7/2013 2:18:05PM

Comments: w/ use of thermocouple

Pulse Chemisorption Report

Experiment 1: H2 pulse chemisorption

Analysis Type: Pulse Chemisorption
Calibration: None
Measured Flow Rate: 25.00 mL STP/min
Signal Offset: -0.02604
Signal Inverted: Yes

Peak Table

Peak Number	Temperature at Maximum (°C)	Volume Adsorbed (mL/g STP)	Cumulative Volume (mL/g STP)
1*	24.7	0.23348	1.55104
2	24.6	0.06220	1.61324
3	24.7	0.02922	1.64246
4	24.7	0.00000	1.64246

* 3 doses were completely adsorbed with a cumulative volume of 1.31756 mL/g.

Pulse Chemisorption Analysis Summary

Element	Percent of Sample Mass (%)	Atomic Weight	Stoichiometry Factor	Atomic Cross-Sectional Area (nm²)	Density (g/cm³)
Ru	5.0000	101.070	2.000	0.0613	12.400

Active Loop Volume at 25.0 °C: 0.04844 mL STP
Cumulative Volume: 1.64246 mL/g STP
Metal Dispersion: 29.6250%
Metallic Surface Area: 5.4110 m²/g sample
Metallic Surface Area: 108.2203 m²/g metal
Active Particle Diameter: 4.4712 nm

Sample: H2 pulse chemisorption 5 wt% Ru/MgO(5g)-c2
File: E:\RESEARCH\CHEMIS~1\REPORT~1\DATA\FANG-019.SMP

Started: 9/15/2011 12:37:10PM
Completed: 9/15/2011 4:45:22PM

Sample Mass: 0.1103 g
Report Time: 1/7/2013 2:18:05PM

Comments: w/ use of thermocouple

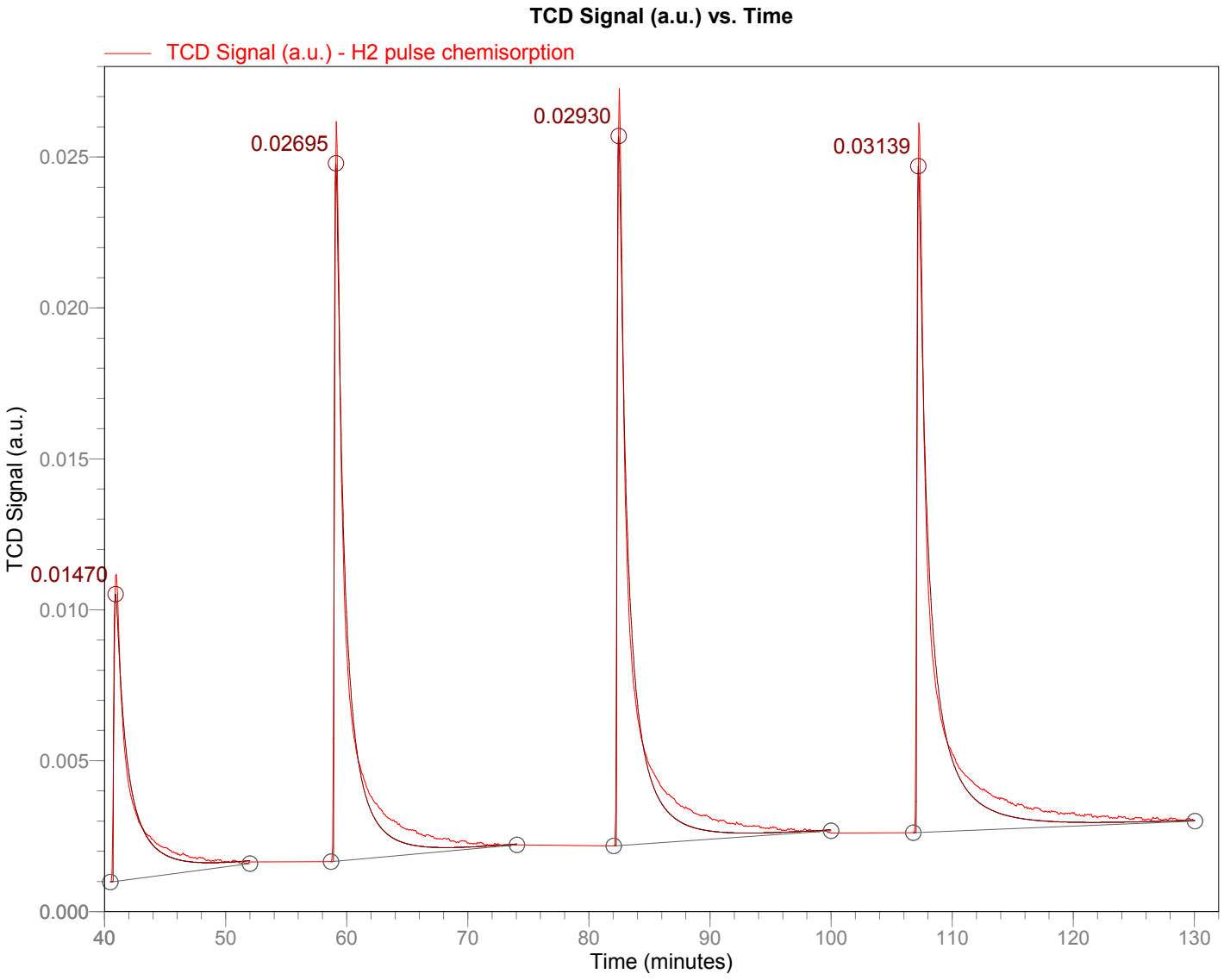

Sample: H2 pulse chemisorption 5 wt% Ru/MgO(s)
File: E:\RESEARCH\CHEMIS~1\REPORT~1\DATA\FANG-025.SMP

Started: 9/26/2011 1:58:35PM
Completed: 9/26/2011 6:24:39PM
Sample Mass: 0.0994 g
Report Time: 1/7/2013 2:18:01PM

Pulse Chemisorption Report

Experiment 1: H2 pulse chemisorption

Analysis Type: Pulse Chemisorption
Calibration: None
Measured Flow Rate: 25.00 mL STP/min
Signal Offset: -0.03628
Signal Inverted: Yes

Peak Table

Peak Number	Temperature at Maximum (°C)	Volume Adsorbed (mL/g STP)	Cumulative Volume (mL/g STP)
1*	24.4	0.12898	1.10531
2	24.4	0.03484	1.14015
3	24.4	0.00000	1.14015

* 2 doses were completely adsorbed with a cumulative volume of 0.97633 mL/g.

Pulse Chemisorption Analysis Summary

Element	Percent of Sample Mass (%)	Atomic Weight	Stoichiometry Factor	Atomic Cross-Sectional Area (nm²)	Density (g/cm³)
Ru	5.0000	101.070	2.000	0.0613	12.400

Active Loop Volume at 24.5 °C: 0.04852 mL STP
Cumulative Volume: 1.14015 mL/g STP
Metal Dispersion: 20.5649%
Metallic Surface Area: 3.7562 m²/g sample
Metallic Surface Area: 75.1237 m²/g metal
Active Particle Diameter: 6.4410 nm

Sample: H2 pulse chemisorption 5 wt% Ru/MgO(s)
File: E:\RESEARCH\CHEMIS~1\REPORT~1\DATA\FANG-025.SMP

Started: 9/26/2011 1:58:35PM
Completed: 9/26/2011 6:24:39PM

Sample Mass: 0.0994 g
Report Time: 1/7/2013 2:18:01PM

TCD Signal (a.u.) vs. Time

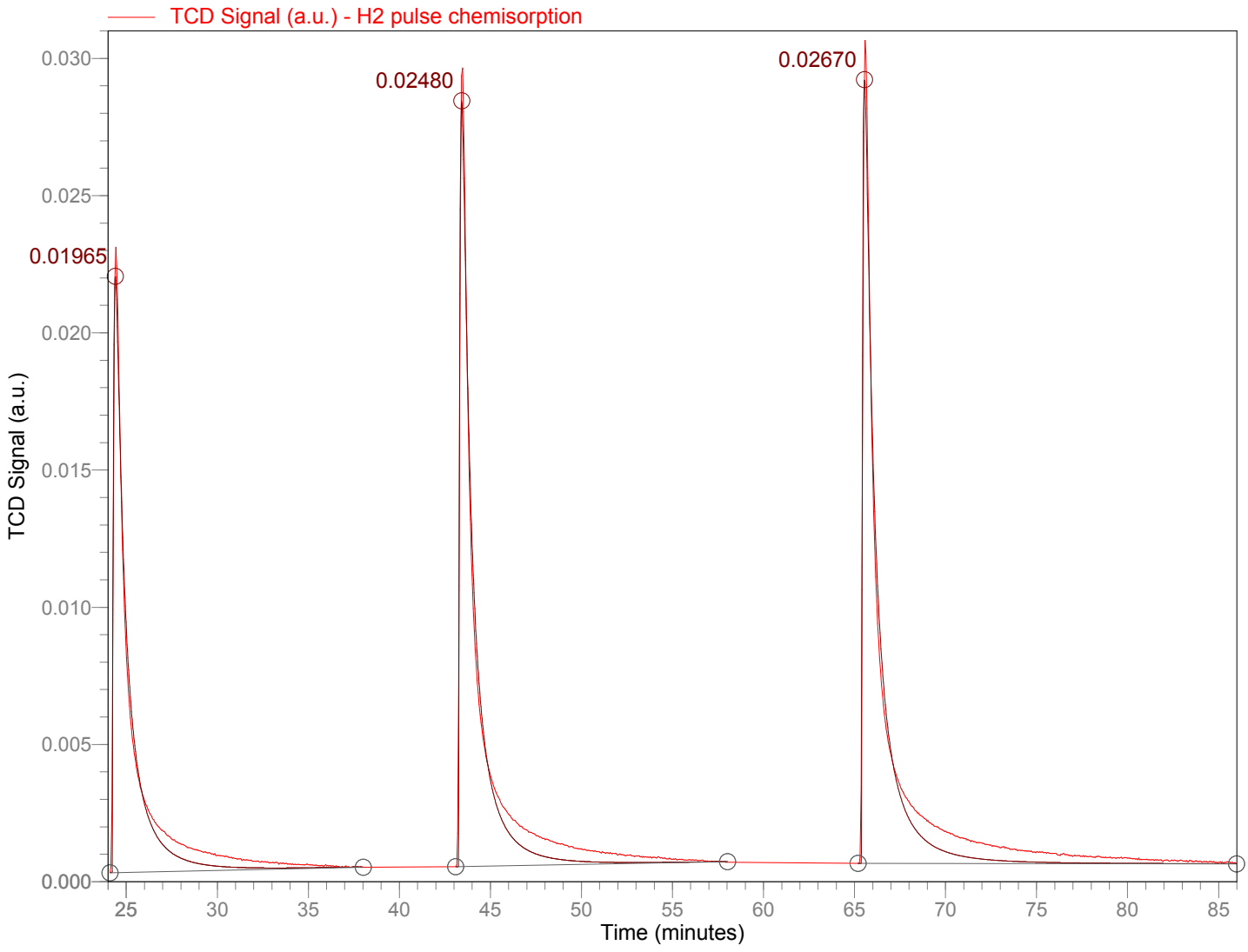

Sample: H2 pulse chemisorption 10 wt% Ru/MgO
File: E:\RESEARCH\CHEMIS~1\REPORT~1\DATA\FANG-023.SMP

Started: 9/22/2011 3:19:12PM
Completed: 9/22/2011 8:04:12PM
Sample Mass: 0.1040 g
Report Time: 1/7/2013 2:18:02PM

Pulse Chemisorption Report

Experiment 1: H2 pulse chemisorption

Analysis Type: Pulse Chemisorption
Calibration: None
Measured Flow Rate: 25.00 mL STP/min
Signal Offset: -0.03135
Signal Inverted: Yes

Peak Table

Peak Number	Temperature at Maximum (°C)	Volume Adsorbed (mL/g STP)	Cumulative Volume (mL/g STP)
1*	24.5	0.21571	2.54858
2	24.5	0.07599	2.62457
3	24.2	0.01066	2.63523
4	24.1	0.00000	2.63523

* 5 doses were completely adsorbed with a cumulative volume of 2.33287 mL/g.

Pulse Chemisorption Analysis Summary

Element	Percent of Sample Mass (%)	Atomic Weight	Stoichiometry Factor	Atomic Cross-Sectional Area (nm²)	Density (g/cm³)
Ru	10.0000	101.070	2.000	0.0613	12.400

Active Loop Volume at 24.5 °C: 0.04852 mL STP
Cumulative Volume: 2.63523 mL/g STP
Metal Dispersion: 23.7657%
Metallic Surface Area: 8.6817 m²/g sample
Metallic Surface Area: 86.8166 m²/g metal
Active Particle Diameter: 5.5735 nm

Sample: H2 pulse chemisorption 10 wt% Ru/MgO
File: E:\RESEARCH\CHEMIS~1\REPORT~1\DATA\FANG-023.SMP

Started: 9/22/2011 3:19:12PM
Completed: 9/22/2011 8:04:12PM

Sample Mass: 0.1040 g
Report Time: 1/7/2013 2:18:02PM

TCD Signal (a.u.) vs. Time

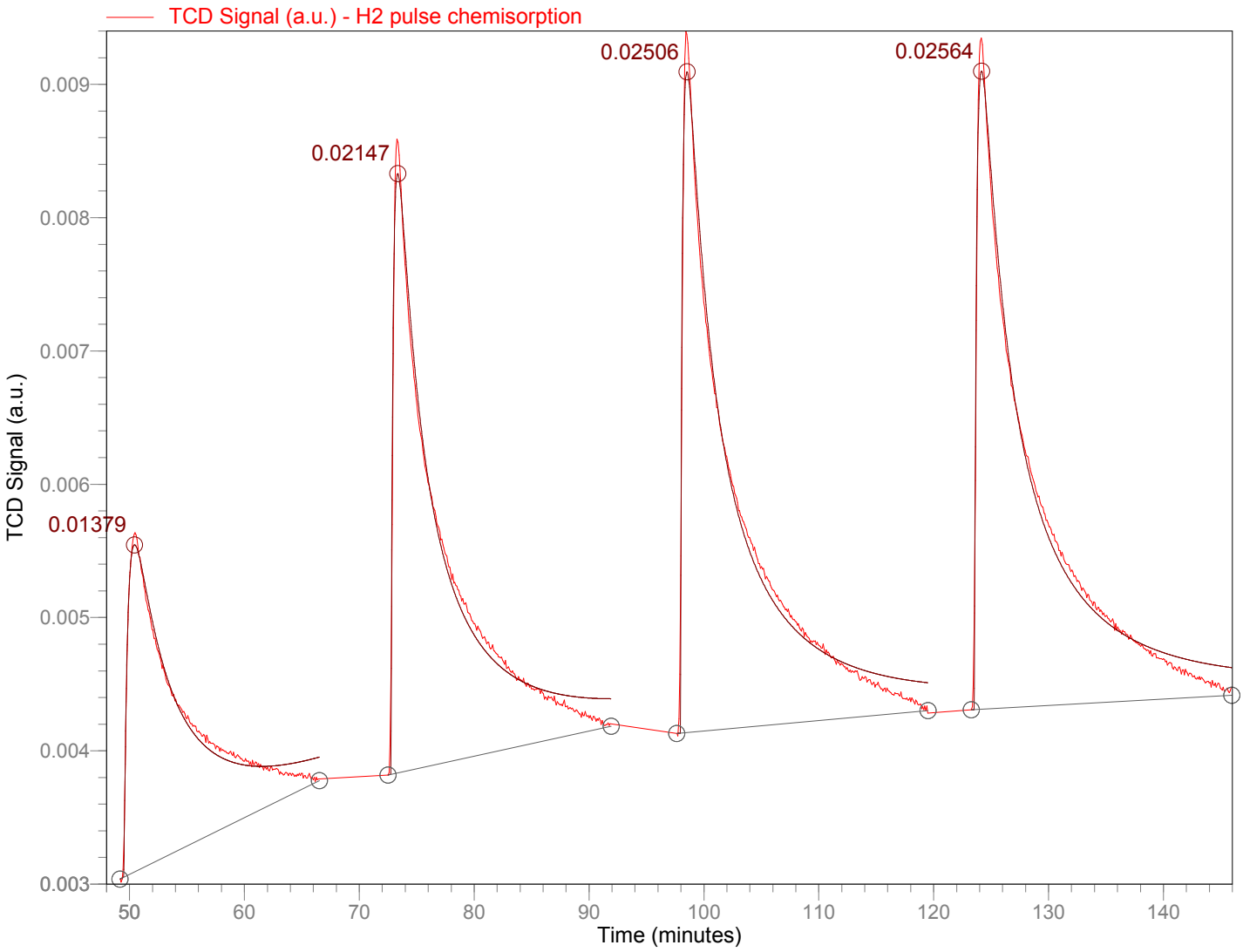

Sample: after 073_CO pulse chemisorption 5 wt% Ru/MgO
File: E:\RESEARCH\CHEMIS~1\REPORT~1\DATA\FANG-074.SMP

Started: 5/3/2012 10:48:24AM
Completed: 5/3/2012 1:55:30PM

Sample Mass: 0.1000 g
Report Time: 1/7/2013 2:17:59PM

Pulse Chemisorption Report

Experiment 1: CO pulse chemisorption

Analysis Type: Pulse Chemisorption
Calibration: None
Measured Flow Rate: 25.00 mL STP/min
Signal Offset: -0.00574
Signal Inverted: No

Peak Table

Peak Number	Temperature at Maximum (°C)	Volume Adsorbed (mL/g STP)	Cumulative Volume (mL/g STP)
1*	25.1	0.43142	2.37498
2	24.9	0.23728	2.61226
3	24.9	0.05305	2.66531
4	24.9	0.02516	2.69047
5	24.8	0.02476	2.71523
6	24.8	0.00000	2.71523

* 4 doses were completely adsorbed with a cumulative volume of 1.94356 mL/g.

Pulse Chemisorption Analysis Summary

Element	Percent of Sample Mass (%)	Atomic Weight	Stoichiometry Factor	Atomic Cross-Sectional Area (nm²)	Density (g/cm³)
Ru	5.0000	101.070	1.000	0.0613	12.400

Active Loop Volume at 25.0 °C: 0.04859 mL STP
Cumulative Volume: 2.71523 mL/g STP
Metal Dispersion: 24.4872%
Metallic Surface Area: 4.4726 m²/g sample
Metallic Surface Area: 89.4521 m²/g metal
Active Particle Diameter: 5.4093 nm

Sample: after 073_CO pulse chemisorption 5 wt% Ru/MgO
File: E:\RESEARCH\CHEMIS~1\REPORT~1\DATA\FANG-074.SMP

Started: 5/3/2012 10:48:24AM
Completed: 5/3/2012 1:55:30PM

Sample Mass: 0.1000 g
Report Time: 1/7/2013 2:17:59PM

TCD Signal (a.u.) vs. Time

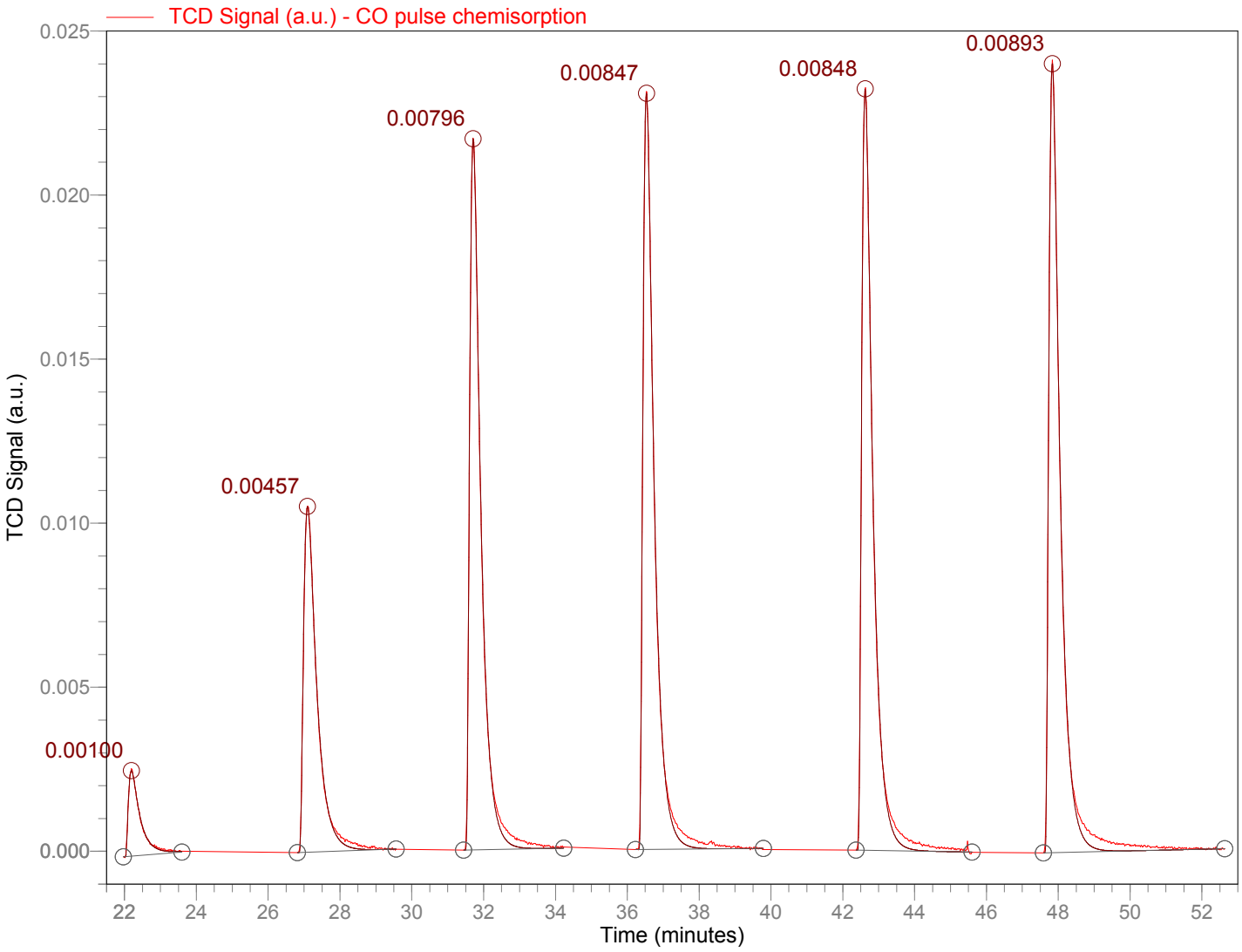

Sample: after 061_CO pulse chemisorption 10 wt% Ru/MgO
File: E:\RESEARCH\CHEMIS~1\REPORT~1\DATA\FANG-062.SMP

Started: 4/23/2012 3:23:00PM
Completed: 4/23/2012 6:09:01PM
Sample Mass: 0.0530 g
Report Time: 1/7/2013 2:18:00PM

Pulse Chemisorption Report

Experiment 1: CO pulse chemisorption

Analysis Type: Pulse Chemisorption
Calibration: None
Measured Flow Rate: 25.00 mL STP/min
Signal Offset: -0.00555
Signal Inverted: No

Peak Table

Peak Number	Temperature at Maximum (°C)	Volume Adsorbed (mL/g STP)	Cumulative Volume (mL/g STP)
1*	24.4	0.53872	4.20582
2	24.2	0.14372	4.34954
3	24.2	0.05308	4.40262
4	24.3	0.04270	4.44532
5	24.1	0.01957	4.46489
6	24.1	0.01869	4.48358
7	24.1	0.00096	4.48453
8	24.2	0.00000	4.48453

* 4 doses were completely adsorbed with a cumulative volume of 3.66710 mL/g.

Pulse Chemisorption Analysis Summary

Element	Percent of Sample Mass (%)	Atomic Weight	Stoichiometry Factor	Atomic Cross-Sectional Area (nm²)	Density (g/cm³)
Ru	10.0000	101.070	1.000	0.0613	12.400

Active Loop Volume at 25.0 °C: 0.04859 mL STP
Cumulative Volume: 4.48453 mL/g STP
Metal Dispersion: 20.2218%
Metallic Surface Area: 7.3871 m²/g sample
Metallic Surface Area: 73.8705 m²/g metal
Active Particle Diameter: 6.5503 nm

Sample: after 061_CO pulse chemisorption 10 wt% Ru/MgO
File: E:\RESEARCH\CHEMIS~1\REPORT~1\DATA\FANG-062.SMP

Started: 4/23/2012 3:23:00PM
Completed: 4/23/2012 6:09:01PM

Sample Mass: 0.0530 g
Report Time: 1/7/2013 2:18:00PM

TCD Signal (a.u.) vs. Time

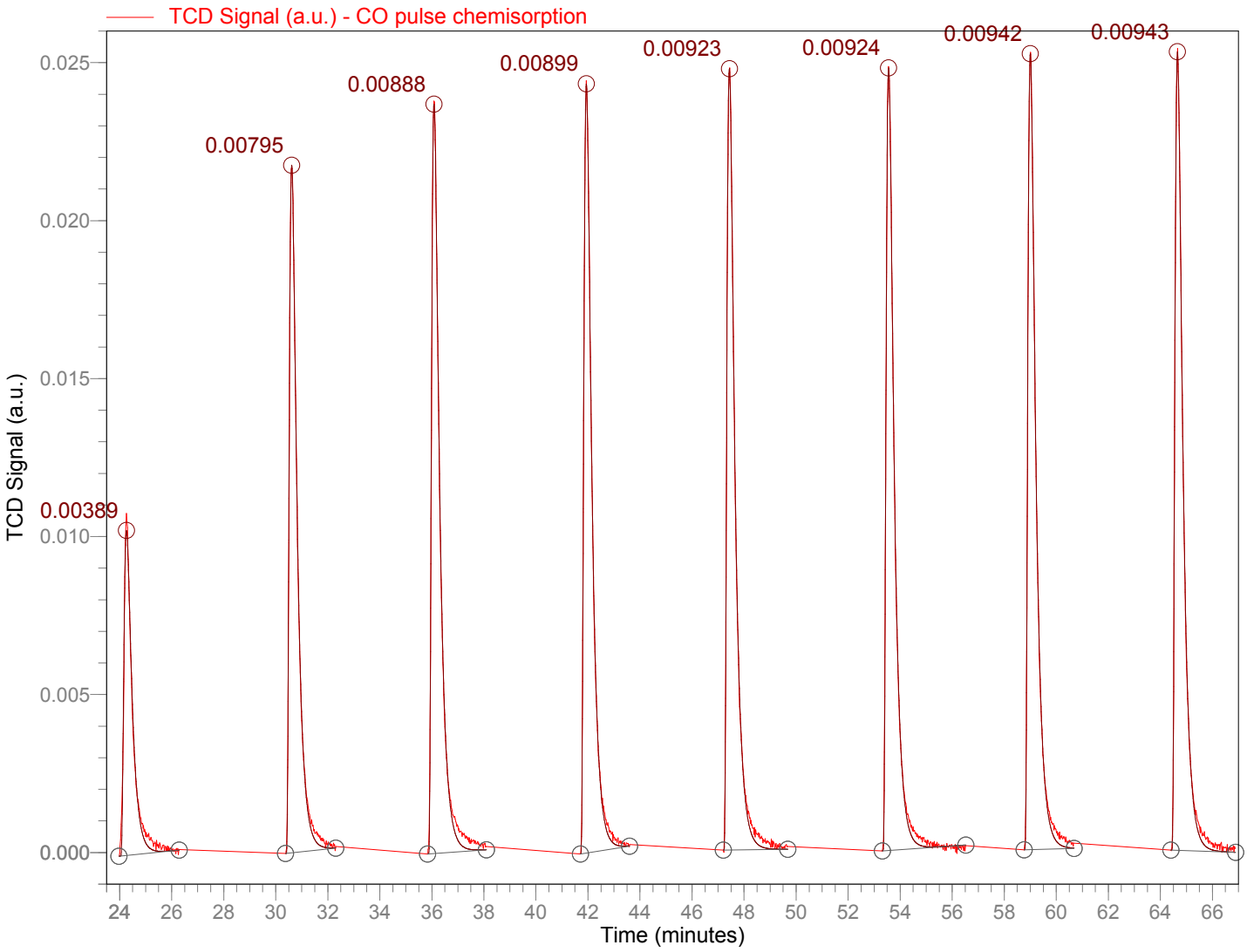

Brooklyn College The City University of New York 44 Ru 45 Rh 46 Pd Inorganic Chemistry Laboratory

Hydrogenation of benzene over Ru/MgO

catalyst	100.0 mg = 0.047 mmol Ru	metal loading: 5.0% metal dispersion: 28.4%
substrate	5.7 mL = 64 mmol PhH	ρ(PhH) = 0.876 g/mL, MW(Tol) = 78
n(sub)/n(Ru_s)	4781	
rxn condition	25 mL THF, 120 °C, 10 atm, w/ 1 h incubation	
analysis	column: SP-2330, high polarity	column temp: 40 °C

Reaction course of hydrogenation of benzene over 5 wt% Ru/MgO

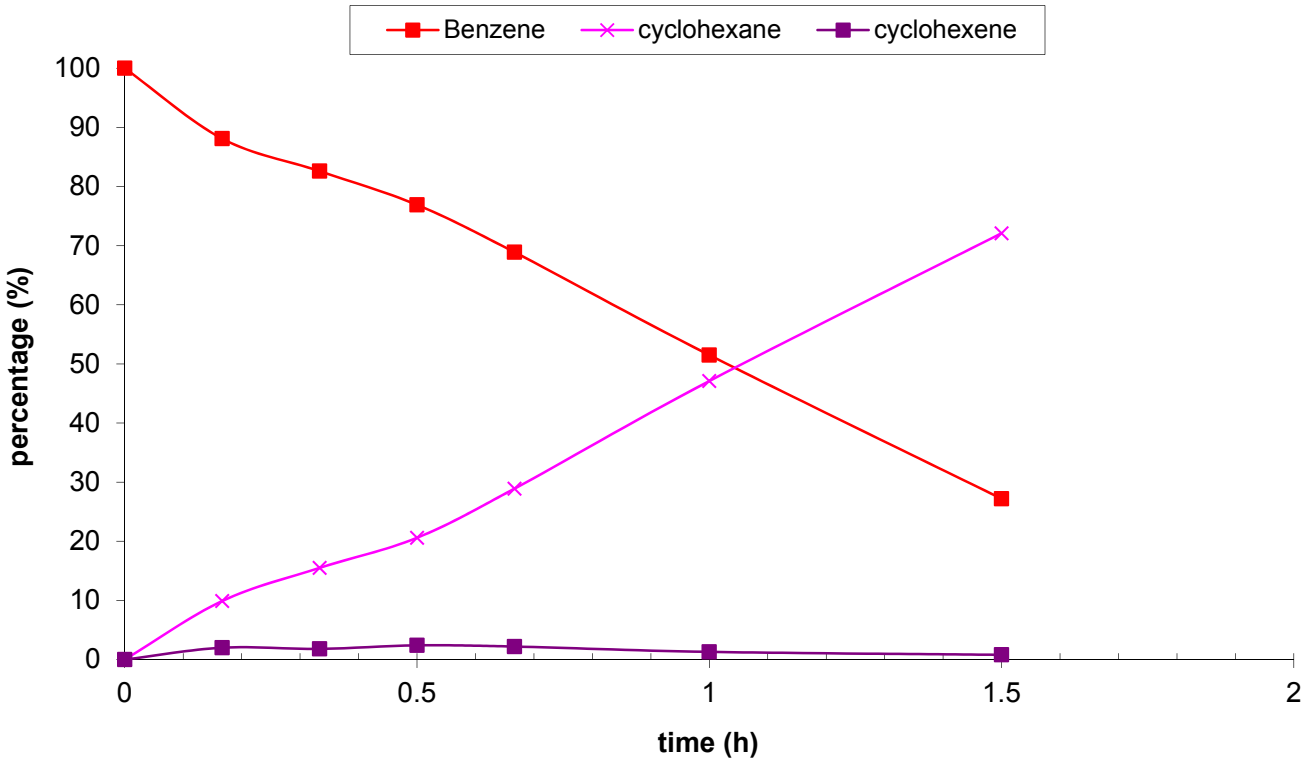

TON vs time

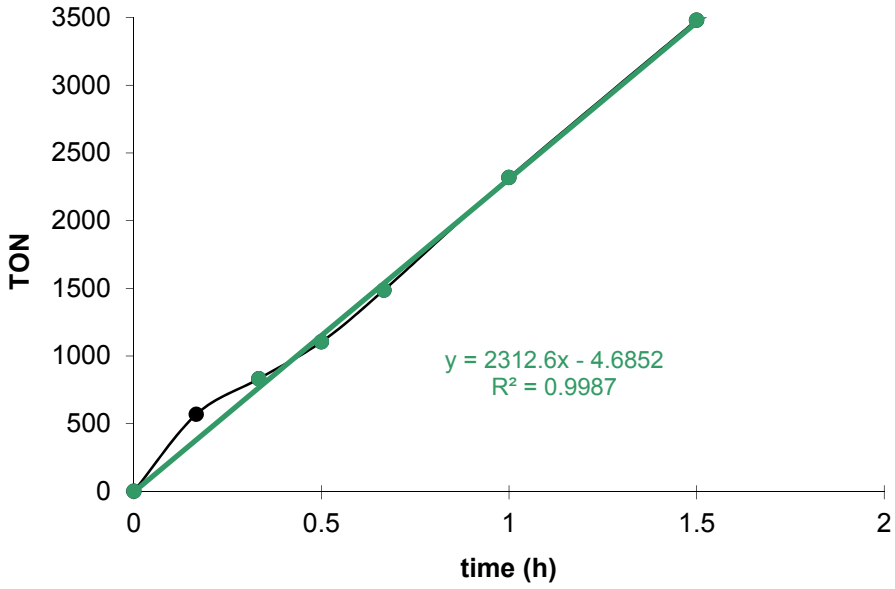

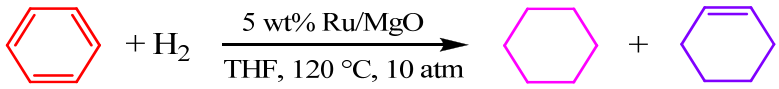

	r.t. /min →							
sample	time /min	/h	CyH%	cy-ene%	PhH%	[PhH] (mol/L)		TON
0	0	0	0	0	100	2.13	100	0
1	10	0.17	9.9	2	88.1	1.88		569
2	20	0.33	15.5	1.8	82.6	1.76		832
3	30	0.50	20.6	2.4	76.9	1.64		1104
4	40	0.67	28.9	2.2	68.9	1.47		1487
5	60	1.00	47.1	1.3	51.5	1.10		2319
6	90	1.50	72.1	0.8	27.2	0.58		3480
7								4781
8								
9								
10								
11								

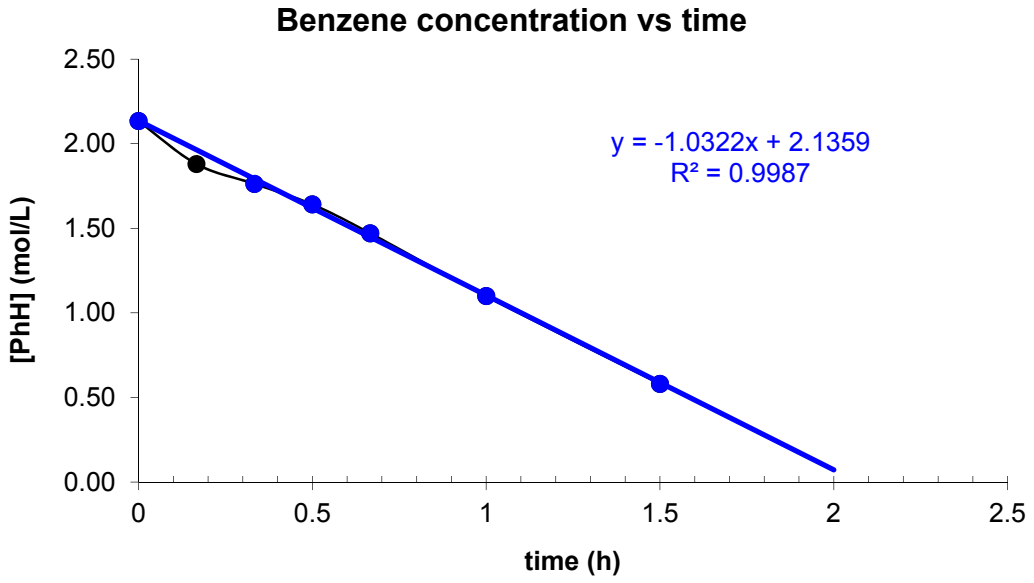

t½ 1.0 h

Brooklyn College The City University of New York 44 Ru 45 Rh 46 Pd Inorganic Chemistry Laboratory

Hydrogenation of toluene over Ru/MgO

catalyst	100.0 mg = 0.047 mmol Ru	metal loading: 5.0% metal dispersion: 28.4%
substrate	5.7 mL = 54 mmol Tol	ρ(Tol) = 0.867 g/mL, MW(Tol) = 92
n(sub)/n(Ru_s)	4012	
rxn condition	25 mL THF, 120 °C, 10 atm, w/ 1 h incubation	
analysis	column: SP-2330, high polarity	column temp: 50 °C

Reaction course of hydrogenation of toluene over 5 wt% Ru/MgO

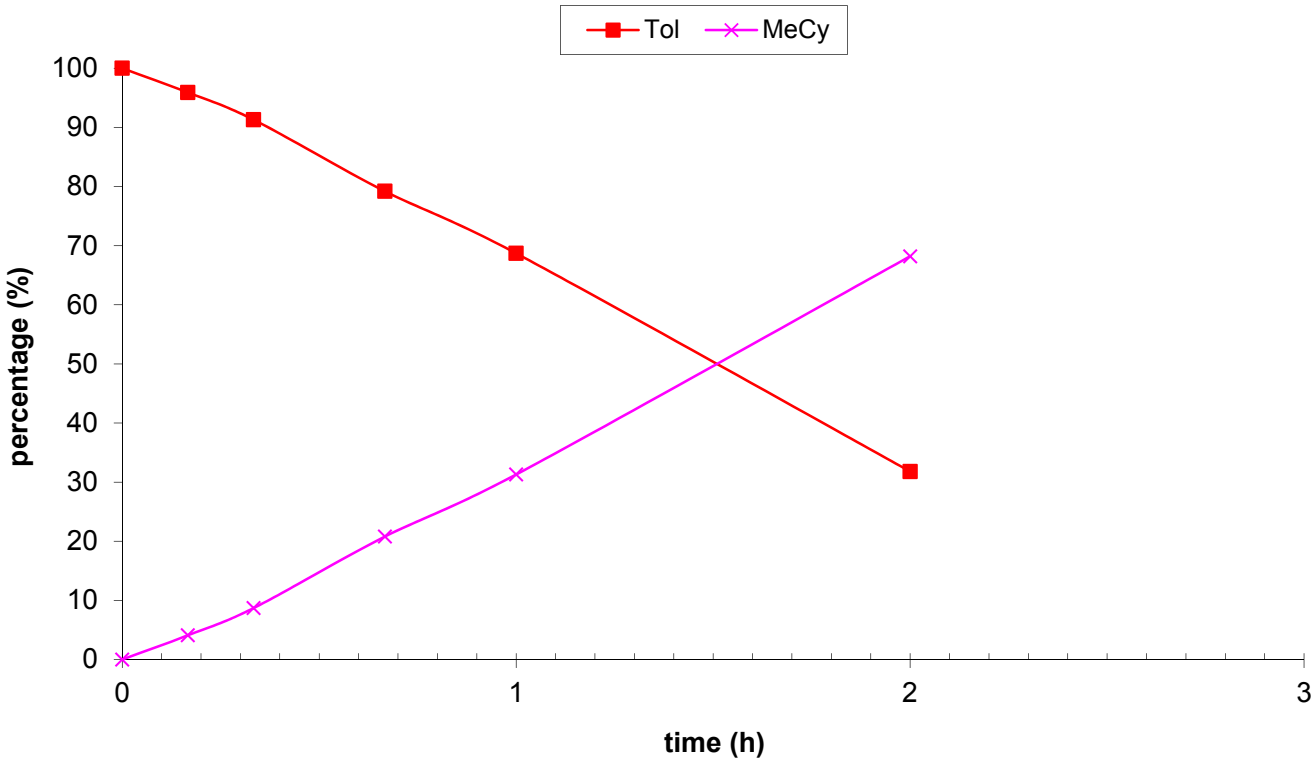

TON vs time

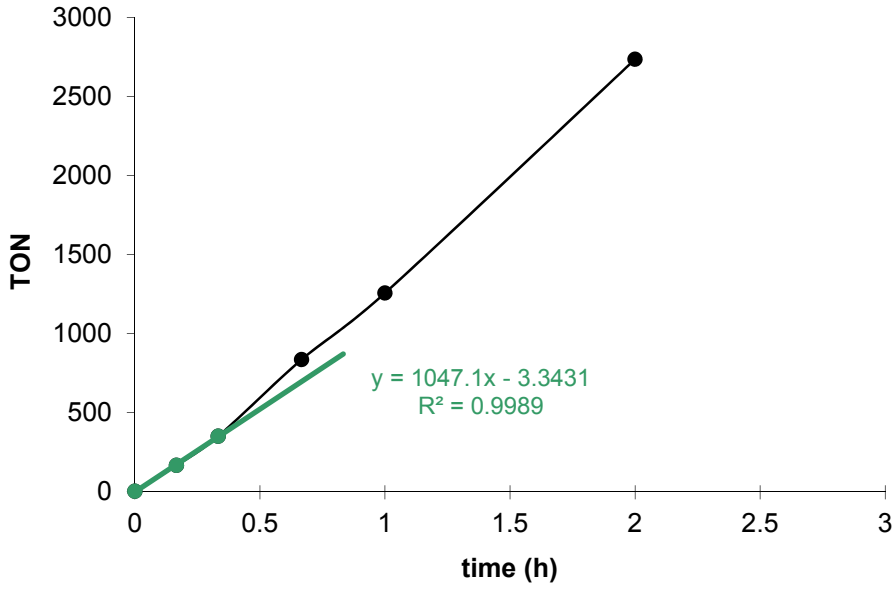

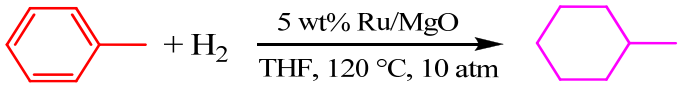

	r.t. /min →							
sample	time /min	/h	MeCy%		Tol%	[Tol] (mol/L)		TON
0	0	0	0		100	1.79	100	0
1	10	0.17	4.1		95.9	1.72		164
2	20	0.33	8.7		91.3	1.63		349
3	40	0.67	20.8		79.2	1.42		834
4	60	1.00	31.3		68.7	1.23		1256
5	120	2.00	68.2		31.8	0.57		2736
6								4012
7								4012
8								
9								
10								
11								

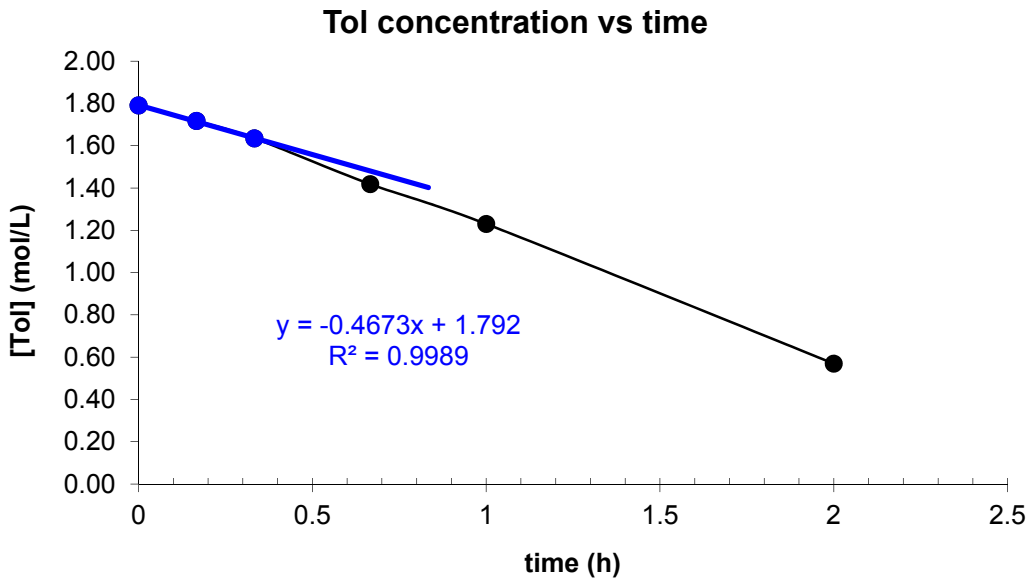

t½ 1.5

Hydrogenation of toluene over 5 wt% Ru/MgO(s)

catalyst	100.0 mg = 0.047 mmol Ru	metal loading: 5.0% metal dispersion: 22.5%
substrate	5.7 mL = 54 mmol Tol	ρ(Tol) = 0.867 g/mL, MW(Tol) = 92
n(sub)/n(Ru_s)	5064	
rxn condition	25 mL THF, 120 °C, 10 atm, w/ 1 h incubation	
analysis	column: SP-2330, high polarity column temp: 50 °C	

Reaction course of hydrogenation of toluene over 5 wt% Ru/MgO(s)

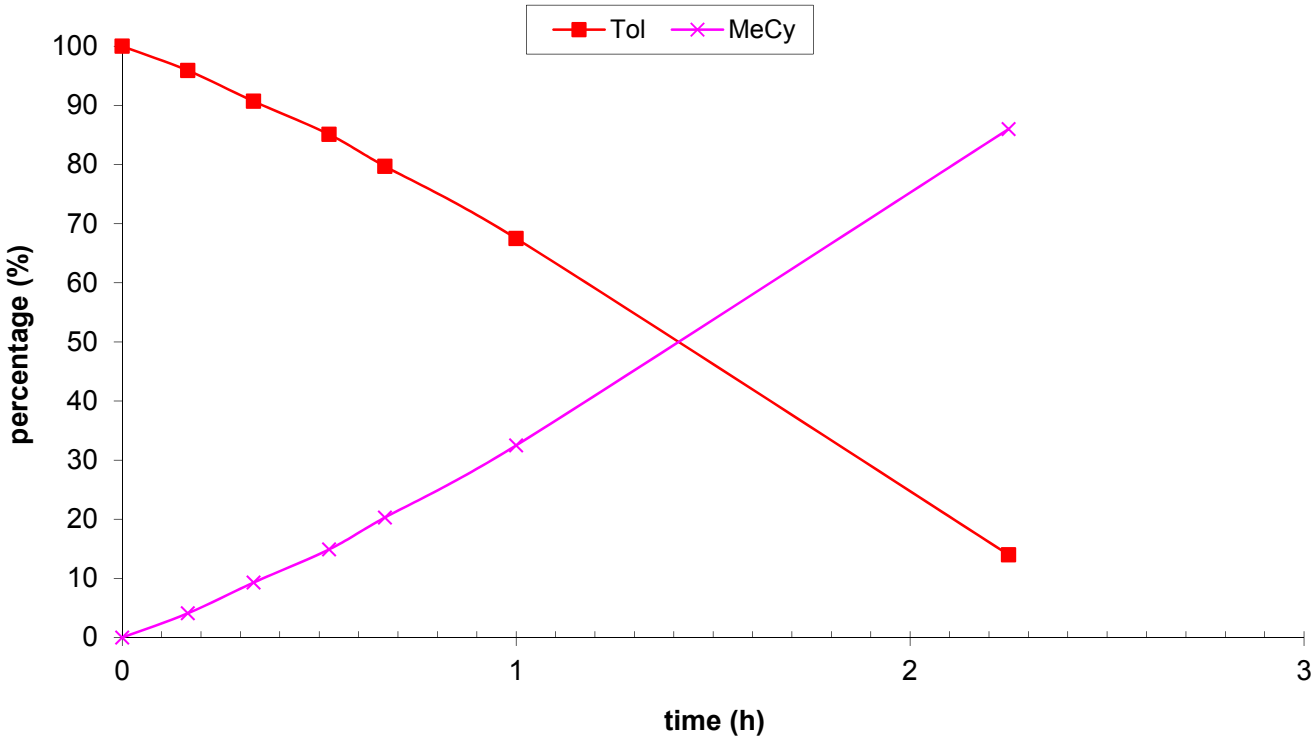

TON vs time

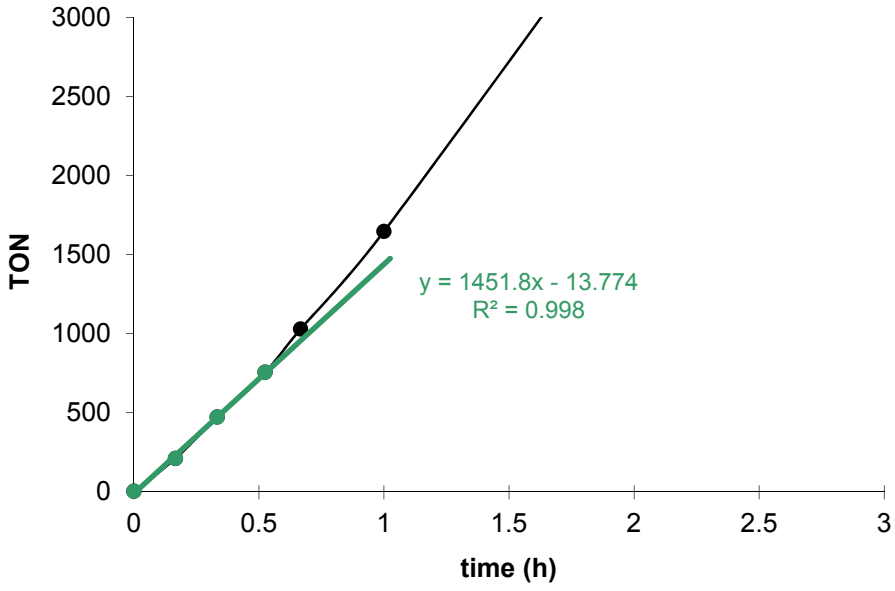

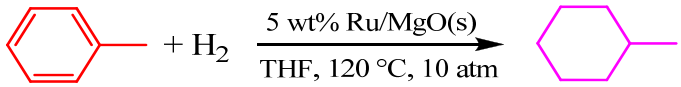

	r.t. /min	→						
sample	time /min	/h	MeCy%		Tol%	[Tol] (mol/L)		TON
0	0	0	0		100	1.79	100	0
1	10	0.17	4.1		95.9	1.72		208
2	20	0.33	9.3		90.7	1.62		471
3	31.5	0.53	14.9		85.1	1.52		754
4	40	0.67	20.3		79.7	1.43		1028
5	60	1.00	32.5		67.5	1.21		1646
6	135	2.25	86.0		14.0	0.3		4355
7								5064
8								
9								
10								
11								

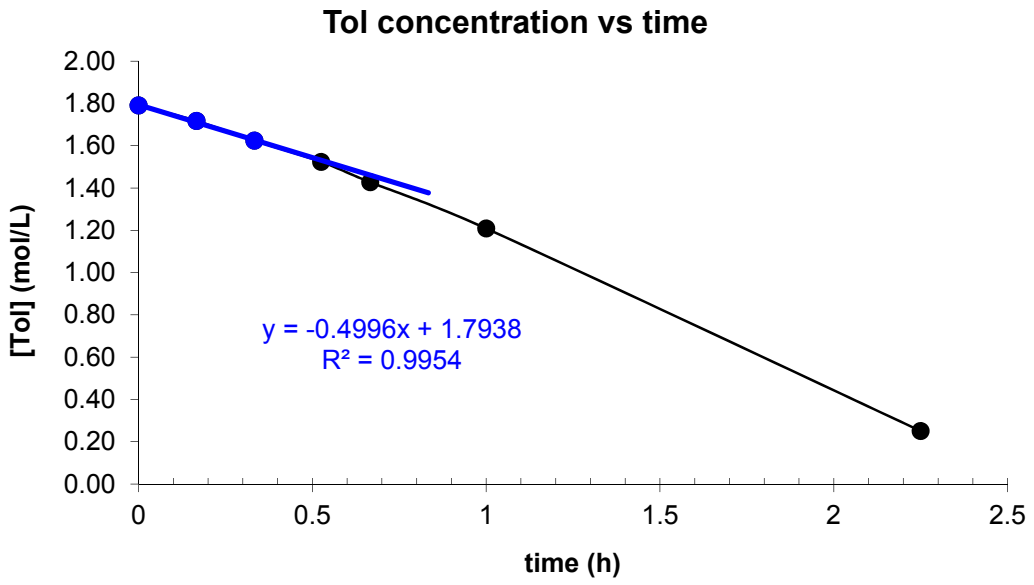

t½

Hydrogenation of *m*-xylene over Ru/MgO

catalyst	100.0 mg = 0.047 mmol Ru	metal loading: 5.0% metal dispersion: 28.4%
substrate	5.7 mL = 46 mmol	ρ(*m*-xylene) = 0.86 g/mL, MW(Tol) = 106
n(sub)/n(Ru_s)	3454	
rxn condition	25 mL THF, 120 °C, 10 atm, w/ 1 h incubation	
analysis	column: SP-2330, high polarity	column temp: 40 °C

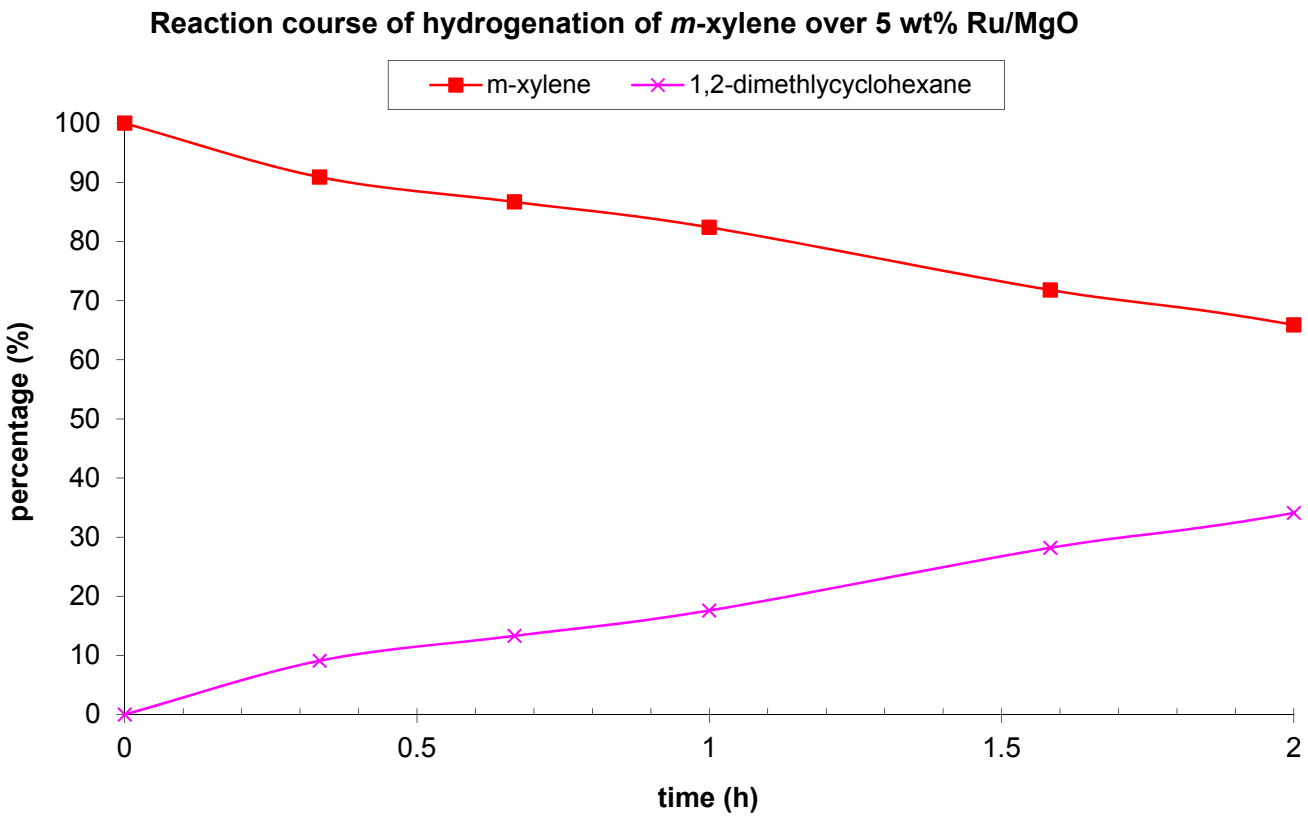

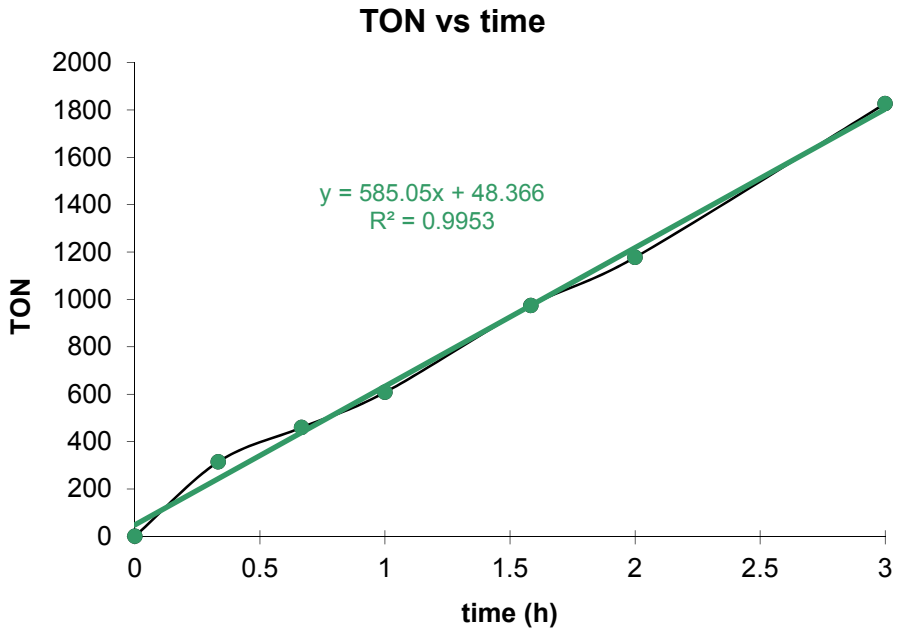

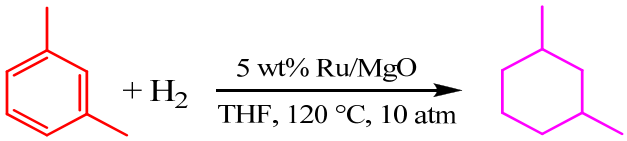

	r.t. /min →							
sample	time /min	/h	DMCy%		*m*-xylene%	[*m*-xylene] (mol/L)		TON
0	0	0	0		100	1.54	100	0
1	20	0.33	9.1		90.9	1.40		314
2	40	0.67	13.3		86.7	1.34		459
3	60	1.00	17.6		82.4	1.27		608
4	95	1.58	28.2		71.8	1.11		974
5	120	2.00	34.1		65.9	1.02		1178
6	180	3.00	52.9		47.1	0.73		1827
7								3454
8								
9								
10								
11								

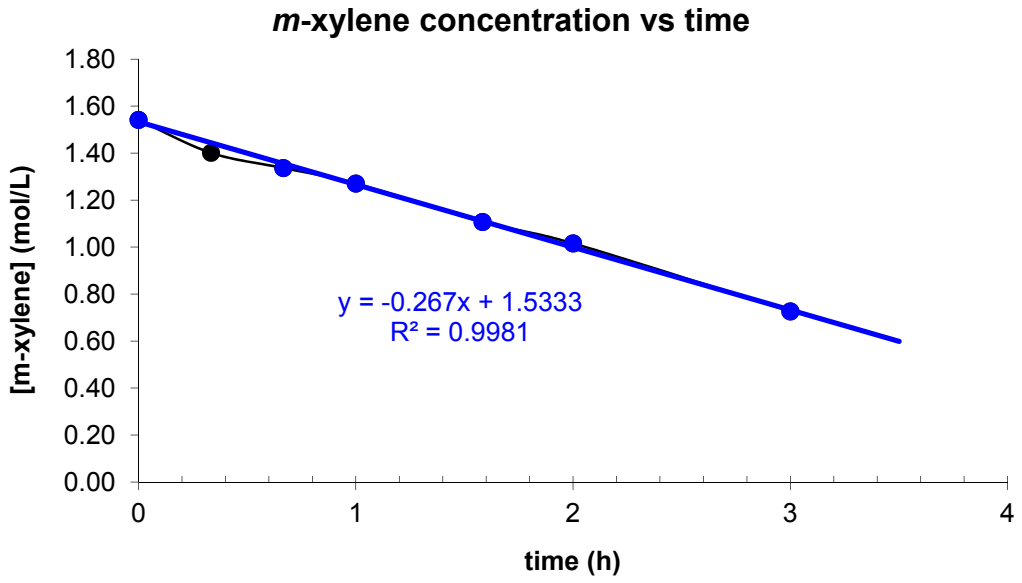

t½ 2.9 h

Hydrogenation of mesitylene over Ru/MgO

catalyst	100.0 mg = 0.047 mmol Ru	metal loading: 5.0% metal dispersion: 28.4%
substrate	5.7 mL = 41 mmol	ρ(mesitylene) = 0.864 g/mL, MW(Tol) = 120
n(sub)/n(Ru_s)	3065	
rxn condition	25 mL THF, 120 °C, 10 atm, w/ 1 h incubation	
analysis	column: SP-2330, high polarity	column temp: 40 °C

Reaction course of hydrogenation of mesitylene over 5 wt% Ru/MgO

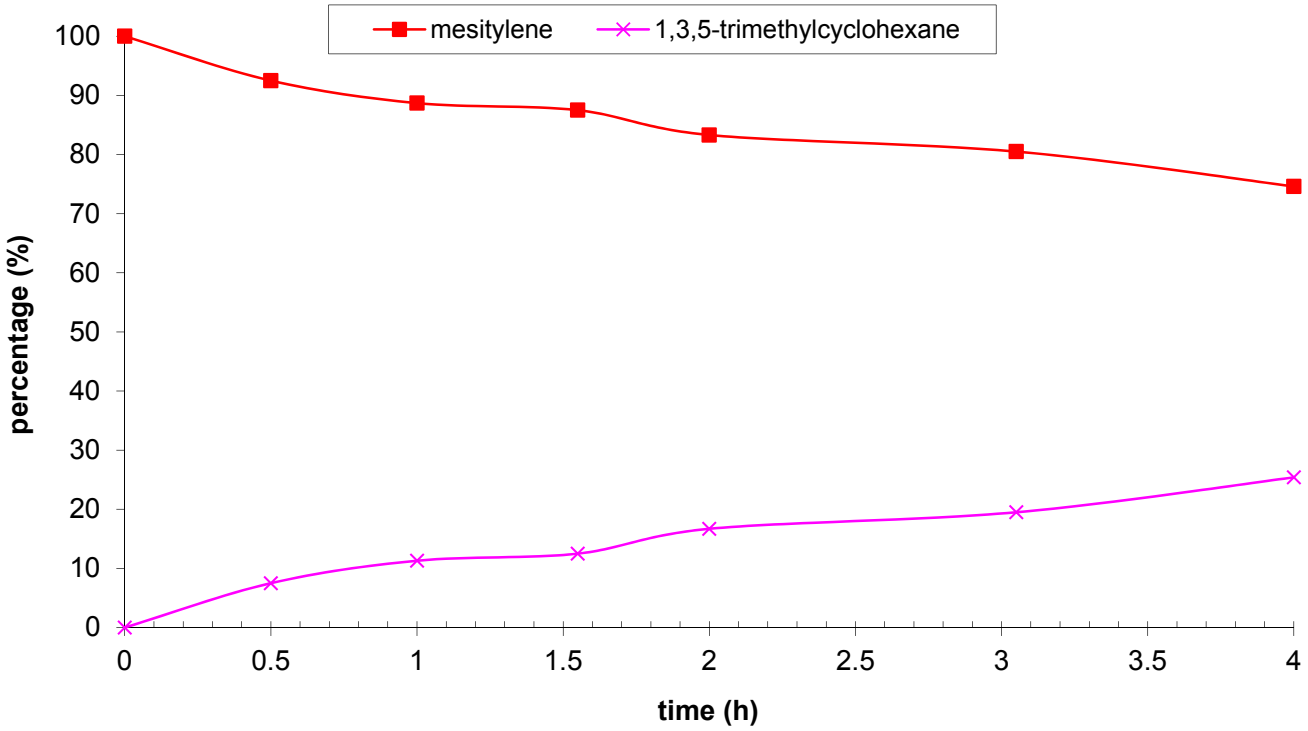

TON vs time

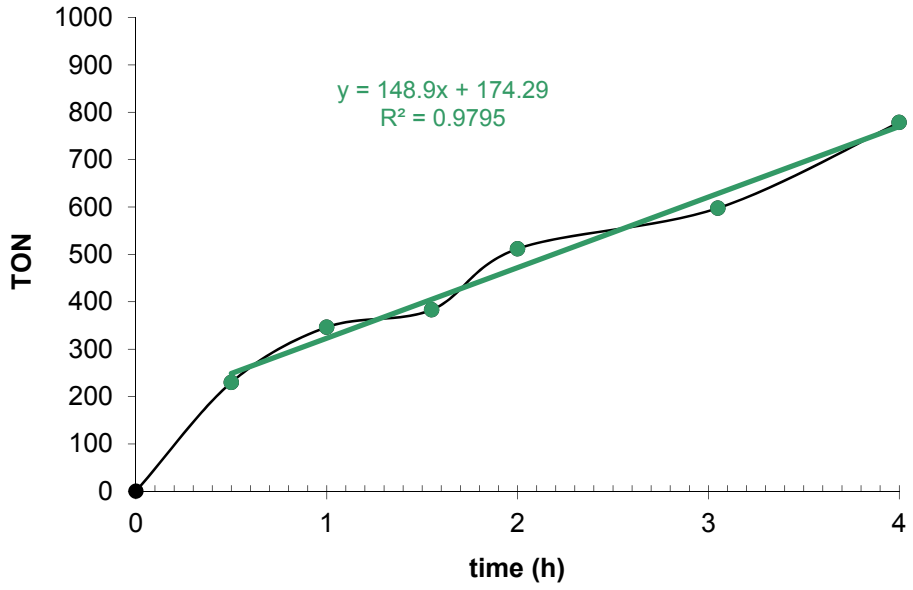

*first 10 min: T not stabilized, went up to 126°C

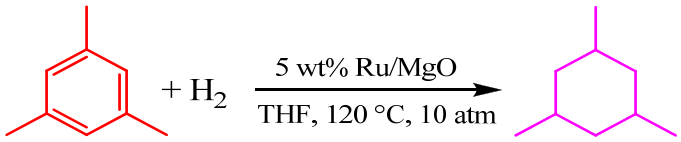

	r.t. /min	→						
sample	time /min	/h	triMeCyH%		mesitylene%	[mesitylene] (mol/L)		TON
0	0	0	0		100	1.37	100	0
1	30	0.50	7.5		92.5	1.27		230
2	60	1.00	11.3		88.7	1.21		346
3	93	1.55	12.5		87.5	1.20		383
4	120	2.00	16.7		83.3	1.14		512
5	183	3.05	19.5		80.5	1.10		598
6	240	4.00	25.4		74.6	1.02		779
7								3065
8								
9								
10								
11								

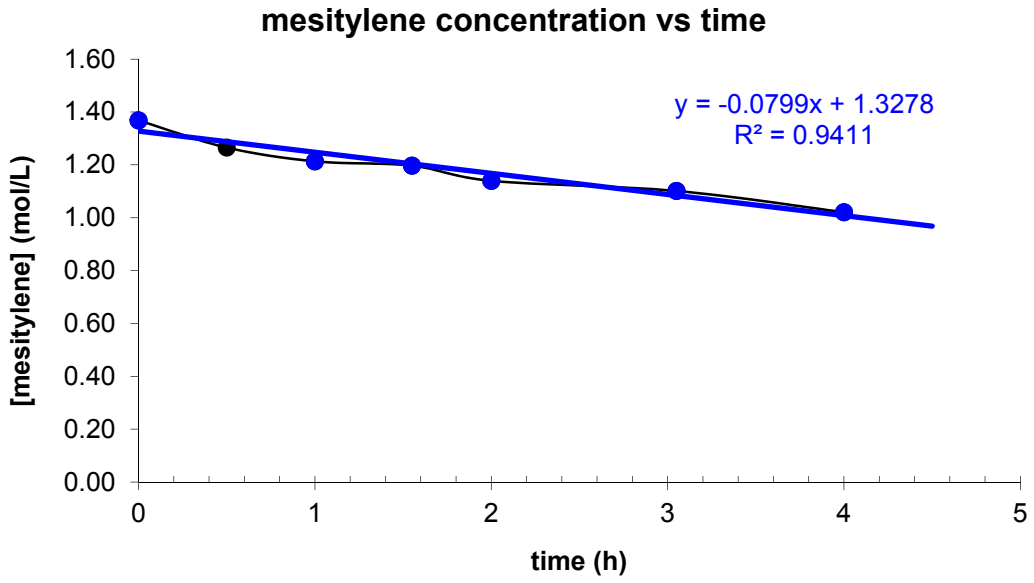

t½ 8.0 h estimated

Hydrogenation of naphthalene over Ru/MgO

catalyst	50.0	mg =	0.024	mmol Ru	metal loading: 5.0%	metal dispersion: 28.4%	
substrate	0.62	g =	4.8	mmol naph	MW(naph) = 128		
n(sub)/n(Ru_s)	723						
rxn condition	30 mL THF, 150 °C, 50 atm, w/ 1 h incubation				50 °C/min		
analysis	column: SP-2330, high polarity				column temp:	50 °C 8 min;150 °C 5 min;200 °C 4 min.	

Reaction course of hydrogenation of naphthalene over 5 wt% Ru/MgO

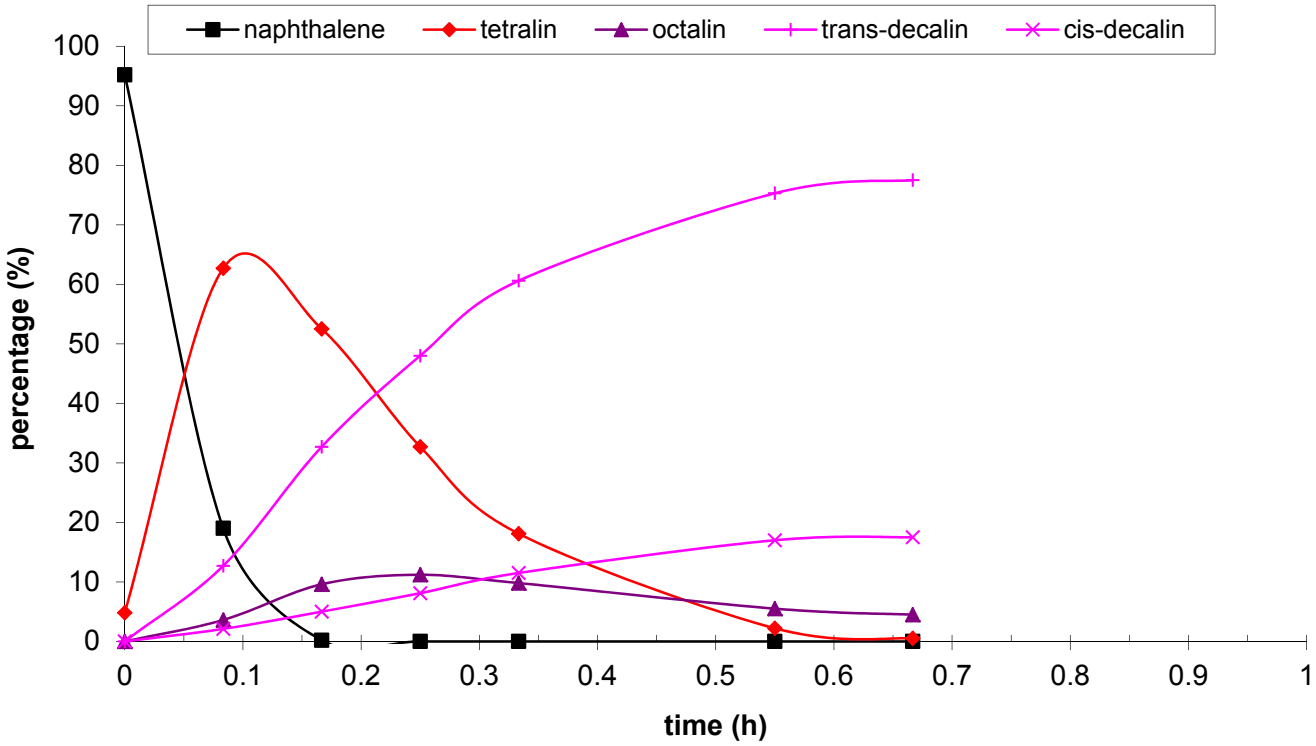

TON vs time

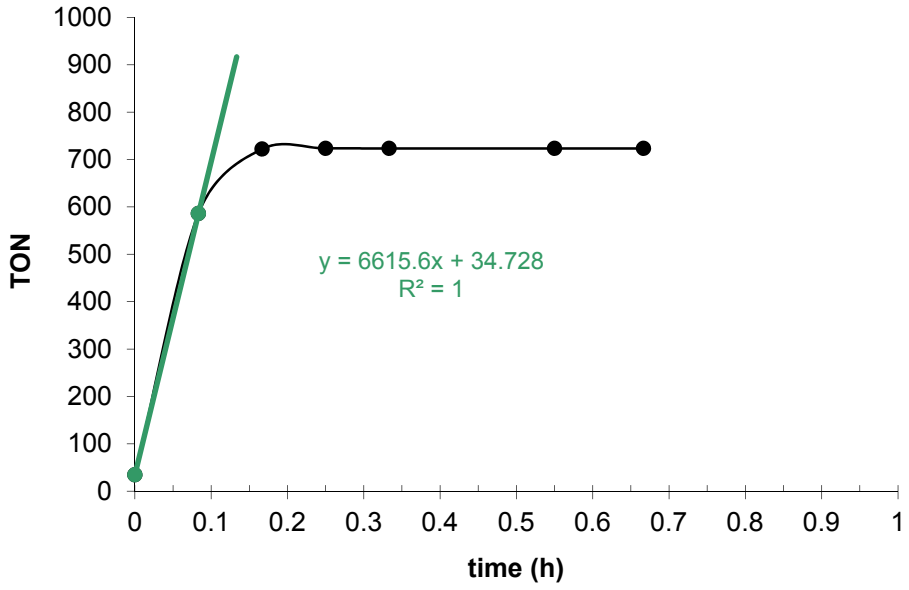

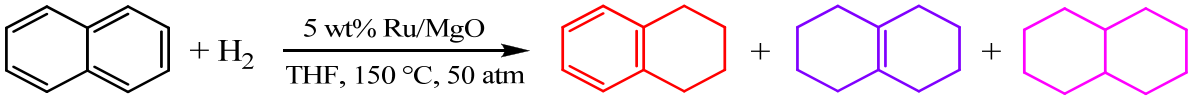

	r.t. /min	→	4.6	6.6	8.2	10.9	12.6		
sample	time /min	/h	*cis* -decalin	*trans* -decalin	octalin	tetralin	naph	[naph] (mol·L^{-1})	TON(naph)
0	0	0	0	0	0	4.8	95.2	0.15	35
1	5	0.08	2.1	12.7	3.6	62.7	19.0	0.03	586
2	10	0.17	5.0	32.7	9.6	52.5	0.2	0.00	722
3	15	0.25	8.1	48.0	11.2	32.7	0.0	0.00	723
4	20	0.33	11.5	60.6	9.8	18.1	0.0	0.00	723
5	33	0.55	17.0	75.3	5.5	2.2	0.0	0.00	723
6	40	0.67	17.5	77.5	4.5	0.5	0.0	0.00	723
7									
8									
9									
10									
11									

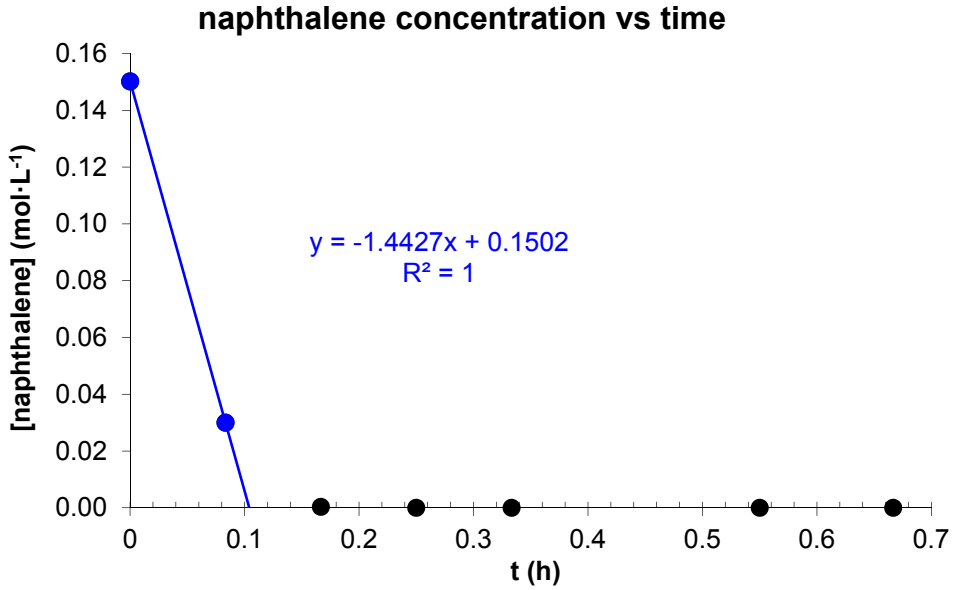

Hydrogenation of anthracene over Ru/MgO

catalyst	50.0 mg = 0.024 mmol Ru	metal loading: 5.0%	metal dispersion: 28.4%
substrate	0.86 g = 4.8 mmol An	MW(An) = 178	*low solubility of An in THF*
n(sub)/n(Ru_s)	722		
rxn condition	30 mL THF, 150 °C, 50 atm, w/o incubation	10 °C/min; 10 °C/min.	
analysis	column: SP-2330, high polarity	column temp:	150 °C 5 min; 180 °C 10min; 200 °C 5 min.

Reaction course of hydrogenation of anthracene over 5 wt% Ru/MgO

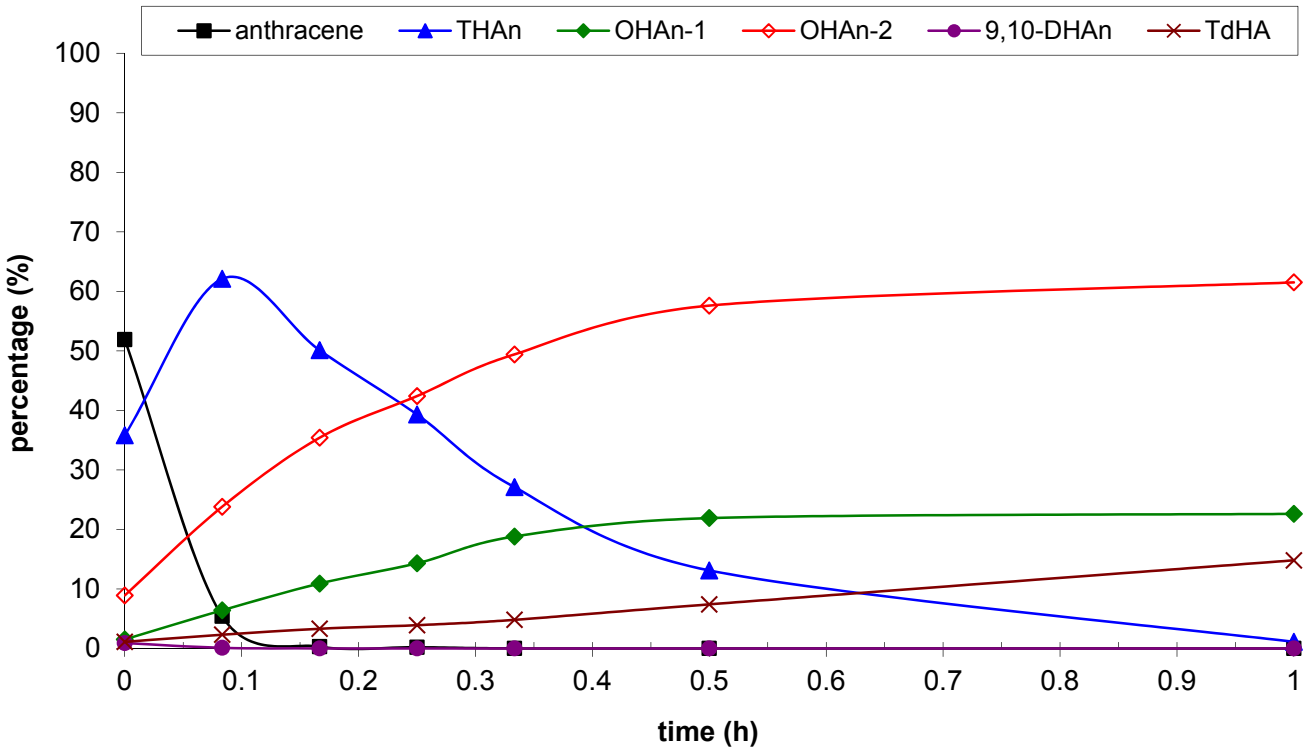

TON vs time

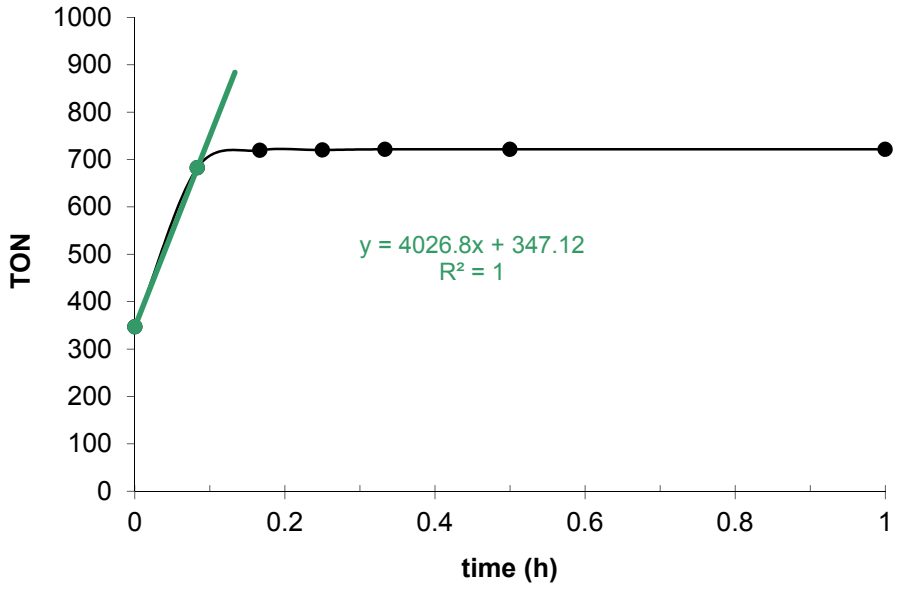

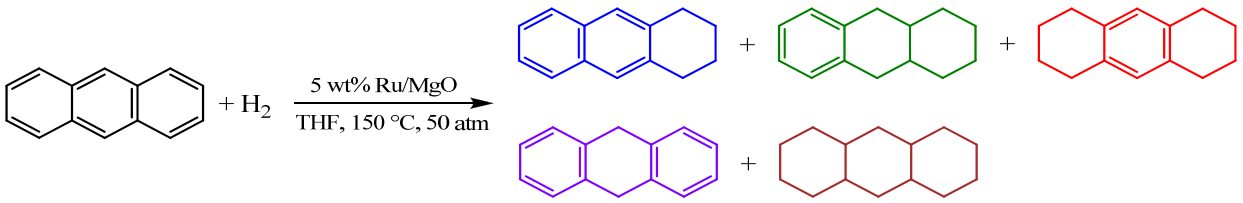

	r.t. /min	→	2.4 & 2.7	6.1	7.4	12.2	14.9	20.3		
sample	t /min	/h	TdHAn	OHAn-1	OHAn-2	THAn	9,10-DHAn	An	[An] (mol·L^{-1})	TON(An)
0	0	0	1.1	1.5	8.9	35.8	0.9	51.9	0.08	347
1	5	0.08	2.3	6.4	23.8	62.1	0.1	5.4	0.01	683
2	10	0.17	3.3	10.9	35.4	50.1	0.0	0.3	0.00	719
3	15	0.25	3.9	14.3	42.4	39.3	0.0	0.2	0.00	720
4	20	0.33	4.8	18.8	49.4	27.1	0.0	0.0	0.00	722
5	30	0.50	7.4	21.9	57.6	13.1	0.0	0.0	0.00	722
6	60	1.00	14.8	22.6	61.5	1.1	0.0	0.0	0.00	722
7										
8										
9										
10										
11										

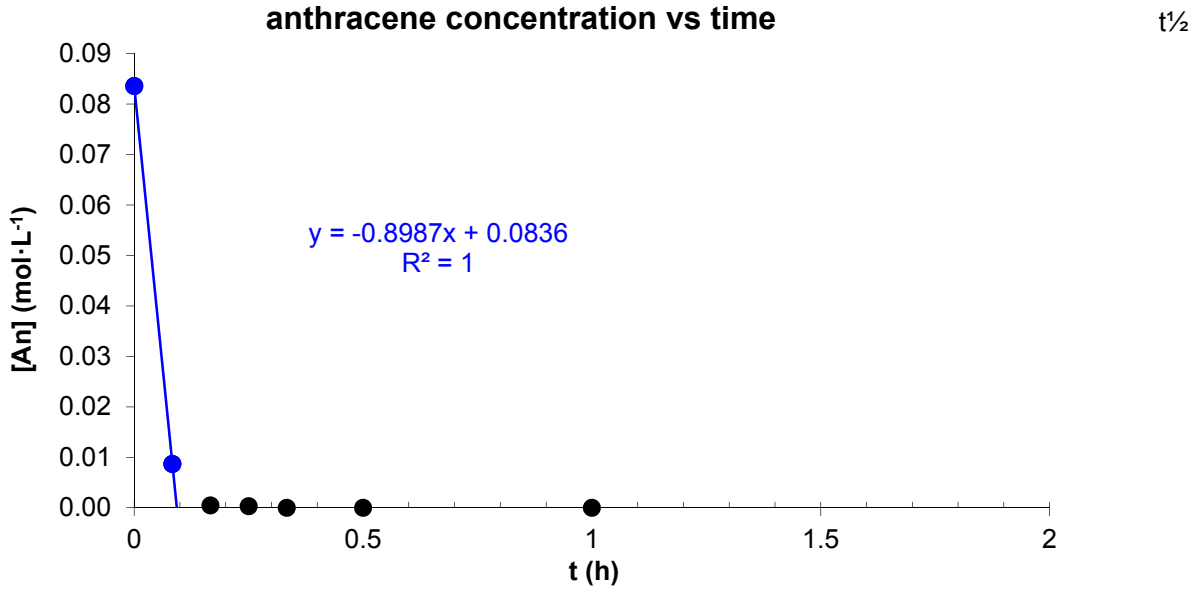

Hydrogenation of pyrrole over Ru/MgO

catalyst	100.0 mg = 0.047 mmol Ru	metal loading: 5.0% metal dispersion: 28.4%
substrate	5.7 mL = 82 mmol	ρ(pyrrole) = 0.967 g/mL, MW(pyrrole) = 67
n(sub)/n(Ru_s)	6144	
rxn condition	25 mL THF, 150 °C, 50 atm, w/ 1 h incubation	
analysis	column: SE-30	column temp: 80 °C

Reaction course of hydrogenation of pyrrole over 5 wt% Ru/MgO

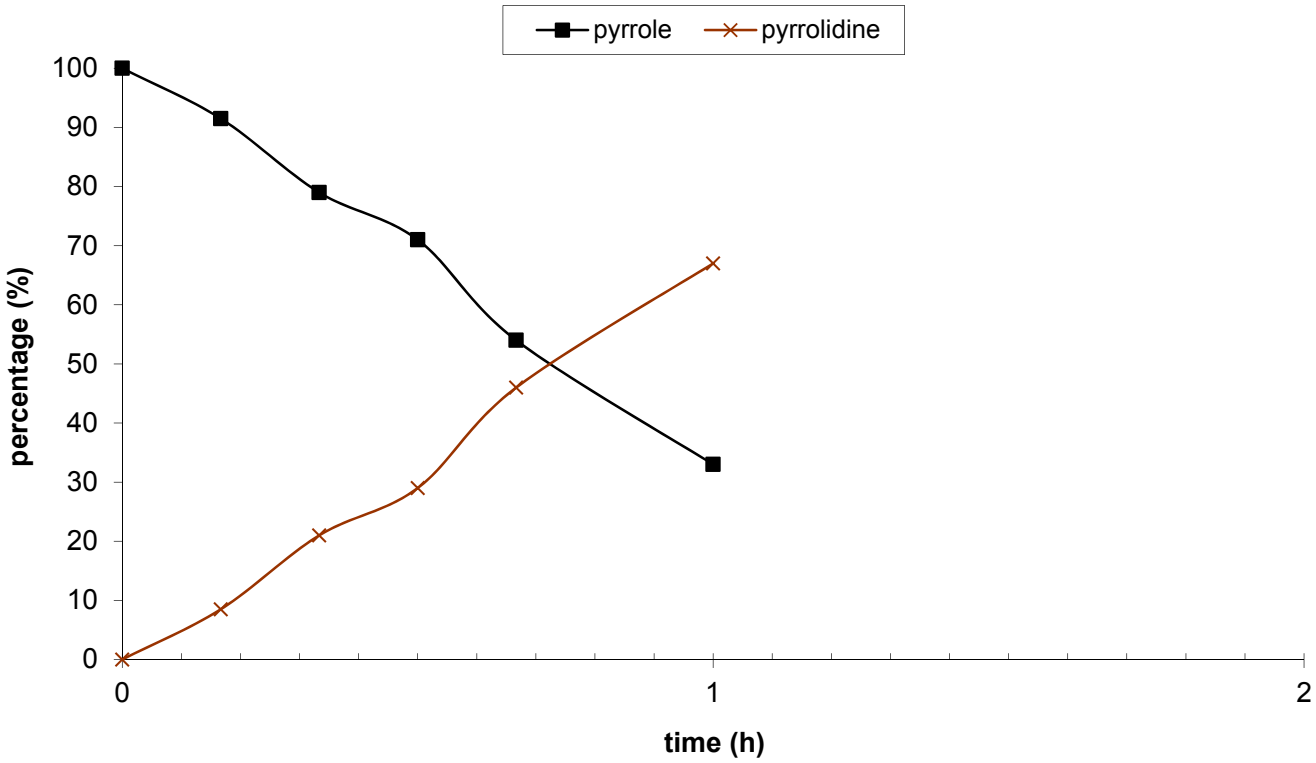

TON vs time

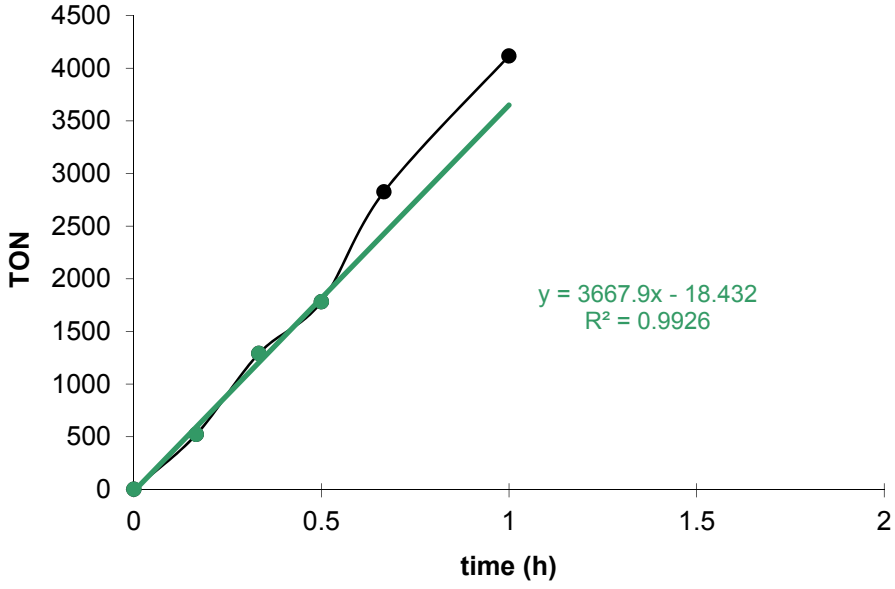

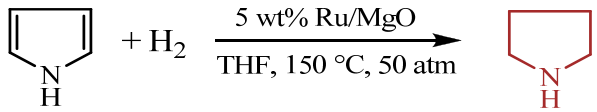

	r.t. /min	→	5		5.5			
sample	time /min	/h	pyrrolidine%		pyrrole%	[pyrrole] (mol/L)		TON
0	0	0	0		100	2.68	100	0
1	10	0.17	8.5		91.5	2.45		522
2	20	0.33	21.0		79.0	2.12		1290
3	30	0.50	29.0		71.0	1.90		1782
4	40	0.67	46.0		54.0	1.45		2826
5	60	1.00	67.0		33.0	0.88		4116
6								6144
7								6144
8								
9								
10								
11								

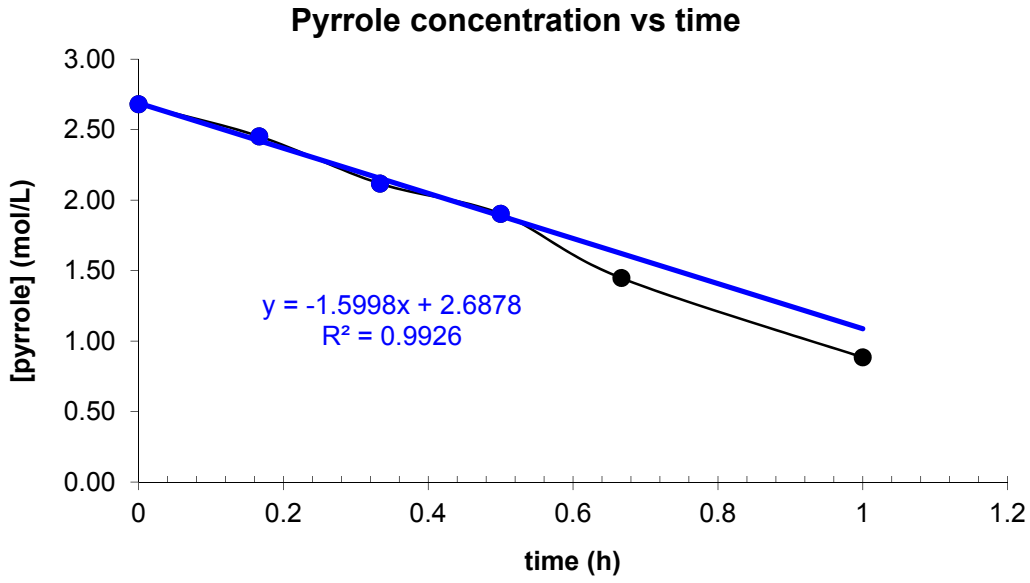

t½ 0.7

Hydrogenation of indole over Ru/MgO

catalyst	50.0	mg =	0.024	mmol Ru	metal loading: 5.0%	metal dispersion: 28.4%	
substrate	0.6	g =	4.8	mmol indole	MW(indole) = 117		
n(sub)/n(Ru_s)	715						
rxn condition	30 mL THF, 150 °C, 50 atm, w/ 1 h incubation				30 °C/min		
analysis	column: SP-2330, high polarity				column temp:	120 °C 5 min;150 °C 5 min;180 °C 8 min.	

Reaction course of hydrogenation of indole over 5 wt% Ru/MgO

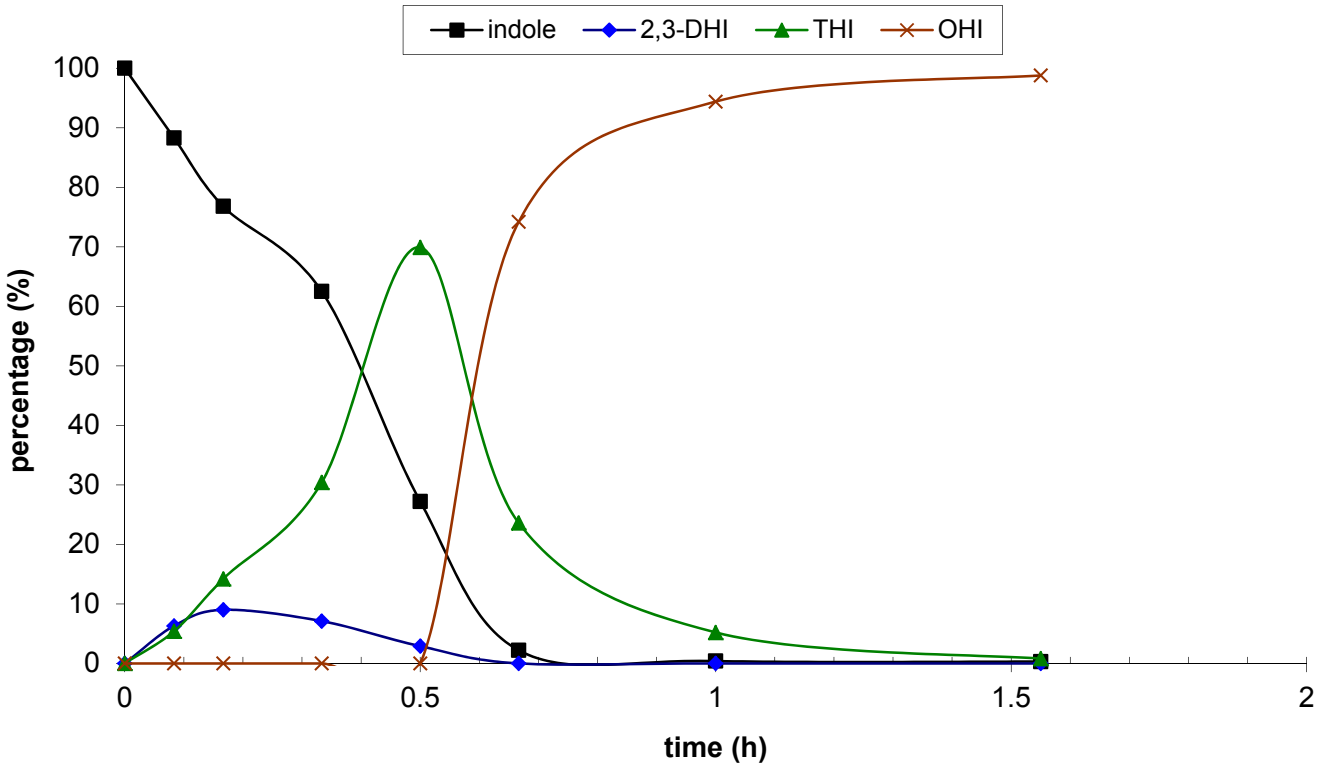

TON vs time

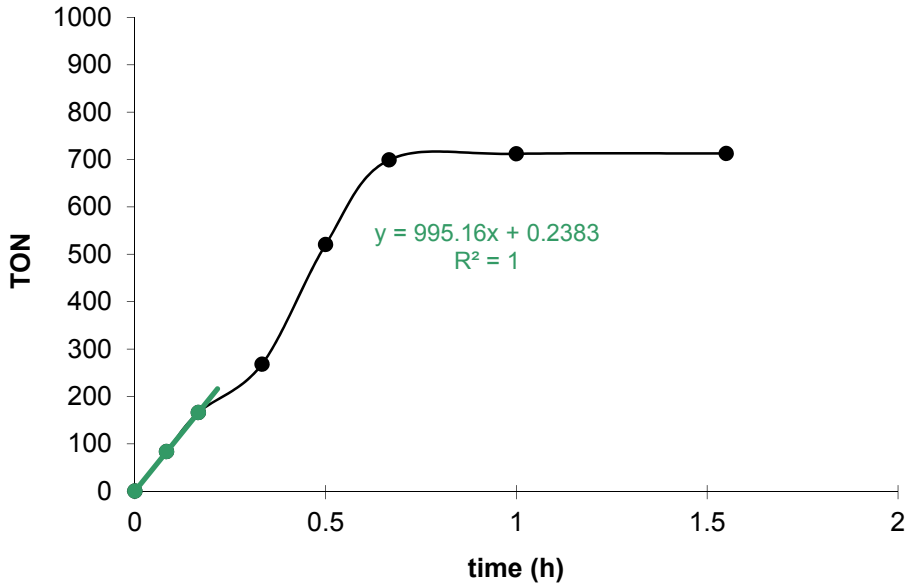

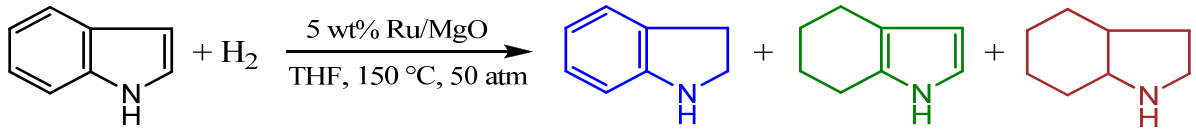

	r.t. /min	→	3.3 & 3.6	9.3	9.6	17.9		
sample	time /min	/h	OHI%	2,3-DHI%	THI%	indole%	[I] (mol·L^{-1})	TON(I)
0	0	0	0	0	0	100	0.16	0
1	5	0.08	0.0	6.3	5.4	88.3	0.14	84
2	10	0.17	0.0	9.0	14.2	76.8	0.12	166
3	20	0.33	0.0	7.1	30.4	62.5	0.10	268
4	30	0.50	0.0	2.9	69.9	27.2	0.04	520
5	40	0.67	74.2	0.0	23.6	2.2	0.00	699
6	60	1.00	94.4	0.0	5.2	0.4	0.00	712
7	93	1.55	98.8	0.0	0.8	0.3	0.00	713
8								
9								
10								
11								

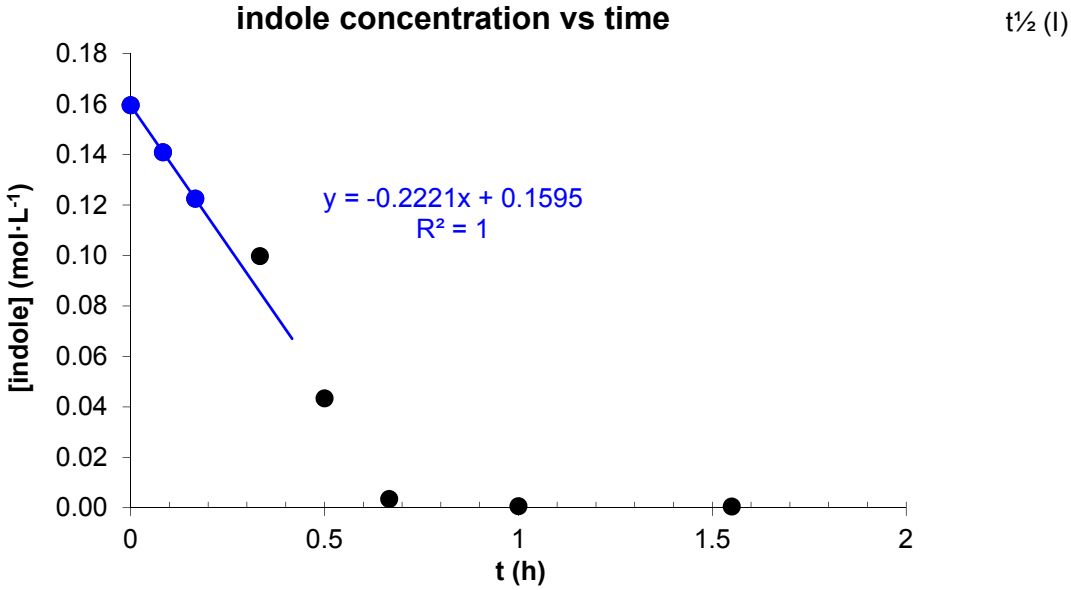

Hydrogenation of carbazole over Ru/MgO

catalyst	50.0 mg = 0.024 mmol Ru	metal loading: 5.0%	metal dispersion: 28.4%
substrate	0.80 g = 4.8 mmol A	MW(carbazole) = 167	
n(sub)/n(Ru_s)	716		
rxn condition	30 mL THF, 150 °C, 50 atm, w/ 1 h incubation	30 °C/min; 20 °C/min	
analysis	column: SP-2330, high polarity	column temp:	150 °C 5 min; 180 °C 5min; 200 °C 5min.

Reaction course of hydrogenation of carbazole over 5 wt% Ru/MgO

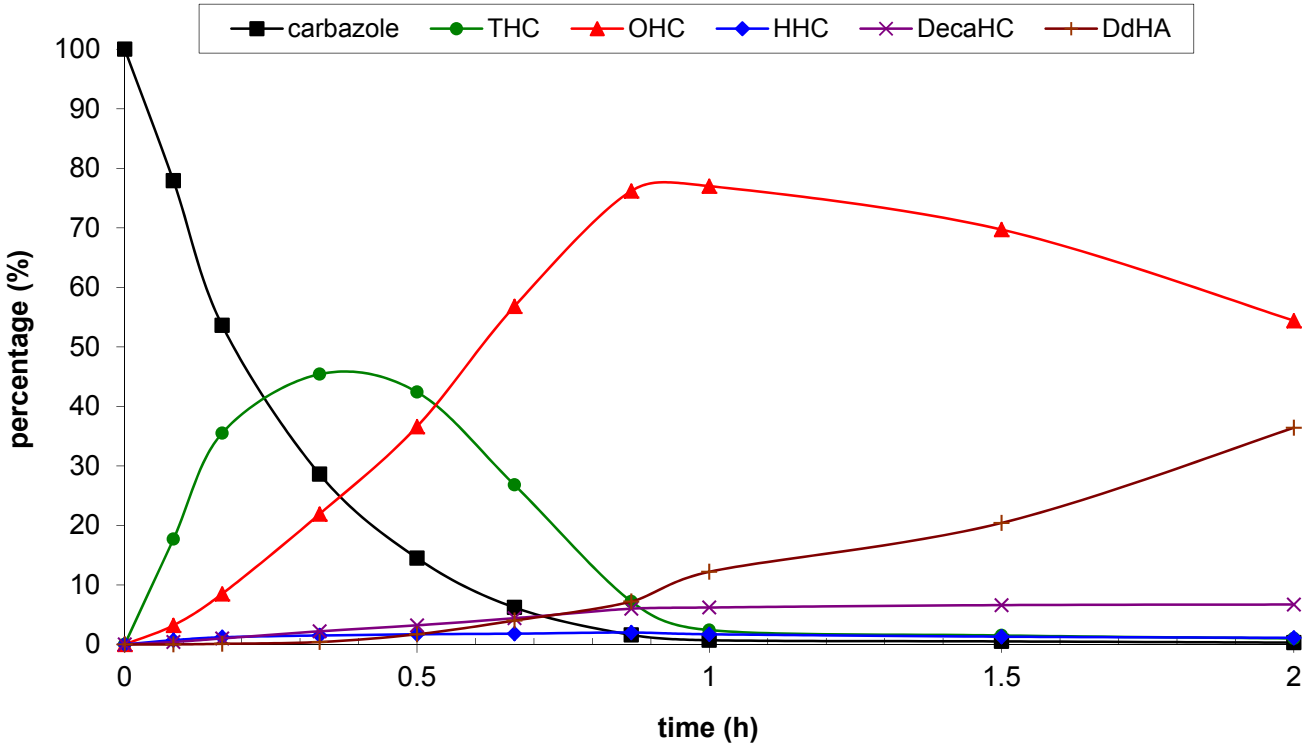

TON vs time

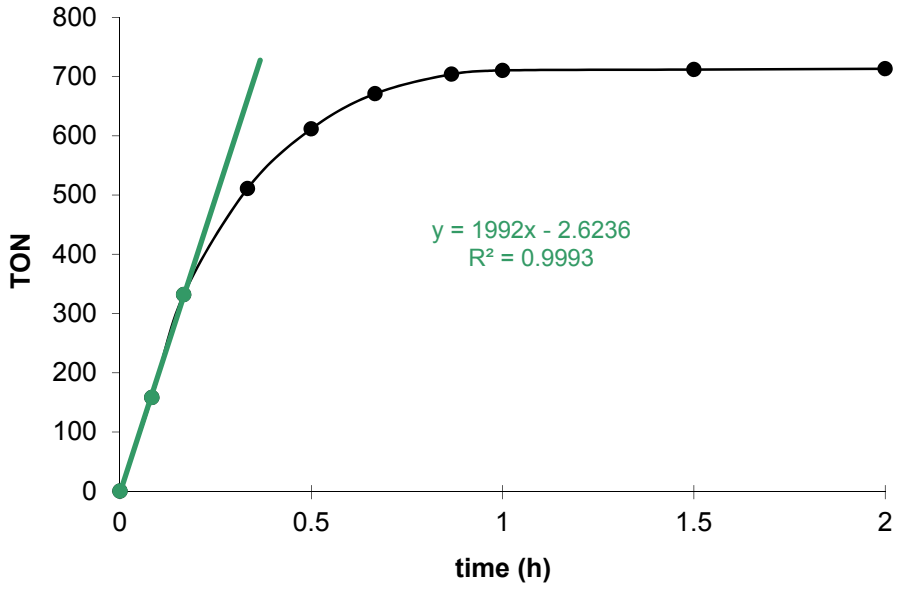

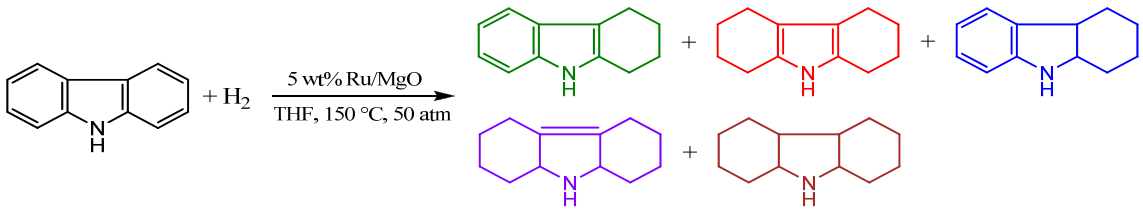

	r.t. /min	→	4.4	6	10 & 16.2	12.6	22.3	32.7		
sample	t /min	/h	DdHC	DecaHC	HHC	OHC	THC	C	[C] (mol·L^{-1})	TON(C)
0	0	0	0	0	0	0	0	100	0.16	0
1	5	0.08	0.0	0.4	0.7	3.2	17.7	77.9	0.12	158
2	10	0.17	0.1	1.0	1.2	8.5	35.5	53.6	0.09	332
3	20	0.33	0.4	2.2	1.5	21.9	45.4	28.6	0.05	511
4	30	0.50	1.7	3.2	1.7	36.6	42.4	14.5	0.02	612
5	40	0.67	4.0	4.4	1.8	56.8	26.8	6.2	0.01	671
6	52	0.87	7.2	6.0	2.0	76.2	7.2	1.6	0.00	704
7	60	1.00	12.2	6.2	1.7	77.0	2.4	0.7	0.00	711
8	90	1.50	20.4	6.6	1.3	69.7	1.5	0.5	0.00	712
9	120	2.00	36.4	6.7	1.1	54.4	1.0	0.3	0.00	713
10										
11										

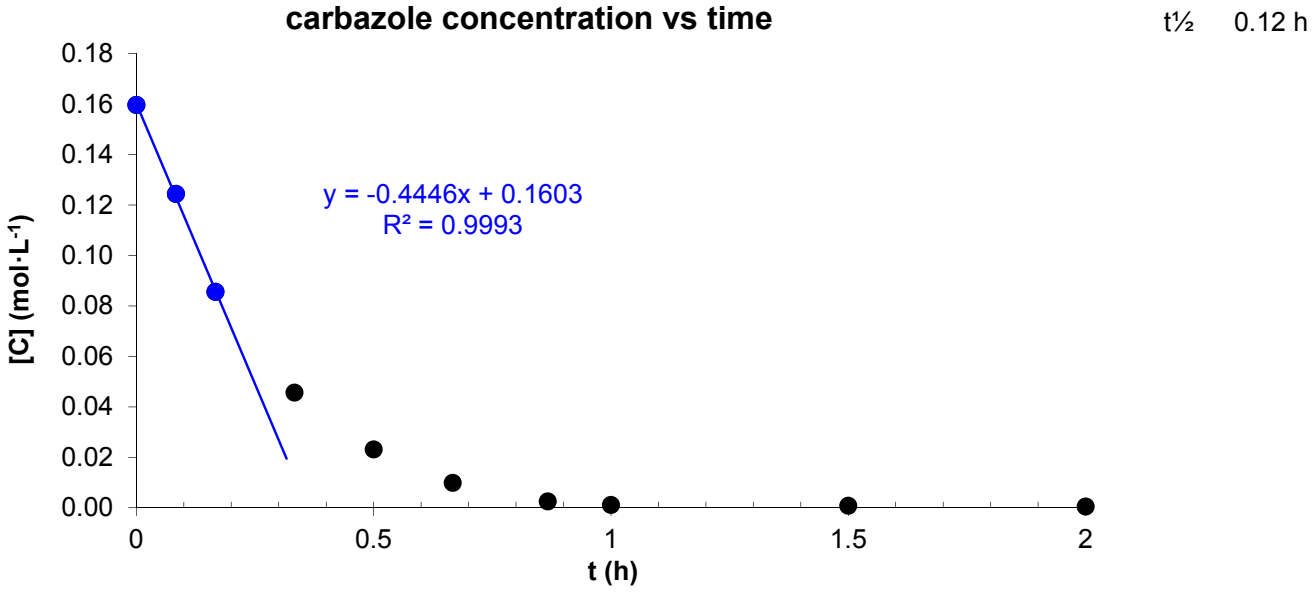

Brooklyn College The City University of New York | 44 Ru | 45 Rh | 46 Pd | Inorganic Chemistry Laboratory

Hydrogenation of pyridine over Ru/MgO

catalyst	100.0 mg = 0.047 mmol Ru	metal loading: 5.0% metal dispersion: 28.4%
substrate	3.9 mL = 48 mmol	ρ(py) = 0.982 g/mL, MW(py) = 79
n(sub)/n(Ru_s)	3621	
rxn condition	26 mL THF, 150 °C, 50 atm, w/ 1 h incubation	
analysis	column: SE-30	column temp: 80 °C

Reaction course of hydrogenation of pyridine over 5 wt% Ru/MgO

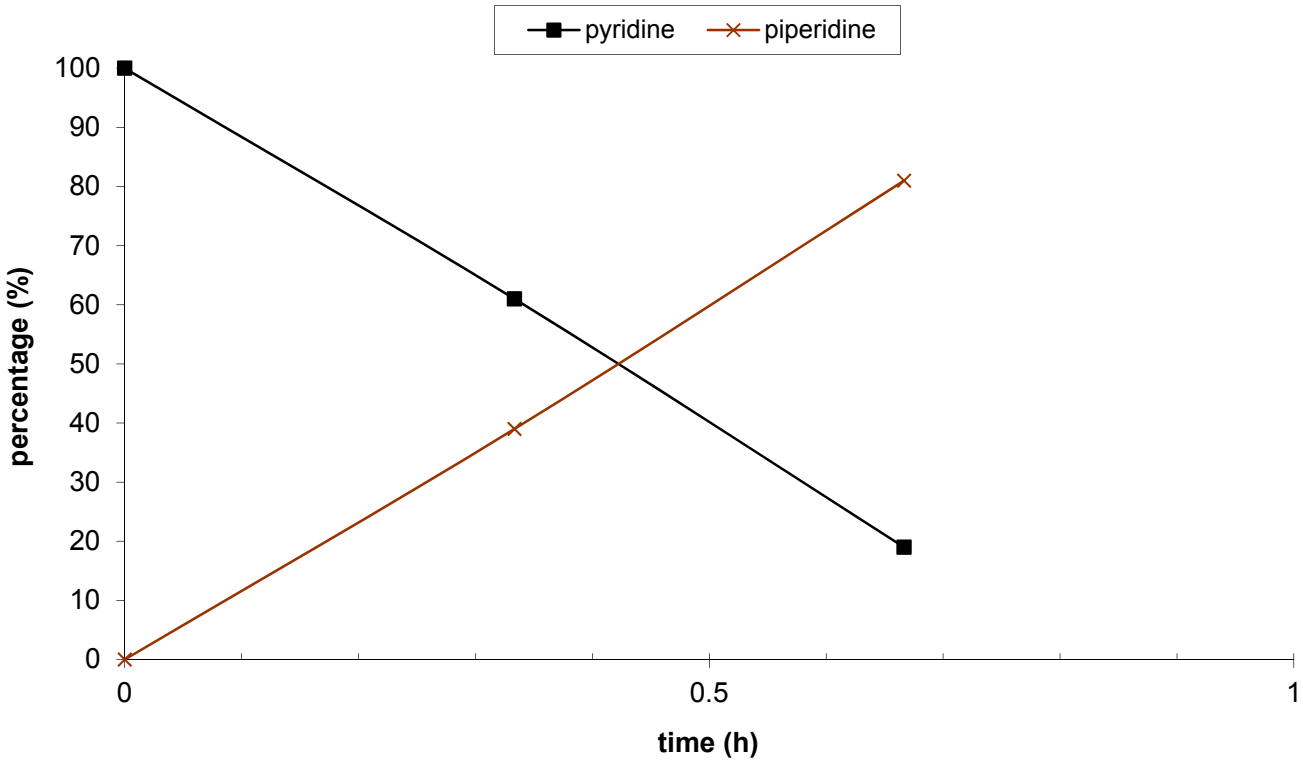

TON vs time

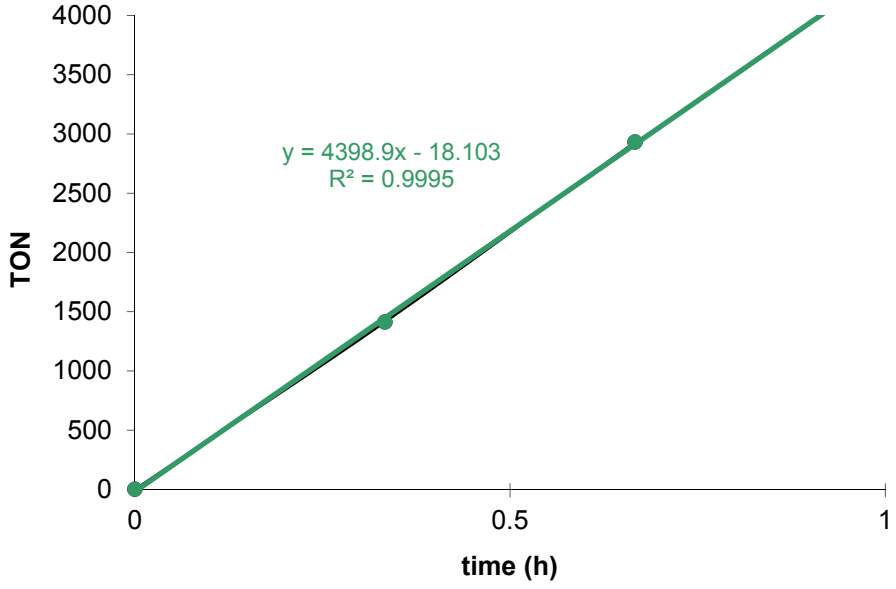

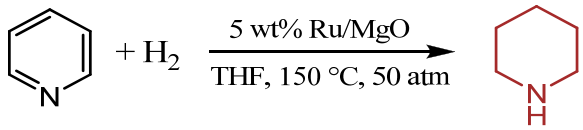

	r.t. /min	→	5.9		5.5			
sample	time /min	/h	piperidine%		pyridine%	[py] (mol/L)		TON
0	0	0	0		100	1.62	100	0
1	20	0.33	39.0		61.0	0.99		1412
2	40	0.67	81.0		19.0	0.31		2933
3	60	1.00	99.0		1.0	0.02		3584
4								
5								
6								
7								
8								
9								
10								
11								

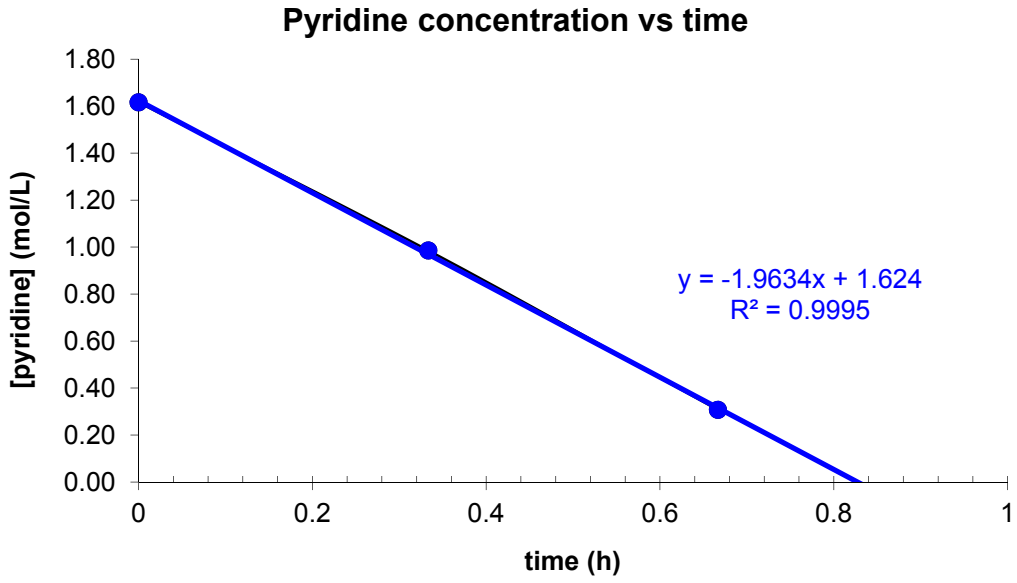

t½ 0.4

Hydrogenation of quinoline over Ru/MgO

catalyst	100.0 mg = 0.047 mmol Ru	metal loading: 5.0% metal dispersion: 28.4%
substrate	5.7 mL = 48 mmol Q	ρ(Q) = 1.09 g/mL, MW(Q) = 129
n(sub)/n(Ru_s)	3597	
rxn condition	25 mL THF, 150 °C, 50 atm, w/ 1 h incubation	
analysis	column: SP-2330, high polarity	column temp: 150 °C 10 min

Reaction course of hydrogenation of Q over 5 wt% Ru/MgO

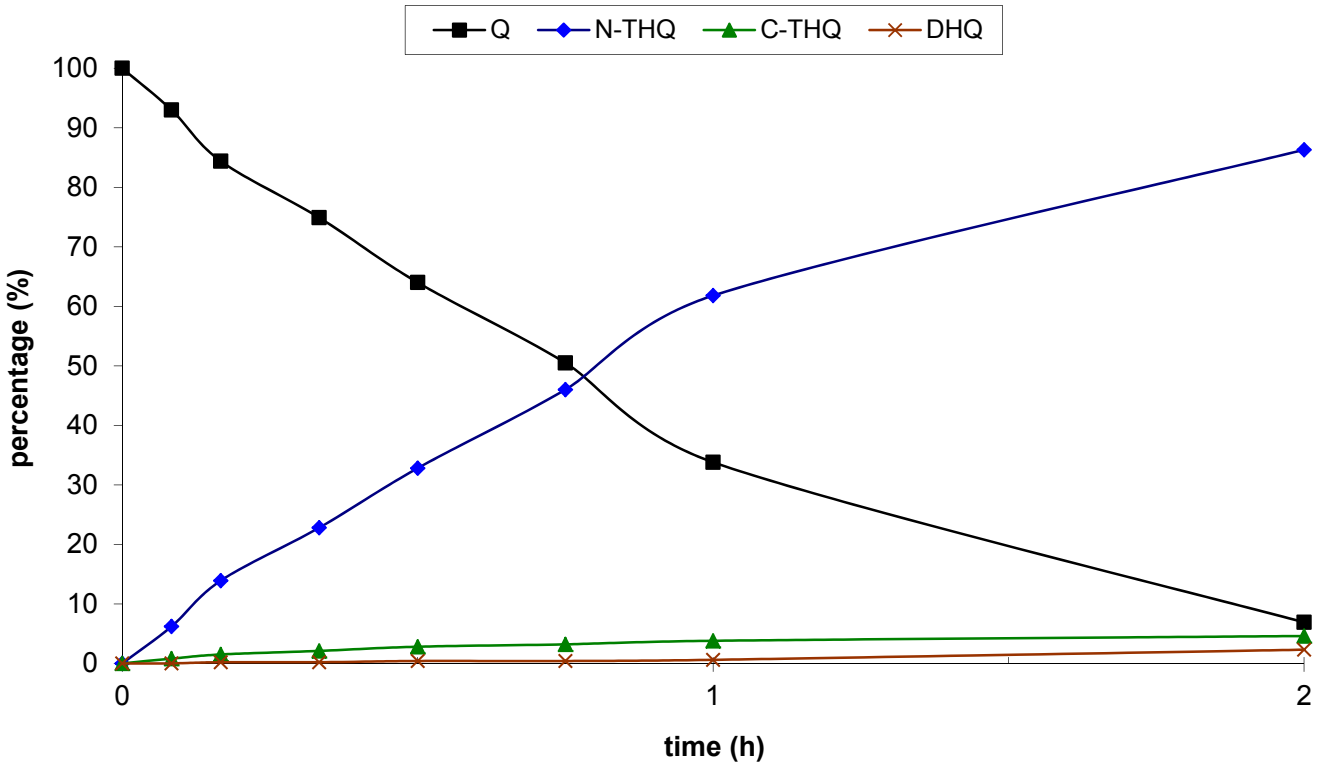

TON vs time

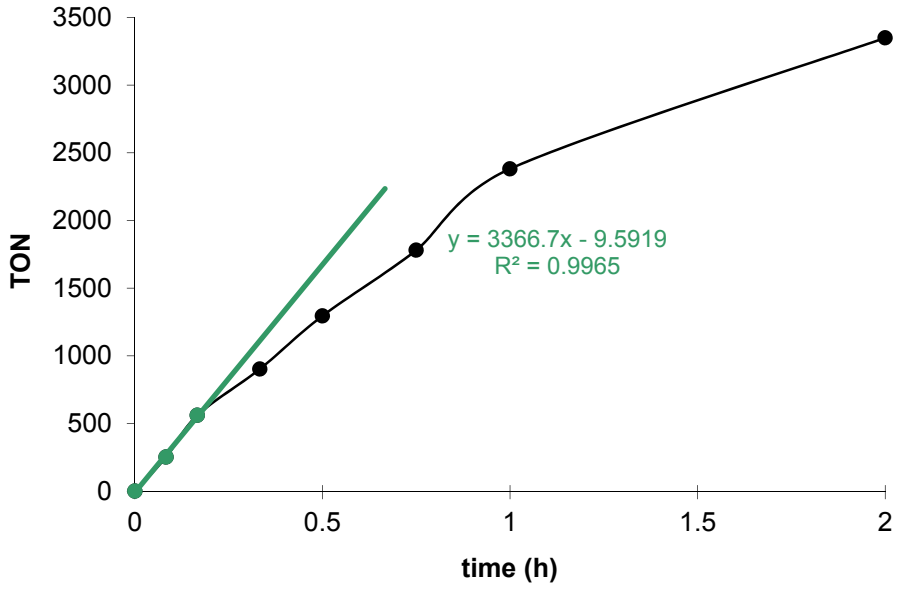

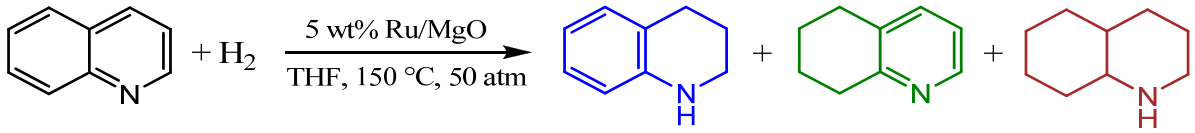

	r.t. /min	→	2.1	3.6	5.9	8.8		
sample	time /min	/h	DHQ%	*C*-THQ%	Q%	*N*-THQ%	[Q] (mol·L^{-1})	TON(Q)
0	0	0	0	0	100	0	1.57	0
1	5	0.08	0.0	0.8	93.0	6.2	1.46	252
2	10	0.17	0.2	1.5	84.4	13.9	1.32	561
3	20	0.33	0.2	2.1	74.9	22.8	1.18	903
4	30	0.50	0.4	2.8	64.0	32.8	1.00	1295
5	45	0.75	0.4	3.2	50.5	46.0	0.79	1780
6	60	1.00	0.6	3.8	33.8	61.8	0.53	2381
7	120	2.00	2.3	4.6	6.9	86.3	0.11	3349
8								
9								
10								
11								

Q concentration vs time

t½ (Q) 0.75 h

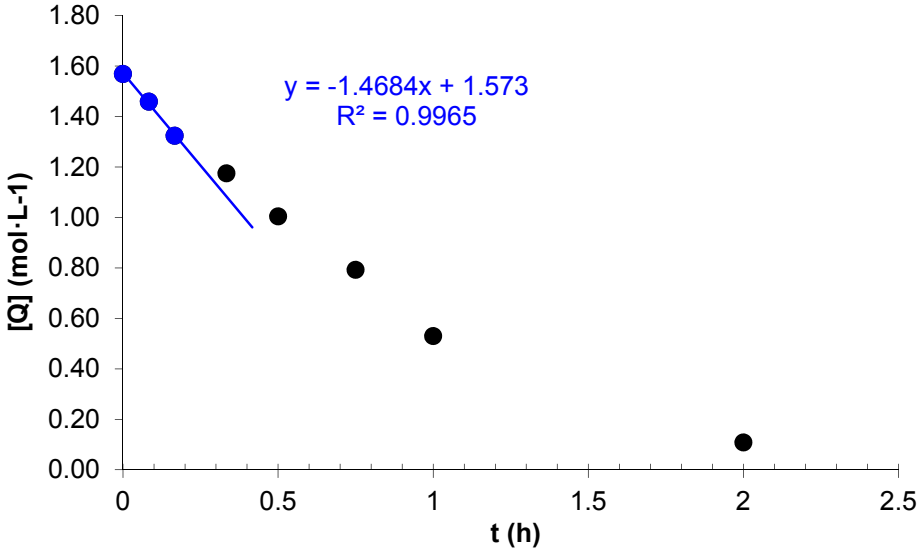

Hydrogenation of quinoline over 5 wt% Ru/MgO(s)

catalyst	100.0 mg = 0.047 mmol Ru	metal loading: 5.0% metal dispersion: 22.5%
substrate	5.7 mL = 48 mmol Q	ρ(Q) = 1.09 g/mL, MW(Q) = 129
n(sub)/n(Ru_s)	4540	
rxn condition	25 mL THF, 150 °C, 50 atm, w/ 1 h incubation	
analysis	column: SP-2330, high polarity column temp: 150 °C 10 min	

Reaction course of hydrogenation of Q over 5 wt% Ru/MgO(s)

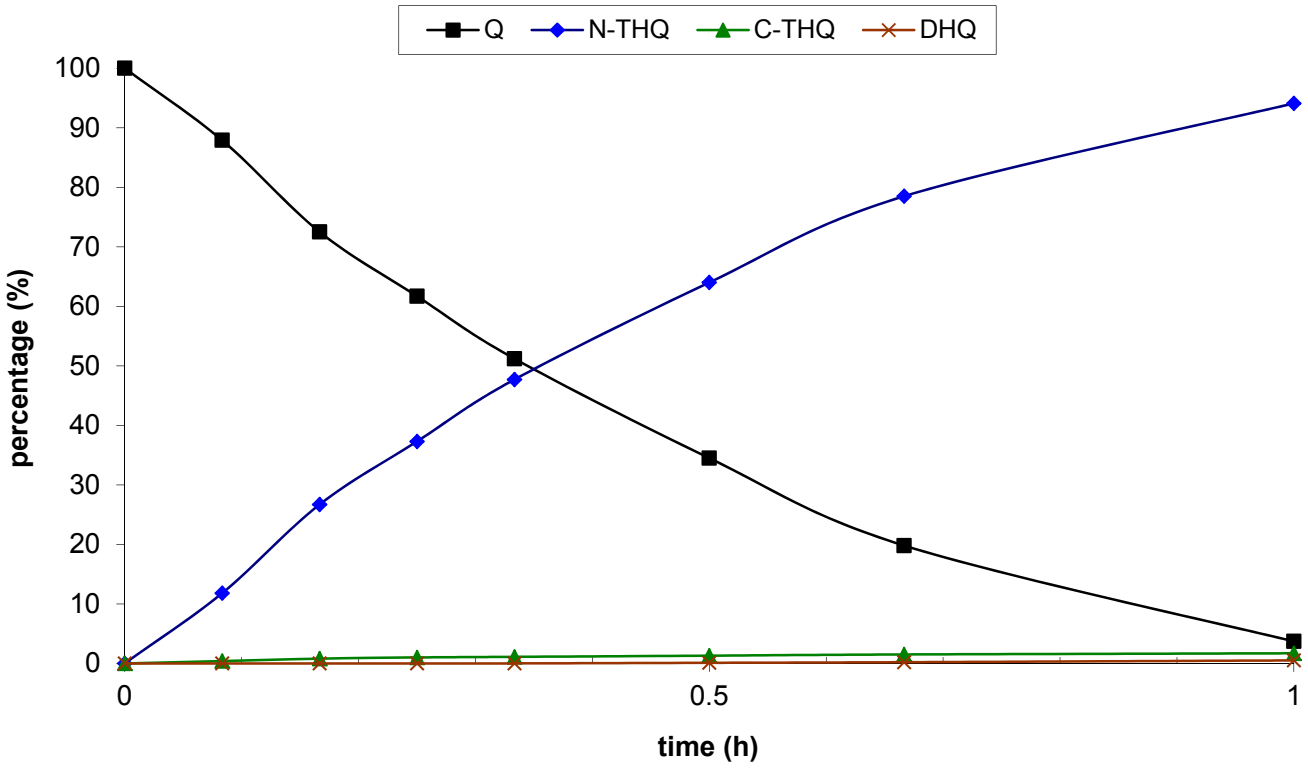

TON vs time

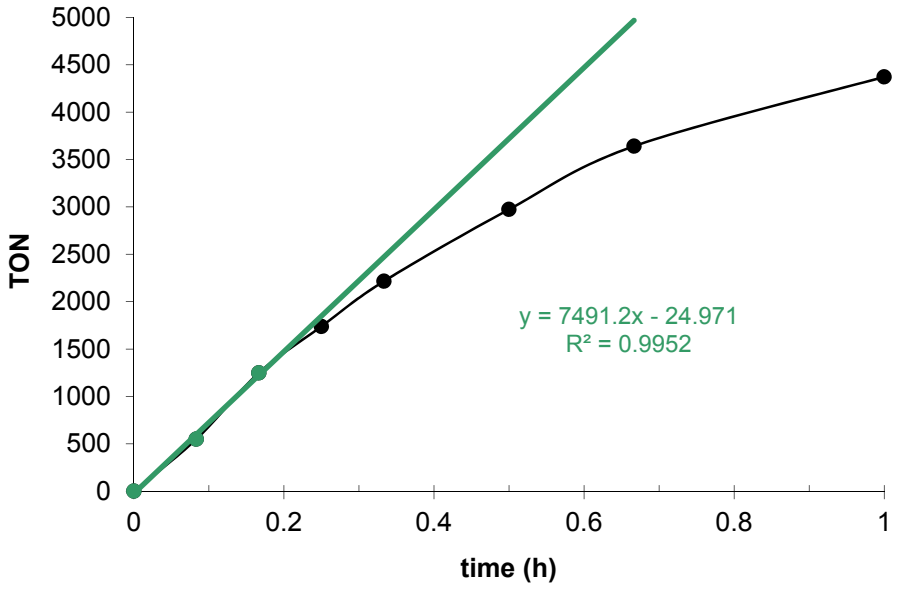

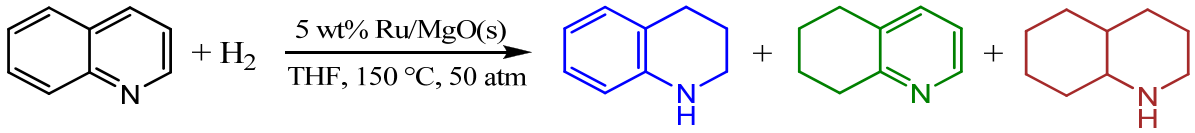

	r.t. /min	→	2.1	3.6	5.9	8.8		
sample	time /min	/h	DHQ%	*C*-THQ%	Q%	*N*-THQ%	[Q] (mol·L^{-1})	TON(Q)
0	0	0	0	0	100	0	1.57	0
1	5	0.08	0.0	0.4	87.9	11.8	1.38	549
2	10	0.17	0.0	0.8	72.5	26.7	1.14	1249
3	15	0.25	0.0	1.0	61.7	37.3	0.97	1739
4	20	0.33	0.0	1.1	51.2	47.7	0.80	2216
5	30	0.50	0.1	1.3	34.5	64.0	0.54	2974
6	40	0.67	0.2	1.5	19.8	78.5	0.31	3641
7	60	1.00	0.5	1.7	3.7	94.1	0.06	4372
8								
9								
10	end, cooled down		0.8	1.7	1.0	96.5		
11								

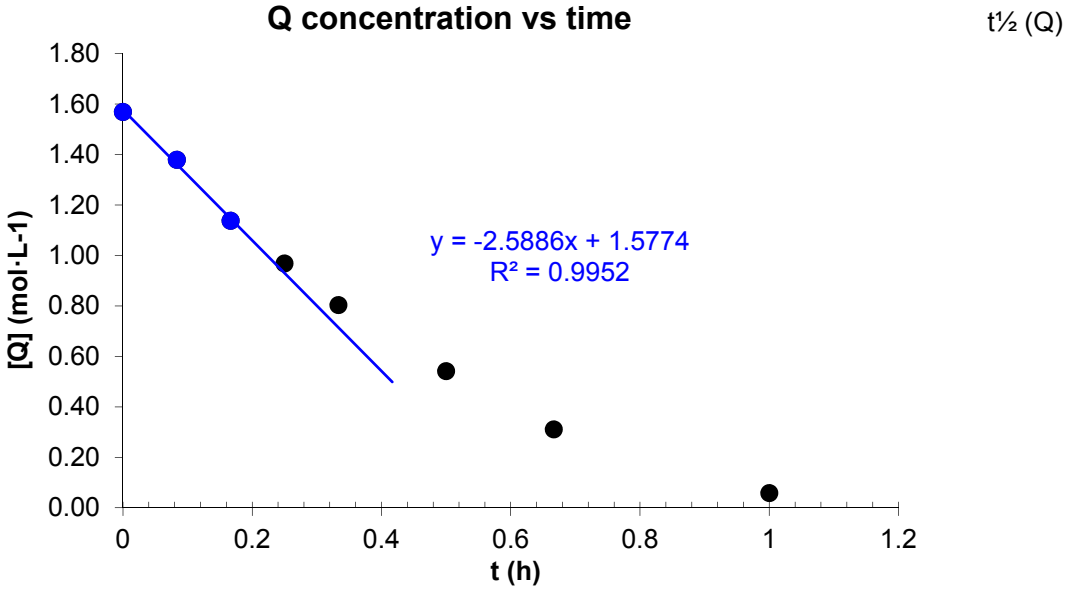

Hydrogenation of acridine over Ru/MgO

catalyst	50.0 mg = 0.024 mmol Ru	metal loading: 5.0% metal dispersion: 28.4%
substrate	0.86 g = 4.8 mmol A	MW(acridine) = 179
n(sub)/n(Ru_s)	718	
rxn condition	30 mL THF, 150 °C, 50 atm, w/ 1 h incubation	50 °C/min; 20 °C/min.
analysis	column: SP-2330, high polarity	column temp: 150 °C 5 min; 200 °C 12min; 220 °C 11 min.

Reaction course of hydrogenation of acridine over 5 wt% Ru/MgO

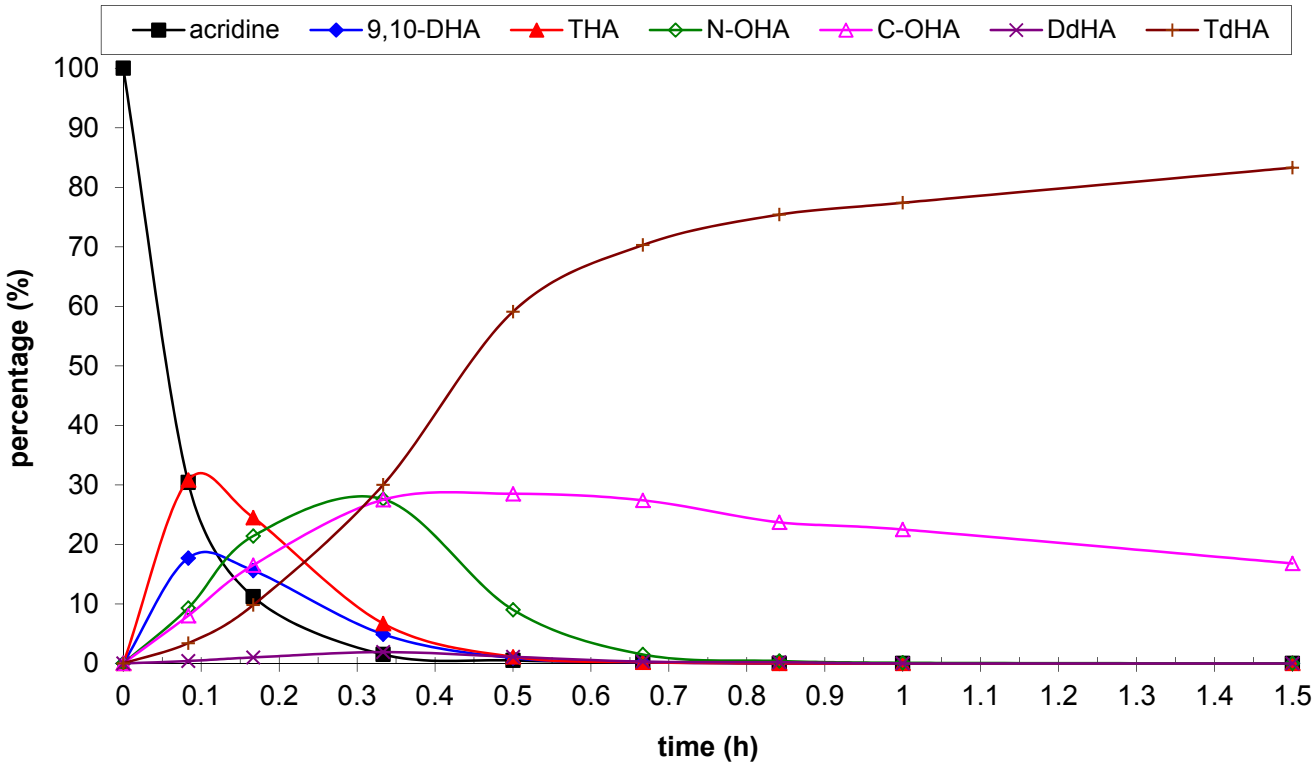

TON vs time

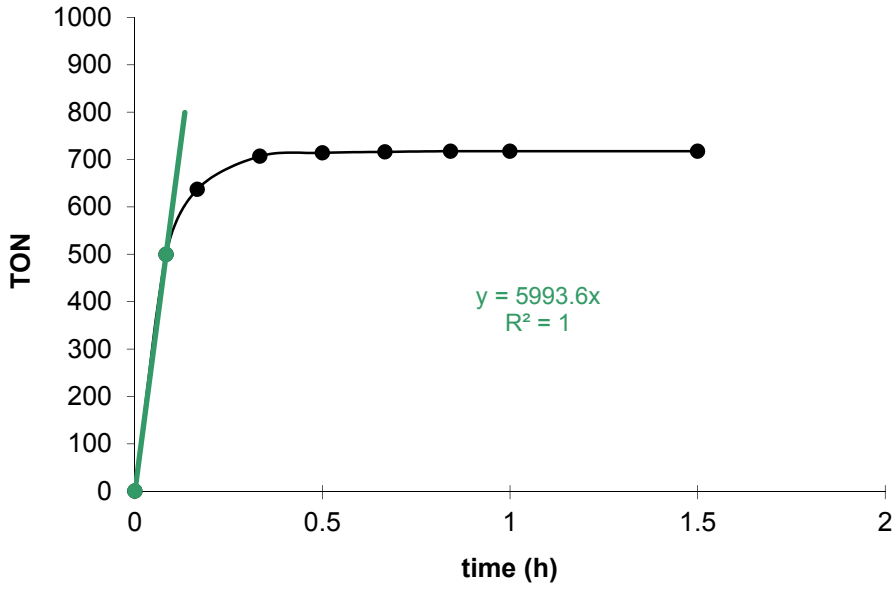

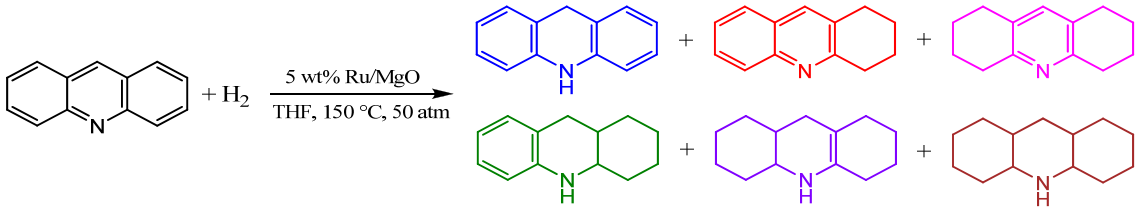

	r.t. /min	→	3.6 & 5.0		8	10.3	11.2	15.6	24.9		
sample	t /min	/h	TdHA	DdHA	*C*-OHA	*N*-OHA	THA	A	9,10-DHA	[A] (mol·L^{-1})	TON(A)
0	0	0	0	0	0	0	0	100	0	0.16	0
1	5	0.08	3.4	0.4	8.0	9.3	30.8	30.4	17.7	0.05	499
2	10	0.17	9.8	1.0	16.5	21.4	24.5	11.2	15.6	0.02	637
3	20	0.33	30.0	1.9	27.5	27.6	6.7	1.5	4.9	0.00	707
4	30	0.50	59.1	1.1	28.5	9.0	1.1	0.5	0.9	0.00	714
5	40	0.67	70.3	0.3	27.4	1.5	0.2	0.2	0.2	0.00	716
6	50.5	0.84	75.4	0.2	23.7	0.4	0.0	0.0	0.0	0.00	718
7	60	1.00	77.4	0.0	22.5	0.1	0.0	0.0	0.0	0.00	718
8	90	1.50	83.3	0.0	16.8	0.0	0.0	0.0	0.0	0	718
9											
10											
11											

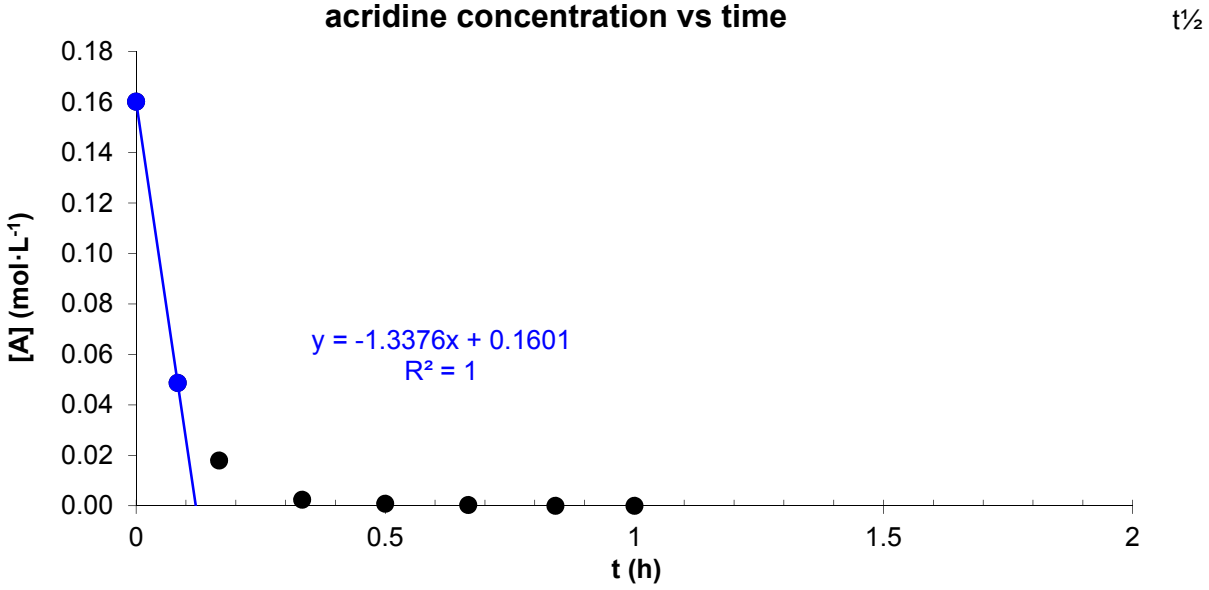

Bibliography

1. Department of Energy - Fossil Fuels. http://www.energy.gov/energysources/fossilfuels.htm (accessed 2011).
2. *Trends in Renewable Energy Consumption and Electricity 2009;* U.S. Energy Information Administration, Washington, DC, 2011.
3. *Annual Energy Outlook 2010, with Projections to 2035;* U.S. Energy Information Administration, Washington, DC, 2010.
4. International Energy Agency. *World Energy Outlook 2010;* Paris, France, 2010.
5. Speight, J. G. *The Chemistry and Technology of Petroleum,* 4th ed.; CRC Press: Boca Raton, FL, 2007; p 178.
6. Regulation of Fuels and Fuel Additives. *Code of Federal Regulations,* Part 80, Title 40, 2011.
7. European Commission. Directive 2009/30/EC of the European parliament and of the council of 23 April 2009 amending directive 98/70/EC as regards the specification of petrol, diesel and gas-oil and introducing a mechanism to monitor and reduce greenhouse gas emissions and amending council directive 1999/32/EC as regards the specification of fuel used by inland waterway vessels and repealing directive 93/12/EEC. *OJ L* 140 of 5.6.2009, 88–113.
8. The California Reformulated Gasoline Regulations. *California Code of Regulations,* Sections 2250-2273.5, Title 13, 2008.
9. The California Diesel Fuel Regulations. *California Code of Regulations,* Sections 2281-2285, Title 13; Section 93114, Title 17, 2004.
10. *Hydroprocessing of Heavy Oils and Residua;* Speight, J. G.; Ancheyta, J., Eds.; CRC Press: Boca Raton, FL, 2007.
11. Sánchez-Delgado, R. A. *Organometallic Modeling of the Hydrodesulfurization and Hydrodenitrogenation Reactions;* Kluwer Academic: Dordrecht, 2002.
12. Topsøe, H.; Clausen, B. S.; Massoth, F. E. In *Hydrotreating Catalysis;* Anderson, J. R., Boudart, M., Eds.; Catalysis Science and Technology, Vol. 11; Springer-Verlag: Berlin, 1996.
13. Stanislaus, A.; Cooper, B. H. Aromatic Hydrogenation Catalysis: A Review. *Cat. Rev. Sci. Eng.* **1994,** *36* (1), 75-123.
14. Ponec, V.; Bond, G. C. In *Catalysis by Metals and Alloys;* Delmon, B., Yates, J. T., Eds.; Studies in Surface Science and Catalysis, Vol. 95; Elsevier: Amsterdam, 1995.
15. Bond, G. C. *Metal-Catalysed Reactions of Hydrocarbons;* Springer: New York, 2005.
16. Astruc, D.; Lu, F.; Aranzaes, J. R. Nanoparticles as recyclable catalysts: The frontier between homogeneous and heterogeneous catalysis. *Angew. Chem. Int. Ed.* **2005,** *44* (48), 7852-7872.
17. Sandoval, C. A.; Ohkuma, T.; Muniz, K.; Noyori, R. Mechanism of asymmetric hydrogenation of ketones catalyzed by BINAP/1,2-diamine-ruthenium(II) complexes. *J. Am. Chem. Soc.* **2003,** *125* (44), 13490-13503.
18. Breysse, M.; Furimsky, E.; Kasztelan, S.; Lacroix, M.; Perot, G. Hydrogen activation by transition metal sulfides. *Cat. Rev. Sci. Eng.* **2002,** *44* (4), 651-735.

19. Frey, M. Hydrogenases: Hydrogen-activating enzymes. *Chembiochem* **2002,** *3* (2-3), 153-160.
20. Astruc, D., Ed. *Nanoparticles and Catalysis;* Wiley-VCH: Weinheim, Germany, 2008.
21. Ertl, G.; Knozinger, H.; Schuth, F.; Weitkamp, J., Eds. *Handbook of Heterogeneous Catalysis,* 2nd ed.; Wiley-VCH: Weinheim, Germany, 2008.
22. de Jong, K. P., Ed. *Synthesis of Solid Catalysts;* Wiley-VCH: Weinheim, Germany, 2009.
23. Liang, C. H.; Wei, Z. B.; Xin, Q.; Li, C. Ammonia synthesis over Ru/C catalysts with different carbon supports promoted by barium and potassium compounds. *Appl. Catal., A* **2001,** *208* (1-2), 193-201.
24. Zhang, Z. G.; Jackson, J. E.; Miller, D. J. Aqueous-phase hydrogenation of lactic acid to propylene glycol. *Appl. Catal., A* **2001,** *219* (1-2), 89-98.
25. Su, F.; Lee, F. Y.; Lv, L.; Liu, J.; Tian, X. N.; Zhao, X. S. Sandwiched ruthenium/carbon nanostructures for highly active heterogeneous hydrogenation. *Adv. Funct. Mater.* **2007,** *17* (12), 1926-1931.
26. Su, F.; Lv, L.; Lee, F. Y.; Liu, T.; Cooper, A. I.; Zhao, X. S. Thermally reduced ruthenium nanoparticles as a highly active heterogeneous catalyst for hydrogenation of monoaromatics. *J. Am. Chem. Soc.* **2007,** *129* (46), 14213-14223.
27. Mazzieri, V.; Coloma-Pascual, F.; Arcoya, A.; L'Argentiere, P.; Figoli, N. S. XPS, FTIR and TPR characterization of Ru/Al2O3 catalysts. *Appl. Surf. Sci.* **2003,** *210* (3-4), 222-230.
28. Okal, J.; Zawadzki, M.; Kepinski, L.; Krajczyk, L.; Tylus, W. The use of hydrogen chemisorption for the determination of Ru dispersion in Ru/gamma-alumina catalysts. *Appl. Catal., A* **2007,** *319*, 202-209.
29. Kumar, N.; Maki-Arvela, P.; Hajek, J.; Salmi, T.; Murzin, D. Y.; Heikkila, T.; Laine, E.; Laukkanen, P.; Vayrynen, J. Physico-chemical and catalytic properties of Ru-MCM-41 mesoporous molecular sieve catalyst: influence of Ru modification methods. *Microporous Mesoporous Mater.* **2004,** *69* (3), 173-179.
30. Zhou, X.; Wu, T.; Hu, B.; Jiang, T.; Han, B. Ru nanoparticles stabilized by poly(N-vinyl-2-pyrrolidone) grafted onto silica: Very active and stable catalysts for hydrogenation of aromatics. *J. Mol. Catal. A: Chem.* **2009,** *306* (1-2), 143-148.
31. Sun, Y.-P.; Fu, H.-Y.; Zhang, D.-l.; Li, R.-X.; Chen, H.; Li, X.-J. Complete hydrogenation of quinoline over hydroxyapatite supported ruthenium catalyst. *Catal. Commun.* **2010,** *12* (3), 188-192.
32. Hulea, V.; Brunel, D.; Galarneau, A.; Philippot, K.; Chaudret, B.; Kooyman, P. J.; Fajula, F. Synthesis of well-dispersed ruthenium nanoparticles inside mesostructured porous silica under mild conditions. *Microporous Mesoporous Mater.* **2005,** *79* (1-3), 185-194.
33. Marconi, G.; Pertici, P.; Evangelisti, C.; Caporusso, A. M.; Vitulli, G.; Capannelli, G.; Hoang, M.; Turney, T. W. Nanostructured ruthenium on gamma-Al2O3 catalysts for the efficient hydrogenation of aromatic compounds. *J. Organomet. Chem.* **2004,** *689* (3), 639-646.
34. Spitaleri, A.; Pertici, P.; Scalera, N.; Vitulli, G.; Hoang, M.; Turney, T. W.; Gleria, M. Supported ruthenium nanoparticles on polyorganophosphazenes: preparation, structural and catalytic studies. *Inorg. Chim. Acta* **2003,** *352*, 61-71.

35. Kantam, M. L.; Rao, B. P. C.; Choudary, B. M.; Sreedhar, B. Selective transfer hydrogenation of carbonyl compounds by ruthenium nanoclusters supported on alkali-exchanged zeolite beta. *Adv. Synth. Catal.* **2006,** *348* (14), 1970-1976.
36. Kusserow, B.; Schimpf, S.; Claus, P. Hydrogenation of glucose to sorbitol over nickel and ruthenium catalysts. *Adv. Synth. Catal.* **2003,** *345* (1-2), 289-299.
37. Zhang, Y.; Kang, D. F.; Aindow, M.; Erkey, C. Preparation and characterization of ruthenium/carbon aerogel nanocomposites via a supercritical fluid route. *J. Phys. Chem. B* **2005,** *109* (7), 2617-2624.
38. Larichev, Y. V. Valence state study of supported ruthenium Ru/MgO catalysts. *J. Phys. Chem. C* **2008,** *112* (38), 14776-14780.
39. Larichev, Y. V.; Moroz, B. L.; Zaikovskii, V. I.; Yunusov, S. M.; Kalyuzhnaya, E. S.; Shur, V. B.; Bukhtiyarov, V. I. XPS and TEM studies on the role of the support and alkali promoter in Ru/MgO and Ru-Cs+/MgO catalysts for ammonia synthesis. *J. Phys. Chem. C* **2007,** *111* (26), 9427-9436.
40. Sanchez-Delgado, R. A.; Machalaba, N.; Ng-a-qui, N. Hydrogenation of quinoline by ruthenium nanoparticles immobilized on poly(4-vinylpyridine). *Catal. Commun.* **2007,** *8* (12), 2115-2118.
41. Miyazaki, A.; Balint, L.; Aika, K.; Nakano, Y. Preparation of Ru nanoparticles supported on gamma-Al2O3 and its novel catalytic activity for ammonia synthesis. *J. Catal.* **2001,** *204* (2), 364-371.
42. Balint, I.; Miyazaki, A.; Aika, K. Methane reaction with NO over alumina-supported Ru nanoparticles. *J. Catal.* **2002,** *207* (1), 66-75.
43. Perkas, N.; Zhong, Z. Y.; Chen, L. W.; Besson, M.; Gedanken, A. Sonochemically prepared high dispersed Ru/TiO2 mesoporous catalyst for partial oxidation of methane to syngas. *Catal. Lett.* **2005,** *103* (1-2), 9-14.
44. Xu, Q. C.; Lin, J. D.; Fu, X. Z.; Liao, D. W. Effects of solvent stabilizer in the preparation of highly active potassium-promoted Ru/MgO catalysts for ammonia synthesis. *Catal. Commun.* **2008,** *9* (6), 1214-1218.
45. Zahmakiran, M.; Tonbul, Y.; Ozkar, S. Ruthenium(0) nanoclusters supported on hydroxyapatite: highly active, reusable and green catalyst in the hydrogenation of aromatics under mild conditions with an unprecedented catalytic lifetime. *Chem. Commun.* **2010,** *46* (26), 4788-4790.
46. Zahmakiran, M.; Kodaira, T.; Ozkar, S. Ruthenium(0) nanoclusters stabilized by zeolite framework as superb catalyst for the hydrogenation of neat benzene under mild conditions: Additional studies including cation site occupancy, catalytic activity, lifetime, reusability and poisoning. *Appl. Catal., B* **2010,** *96* (3-4), 533-540.
47. Zahmakiran, M.; Tonbul, Y.; Ozkar, S. Ruthenium(0) Nanoclusters Stabilized by a Nanozeolite Framework: Isolable, Reusable, and Green Catalyst for the Hydrogenation of Neat Aromatics under Mild Conditions with the Unprecedented Catalytic Activity and Lifetime. *J. Am. Chem. Soc.* **2010,** *132* (18), 6541-6549.
48. Moggi, P.; Predieri, G.; Maione, A. Ru/MgO sol-gel prepared catalysts for ammonia synthesis. *Catal. Lett.* **2002,** *79* (1-4), 7-15.
49. Iwamoto, J.; Itoh, M.; Kajita, Y.; Saito, M.; Machida, K. Ammonia synthesis on magnesia supported ruthenium catalysts with mesoporous structure. *Catal. Commun.* **2007,** *8* (6), 941-944.

50. http://www.nobelprize.org/educational/physics/microscopes/tem/images/tem1-2.gif (accessed 2012).
51. http://users.humboldt.edu/rpaselk/C431.F08/C431Notes/C431nLec12_slide.htm (accessed 2012).
52. http://www.texample.net/media/tikz/examples/PNG/principle-of-x-ray-photoelectron-spectroscopy-xps.png (accessed 2012).
53. Takasaki, M.; Motoyama, Y.; Higashi, K.; Yoon, S.-H.; Mochida, I.; Nagashima, H. Ruthenium nanoparticles on nano-level-controlled carbon supports as highly effective catalysts for arene hydrogenation. *Chem. Asian J.* **2007,** *2* (12), 1524-1533.
54. Bianchini, C.; Dal Santo, V.; Meli, A.; Moneti, S.; Moreno, M.; Oberhauser, W.; Psaro, R.; Sordelli, L.; Vizza, F. A comparison between silica-immobilized ruthenium(II) single sites and silica-supported ruthenium nanoparticles in the catalytic hydrogenation of model hetero- and polyaromatics contained in raw oil materials. *J. Catal.* **2003,** *213* (1), 47-62.
55. Huang, J.; Jiang, T.; Han, B. X.; Wu, W. Z.; Liu, Z. M.; Xie, Z. L.; Zhang, J. L. A novel method to immobilize Ru nanoparticles on SBA-15 firmly by ionic liquid and hydrogenation of arene. *Catal. Lett.* **2005,** *103* (1-2), 59-62.
56. Boujday, S.; Blanchard, J.; Villanneau, R.; Krafft, J.-M.; Geantet, C.; Louis, C.; Breysse, M.; Proust, A. Polyoxomolybdate-stabilized Ru-0 nanoparticles deposited on mesoporous silica as catalysts for aromatic hydrogenation. *ChemPhysChem* **2007,** *8* (18), 2636-2642.
57. Miao, S.; Liu, Z.; Han, B.; Huang, J.; Sun, Z.; Zhang, J.; Jiang, T. Ru nanoparticles immobilized on montmorillonite by ionic liquids: a highly efficient heterogeneous catalyst for the hydrogenation of benzene. *Angew. Chem. Int. Ed.* **2005,** *45* (2), 266-9.
58. Song, L.; Li, X.; Wang, H.; Wu, H.; Wu, P. Ru Nanoparticles Entrapped in Mesopolymers for Efficient Liquid-phase Hydrogenation of Unsaturated Compounds. *Catal. Lett.* **2009,** *133* (1-2), 63-69.
59. Corain, B.; Kralik, M. Dispersing metal nanoclusters inside functional synthetic resins: scope and catalytic prospects. *J. Mol. Catal. A: Chem.* **2000,** *159* (2), 153-162.
60. Kralik, M.; Biffis, A. Catalysis by metal nanoparticles supported on functional organic polymers. *J. Mol. Catal. A: Chem.* **2001,** *177* (1), 113-138.
61. Malynych, S.; Luzinov, I.; Chumanov, G. Poly(vinyl pyridine) as a universal surface modifier for immobilization of nanoparticles. *J. Phys. Chem. B* **2002,** *106* (6), 1280-1285.
62. Hoffmann, M.; Lima Neto, B.; Massabni, A.; Franco, D. Synthesis and characterization of ruthenium complexes immobilized on poly(4-vinylpyridine). *J. Inorg. Organomet. Polym.* **1993,** *3* (2), 155-168.
63. Ramos, J.; Millan, A.; Palacio, F. Production of magnetic nanoparticles in a polyvinylpyridine matrix. *Polymer* **2000,** *41* (24), 8461-8464.
64. Sulman, E.; Bodrova, Y.; Matveeva, V.; Semagina, N.; Cerveny, L.; Kurtc, V.; Bronstein, L.; Platonova, O.; Valetsky, P. Hydrogenation of dehydrolinalool with novel catalyst derived from Pd colloids stabilized in micelle cores of polystyrene-poly-4-vinylpyridine block copolymers. *Appl. Catal., A* **1999,** *176* (1), 75-81.
65. Bronstein, L. M.; Chernyshov, D. M.; Volkov, I. O.; Ezernitskaya, M. G.; Valetsky, P. M.; Matveeva, V. G.; Sulman, E. M. Structure and properties of bimetallic

colloids formed in polystyrene-block-poly-4-vinylpyridine micelles: Catalytic behavior in selective hydrogenation of dehydrolinalool. *J. Catal.* **2000,** *196* (2), 302-314.
66. Drelinkiewicza, A.; Waksmundzka, A.; Makowski, W.; Sobczak, J. W.; Krol, A.; Zieba, A. Acetophenone hydrogenation on polymer-palladium catalysts. The effect of polymer matrix. *Catal. Lett.* **2004,** *94* (3-4), 143-156.
67. Powder Diffraction File, Card # 06-0663, PDF-2/Release 2004; International Center for Diffraction Data (ICDD), Newton Square, PA, USA.
68. Moulder, J. F.; Stickle, W. F.; Sobol, P. E.; Bomben, K. D. In *Handbook of X-ray Photoelectron Spectroscopy: a Reference Book of Standard Spectra for Identification and Interpretation of XPS Data;* Chastain, J., Ed.; Perkin-Elmer: Eden Prairie, MN, 1992.
69. Beamson, G; Briggs, D. *High Resolution XPS of Organic Polymers: The Scienta ESCA300 Database;* John Wiley & Sons: Chichester, UK, 1992.
70. Crabtree, R. H. *The Organometallic Chemistry of the Transition Metals,* 5th ed.; John Wiley & Sons: Hoboken, NJ, 2009.
71. Fang, M.; Machalaba, N.; Sanchez-Delgado, R. A. Hydrogenation of arenes and N-heteroaromatic compounds over ruthenium nanoparticles on poly(4-vinylpyridine): a versatile catalyst operating by a substrate-dependent dual site mechanism. *Dalton Trans.* **2011,** *40* (40), 10621-10632.
72. Fonseca, G. S.; Silveira, E. T.; Gelesky, M. A.; Dupont, J. Competitive hydrogenation of alkyl-substituted arenes by transition-metal nanoparticles: Correlation with the alkyl-steric effect. *Adv. Synth. Catal.* **2005,** *347* (6), 847-853.
73. Campanati, M.; Vaccari, A.; Piccolo, O. Mild hydrogenation of quinoline 1. Role of reaction parameters. *J. Mol. Catal. A: Chem.* **2002,** *179* (1-2), 287-292.
74. Ardizzone, S.; Bianchi, C. L.; Vercelli, B. MgO powders: interplay between adsorbed species and localisation of basic sites. *Appl. Surf. Sci.* **1998,** *126* (1-2), 169-175.
75. Ardizzone, S.; Bianchi, C. L.; Vercelli, B. Acid/base and surface features of pure phase magnesia powders. *Colloid Surf. A-Physicochem. Eng. Asp.* **1998,** *144* (1-3), 9-17.
76. Cortes-Concepcion, J. A.; Patcas, F.; Amiridis, M. D. Effect of Li on the catalytic activity of MgO for the synthesis of flavanone. *Appl. Catal., A* **2010,** *386* (1-2), 1-8.
77. http://www.fhi-berlin.mpg.de/~hermann/Balsac/BalsacPictures/MgOlattice.gif (accessed 2012).
78. Hattori, H. HETEROGENEOUS BASIC CATALYSIS. *Chem. Rev.* **1995,** *95* (3), 537-558.
79. Hattori, H. Solid base catalysts: generation of basic sites and application to organic synthesis. *Appl. Catal., A* **2001,** *222* (1-2), 247-259.
80. Hornung, A.; Muhler, M.; Ertl, G. The reduction of NO with H-2 over Ru/MgO. *Catal. Lett.* **1998,** *53* (1-2), 77-81.
81. Hornung, A.; Muhler, M.; Ertl, G. On the mechanism of the selective catalytic reduction of NO to N-2 by H-2 over Ru/MgO and Ru/Al2O3 catalysts. *Top. Catal.* **2000,** *11* (1-4), 263-270.
82. Kantam, M. L.; Reddy, R. S.; Pal, U.; Sreedhar, B.; Bhargava, S. Transfer Hydrogenation of Carbonyl Compounds Catalyzed by Ruthenium Nanoparticles Stabilized on Nanocrystalline Magnesium Oxide by Ionic Liquids. *Adv. Synth. Catal.* **2008,** *350* (14-15), 2231-2235.
83. Powder Diffraction File, Card # 65-0476, PDF-2/Release 2004; International Center for Diffraction Data, Newton Square, PA, USA.

84. Peng, X.; Barteau, M. A. Acid-base properties of model magnesium oxide surfaces. *Langmuir* **1991,** *7* (7), 1426-1431.
85. Umpierre, A. P.; de Jesus, E.; Dupont, J. Turnover Numbers and Soluble Metal Nanoparticles. *ChemCatChem* **2011,** *3* (9), 1413-1418.
86. Mevellec, V.; Roucoux, A. Nanoheterogeneous catalytic hydrogenation of N-, O- or S -heteroaromatic compounds by re-usable aqueous colloidal suspensions of rhodium(0). *Inorg. Chim. Acta* **2004,** *357* (10), 3099-3103.
87. Beckers, N. A.; Huynh, S.; Zhang, X.; Luber, E. J.; Buriak, J. M. Screening of Heterogeneous Multimetallic Nanoparticle Catalysts Supported on Metal Oxides for Mono-, Poly-, and Heteroaromatic Hydrogenation Activity. *ACS Catal.* **2012,** *2*, 1524-1534.
88. Meille, V.; Schulz, E.; Lemaire, M.; Vrinat, M. Hydrodesulfurization of alkyldibenzothiophenes over a NiMo/Al2O3 catalyst: Kinetics and mechanism. *J. Catal.* **1997,** *170* (1), 29-36.